2015

CATALIZADORES NANOESTRUCTURADOS PARA REACCIONES
INVOLUCRADAS EN LAS PILAS DE COMBUSTIBLE DE ALCOHOL DIRECTO

J.F.M

ULL Universidad de La Laguna

TESIS DOCTORAL

CATALIZADORES NANOESTRUCTURADOS PARA REACCIONES INVOLUCRADAS EN LAS PILAS DE COMBUSTIBLE DE ALCOHOL DIRECTO

JONATHAN FLÓREZ MONTAÑO

IΣN INSTITUTO UNIVERSITARIO de MATERIALES Y NANOTECNOLOGÍA

Directora: **Elena Pastor Tejera**
Co-director: **José Luis Rodríguez Marrero**
Co-director: **Gabriel Ángel Planes**

2015

Universidad
de La Laguna

Departamento de Química

ELENA PASTOR TEJERA Y JOSÉ LUIS RODRIGUEZ MARRERO, PROFESORES TITULARES DEL DEPARTAMENTO DE QUÍMICA DE LA UNIVERSIDAD DE LA LAGUNA, Y GABRIEL ANGEL PLANES, INVESTIGADOR ADJUNTO DEL CONSEJO NACIONAL DE INVESTIGACIONES CIENTIFICAS Y TECNICAS, EN CALIDAD DE DIRECTORA Y CO-DIRECTORES, RESPECTIVAMENTE, DE LA PRESENTE TESIS DOCTORAL

INFORMAN

Que la presente memoria de Tesis titulada: **CATALIZADORES NANOESTRUCTURADOS PARA REACCIONES INVOLUCRADAS EN LAS PILAS DE COMBUSTIBLE DE ALCOHOL DIRECTO**, presentada por D. Jonathan Flórez Montaño para optar al grado de Doctor en Química por la Universidad de La Laguna, ha sido realizada bajo nuestra dirección en los laboratorios del Departamento de Química de la Universidad de La Laguna, y autorizamos con esta fecha su presentación para que pueda procederse a su lectura y defensa pública.

San Cristóbal de La Laguna, a 13 de noviembre de 2015.

Fdo.: Dra. Elena Pastor Tejera

Fdo.: Dr. José Luis Rodríguez Marrero

Fdo.: Dr. Gabriel Ángel Planes

ULL
Universidad
de La Laguna

IΣN INSTITUTO UNIVERSITARIO de
MATERIALES Y
NANOTECNOLOGÍA

TESIS DOCTORAL

CATALIZADORES NANOESTRUCTURADOS PARA REACCIONES INVOLUCRADAS EN LAS PILAS DE COMBUSTIBLE DE ALCOHOL DIRECTO

JONATHAN FLÓREZ MONTAÑO

Diciembre 2015

Directora: **Elena Pastor Tejera**
Profesora Titular del Dpto. de Química
Universidad de La Laguna (España)

Co-director: **José Luis Rodríguez Marrero**
Profesor Titular del Dpto. de Química
Universidad de La Laguna (España)

Co-director: **Gabriel Ángel Planes**
Investigador Adjunto del CONICET
Universidad Nacional de Rio Cuarto (Argentina)

A mis hijos Santiago y Catalina, Nadja, mis hermanos

y la memoria de mis padres Anselmo y Sofía.

"La ciencia será siempre una búsqueda, jamás un descubrimiento real.

Es un viaje, nunca una llegada"

Karl Raiumd Popper

"A Person Who Never Made a Mistake, Never Tried Anything New"

Albert Einstein

AGRADECIMIENTOS

Ha sido un largo camino que no solo me ha permitido crecer a nivel profesional sino también en lo personal. Y esto no lo habría conseguido de no ser por todas las personas que me han acompañado y me echaron una mano para superar los diferentes miedos y obstáculos con los que me he encontrado, personas de las que estoy totalmente agradecida.

Quiero agradecer a la Dra. Elena Pastor, primero por brindarme la oportunidad de venir a trabajar a Tenerife y por el apoyo constante que me permitió culminar con éxito esta tesis doctoral, así como también a mis co-directores Dr. Gabriel Planes y Dr. José Luis Rodríguez por sus consejos dentro y fuera del laboratorio.

También agradecer de manera muy especial a Olmedo y Yurima por hacerme sentir parte de su familia desde el primer momento que pise tierras tinerfeñas. Así mismo, deseo dar mi más sincero agradecimiento a mis amigos y compañeros de laboratorio, Lucho, Juan Carlitos, Rubén, Gonzalo y Alejandro quienes lograron que trabajar en este grupo sea un aprendizaje constante junto a innumerables risas.

A la Agencia Canaria de Investigación, Innovación y Sociedad de la Información por la beca pre-doctoral del Gobierno de Canarias. A la UD de Química Física y Al personal del SEGAI que fueron parte importante en el desarrollo de mi trabajo, en especial a Juan Luis, Fernando, Celso y María del Pino.

Agradecer también a las personas con las que colaboré en el grupo CSE y dejaron su granito de arena en mi formación, Verónica, Daniela, Dalila, el profe Marco, Katia,

America, Fabiola, Carlicos, Azgardi, Vicente, Dani Sara, Dani, Thais, Miguel, Maricarmen, Jacob, Bea, Etienne, John, Alfredo y William. Y por supuesto, a aquellos que me acogieron y con los que trabajé durante mis estancias en La Universidad Nacional de Rio Cuarto (Argentina), Angélica, Paula, Rusbel y Pablo. Al Dr. Gaetano Granozzi y su grupo de ciencia de superficies en la Università degli studi di Padova (Italia) por permitirme trabajar y acogerme en su grupo.

A mi familia que desde muy lejos me han brindado su apoyo incondicional y me apoyaron en los momentos más difíciles. A Diana, Carlos, Jorge, Carla con los que compartí momentos inolvidables

A mis amigos y compañeros del equipo de Ultimate Frisbee Guayota y toda la familia ultimatera con los que he compartido momentos inolvidables detrás de un frisbee. A la gente que convivió conmigo en la calle catedral 17 y calle Pasteur 12, y todos aquellos que aportaron de alguna u otra forma su granito de arena en este viaje.

Por último y no menos importante, agradecer profundamente a la persona que ha caminado conmigo estos últimos años y ha tenido la paciencia y capacidad de aguantarme y apoyarme constantemente. ¿Quién más sino tú? Gracias Nadja por estar siempre y no dejar de creer en mí, contigo las cosas son menos difíciles.

Tabla de contenido

6. ANEXO I (Publicaciones de la Tesis)

7. ANEXO II (Publicaciones relacionadas con la Tesis)

Summary/Resumen

RESUMEN

Las pilas de combustible y los electrolizadores son dispositivos electroquímicos que jugarán un papel muy importante en la implantación de un nuevo sistema energético en el que se empleen fuentes de energía cuya utilización conlleve un menor impacto sobre el medioambiente y la salud humana. El funcionamiento eficiente de los mismos requiere del uso de materiales que catalicen las reacciones electródicas para formar combustibles (en los electrolizadores) y generar energía eléctrica (en las pilas de combustible).

El objetivo central de esta Tesis Doctoral es la síntesis y caracterización de nuevos materiales electrocatalíticos que incrementen la eficiencia energética de las celdas de combustible de membrana de electrolito polimérico y la eficiencia de los electrolizadores en la obtención de combustibles (hidrógeno y biocombustibles).

El reciente avance experimentado por los dispositivos electrónicos a microescala ha motivado el impulso del diseño de micropilas de combustible que garanticen su funcionamiento. Por ello, en este trabajo se propone el desarrollo de catalizadores mesoporosos (MP), los cuales pueden ser preparados *in situ* en la micropila, y además, poseen una elevada área superficial en una baja densidad de volumen. Con este fin se han sintetizado electrodos mesoporosos de Pt (MPPt) y se modificaron superficialmente con adátomos de Ru y Sn (MPPt/Ru y MPPt/Sn). Los electrodos de MPPt presentan una elevada actividad hacia la electrooxidación de metanol, sólo comparable con electrodos de Pt lisos. Esta actividad se suele atribuir a la activación de las moléculas de agua, la presencia de planos cristalográficos apropiados sobre la superficie del metal, y/o a la importancia de la existencia de vías paralelas de reacción. En el presente trabajo se ha realizado un estudio electroquímico *in situ* sobre la influencia de las especies presentes

en la superficie de este tipo de nanoestructuras y su papel en la catálisis de la oxidación de las especies intermedias adsorbidas, y en definitiva, de los alcoholes utilizados como combustible.

La determinación de la estructura morfológica de los catalizadores MP sintetizados se realizó mediante las técnicas de microscopía de efecto túnel (STM) y microscopía de barrido electrónico (SEM). En las primeras etapas de crecimiento del material MP, las imágenes de STM muestran la existencia de canales que dan lugar a la posterior formación de una estructura mesoporosa observada por SEM.

El estudio del comportamiento electroquímico del MPPt y MPPt/Ru por medio de técnicas voltamperométricas y cronoamperométricas, indica que estos electrodos presentan una elevada actividad catalítica hacia la reacción de oxidación de metanol comparados con la aleación de PtRu soportada en carbón comercial, siendo el catalizador MPPt/Ru el que presentó las densidades de corriente más elevadas. Los resultados sugieren que esta elevada actividad catalítica está favorecida por la difusión de las especies reactivas a través de la estructura porosa del electrodo, así como por la disposición de los sitios activos en la superficie del electrodo.

El estudio de la electrooxidación de metanol sobre estos catalizadores mesoporosos mediante la espectrometría de masas diferencial electroquímica (DEMS) ha permitido evaluar y correlacionar la eficiencia de producción de CO_2 con la actividad catalítica y la estructura porosa de estos catalizadores.

El comportamiento electroquímico del MPPt/Sn se estudió a dos temperaturas (25 y 60 ºC) mediante técnicas electroquímicas convencionales, comparando su actividad hacia la oxidación de CO adsorbido y el metanol con el catalizador comercial de PtSn (3:1) soportado en carbón. Se observó que al aumentar la temperatura estos catalizadores aumentan su actividad, siendo ésta más importante en el material mesoporoso. Al evaluar la eficiencia de conversión de metanol hasta CO_2 mediante la técnica DEMS, se registraron en ambas temperaturas mayores densidades de corriente y eficiencia de conversión a CO_2 para el MPPt/Sn frente al catalizador convencional de aleaciones de PtSn/C (3:1). Mediante la espectroscopía fotoelectrónica de rayos X (XPS) fue posible determinar la composición superficial y se identificaron los diferentes estados de oxidación de los metales presentes en los catalizadores.

Los problemas que genera la toxicidad del metanol han llevado al planteamiento de usar otros alcoholes menos tóxicos en las celdas de combustible, como el etanol. En esta línea se han desarrollado los primeros estudios electroquímicos y espectroelectroquímicos (mediante DEMS) de la reactividad del etanol sobre catalizadores MPPt en medio ácido. El estudio a diferentes concentraciones de etanol y la utilización de una nueva configuración del espectrómetro de masas electroquímico, mucho más sensible a la detección de especies formadas en muy bajas cantidades en el transcurso del proceso, han permitido la determinación del mecanismo de reacción. Además, ha sido posible detectar la formación de los principales productos de reacción como el acetaldehído, el ácido acético y el CO_2 durante la electrooxidación, y calcular la eficiencia de conversión a este último.

Los resultados más importantes indican que cuando aumenta la concentración de etanol, se favorecen las reacciones paralelas que llevan a la formación de acetaldehído y ácido acético y se mantiene constante la formación de CO_2. Como consecuencia, las mayores eficiencias de conversión a CO_2 (~11 %) se obtuvieron con las concentraciones más bajas (0,01 M). Los resultados han sido analizados en términos de densidad de corriente, el tipo de sitios activos en la superficie, el potencial aplicado y la concentración de alcohol. Las pendientes de Tafel obtenidas a partir de las cronoamperometrías realizadas, permiten proponer que el paso determinante de velocidad en la reacción de oxidación completa a CO_2 es la reacción de disociación de agua, mientras que en las reacciones paralelas que llevan a la formación de acetaldehído y ácido acético es la deshidrogenación del etanol.

Otro tipo de material investigado durante el desarrollo de esta Tesis Doctoral han sido las nanoestructuras bimetálicas tipo "core shell" (CS), en concreto las formadas por núcleos de Au cubiertas de Pd, y se han utilizado para la electrooxidación de ácido fórmico, dado su posible uso como combustible líquido en pilas de combustible. Mediante las técnicas espectroelectroquímicas de DEMS y la espectroscopía de infrarrojo por transformada de Fourier (FTIRS) se ha estudiado la influencia del espesor de la capa superficial de Pd (1 y 10 nm) en la oxidación de moléculas de CO adsorbido y en la reactividad del ácido fórmico. El análisis por XPS de las estructuras bimetálicas ha permitido determinar la importancia de la formación de los óxidos superficiales y la influencia electrónica del Au sobre la electrocatálisis. A partir de los estudios de DEMS y FTIRS se observó que el potencial de inicio de oxidación de CO adsorbido cambia a potenciales más positivos con el decrecimiento de la capa externa de Pd. Adicionalmente, la espectroscopía FTIR permitió poner de manifiesto el diferente comportamiento de las especies adsorbidas (grupos OH_{ad} y $HCOO_{ad}$) con el espesor de Pd, confirmando la existencia de un efecto electrónico superficial que implica que la oxidación de CO y HCOOH ocurre por diferentes vías en cada uno de los catalizadores estudiados.

Al considerar la capacidad que tienen las estructuras de Pd para absorber hidrógeno y dado el interés existente en generar combustibles a partir de la reducción de CO_2, se evaluó la eficiencia de las nanoestructuras de Au recubiertas de Pd en la reducción electroquímica del CO_2 mediante la técnica DEMS. Los resultados muestran que la eficiencia de conversión se duplica cuando el espesor de la cubierta de Pd disminuye de 10 a 1 nm.

Por último, en el desarrollo de los electrolizadores avanzados para la generación de hidrógeno, la hidrólisis básica del agua resulta muy interesante ya que permite el uso de electrocatalizadores no nobles, como los materiales basados en Ni, que son económicamente muy interesantes. Por ello, teniendo en cuenta los requisitos de alta conductividad del soporte y de alto grado de dispersión del catalizador, se han sintetizado catalizadores de NiMo soportados sobre óxido de grafeno reducido (RGO) para la reacción de evolución de hidrógeno. La caracterización fisicoquímica, realizada por diferentes técnicas de rayos X como XPS, XRD (difracción) y EDX(energía dispersiva), microscopía de fuerza atómica (AFM) y espectroscopía Raman, mostró la formación de nanodiscos de Ni sobre la superficie del grafeno. También se estableció que cuando la síntesis se realiza en presencia de Mo, estos nanodiscos se cubren con capas de óxido de molibdeno amorfo. El estudio realizado por DEMS muestra que este tipo de estructuras presentan una actividad electroquímica mayor cuando se encuentran soportadas sobre RGO que sobre carbón Vulcan XC-72R. Los catalizadores de NiMo con las composiciones 1:3 y 1:2 son los que producen hidrógeno a potenciales más negativos.

SUMMARY

Fuel cells and electrolysers are electrochemical devices that play a very important role in the implementation of a new energy system in which energy sources with lower impact on the environment and human health are used. Their efficient operation requires the use of materials which catalyze the electrode reactions to obtain fuels and electric energy from electrolyzers and fuel cells, respectively.

The objective of this Ph.D. is the synthesis and characterization of new electrocatalytic materials, which increase the energy efficiency of the polymer electrolyte membrane fuel cells and the efficiency of electrolyzers in the production of obtain fuels (hydrogen and biofuels).

The recent development of microscale electronic devices requires micro fuel cells to ensure its operation. So, in this work the development of mesoporous catalysts (MP) with high area surface in a low bulk density, which can be prepared *in situ* in the micro fuel cell, has been proposed. With this purpose, mesoporous Pt electrodes (MPPt) and surface-modified with Ru and Sn adatoms (MPPt/Ru and MPPt/Sn, respectively) were synthesized. MPPt electrodes show high activity toward methanol electrooxidation, only comparable with smooth Pt electrode. This activity is commonly attributed to activated water molecules, the presence of appropriate crystallographic planes on the metal surface, and/or the importance of the existence of parallel reaction pathways. In the present work, an *in situ* study on the influence of the species present on the surface of such nanostructures and their catalytic role in the oxidation of the adsorbed intermediates and alcohols used in fuel cells has been performed.

The structure of the mesoporous catalysts was determined by different techniques as scanning tunneling microscopy (STM) and scanning electron microscopy (SEM). The

development of channels at the early stages of growth of the MP structure was observed by STM, which finally lead to the subsequent formation of a mesoporous structure observed by SEM.

Electrochemical behavior study of MPPt and MPPt/Ru catalysts applying voltammetric and chronoamperometric techniques, indicates that these electrodes exhibit a high catalytic activity towards methanol oxidation reaction compared to the PtRu alloy supported on commercial carbon, being the MPPt/Ru catalyst the one with the highest current densities. The results suggest that the high catalytic activity is favored by the diffusion of the reactives through the porous structure of the electrode, as well as the disposition of the actives sites on the electrode surface.

Methanol electrooxidation studies on MP catalysts through differential mass spectrometry electrochemical (DEMS) have allowed to evaluate and correlate the CO_2 production efficiency with the catalytic activity and the porous structure of these catalysts.

The electrochemical behavior of MPPt/Sn was studied at two temperatures (25 and 60 °C) using conventional electrochemical techniques, comparing its activity towards the adsorbed CO and methanol oxidation with the commercial catalysts PtSn (3: 1) supported on carbon. It was observed an increase in their activity with the temperature, the mesoporous material presenting the highest activity. The conversion efficiency of methanol to CO_2 was evaluated by DEMS and higher current densities and conversion efficiency to CO_2 were observed at both temperatures for the MPPt/Sn catalyst in comparison conventional PtSn/C (3:1) alloy catalyst. The surface composition was determined by X-ray photoelectron spectroscopy (XPS) that allows to identify the different oxidation states of the metals present in the surface catalysts.

Because of the problems caused by the toxicity of methanol, it was considered the use other less toxic alcohols in the fuel cells, such as ethanol. Thus, first electrochemical and spectroelectrochemical studies concerning ethanol reactivity on MPPt in an acidic medium using DEMS were performed. The study using different ethanol concentrations with a new electrochemical mass spectrometer configuration, more sensitive for the detection of species formed in very low amounts during the electrochemical reaction, allowed identifying several intermediates and elucidating the reaction mechanism. In addition, it was possible to monitor the formation of the main reaction products as acetaldehyde, acetic acid and CO_2 during electrooxidation, and to calculate the efficiency of conversion from ethanol to CO_2.

The most important results indicate that with increasing ethanol concentration, parallel reactions leading to the formation of acetaldehyde and acetic acid are favored, whereas CO_2 formation remains constant. Consequently, the highest CO_2 conversion efficiency (~ 11%) was obtained with the lowest concentration used (0.01 M). The results have been analyzed in terms of current density, the type of active sites on the surface, the applied potential and the alcohol concentration. Tafel slopes obtained from chronoamperometric curves allow proposing that the rate determining step in the complete ethanol oxidation to CO_2 is the water splitting reaction, while in parallel reactions leading to the formation of acetaldehyde and acetic acid is the ethanol dehydrogenation.

Other materials studied in this Ph.D. were the bimetallic nanostructures "core shell" (CS) type, in concrete Au nucleus (core) coated with Pd (shell), that have been used for the formic acid electrooxidation, regarding its possible use as a liquid fuel in fuel cells. DEMS and Fourier transform infrared spectroscopy (FTIRS) were applied for the study of the influence of the Pd overlayer thickness (from 1 to 10 nm) on adsorbed CO and formic acid oxidation. XPS data showed the importance of the formation of surface oxides and electronic influence of Au on the electrocatalysis. DEMS and FTIRS analysis allowed establishing that the onset potential for adsorbed CO oxidation shifted to more positive potential with decreasing the thickness of the Pd overlayer. Additionally, FTIR spectroscopy showed the different behavior of the adsorbed species (OH_{ad} and $HCOO_{ad}$ groups) with the Pd thickness, confirming the existence of a surface electronic effect, which implies that the oxidation of CO and HCOOH occurs in different ways for the catalysts studied.

Considering the ability of the Pd structures to absorb hydrogen and the interest in the generation of liquid fuels from CO_2 reduction, the efficiency of electrochemical CO_2 reduction on Au-Pd core-shells was evaluated by DEMS. Results revealed that the efficiency conversion is doubled when the thickness of the Pd layer decreases from 10 to 1 nm.

Finally, in the development of advanced electrolyzers for hydrogen generation, basic hydrolysis of the water has become very important because it allows the use of non-noble electrocatalysts such as Ni-based materials, which are economically very interesting. Therefore, given the requirements of high conductivity of the substrate and high degree of dispersion of the catalyst, NiMo materials have been synthesized supported on reduced graphene oxide (RGO) for the hydrogen evolution reaction.

The physicochemical characterization made by different X-ray techniques such as XPS, XRD (diffraction) and EDX (energy dispersive), atomic force microscopy (AFM) and Raman spectroscopy, confirmed the formation of Ni nanodiscs on the graphene surface. When the synthesis was performed in the presence of Mo, these nanodiscs are covered with layers of amorphous molybdenum oxide as identified by Raman spectroscopy. The DEMS study showed that these structures have a higher electrochemical activity when they are supported on RGO than on Vulcan XC-72R. NiMo catalysts with compositions 1: 3 and 1: 2 are those that produce hydrogen at more negative potentials.

Justificación

La población mundial ha sobrepasado el umbral de los 7.000.000.000 de habitantes en el año 2011 [Banco mundial, 2015]. En paralelo, el gran incremento en el consumo de energía a nivel mundial ha provocado una fuerte dependencia de los combustibles fósiles y ha hecho que la demanda de éste supere la capacidad de suministro [Gallagher, 2011; Reynolds, 2014]. Como consecuencia, este crecimiento ha traído aparejado un incremento en la emisión de gases que contribuyen al calentamiento global como el dióxido de carbono (CO_2), el monóxido de carbono (CO) y el dióxido de azufre (SO_2), entre otros [Ahmadi, 2015].

Por tanto, actualmente se están realizando grandes esfuerzos en investigación con el objetivo de alcanzar, a corto, medio y largo plazo, una mejora de la eficiencia en la generación, empleo y utilización de las fuentes tradicionales, con la consiguiente "utilización racional de la energía". En paralelo, desde hace algunos años se está promoviendo el desarrollo de fuentes de energía diferentes a las provenientes de los combustibles fósiles, cuya utilización conlleve un menor impacto sobre el medio ambiente y la salud humana.

Las fuentes renovables y sostenibles (como la energía fotovoltaica y la eólica) surgen como la mejor opción para suplir las necesidades de los diferentes sistemas que consumen energía. Sin embargo, a pesar de las ventajas medioambientales que presentan, éstas tienen el inconveniente de que su generación ocurre de forma intermitente; es decir, son fuentes de energía discontinuas que dependen de las condiciones meterológicas (de la insolación en la energía fotovoltaica, y de la velocidad del viento en la energía eólica), por lo que resulta necesario acoplar a esta producción sistemas de conversión y almacenamiento de energía. Entre estos sistemas se encuentran los dispositivos electroquímicos, como los *electrolizadores* y las *pilas de combustible*, con los que se podría almacenar energía produciendo hidrógeno (en los primeros) y utilizándolo para obtener electricidad en los segundos. El funcionamiento de los mismos requiere el uso de materiales conocidos como *catalizadores* que faciliten los procesos que se llevan a cabo.

Uno de los problemas que presentan los *electrolizadores* y las *pilas de combustible* en la actualidad es su elevado costo, debido, entre otros aspectos, a la utilización de platino (Pt) y sus aleaciones como catalizador. El Pt es un metal noble muy caro y presenta los mejores rendimientos para obtener hidrógeno en un electrolizador (99,999 %). Actualmente el hidrógeno que se utiliza en las pilas de combustible se obtiene, casi en su totalidad, a partir del reformado gaseoso, gasificación u oxidación parcial de fuentes fósiles y, como consecuencia de este tratamiento, presenta trazas de CO, el cuál es el responsable de la pérdida de eficiencia de las pilas de combustible de baja temperatura al "envenenar" la superficie del catalizador de Pt.

Con el fin de conseguir que estos dispositivos sean competitivos en el mercado es necesario bajar costes, y por tanto, resulta imprescindible el desarrollo de catalizadores que exhiban mayor actividad y durabilidad con menores contenidos de Pt y que, en el caso de las pilas de combustibles de baja temperatura, sean más tolerantes al CO para mantener la eficiencia.

Entre los diferentes tipos de pilas de combustible de baja temperatura, se encuentran las que usan membranas poliméricas como electrolito, y que pueden utilizar como combustibles tanto hidrógeno (PEMFCs; *Polymer Eletrolyte Membrane Fuel Cells*) como metanol (DMFCs; *Direct Methanol Fuel Cells*) o etanol (DEFCs; *Direct Ethanol Fuel Cells*). Una de las grandes ventajas de trabajar con combustibles líquidos a temperatura ambiente, es que los procesos de almacenamiento y manipulación son menos complejos que los utilizados para el hidrógeno. Con el empleo de estos combustibles líquidos no es necesario cambiar la infraestructura existente relacionada con la distribución de los derivados del petróleo, lo que permite estimar una disminución en el impacto y el coste que acarrea su implementación. Aunque los biocombustibles utilizados pueden ser producidos por fermentación de la biomasa con altos contenidos de azúcar, la idea de convertir fuentes importantes de alimento en combustible ha causado una gran controversia, ya que la competencia entre la industria de los alimentos y el combustible causará una escasez y un aumento en el precio del producto. De aquí surge el gran interés en el uso de los métodos electroquímicos (los cuales se pueden controlar fácilmente mediante el potencial aplicado) como una posibilidad, no sólo de generar hidrógeno con alta pureza o almacenarlo en forma de ácido fórmico, sino también como alternativa para generar combustibles líquidos a partir de CO_2 que a su vez puedan utilizarse en una pila de combustible [Enthaler, 2010; Qin, 2014].

Entre tanto, mientras se continua la búsqueda de materiales que permitan realizar los procesos mencionados anteriormente de manera eficiente, debido a la falta de efectividad para reducir el tamaño de las tecnologías de almacenamiento de hidrógeno, las pilas de combustible que funcionan con hidrógeno podrán aplicarse en estaciones generadoras o de respaldo de potencia (como en el autoabastecimiento eléctrico de hogares, de centros comerciales e iluminación de calles) ya que con ellas se puede obtener cientos de megavatios, mientras que los combustibles líquidos son ideales para usarse en sistemas móviles y portátiles (transporte y dispositivos electrónicos) para los que son necesario entre 10 a 1.000 kW o en el caso de las mini o micro fuentes de suministro, inferiores al vatio.

En este sentido, la necesidad de satisfacer las exigencias de estos dispositivos electrónicos ha estimulado a los investigadores y a la industria a desarrollar micropilas portátiles avanzadas que superen las limitaciones sistemáticas de las baterías convencionales de litio y níquel. La medicina por ejemplo, necesita de la creación de micropilas para usarlas como fuentes de energía implantables [Kundu, 2007]. Recientemente, varias compañías como Toshiba, Hitashi, Fujitzu, Samsung e IBM, ya han registrado algunos avances para aplicaciones en sistemas portátiles [Kundu, 2007; Falcão, 2014]. Debido a esta tendencia a miniaturizar los dispositivos tecnológicos es necesario desarrollar micro y nanoestructuras organizadas para micropilas que se puedan construir a costos aceptables y con el mismo rendimiento que un catalizador convencional (nanopartículas soportadas en carbón).

En esta Tesis Doctoral se aborda la síntesis y caracterización de diferentes materiales nanoestructurados no soportados que actúen como electrocatalizadores anódicos en micropilas de combustible de alcohol directo, y como electrocatalizadores catódicos en electrolizadores para generar hidrógeno o combustibles líquidos utilizables en pilas de combustible de electrolito de membrana polimérica.

Bibliografía

Ahmadi Moghaddam, E., Ahlgren, S., Hulteberg, C. & Nordberg, Å., 2015. Energy balance and global warming potential of biogas-based fuels from a life cycle perspective. *Fuel Processing Technology,* **132**, pp. 74-82.

Banco mundial, B.A. 2015, 06/2015-last update, *POBLACION*, *TOTAL*. Available: http://datos.bancomundial.org/indicador/SP.POP.TOTL/countries?display=graph [2015, 07/08].

Enthaler, S., von Langermann, J. & Schmidt, T., 2010. Carbon dioxide and formic acid-the couple for environmental-friendly hydrogen storage. *Energy & Environmental Science,* **3**, pp. 1207-1217.

Falcão, D.S., Oliveira, V.B., Rangel, C.M. & Pinto, A.M.F.R., 2014. Review on micro-direct methanol fuel cells. *Renewable and Sustainable Energy Reviews,* **34**, pp. 58-70.

Gallagher, B., 2011.Peak oil analyzed with a logistic function and idealized Hubbert curve. *Energy Policy,* **39**, pp. 790-802.

Kundu, A., Jang, J.H., Gil, J.H., Jung, C.R., Lee, H.R., Kim, S., Ku, B. & Oh, Y.S., 2007. Micro-fuel cells-Current development and applications. *Journal of Power Sources,* **170**, pp. 67-78.

Qin, Y., Wang, J., Wu, Y. & Wang, L., 2014. Improved hydrogen production from formic acid under ambient conditions using a PdAu catalyst on a graphene nanosheets-carbon black support. *RSC Advances,* **4**, pp. 30068-30073.

Reynolds, D.B., 2014. World oil production trend: Comparing Hubbert multi-cycle curves. *Ecological Economics,* **98**, pp. 62-71.

1. INTRODUCCIÓN

1.1 PILAS DE COMBUSTIBLE

Las pilas de combustible son dispositivos electroquímicos que, en presencia de un catalizador, convierten directamente, de manera continua y con un rendimiento elevado, la energía química de un combustible en energía eléctrica. Esta obtención de electricidad en forma de corriente continua se lleva a cabo sin la necesidad de ningún proceso de combustión, ya que la oxidación del combustible y la reducción del comburente se producen en lugares físicos diferentes [Litster, 2004; Moliner, 2005; Sharaf, 2014].

Las altas eficiencias son quizás la ventaja más importante que presentan las pilas de combustible con respecto a otros dispositivos creados con el mismo fin (figura 1.1). La conversión directa de combustible a energía presenta eficiencias entre el 30 % y el 65 %, dependiendo del sistema de pila de combustible, y además, el calor generado durante el proceso también puede aprovecharse (cogeneración). Por el contrario, la generación de energía basada en la combustión convierte previamente el combustible en calor, proceso limitado termodinámicamente por la ley de Carnot, y después a energía mecánica, la cual produce movimiento para realizar un trabajo determinado. Estas etapas adicionales involucradas en la combustión hacen que la energía se libere en forma de calor, fricción, entre otras pérdidas de conversión, provocando una disminución de la eficiencia en el proceso global [Aricò, 2001; Kunze, 2009; Vieltstich, 2003]. En conclusión, la conversión electroquímica asegura un elevado rendimiento en el proceso de transformación energética, mayor del que se obtendría en las maquinas térmicas, ya que éstas últimas presentan la limitación impuesta por el ciclo de Carnot.

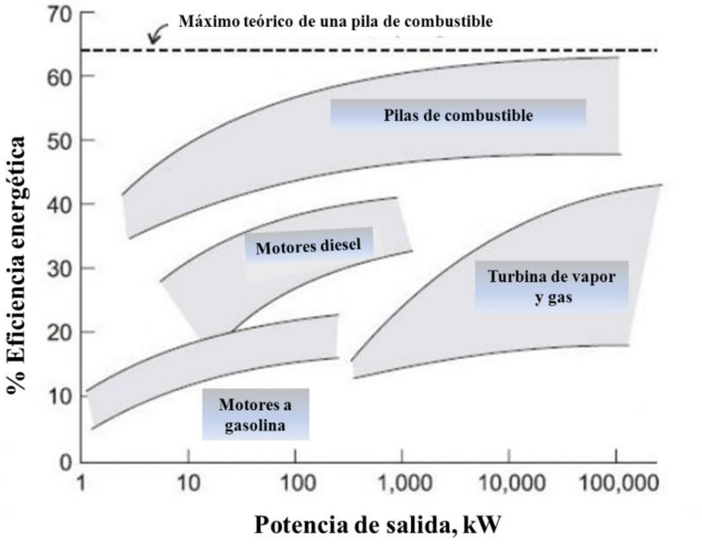

Figura 1.1. Comparación de la eficiencia energética de diferentes sistemas que generan energía. Tomado y modificado de [Behret 1996].

A diferencia de una pila eléctrica o batería, una pila de combustible no se acaba ni necesita ser recargada, funciona mientras se le suministre constantemente el combustible y el oxidante desde fuera de la pila. El funcionamiento consiste de un ánodo al que se inyecta el combustible; en los casos más conocidos hidrógeno o alcoholes, y en el cátodo se introduce un oxidante, normalmente oxígeno del aire. El combustible se oxida y libera una cantidad de electrones que genera una corriente eléctrica que fluye a través de un circuito externo. Los iones positivos generados en el ánodo atraviesan el electrolito que separa el ánodo del cátodo para llegar a este último, donde reaccionan con el oxígeno o la sustancia oxidante y los electrones que han pasado por el circuito para formar así una especie neutra que dependerá del tipo de pila y del combustible utilizado.

1.1.1 Tipos de pilas de combustible

Las celdas de combustible se clasifican usualmente por el tipo de electrolito empleado, el cual determina la temperatura de operación. En la tabla 1.1 se muestran, de forma comparativa, algunas de las características de los diferentes tipos de celda.

Tabla 1.1. Características más importantes de las diferentes celdas de combustible

Tipo de celda	Electrolito	Ion móvil	Temperatura de operación	Eficiencia	Ventajas	Desventajas
Alcalina (AFC)	KOH	OH^-	50-200 ºC	70 %	Reacción catódica rápida; mayor eficiencia	Sensible al CO_2
Membrana de intercambio protónico (PEMFC)	Nafion^{TM}	H^+	25-90 ºC	40-50 %	Electrolito sólido reduce corrosión y mantenimiento; baja temperatura	Catalizadores costosos; sensible al CO, hidratación de la membrana
Alcohol directo (DMFC), (DEFC)						
Ácido fosfórico (PAFC)	H_3PO_4	H^+	200 ºC	40-70 %	85 % de eficiencia con cogeneración; no afectan las impurezas del H_2	Catalizador de Pt; baja corriente y potencia; gran volumen y peso
Carbonato fundido (MCFC)	Carbonatos (Li, Na, K)	CO_3^{2-}	650 ºC	60-70 %	Mayor eficiencia; catalizadores económicos	Corrosión por alta temperatura; vida útil baja
Oxido sólido (SOFC)	YSZ	O^{2-}	500-1000 ºC	60-80 %	Ventajas debidas a altas temperaturas; electrolito sólido	Corrosión por alta temperatura; vida útil baja

Dentro de los diferentes tipos de celdas de combustible, aquellas que funcionan utilizando alcohol directo como combustible (DAFCs – Direct Alcohol Fuel Cells) son las mejores candidatas para el uso en dispositivos móviles y portátiles, ya que pueden trabajar a temperatura ambiente. Además, al ser fuentes energéticas que producen bajo nivel de ruido mientras están operando, son adecuadas para abastecer lugares aislados como sistemas autónomos de producción de energía eléctrica, sobre todo en aquellos en los que es costosa la instalación de líneas de transmisión de electricidad [Carter, 2013].

1.1.2 Pilas de combustible de membrana intercambiadora de protones (PEMFCs)

En las pilas tipo PEM se utiliza como electrolito una membrana de un polímero sólido conductor de protones, de fuerte carácter ácido y con un espesor comprendido entre 50 y 250 μm. El polímero que más se utiliza actualmente es el Nafion^{TM} (DuPont) y es un derivado del tetrafluoroetileno.

Estas membranas se preparan a partir de un polímero de ácido sulfónico perfluorado (PSAP), que contiene grupos $–(CF_2)_n–$ a los cuales se le adiciona un número de segmentos que contienen grupos ácidos sulfónico, $–SO_3H$. Cuando la membrana se humedece adecuadamente, los grupos del ácido sulfónico se disocian, y a una temperatura de 80 ºC presentan una alta conductividad cercana a 0,1 S cm^{-1}, tres o cuatro veces mayor que las primeras membranas intercambiadoras de protones utilizadas [Bagotsky, 2010].

Una de las desventajas de estas membranas es el complicado proceso de fabricación y su elevado precio. El coste aproximado de una membrana de Nafion^{TM} es de 400 € m^{-2} o alrededor de 100 € kV^{-1} producido para una celda con una densidad de potencia de 600 mW cm^{-2} [Bagotsky, 2010].

Las reacciones que tienen lugar en una celda de combustible tipo PEM son las siguientes:

Ánodo: $2H_2 + 4H_2O \rightarrow 4H_3O^+ + 4e^-$ (1.1)

Cátodo: $4H_3O^+ + 4e^- + O_2 \rightarrow 6H_2O$ (1.2)

Reacción global: $2H_2 + O_2 \rightarrow 2H_2O$ (1.3)

La figura 1.2 muestra un esquema general de los componentes y del funcionamiento de las PEMFCs.

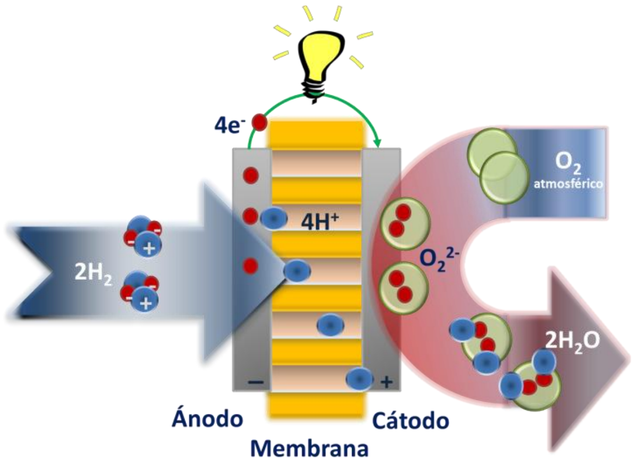

Figura 1.1.2 Componentes y funcionamiento de una PEMFC.

El catalizador anódico empleado usualmente es Pt soportado en una matriz hidrófoba de carbono. Debido a la baja temperatura de operación, en las PEMFCs debe utilizarse hidrógeno con muy bajo contenido de CO para evitar el envenenamiento de los electrodos, mientras que el aire puede usarse como agente oxidante. Los mejores métodos de reformado producen un gas combustible que contiene aproximadamente un 1 % de CO, siendo posible reducirlo hasta un contenido de 10 ppm, por ejemplo, a través de una oxidación selectiva con un catalizador de Pt/alúmina. Sin embargo, estas pequeñas cantidades de CO pueden aún afectar a un ánodo de Pt. La utilización de catalizadores alternativos basados en aleaciones de Pt y Ru u otros materiales con capacidad de formar óxidos a bajos potenciales, conlleva un aumento de la tolerancia al CO y, en este caso, podría emplearse hidrógeno con un contenido de CO del orden de 20 ppm [Vielstich, 2003; Sundmacher, 2010].

1.1.3 Pilas de combustible de metanol directo (DMFCs)

La mayoría de las pilas de combustible funcionan con hidrógeno, que puede suministrarse directamente en el sistema, o ser generado dentro de la pila convirtiendo combustibles ricos en hidrógeno (como por ejemplo metanol, etanol e hidrocarburos).

Sin embargo, las DMFC funcionan con metanol puro mezclado con vapor de agua y suministrado directamente al ánodo de la pila sin necesidad de un reformado previo. Por tanto, se elimina el problema de almacenamiento que ocurre con las otras pilas, ya que el metanol tiene mayor densidad energética que el hidrógeno (aunque menos que la gasolina) y al ser líquido es más fácil el transporte y suministro a la infraestructura existente.

Las DMFCs tienen en común con las PEMFCs el uso de un polímero capaz de transportar iones H^+ como electrolito. Estas pilas han sido probadas en rangos de temperatura entre 50-120 ºC. Esta baja temperatura de operación y el no requerir un reformador de combustible hace a las DMFCs unos excelentes candidatos para aplicaciones de pequeña y mediana escala, como teléfonos móviles, ordenadores portátiles, automóviles, etc. [Corti, 2014].

La reacción global de los procesos anódicos y catódicos que ocurren en una DMFC se muestra en las siguientes reacciones:

Ánodo: $CH_3OH + 7H_2O \rightarrow CO_2 + 6H_3O^+ + 6e^-$ (1.4)

Cátodo: $3/2O_2 + 6H_3O^+ + 6e^- \rightarrow 9H_2O$ (1.5)

Reacción global: $CH_3OH + 3/2O_2 \rightarrow CO_2 + 2H_2O$ (1.6)

La figura 1.3 muestra el esquema del funcionamiento de este tipo de celdas de combustible.

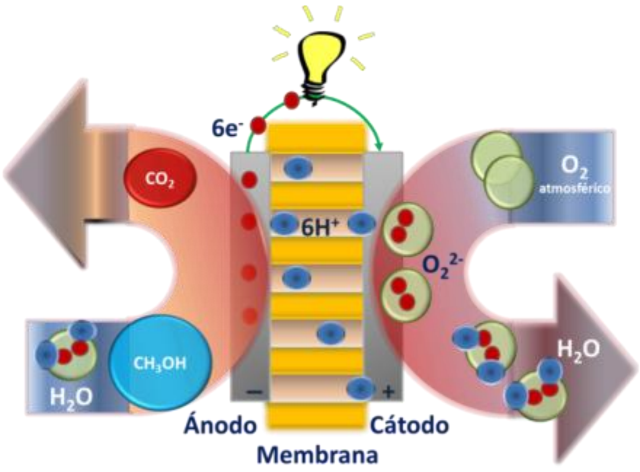

Figura 1.1.3. Componentes y funcionamiento de una DMFC.

Entre los inconvenientes más importantes de las DMFCs se puede señalar que la oxidación a baja temperatura de metanol necesita una cantidad mayor de catalizador de Pt, lo que aumenta su coste con respecto a las PEMFCs; aunque este incremento de precio podría estar contrarrestado por la utilización del combustible líquido y la capacidad de funcionar sin una unidad de reformado, es necesaria la optimización de la cantidad de Pt para su posible comercialización. Adicionalmente, al considerar el impacto medioambiental, debemos mencionar que el metanol es un combustible tóxico y por tanto, se ha planteado el uso de etanol.

1.1.4 Pilas de combustible de etanol directo (DEFCs)

El etanol tiene dos grandes ventajas respecto al metanol: se trata de un líquido no tóxico y es menos inflamable que el metanol. Además es relativamente fácil obtenerlo de la biomasa mediante procesos de fermentación de azúcar proveniente de cultivos de maíz, trigo, caña de azúcar, etc., o desde residuos agrícolas y forestales. Las emisiones netas de CO_2 son inferiores a las que se producen en el procesado de combustibles a partir de combustibles fósiles, ya que parte de este CO_2 es absorbido por los cultivos empleados como biomasa [Mielenz, 2001; Kamarudin, 2013].

En las DEFCs, la reacción anódica del alcohol (1.7) junto con la reacción de reducción de oxígeno que ocurre en el cátodo (1.8) suministra una fuerza electromotriz de aproximadamente 1,15 V bajo condiciones estándar [Antolini, 2011; Kamarudin, 2013].

Ánodo: $CH_3CH_2OH + 15H_2O \rightarrow 2CO_2 + 12H_3O^+ + 12e^-$ (1.7)

Cátodo: $3O_2 + 12H_3O^+ + 12e^- \rightarrow 18H_2O$ (1.8)

Reacción global: $CH_3CH_2OH + 3O_2 \rightarrow 2CO_2 + 3H_2O$ (1.9)

El funcionamiento de las DEFCs se esquematiza en la figura 1.4.

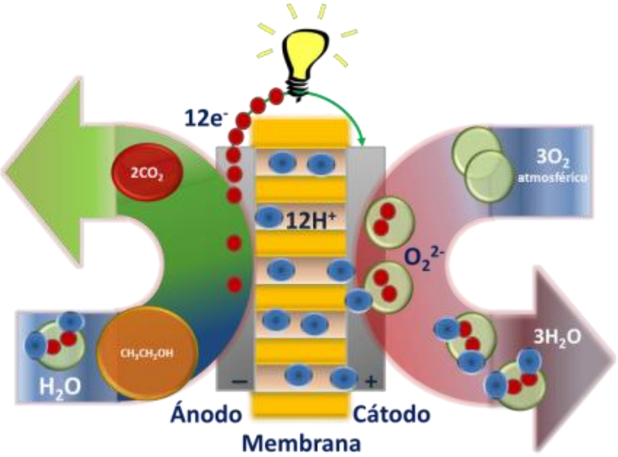

Figura 1.1.4. Componentes y funcionamiento de una DEFC.

Aunque el funcionamiento y el sistema de operación de una DEFC es similar al de una DMFC, la DEFC tiene ciertas características distintas, tales como los mayores sobrepotenciales que se originan por la ruptura del enlace C-C, una cinética de oxidación más lenta, y una reacción global más compleja por la mayor producción de CO_2, acetaldehído y ácido acético. En contraste a la reacción de oxidación de metanol, donde ambos intermediarios (formaldehido y ácido fórmico) pueden ser oxidados hasta CO_2, en la oxidación del etanol se obtienen especies parcialmente oxidadas [Antolini, 2007]. Este resultado es la principal barrera para la utilización de este combustible, ya que se necesitan electrocatalizadores suficientemente activos para realizar la ruptura del enlace C-C y remover los intermediarios que se adsorben fuertemente sobre la superficie. Esta etapa desempeña un papel determinante en el proceso de electrooxidación, la eficiencia del combustible y el rendimiento eléctrico de la pila, y representa la diferencia más importante con respecto al metanol.

1.2 SISTEMAS PARA GENERAR COMBUSTIBLE PARA PILAS TIPO PEM

1.2.1 Electrolisis

Actualmente, el principal proceso industrial para la producción de hidrógeno con alto grado de pureza es la electrolisis del agua, y se espera que en el futuro incremente su grado de importancia para el desarrollo de nuevas tecnologías energéticas. La electrólisis del agua consiste en hacer circular directamente una corriente eléctrica a través de agua para separar sus moléculas en hidrógeno y oxígeno [Bockris, 1981]. La corriente fluye entre dos electrodos separados y sumergidos en un electrolito para aumentar la conductividad iónica. Los electrodos han de ser resistentes a la corrosión, tener una buena conductividad eléctrica, presentar buenas propiedades catalíticas y mostrar una integridad estructural adecuada. El electrolito no puede sufrir cambios durante el proceso, debe ser inerte [Ursúa, 2013].

Para evitar la mezcla del hidrógeno y oxígeno generados se utiliza un diafragma o separador, que debería tener una alta estabilidad física y química, así como también una alta conductividad iónica [Ursúa, 2013].

Los electrodos, el diafragma y el electrolito son los elementos constituyentes que configuran la celda electrolítica. La reacción química global de la electrolisis del agua es:

$$H_2O(l) \rightarrow H_2(g) + 1/2O_2(g) \qquad (1.10)$$

Al conectar la celda electrolítica a una pila, la formación de hidrógeno tiene lugar en el electrodo polarizado negativamente (cátodo) que es dónde ocurre la semirreacción de reducción, y el oxígeno es generado en el electrodo polarizado positivamente (ánodo) dónde ocurre la semirreacción de oxidación.

Los electrolizadores de agua y las pilas de combustible usan una tecnología similar, pero el proceso en la pila de combustible es inverso al que ocurre en un electrolizador: el hidrógeno es convertido en electricidad y calor. En general, los electrolizadores de agua son más eficientes que las pilas de combustible [Decourt, 2014].

La producción de hidrógeno es directamente proporcional a la corriente que pasa a través de los electrodos, de acuerdo a las leyes de Michael Faraday [Carmo, 2013]:

I) La masa de una sustancia alterada en un electrodo durante el proceso de electrolisis es directamente proporcional a la cantidad de carga eléctrica (Q) transferida.

II) Para una cantidad dada de carga eléctrica Q, la masa de un material elemental alterada en un electrodo es directamente proporcional al peso equivalente del elemento. El equivalente de una sustancia es igual a su masa molar dividida por el cambio en el estado de oxidación sometido a electrolisis.

Las principales tecnologías de electrolisis existentes son: electrolizadores alcalinos, electrolizadores de membrana de electrolito polimérico y electrolizadores de óxido sólido. A continuación se describe el proceso de electrolisis y las características de las dos primeras ya que son las que trabajan a baja temperatura.

1.2.1.1 Electrolisis alcalina

La electrolisis alcalina se ha convertido en la tecnología más desarrollada para la producción de hidrógeno en un rango desde 1,8 a 5.300 MW. La velocidad de producción de hidrógeno (f_{H2}) para un sistema comercial se encuentra entre 0,25-760 Nm^3/h [Bertuccioli, 2014]. Actualmente, los electrolizadores alcalinos son la opción más adecuada para la producción de hidrógeno a gran escala. El esquema de una celda para electrolisis alcalina de agua se muestra en la figura 1.2.1.

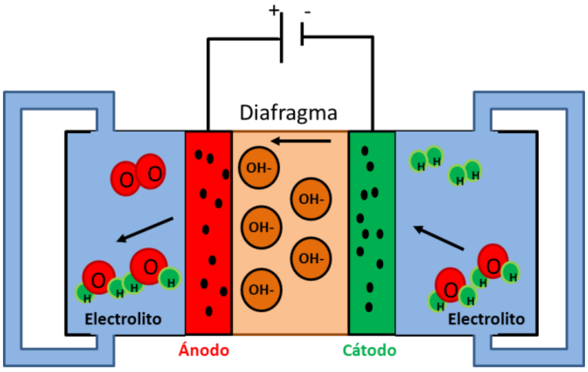

Figura 1.2.1. Principio de operación de una celda de electrolisis alcalina. Un voltaje DC aplicado descompone la molécula de agua y los iones hidroxilos pasan a través del diafragma desde el cátodo al ánodo. El hidrógeno se forma en el cátodo, mientras que el oxígeno en el ánodo.

En una celda de electrolisis alcalina los dos electrodos están separados por un diafragma impermeable a los gases y sumergidos en un electrolito líquido, que normalmente está contenido en un compartimento de acero. Para maximizar la conductividad iónica del electrolito, se usa una disolución acuosa muy concentrada de KOH, del orden de 20-40 % en peso. El agua se suministra continuamente a medida que se va consumiendo durante la electrolisis [Lehner, 2014]. Opera en un rango de temperatura entre 60 y 100 °C. Los gases generados que salen de la celda, se separan del electrolito restante que se bombea de vuelta a la celda. El sistema de distribución del electrolito y la separación de los gases se ilustra en la figura 1.2.2.

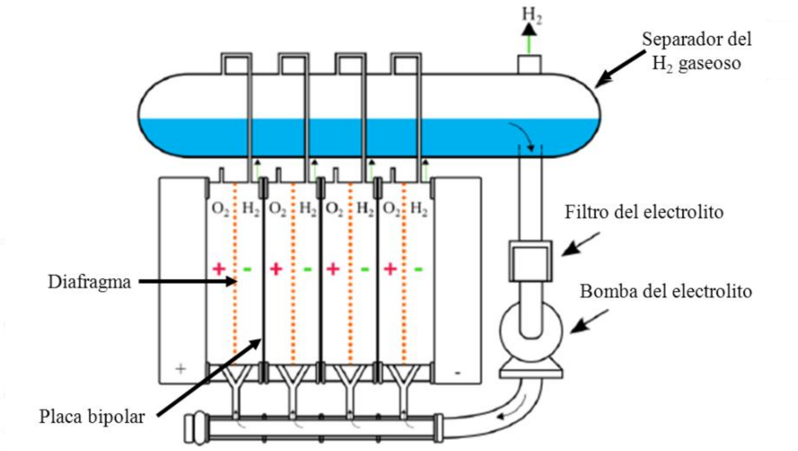

Figura 1.2.2. Esquema de una planta de electrolisis alcalina. Los gases producidos en los electrolizadores se purifican del electrolito en el tanque de separación. El oxígeno formado es tratado en otro tanque individual. El agua se adiciona constantemente al sistema para mantener la concentración del electrolito adecuada. Tomado y modificado de [Bockris, 1981].

Se utilizan electrodos de Ni o de acero niquelado para evitar los problemas de corrosión que se generarían a los altos valores de pH del electrolito, [Bertuccioli, 2014].

El diafragma debe mantener los gases producidos apartados, para mantener la eficiencia y la seguridad del sistema, y además debe ser permeable a los iones hidroxilo y a las moléculas de agua. Con este fin se utilizan membranas intercambiadoras de iones inorgánicos basadas en polímeros sulfonados, sulfuro de polifenileno, polibencimidazoles, y materiales composites. La resistencia eléctrica del diafragma es frecuentemente tres o cinco veces mayor que la del electrolito. [Otero, 2014]

Las reacciones que se llevan a cabo en una celda de electrolisis alcalina se describen a continuación:

Cátodo: $2H_2O + 2e^- \rightarrow H_2(g) + 2OH^-$ (1.11)

Ánodo: $2OH^-(ac) \rightarrow \frac{1}{2}\, O_2(g) + H_2O(l) + 2e^-$ (1.12)

El hidrógeno se forma en el cátodo donde el agua se reduce de acuerdo a la ecuación (1.11) produciendo iones hidroxilo, que circulan a través del diafragma hacia el ánodo debido al campo eléctrico impuesto por la fuente externa. Los iones hidroxilo se recombinan sobre la superficie del ánodo produciendo oxígeno y liberando electrones que, a través del circuito externo, se dirigen a la fuente externa. El hidrógeno formado puede alcanzar un nivel de pureza entre 99,5-99,9998 %. El agua que se suministra a un electrolizador alcalino debe ser pura, con una conductividad eléctrica por debajo de 5 μS/cm.

Los mayores problemas que se asocian a los electrolizadores alcalinos se deben principalmente a que el diafragma no es totalmente impermeable a los gases producidos, los cuales pueden pasar por difusión de un lado del electrodo al otro, ocasionando una disminución en la eficiencia del electrolizador. Recientemente se han llevado a cabo diferentes avances para mejorar la eficiencia de estos dispositivos, de manera que se denominan electrolizadores alcalinos avanzados; Ulleberg et al. [Ulleberg, 2003] describen las tres líneas básicas de mejora: i) una nueva configuración de la celda que minimice el espacio entre los electrodos para reducir las pérdidas óhmicas y poder trabajar con densidades de corriente más altas; ii) incrementar la temperatura de trabajo hasta 160 ºC para aumentar la conductividad del electrolito y favorecer la cinética de las reacciones electródicas y iii) desarrollar nuevos electrolizadores para reducir el sobrepotencial del electrodo (óxidos de cobalto en el ánodo y revestimientos de Raney-níquel en el cátodo).

Algunas de las principales características de los electrolizadores alcalinos se resumen en la tabla 1.2.

1.2.1.2 Electrolizadores con membrana de intercambio protónico (PEM)

Estos electrolizadores se caracterizan por que el electrolito que usan es una membrana polimérica delgada (espesor inferior a 0,2 mm), impermeable a gases y conductora de protones (H^+) (ver sección 1.1.2 correspondiente a las celdas de combustible tipo PEM), en lugar de un electrolito líquido usado típicamente en los electrolizadores alcalinos [Bertuccioli, 2014].

El funcionamiento de una celda electrolítica tipo PEM se ilustra en el esquema de la figura 1.2.3; las reacciones que se llevan a cabo durante la electrolisis son las siguientes:

Ánodo: $H_2O(l) \rightarrow \frac{1}{2} O_2(g) + 2H^+ + 2e^-$ (1.13)

Cátodo: $2H^+ + 2e^- \rightarrow H_2(g)$ (1.14)

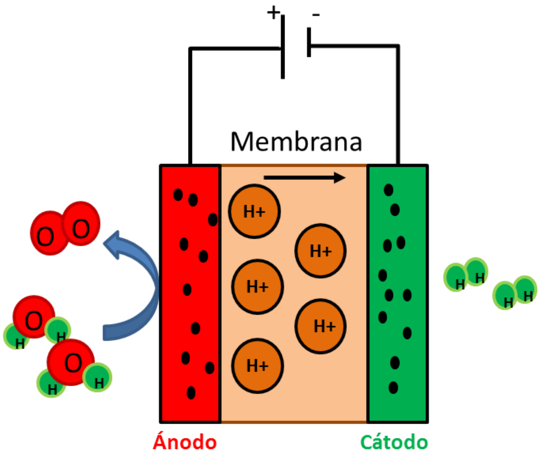

Figura 1.2.3. Principio de operación de un electrolizador con membrana intercambiadora de protones. El electrolito es una delgada capa de membrana polimérica que es conductora de protones. Los protones que atraviesan la membrana se combinan en el cátodo con los electrones para formar hidrógeno.

En el ánodo, el agua es oxidada de acuerdo con la semirreacción (1.13) produciendo oxígeno, electrones y protones que pasan a través de la membrana hacia el cátodo, donde se combinan con los electrones, que han llegado por el circuito externo, y son reducidos según (1.14) formando hidrógeno.

En la tabla 1.2 se comparan algunas de las principales características de la hidrolisis alcalina y tipo PEM.

Tabla 1.2. Estado del arte para las especificaciones de los electrolizadores alcalinos y tipo PEM

Especificaciones	**Electrolisis alcalina**	**Electrolisis en una PEM**
Madurez	Comercial	Poco comercial y aplicaciones a pequeña escala
Área de la celda	< 4 m^2	< 0.3 m^2
Temperatura	60-80 ºC	50-80 ºC
Densidad de corriente	0,2-0,4 mA cm^{-2}	0,6-2,0 mA cm^{-2}
Pureza de H_2	99,5-99,9998 %	99,9-99,999 %
Presión de salida H_2	0,05-30 bar	10-30 bar < 200 bar
Potencial de la pila	1,8-2,4 V	1,8-2,2 V
Eficiencia de Voltaje	62-68 %	67-82 %
Costo indicativo	1,0-1,2 €/W	1,8-2,3 €/W

Electrolizador alcalino	**Electrolizador tipo PEM**
Ventajas	
Tecnología madura	Altas densidades de corriente
Uso de catalizadores no nobles	Alto voltaje de eficiencia
Largo tiempo de operación	Respuesta rápida del sistema
Costo relativamente bajo	Operación dinámica
Desventajas	
Bajas densidades de corriente	Componentes altamente costosos
"Crossover" de gases	Baja durabilidad
Bajas presiones de operación	No se comercializa
Electrolito líquido corrosivo	Electrolito corrosivo

La electrolisis con membrana intercambiadora de protones o membrana de electrolito polimérico (PEM), normalmente presentan una mayor densidad de corriente respecto a los electrolizadores alcalinos. Los electrolizadores comerciales tipo PEM operan con densidades de corriente entre 0,6-2,0 A cm^{-2} [Carmo, 2013].

Aunque, la electrolisis tipo PEM se considera como una tecnología comercial solamente para aplicaciones de mediana y pequeña escala, Siemens AG ha puesto en funcionamiento el pasado mes de julio del presente año un sistema de electrolisis tipo PEM a gran escala con una capacidad de 6 MW [Siemens, 2015]. Hasta ahora, son muy pocas las compañías que desarrollan electrolizadores de agua tipo PEM debido a su mayor coste de inversión y, típicamente, su menor tiempo de vida comparado a los electrolizadores alcalinos. El alto coste de inversión se debe principalmente al uso de catalizadores nobles (Pt, Ir y Ru) y colectores de corriente a base de Ti para aguantar las severas condiciones corrosivas en los que funciona la membrana electrolítica. [Carmo, 2013].

En resumen, la electrolisis alcalina y tipo PEM son las dos principales tecnologías que se encuentran disponibles comercialmente. La electrolisis alcalina es la más desarrollada, madura y generalizada. El alto coste de los componentes y procedimientos a gran escala han limitado el desarrollo de los electrolizadores tipo PEM. Además, los electrolizadores alcalinos suelen tener más tiempo de operación que las de tipo PEM. Sin embargo, la tecnología tipo PEM tiene varias ventajas sobre los sistemas alcalinos, tales como el diseño compacto del sistema, la falta de electrolito líquido, amplia gama de carga parcial, y alta flexibilidad en los tiempo de operación. Por lo tanto, la electrolisis tipo PEM es una opción interesante cuando se considera la integración en sistemas de generación de energía renovable.

Adicionalmente, la tecnología PEM ha sido estudiada en sistemas unificados de pilas de combustible regenerativo (URMC). Una URMC es un dispositivo electroquímico reversible, que puede operar como un electrolizador para la producción de hidrógeno y oxígeno a partir de agua o como una pila de combustible tipo PEMFC para generar electricidad y calor.

1.2.2 Reducción de CO_2 como almacenamiento de H_2 y fuente de biocombustibles

En los últimos años se ha propuesto la captura de CO_2 como estrategia para almacenar hidrógeno en forma de ácido fórmico o metanol mediante métodos que se basan en la reducción de CO_2 con hidrógeno molecular [Podlovchenko, 1994; Li, 2010; Hu, 2010]. Aunque el metanol tiene una mayor capacidad de almacenamiento de moléculas de hidrógeno comparado con la del ácido fórmico (proporción dos a uno), se prefiere usar el CO_2 para sintetizar ácido fórmico debido a que es más eficiente [Enthaler, 2010].

Por otro lado, a diferencia de la electricidad renovable que puede obtenerse por varias fuentes (hidráulica, solar, geotérmica, eólica, entre otras), los biocombustibles sólo se producen a partir de la biomasa o por la reducción química de CO_2 [Peterson, 2012]. Por tanto, sería importante buscar nuevas fuentes para obtener biocombustibles y es aquí donde la conversión de CO_2 utilizando los métodos electroquímicos es de gran interés por presentar varias ventajas: (1) el proceso es controlable por el potencial del electrodo y la temperatura de reacción; (2) el electrolito soporte puede ser completamente reciclado de manera que el consumo de productos químicos, en general, se puede minimizar simplemente a agua (o incluso aguas residuales); (3) la electricidad usada para llevar a cabo el proceso puede ser obtenida sin generar nuevas fuentes de CO_2, por ejemplo a partir de energía solar, eólica, hidroeléctrica, geotérmica y procesos termoeléctricos; y (4) los sistemas electroquímicos son compactos, modulares, de baja demanda y fáciles de adaptar para aplicaciones a gran escala [Qiao, 2014]. De esta manera, los sistemas electroquímicos permitirían obtener mediante procesos sencillos y rápidos ácido fórmico o biocombustible (metanol o etanol) dependiendo de la necesidad de consumo a nivel local o global. Así, podemos abordar simultáneamente los problemas de almacenamiento de los excedentes de energía (que no se produce de forma continua a partir de las fuentes renovables) y la formación de combustibles líquidos para las pilas DAFC. Sin embargo, uno de los principales desafíos que presenta la electrorreducción de CO_2 es el bajo rendimiento de los electrocatalizadores por su pobre actividad catalítica y poca estabilidad.

1.3 CATALIZADORES PARA PILAS DE COMBUSTIBLE

1.3.1 Preparación de catalizadores para pilas de combustible

En la bibliografía se describen diversas formas de preparar catalizadores para ser utilizados en una PEMFC o DAFC, presentando eficiencias electroquímicas diferentes para una misma reacción [Lizcano-Valbuena, 2003; Lizcano-Valbuena, 2004], que pueden estar condicionadas, al menos en parte, por la limpieza final de las nanopartículas metálicas generadas con los diferentes métodos de síntesis [Lizcano-Valbuena, 2003; Lizcano-Valbuena, 2004]. Los electrocatalizadores soportados en carbono son los más estudiados tanto para la oxidación de alcoholes e hidrógeno como para la reducción de oxígeno. Es posible sintetizar materiales soportados sobre carbono de alta área superficial, con el fin de optimizar la cantidad de Pt utilizado y así reducir el coste de fabricación. Algunos métodos de preparación considerados como limpios son la reducción de sales de los precursores metálicos con compuestos orgánicos como el ácido fórmico [Lizcano-Valbuena, 2003], el borohidruro de sodio [Antolini, 2006] y la reducción en atmósfera de hidrógeno [Bernard, 2010].

Una mención aparte deben recibir las microceldas de combustible. En los últimos años, la tendencia hacia la miniaturización de los dispositivos tecnológicos ha llevado a la aparición de áreas de investigación tales como la nanociencia o la nanotecnología. El progreso en estas áreas se fundamenta en la construcción organizada de estructuras del tamaño del nanómetro a costos aceptables. A diferencia de los electrodos tradicionales (nanopartículas de Pt y aleaciones de este metal soportadas sobre carbón), en una microcelda de combustible se pueden utilizar electrodos no soportados, como es el caso de los metales mesoporosos, que poseen una microestructura porosa que les confiere una superficie electroactiva elevada. [Guo, 2012]

1.3.2 Materiales mesoporosos y su aplicación en microceldas de combustible

La síntesis de materiales nanoestructurados con elevada superficie ha llamado mucho la atención en los últimos años debido a que estos materiales presentan propiedades únicas y un número de aplicaciones de gran interés en catálisis, sensores químicos y celdas de combustible. Por ejemplo, un electrodo de Pt mesoporoso tiene más área electroactiva que un electrodo de Pt liso y puede ser equivalente o superior a un catalizador soportado. Esta diferencia tiene consecuencias importantes en distintas áreas de la electroquímica, como es el caso de la electrocatálisis.

La bibliografía sobre el tema muestra que se han desarrollado diversos métodos para la preparación de nanoestructuras metálicas [Guo, 2012]. Por lo general, estas metodologías se basan en la fabricación de estructuras mediante moldes o “templates”, entre los que destacan las membranas de policarbonato [Breulmann, 2000], los cristales líquidos [Velev, 1999] o la alúmina/sílice porosa [Baena-Moncada, 2014]. En microelectrónica es común el uso de técnicas como el electrodepósito en un molde o el empleo de capas autoensambladas, que permite producir canales de flujo, capas de difusión, sellos, etc. [Dong, 2011; Kitahara, 2003; Kopitkovas, 2003; Wang, 2010]. Para el caso del Pt, es posible realizar el electrodepósito de una capa de metal mesoporoso en presencia de un surfactante utilizado como "template". De esta forma se puede preparar el material *in situ* en los diferentes dispositivos, lo que le confiere gran interés ya que puede ser integrado fácilmente en la fabricación de pequeñas microceldas de combustibles.

1.3.3 Catalizadores de Pt no soportados

Como se ha indicado anteriormente, uno de los métodos más comunes para generar nanomateriales de base Pt es el electrodepósito [Attard, 2001; Franceschini, 2011; Tiwari, 2008; Walcarius, 2008; Walcarius, 2013; Zhao, 2008]. Este procedimiento involucra el uso de un sistema de dos o tres electrodos, con el electrolito que actúa como fuente del metal y como medio conductor. El depósito se produce controlando el potencial o la corriente del electrodo de trabajo en una celda electroquímica. Esta técnica se utiliza para fabricar películas delgadas o capas compuestas tanto de nanoparticulas o nanocristales, [Lee, 2006; Tiwari, 2008; Tsai, 2006] como de nanofibras y nanoalambres [Nagle, 2008; Suzuki, 2008; Zhong, 2008].

Se han empleado diferentes técnicas electroquímicas para facilitar el depósito de Pt y nanomateriales basados en Pt, incluyendo la cronoamperometría, la voltamperometría cíclica, así como también pulsos de potencial. Por ejemplo, Tirawi et. al [Tiwari, 2008] utilizaron un pulso de potencial para depositar Pt sobre una superficie de SiO_2.

En la literatura se encuentra que este tipo de sistemas, independientemente del método de obtención, presentan áreas electroactivas grandes. Además, se ha descrito que el potencial de oxidación del CO depende de la morfología de la superficie de estos catalizadores, lo que puede facilitar o desfavorecer su oxidación y la de otras moléculas como el metanol [Attard, 2001; Garcia, 2008; Lebedeva, 2000].

1.3.4 Catalizadores de Pt modificados con otros metales

Son muchos los trabajos realizados con aleaciones de Pt y con Pt modificado con otros metales (Ru [Du, 2005; Engstfeld, 2015; Kim, 2012; Liu, 2012; Velázquez-Palenzuela,2013; Wang, 2015], Sn [Campbell, 1992; Del Colle, 2011; Flórez-Montaño, 2015; Wei, 2006] y Pd [Choi, 2015; Jung, 2014; Mahapatra, 2011; Zielińska-Jurek 2014], entre otros [Perales-Rondón, 2014; Tripkovic, 2015]) para obtener una mayor tolerancia frente al CO y una mayor eficiencia catalítica hacia el metanol, el etanol o el ácido fórmico. En el caso de los catalizadores no soportados, la mayoría de los estudios se han llevado a cabo sobre superficies mono o policristalinas de Pt.

En el caso concreto de los electrodos de Pt modificados con Ru, se han aplicado diferentes técnicas para su preparación, entre los que destaca el método de la formación espontánea de depósitos. Éste se ha descrito tanto para nanopartículas de Pt soportadas sobre materiales carbonosos [Franaszczuk, 1992; Jiang, 2004; Waszczuk, 2001] como para superficies de Pt liso [Crown, 2001]. En el caso de superficies decoradas sobre Pt(hkl), se ha observado que el Ru se deposita en forma de nanoislas [Chrzanowski 1997; Crown, 2002; Strbac, 2004; Vieltstich, 2003], al igual que sobre nanopartículas [Strbac, 2004]. De los metales con los que se ha modificado el Pt, el Ru es el que ha presentado mejores resultados frente a la tolerancia de CO y mayor actividad catalítica para la oxidación de metanol. Este comportamiento es atribuido principalmente al mecanismo bifuncional, que se basa en que la presencia del Ru en la superficie facilita la formación de especies oxigenadas que ayudan a oxidar al CO generado como intermediario durante la oxidación de metanol, a potenciales más negativos que el Pt.

Para los electrodos de Pt modificado con adátomos de Sn, los primeros estudios realizados por Motoo et al. [Motoo, 1976; Motoo, 1980] mostraron que la presencia de aproximadamente la mitad de una monocapa de adátomos de Sn sobre una superficie de Pt policristalino, hace que el potencial cambie alrededor de 0,40 V a valores más negativos con respecto al Pt sin modificar. La explicación para tal efecto se basa, al igual que en el caso del Ru, en que los adátomos de Sn adsorben oxígeno a potenciales alrededor de 0,45 V (frente al electrodo de referencia de hidrógeno, ERH), valor mucho más negativo que el correspondiente a una superficie de Pt. Esta adsorción de oxígeno sobre los adátomos de Sn podría facilitar el comienzo de la electrooxidación del CO en estos electrodos.

Por otro lado, también se encuentran en la bibliografía muchos estudios relacionados con la influencia del Pd como segundo metal sobre una superficie de Pt, para la oxidación electroquímica del ácido fórmico [Babu, 2004; Vidal-Iglesias, 2012; Vidal-Iglesias, 2010; Wu, 2010]. Aunque es una reacción que ha sido ampliamente estudiada, hasta el momento existe una gran controversia sobre el mecanismo por el cual se lleva a cabo esta electrooxidación, debido a que el Pd no tiene buena tolerancia hacia el CO y, sin embargo, los catalizadores que contienen Pt y Pd son muy buenos para oxidar el ácido fórmico hasta CO_2 a muy bajos potenciales. Al igual que con los catalizadores que contienen Ru y Sn, los resultados en la literatura para el caso de electrodos no soportados están principalmente relacionados con superficies monocristalinas, donde se ha determinado que los adátomos de Pd se depositan preferiblemente sobre orientaciones cristalinas de Pt (100) [Babu, 2004; Vidal-Iglesias, 2012; Vidal-Iglesias, 2010].

1.3.5 Catalizadores de Pt aleado con otros metales

Normalmente, las aleaciones poseen propiedades químicas y físicas diferentes a las del metal puro. Estas son utilizadas generalmente para aumentar los sitios de actividad específica y por otro disminuir el contenido de carga de Pt. J. Jiang y A. Kucernak [Jiang, 2003; Jiang, 2009] llevaron a cabo investigaciones detalladas de la síntesis y la caracterización de aleaciones de PtRu mesoporosas, obteniendo desplazamientos bastante considerables a valores más negativos del potencial de oxidación de CO y metanol con respecto al catalizador comercial de PtRu soportado. Además, en relación al mecanismo de dos vías que describe la oxidación de metanol sobre electrodos de Pt y PtRu policristalino, se propone que en este caso la oxidación de metanol en los electrodos mesoporosos ocurre principalmente a través de la oxidación directa con CO_2 como producto final.

En otros estudios [Walcarius, 2013; Xu, 2014)] se han utilizado formas similares de síntesis de estos catalizadores mesoporosos pero con diferentes moldes o "templates", para conseguir estructuras cada vez más porosas. De esta manera se han obtenido materiales mesoporosos estructurados, con tamaños de poros entre 2-3 nm de diámetro y alta interconectividad entre ellos, lo que en teoría permitiría mejorar las condiciones difusivas del sistema catalítico. Sin embargo, los resultados obtenidos no son muy diferentes a los alcanzados con anterioridad. Por otra parte, se ha realizado la síntesis de catalizadores con microesferas mesoporosas de Pt y PtRu obtenidas por medio de la electroreducción de una disolución de una sal del metal en presencia de una matriz de negro de carbón (Ketjen Black International) [Knutson, 2008]. Este método permite que el metal crezca dentro del carbón y se pueda obtener un catalizador con un área superficial alta. En este caso, al igual que en los materiales mesoporosos anteriormente descritos, se obtiene una superficie elevada (aproximadamente 70-80 m^2 g^{-1}) y una mayor tolerancia al CO que los electrodos comerciales de Pt y PtRu soportados.

Las nanopartículas de PtSn soportadas en carbón también han presentado buenos rendimientos [Almeida, 2012; Michalak, 2014; Sims, 2015]. Los resultados muestran que, de manera general, éstas permiten la oxidación más fácil no sólo del metanol sino también del etanol. Aunque en la bibliografía se encuentran trabajos de aleaciones no soportadas de PtSn, la mayoría solo reportan cuanto mejora el potencial de oxidación de metanol respecto a catalizadores de Pt, y son muy pocos los que enfatizan un poco más sobre la influencia del Sn en el mecanismo de electrooxidación. Razón por la que este trabajo plantea dar un paso más en este sentido.

1.4 CATALIZADORES PARA LA REACCIÓN DE EVOLUCIÓN DE HIDRÓGENO

1.4.1 Electrocatalizadores basados en metales preciosos

Los mejores electrocatalizadores conocidos para la reacción de evolución de hidrógeno (HER) son los metales que pertenecen al grupo del Pt de la tabla periódica (incluyendo Pt, Ru, Rh, Ir y Pd), los cuales se localizan cerca del vértice del diagrama de Volcano (figura 1.4.1). Entre ellos, el Pt es el más utilizado, y frecuentemente se usa como punto de referencia respecto a otros electrocatalizadores para la HER. [Nørskov, 2005]

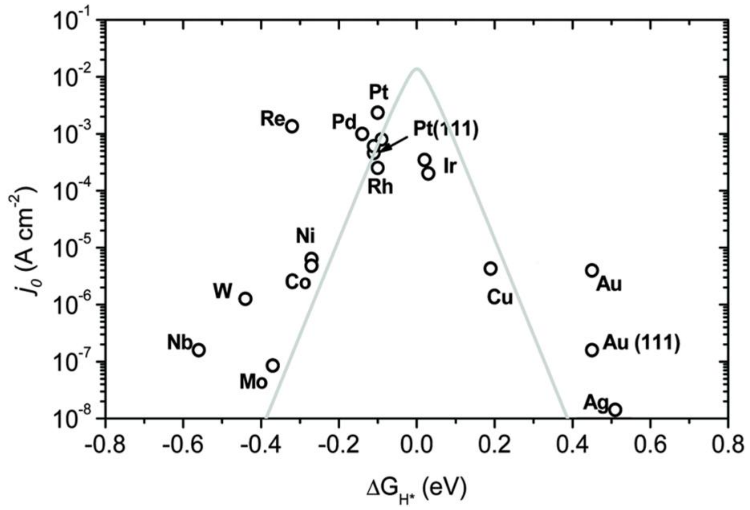

Figura 1.4.1. Curva tipo volcán correspondiente al intercambio de la densidad de corriente j_0 en función de la energía libre de Gibbs calculada por DFT de la adsorción de hidrógeno sobre metales puros. Tomado de [Nørskov, 2005].

Desafortunadamente, como ya se ha mencionado en este capítulo, la gran cantidad de aplicaciones de este grupo de metales nobles está limitada por su alto coste y baja abundancia. Para abordar este problema se han tenido en cuenta dos estrategias generales. La primera corresponde al uso de electrocatalizadores microestructurados o nanoestructurados con una relación superficie/volumen grande, como las estructuras mesoporosas mencionadas en el apartado 1.3 o el uso de monocapas de Pt soportadas sobre un material económico, como alternativa a los electrocatalizadores nobles (figura 1.4.2).

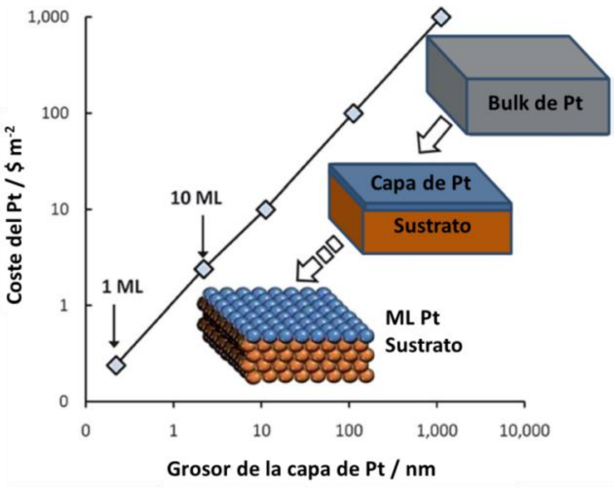

Figura 1.4.2. Relación entre el costo de Pt y el espesor de capas externas para un catalizador con una superficie plana. Modificado de [Esposito, 2011].

Mediante cálculos de la teoría del funcional de la densidad (DFT), Chen *et al.* demostraron que la actividad de monocapas de Pt soportadas sobre WC tienen una actividad comparable a la de un "bulk" de Pt, logrando a su vez que la carga metálica de Pt utilizada y el coste disminuya hasta un orden de magnitud [Esposito, 2011]. Estos resultados mostraron que todas las capas excepto, la capa más superficial de Pt, podrían reemplazarse por WC sin comprometer la actividad electrocatalítica. Este método se extendió para obtener otras sobrecapas metálicas (Pd y Au) y también utilizar otros sustratos o soportes como el Mo_2C. Los resultados electrocatalíticos exhiben una excelente actividad y estabilidad hacia la HER en medio ácido [Kelly, 2014; Esposito, 2012].

En segundo lugar, al igual que en los catalizadores para pilas de combustible, las aleaciones de los metales nobles es otra de las estrategias que se utiliza con mayor frecuencia. De 700 compuestos binarios evaluados por Nøskov *et al.* mediante la aplicación de un procedimiento de detección computacional de alto rendimiento basado en cálculos de DFT, se encontró que el candidato más prometedor correspondió a las aleaciones superficiales de Pt y Bi. Los cálculos realizados sugieren que el ΔG_H al igual que la actividad hacia la HER de un catalizador de PtBi es muy comparable al registrado para el Pt puro [Greeley, 2006].

1.4.2 Electrocatalizadores no nobles y sus aleaciones

En la industria, los electrocatalizadores alcalinos se basan en electrodos compuestos de Ni que se emplean comúnmente para la producción de hidrógeno debido a su bajo costo y por su resistencia a la corrosión en altos valores de pH [Kreuter, 1998]. Sin embargo, el Ni tiende a sufrir una insuficiente actividad electrocatalítica y más importante aún, un desactivación hacia la HER por la formación de especies de hidruros de níquel [Kreuter, 1998; Rommal, 1988; Soares, 1992]. Se han dedicado grandes esfuerzos para hacer aleaciones de Ni que mejoren la actividad y la durabilidad de los electrodos. Uno de las aleaciones más utilizadas a nivel industrial, desde su desarrollo en 1926, son las aleaciones de Ni-Al conocida también como Raney®-Níquel. Cuando se somete a una disolución alcalina para disolver principalmente la fase que contiene Al, se crea una estructura porosa de Ni altamente dispersa para la HER. Además del Raney®-Níquel, también se han estudiado la actividad catalítica de aleaciones electrodepositadas Ni–Mo, Ni–Zn, Ni–Co, Ni–W, Ni–Fe y Ni–Cr sobre láminas de acero. En trabajos realizados por Vasu *et al.* se concluye que la aleación de Ni-Mo es la más activa y estable para la electrocatálisis de la HER con un sobrepotencial de -0.18 V a 300 mA cm^{-2} durante 1.500 h en una electrolisis continua de una disolución de KOH 6 M a 80 ºC. El excelente desempeño electrocatalítico del Ni-Mo se relaciona con el efecto electrónico interactivo entre los orbitales tipo *d* del Mo y el Ni, que ocasionan un sinergismo bien pronunciado que aumenta la actividad electrocatalítica hacia la HER, en algunas ocasiones mayor que la de los metales nobles [Wang, 2014; Jakšić, 2000; Raj, Vasu 1990].

1.4.3 Electrocatalizadores basados en carbón para la electrolisis del agua

A parte de las propiedades electrocatalíticas intrínsecas del propio material, la fabricación del catalizador también es una etapa crucial. Un alto rendimiento del catalizador es esencial para reducir el sobrepotencial, aumentar la cinética de la reacción y por lo tanto, mejorar la eficiencia energética, pero a menudo la actividad práctica está limitada por cuestiones relacionadas con el montaje de los materiales del catalizador en un electrodo de trabajo. Para el uso comercial, estas cuestiones son a veces incluso más importantes que la síntesis del catalizador. La mayoría de los electrodos reportados para la electrolisis del agua se fabrican mediante depósito de una película delgada o un aglomerado de partículas del catalizador (metal noble, óxido de un metal de transición, o un catalizador no-noble) sobre un carbón vítreo, espuma de níquel, fluoruro de óxido de estaño (FTO) cubierto de vidrio o algún otro sustrato conductor [Jin, 2014; Gong, 2013; Tian, 2014; Ma, 2014]. Sin embargo, la preparación de este tipo de electrocatalizadores por este método toma mucho tiempo y es difícil de controlar. Además, científicamente las actividades de medición son difíciles de comparar debido a la falta de homogeneidad en la morfología. Electrodos preparados de una manera tan general también conllevan una durabilidad limitada, ya que el material revestido se despega fácilmente durante la evolución de los gases formados en la superficie. Para superar este tipo de problemas es común usar aditivos y aglutinantes, pero éstos añaden un peso que en muchos casos no es conveniente para el sistema y limitan o disminuyen la conductividad del material catalítico y del sustrato conductor. Recientemente se ha desarrollado una nueva generación de materiales electrocatalíticos en la que el material electroactivo se hace crecer directamente sobre la superficie colectora de corriente [Shen, 2014; Xin, 2012; Wang, 2014]. El uso de este tipo de catalizadores en celdas de electrolisis de agua es favorable, debido a que la firme fijación del electrocatalizador en la superficie del colector de corriente mejora la estabilidad del electrodo durante la evolución de hidrógeno y, también, permite el aumento a una mayor escala. Para mejorar la pobre conductividad de los óxidos metálicos, la utilización de materiales híbridos basados en carbono metal/C ha demostrado ser una mejora significativa en las propiedades del electrodo para la HER mediante el anclaje de metales nanoestructurados tales como MoS_2, Ni-Co o M-Fe (M = Ni, Co) sobre materiales de carbono como carbón mesoporoso [Shen, 2014; Dong, 2014], nanotubos de carbono [Wang, 2014; Ma, 2014] o grafeno [Mao, 2014; Liang, 2011].

1.5 CATALIZADORES PARA LA ELECTROREDUCCIÓN DE CO_2

Al igual que el Fe y el Co, el Ni produce H_2 y CO e hidrocarburos en la electrorreducción del CO_2 bajo condiciones estándar. Sin embargo, todos estos metales tienen alta actividad para la hidrogenación de CO y/o CO_2 en reacciones de catálisis heterogénea (principalmente, la reacción de Fisher-Tropsch). Bajo condiciones de alta presión de CO_2, la eficiencia faradaica para la reducción de CO_2 sobre electrodos de Ni podría incrementarse bajando la temperatura y polarizando el potencial del electrodo a valores más negativos; este hecho sugiere que la formación de hidrocarburos sobre estos electrodos tiene lugar por un mecanismo similar al propuesto para la reacción de Fisher-Tropsch [Huang, 2011]. En la electrorreducción catalizada por Ni se observó, por medio de la espectroscopía IR, que la actividad catalítica está fuertemente relacionada al enlace entre el CO y la superficie metálica [Huang, 2011].

En la bibliografía se puede encontrar un gran número de estudios de la electrorreducción del CO_2 con complejos que contienen Ni como centro metálico, como las porfirinas, las ftalocianinas, los corroles o los tetraazamacrociclos, entre otros. Sin embargo, la reacción con todos estos complejos se han estudiado en disolventes orgánicos o disoluciones buffer de fosfato [Oh, 2013].

En el caso de catalizadores metálicos soportados en materiales carbonosos, las nanopartículas de Fe son las que han sido más exploradas [Qiao, 2014]. Se ha encontrado que cuando las nanopartículas están soportadas en nanotubos de carbono (Fe/CNTs) la actividad electrocatalítica hacia la reducción de CO_2 se incrementa pero no son estables [Qiao, 2014; Arrigo, 2012; Pérez-Rodríguez, 2012]. Por otra parte, estudios recientes han mostrado que la preparación de nanoparticulas de Ni soportadas, incrementa la actividad catalítica de éstas tanto para la reacción de reducción de oxígeno como para la de evolución de hidrógeno, al permitir una mejor distribución en el soporte, y de esta manera obtener una mayor área superficial que aumenta la actividad catalítica [Domínguez-Crespo, 2009; Chang, 2003].

Al igual que el Ni, los materiales que contienen nanopartículas de Pd soportadas en superficies carbonosas se han utilizado para la reacción de reducción de oxígeno como cátodo en las pilas de combustible y para la oxidación de ácido fórmico en el ánodo [Lee, 2014; Jiang, 2014; Maiyalagan, 2014]. En el caso de la reducción de CO_2, como se mencionó anteriormente, los materiales con bajo sobrepotencial para la generación de hidrógeno como el Pt y el Pd han sido escasamente estudiados, principalmente debido a la pérdida de eficiencia por la evolución de hidrógeno y al auto-envenenamiento por la adsorción de CO observado sobre las superficies de Pt [Choi, 2015; Wang, 2015; Dicks 2012; Giddey, 2012]. En contraste con otras aplicaciones electrocatalíticas, el Pd ha mostrado un comportamiento significativamente diferente hacia la reducción de CO_2, debido a diferentes interacciones con los intermediarios adsorbidos, como el CO o el COOH, y a la presencia de hidrógeno absorbido [Plana, 2013]. Sobre Pd se han detectado el CO y el ácido fórmico como productos a bajos sobrepotenciales, mientras que a altos sobrepotenciales se ha observado la producción de alcanos [Podlovchenko, 1994; Azuma, 1990].

1.6 PRESENTACIÓN DE LA TESIS DOCTORAL

La presente Tesis Doctoral pretende contribuir a la mejora de la eficiencia de pilas de combustible tipo PEM y de electrolizadores que permitan obtener combustibles (hidrógeno y biocombustibles). Se han desarrollado y caracterizado diferentes materiales catalíticos que intervienen en las reacciones electródicas de los correspondientes dispositivos electroquímicos.

Se han sintetizado y estudiado materiales con nanoestructura y propiedades jerárquicas capaces de catalizar eficientemente algunas reacciones anódicas y cátodicas. Con este fin se recurrió a métodos de síntesis de materiales con estructura porosa en diferentes niveles de organización, que poseen una superficie electrocatalítica grande en pequeñas dimensiones. Partiendo inicialmente de estrategias de construcción que se llevan a cabo por medio de procesos de autoensamblado, se obtuvieron materiales que se pueden utilizar como modelos para estudios electrocatáliticos que presentan alta área superficial, como los materiales mesoporosos y composites basados en grafeno.

En general, se han intentado abordar alguno de los problemas que afectan a las reacciones que ocurren en la interfase electródica de las PEMFCs y de los electrolizadores aportando posibles soluciones, fundamentadas en el conocimiento y elucidación de los correspondientes mecanismos de reacción mediante técnicas electroquímicas y espectroelectroquímicas.

Hay que señalar que algunos de estos estudios se han realizado en colaboración con otros grupos de investigación, lo que ha permitido complementarlos con otras técnicas y métodos no disponibles en la Universidad de La Laguna.

Esta Tesis Doctoral se presenta en la modalidad de compendio por publicaciones. En relación a su estructura, en primer lugar se considera un grupo de cuatro trabajos relacionados con la preparación y evaluación de catalizadores para la oxidación de combustibles alternativos (metanol, etanol y ácido fórmico). A continuación se presenta un segundo grupo de trabajos relacionados con en el desarrollo de nuevos materiales que permitan obtener dichos combustibles mediante procesos de electrorreducción. Y por último, se relacionan otros trabajos realizados durante el desarrollo de la Tesis Doctoral en colaboración con otros grupos de investigación, sobre catalizadores soportados en diferentes materiales carbonosos para la oxidación de combustibles, que permitieron complementar la discusión de la misma y que también se relacionan con ella, aunque directamente no han sido contemplados en este compendio.

1.6.1 Catalizadores para la electrooxidación de combustibles alternativos

A. Gonzalo García, **Jonathan Flórez-Montaño**, Alberto Hernández-Creus, Elena Pastor, Gabriel A. Planes, *Methanol electrooxidation at mesoporous Pt and Pt–Ru electrodes: A comparative study with carbon supported materials.* Journal of Power Sources, **2011**, 196, p. 2979-2986. Índice de impacto **según el *Journal Citation Reports*: 4.951 (2011). Posición con relación al índice de impacto de la revista en el año de publicación dentro de su categoría:**

Categoría	Total de revista en la categoría	Posición en la categoría	Cuartil de la categoría
Energías y combustibles	81	9	Q1

B. **Jonathan Flórez-Montaño**, Gonzalo García, José L. Rodríguez, Elena Pastor, Paula Cappellari, Gabriel A. Planes, *On the design of Pt based catalysts. Combining porous architecture with surface modification by Sn for electrocatalytic activity enhancement*. Journal of Power Sources, **2015**, 282, p. 34-44. Índice de impacto **según el *Journal Citation Reports*: 6.217 (2014). Posición con relación al índice de impacto de la revista en el año de publicación dentro de su categoría:**

Categoría	**Total de revista en la categoría**	**Posición en la categoría**	**Cuartil de la categoría**
Energías y combustibles	88	6	Q1

C. **Jonathan Flórez-Montaño**, Gonzalo García, Olmedo Guillén-Villafuerte, Gabriel A. Planes, Elena Pastor, *Mechanism of ethanol electrooxidation on mesoporous Pt electrode in acidic medium studied by a novel electrochemical mass spectrometry set-up.* Electrochimica Acta, enviado, número de manuscrito: ELECTACTA-S-15-05905. Índice de impacto **según el *Journal Citation Reports*: 4.504 (2014). Posición con relación al índice de impacto de la revista en el año de publicación dentro de su categoría:**

Categoría	**Total de revista en la categoría**	**Posición en la categoría**	**Cuartil de la categoría**
Electroquímica	28	4	Q1

D. **Jonathan Flórez-Montaño**, Verónica Celorrio, Daniela Plana, David J. Fermín, Elena Pastor, *Spectroscopic evidences of core electronic effects on CO and HCOOH electrooxidation at Au-Pd core-shells.* En preparación.

1.6.2 Catalizadores para obtener combustibles alternativos mediante procesos de electroreducción.

A. Daniela Plana, **Jonathan Flórez-Montaño**, Veronica Celorrio, Elena Pastor, David J. Fermín, *Tuning CO_2 electroreduction efficiency at Pd shells on Au nanocores.* Chemical Communication, **2013**, 49, p. 10962-10964. Índice de impacto **según el *Journal Citation Reports*: 6.718 (2013). Posición con relación al índice de impacto de la revista en el año de publicación dentro de su categoría:**

Categoría	**Total de revista en la categoría**	**Posición en la categoría**	**Cuartil de la categoría**
Química multidisciplinar	148	20	Q1

B. **Jonathan Flórez-Montaño**, Elena Pastor, *Ni and NiMo nanostructures supported on reduced graphene oxide with enhanced activity towards the hydrogen evolution reaction*. En preparación.

1.6.3 Catalizadores soportados en diferentes materiales carbonosos para la oxidación de combustibles.

A. Angélica M. Baena-Moncada, Gustavo M. Morales, Cesar Barbero, Gabriel A. Planes, **Jonathan Flórez-Montaño** and Elena Pastor, *Formic Acid Oxidation over Hierarchical Porous Carbon Containing PtPd Catalysts.* Catalysts **2013**, 3, p. 902-913.

B. Angélica M. Baena-Moncada, Rusbel Coneo-Rodríguez, Juan C. Calderón, **Jonathan Flórez-Montaño**, Cesar A. Barbero, Gabriel A. Planes, José L. Rodríguez, Elena Pastor, *Macroporous carbon as support for PtRu catalysts*. International Journal of Hydrogen Energy, **2014**, 39, p. 3964-3969.

C. Veronica Celorrio, **Jonathan Flórez-Montaño**, Rafael Moliner, Elena Pastor, María J. Lázaro, *Fuel cell performance of Pt electrocatalysts supported on carbon nanocoils* International Journal of Hydrogen Energy, **2014**, 39, p. 5371-5377.

D. Paula Cappellari, Gonzalo García, **Jonathan Flórez-Montaño**, Cesar A. Barbero, Elena Pastor, Gabriel A. Planes, *Enhanced formic acid oxidation on polycrystalline platinum modified by spontaneous deposition of gold. Fourier transform infrared spectroscopy studies.* Journal of Power Sources, **2015**, 296, p. 290-297.

Bibliografía

Almeida, T.S., Palma, L.M., Leonello, P.H., Morais, C., Kokoh, K.B. and De Andrade, A.R., 2012. An optimization study of PtSn/C catalysts applied to direct ethanol fuel cell: Effect of the preparation method on the electrocatalytic activity of the catalysts. *Journal of Power Sources,* **215**, pp. 53-62.

Antolini, E. and González, E.R., 2011. Effect of synthesis method and structural characteristics of Pt–Sn fuel cell catalysts on the electro-oxidation of CH_3OH and CH_3CH_2OH in acid medium. *Catalysis Today,* **160**, pp. 28-38.

Antolini, E., Salgado, J.R.C., Santos, L.G.R.A., Garcia, G., Ticianelli, E.A., Pastor, E. and González, E.R., 2006. Carbon supported Pt/Cr alloys as oxygen-reduction catalysts for direct methanol fuel cells. *Journal of Applied Electrochemistry,* **36**, pp. 355-362.

Antolini, E., 2007. Catalysts for direct ethanol fuel cells. *Journal of Power Sources,* **170**, pp. 1-12.

Arenz, M., Stamenkovic, V., Ross, P.N. and Markovic, N.M., 2004. Surface (electro-) chemistry on Pt(111) modified by a pseudomorphic Pd monolayer. *Surface Science,* **573**, pp. 57-66.

Aricò, A.S., Srinivasan, S. and Antonucci, V., 2001. DMFCs: From fundamental aspects to technology development. *Fuel Cells,* **1**, pp. 133-161.

Arrigo, R., Schuster, M.E., Wrabetz, S., Girgsdies, F., Tessonnier, J., Centi, G., Perathoner, S., Su, D.S. & Schlögl, R. 2012, New insights from microcalorimetry on the FeO_x/CNT-Based electrocatalysts active in the conversion of CO_2 to fuels, ChemSusChem, **5**, pp. 577-586.

Attard, G.S., Leclerc, S.A.A., Maniguet, S., Russell, A.E., Nandhakumar, I. and Bartlett, P.N., 2001. Mesoporous Pt/Ru alloy from the hexagonal lyotropic liquid crystalline phase of a nonionic surfactant. *Chemistry of Materials,* **13**, pp. 1444-1446.

Azuma, M., Hashimoto, K., Watanabe, M. & Sakata, T. 1990, Electrochemical reduction of carbon dioxide to higher hydrocarbons in a $KHCO_3$ aqueous solution, *Journal of Electroanalytical Chemistry and Interfacial Electrochemistry,* **294**, pp. 299-303.

Babu, P.K., Kim, H.S., Chung, J.H., Oldfield, E. and Wieckowski, A., 2004. bonding and motional aspects of CO adsorbed on the surface of Pt nanoparticles decorated with Pd. *The Journal of Physical Chemistry B,* **108**, pp. 20228-20232.

Badwal, S.P.S., Giddey, S., Kulkarni, A., Goel, J. and Basu, S., 2015. Direct ethanol fuel cells for transport and stationary applications – A comprehensive review. *Applied Energy,* **145**, pp. 80-103.

Baena-Moncada, A.M., Coneo-Rodríguez, R., Calderón, J.C., Flórez-Montaño, J., Barbero, C.A., Planes, G.A., Rodríguez, J.L. and Pastor, E., 2014. Macroporous carbon as support for PtRu catalysts. *International Journal of Hydrogen Energy,* **39**(8), pp. 3964-3969.

Behret, H. 1996, Karl Kordesch und Günter Simader: Fuel Cells and Their Applications, VCH, Weinheim, 1996. ISBN 3-527-28579-2, DM 248, Berichte der Bunsengesellschaft für physikalische Chemie, vol. 100, no. 11, pp. 1922-1922.

Bernardi, F., Alves, M.C.M. and Morais, J., 2010. Monitoring of Pt nanoparticle formation by H_2 reduction of PtO_2: An in situ dispersive X-ray absorption spectroscopy study. *The Journal of Physical Chemistry C,* **114**, pp. 21434-21438.

Bertuccioli, L., Chan, A., Hart, D., Lehner, F., Madden, B. and Standen, E., 2014. Study on development of water electrolysis in the EU. *Fuel Cells and Hydrogen Joint Undertaking.*

Bockris, B.J.O., Conway, B.E., Yeager, E. & White, R.E. 1981, Electrochemical Materials Science, Volumen 4 edn, Springer, Verlag US.

Breulmann, M., Davis, S.A., Mann, S., Hentze, H.-. and Antonietti, M., 2000. Polymer/Gel templating of porous inorganic macro-structures using nanoparticle building blocks. *Advanced Materials,* **12**, pp. 502-507.

Campbell, S.A. and Parsons, R., 1992. Effect of Bi and Sn adatoms on formic acid and methanol oxidation at well-defined platinum surfaces. *Journal of the Chemical Society, Faraday Transactions,* **88**, pp. 833-841.

Carmo, M., Fritz, D.L., Mergel, J. and Stolten, D., 2013. A comprehensive review on PEM water electrolysis. *International Journal of Hydrogen Energy,* **38**, pp. 4901-4934.

Carter, D. and Wing, J., 2013. Fuel Cell Today. The fuel cell industry review. Fuel cell Today.

Chang, F., Kuo, M., Tsay, M. & Hsieh, M. 2003, Hydrogenation of CO_2 over nickel catalysts on rice husk ash-alumina prepared by incipient wetness impregnation, *Applied Catalysis A: General*, **247**, pp. 309-320.

Choi, B., Nam, W., Chung, D.Y., Park, I., Yoo, S.J., Song, J.C. and Sung, Y., 2015. Enhanced methanol tolerance of highly Pd rich Pd-Pt cathode electrocatalysts in direct methanol fuel cells. *Electrochimica Acta*, **164**, pp. 235-242.

Chrzanowski, W. and Wieckowski, A., 1997. Ultrathin films of ruthenium on low index platinum single crystal surfaces: An electrochemical study. *Langmuir,* **13**, pp. 5974-5978.

Corti, H.R. and Gonzalez, E.R., 2014. Introduction to Direct Alcohol Fuel Cells. In: H.R. CORTI and E.R. GONZALEZ, eds, *Direct Alcohol Fuel Cells: Materials, Performance, Durability and Applications.* Dorchdret: Springer Science, pp. 1.

Crown, A., Johnston, C. and Wieckowski, A., 2002. Growth of ruthenium islands on Pt(hkl) electrodes obtained via repetitive spontaneous deposition. *Surface Science,* **506**, pp. L268-L274.

Crown, A., Moraes, I.R. and Wieckowski, A., 2001. Examination of Pt(111)/Ru and Pt(111)/Os surfaces: STM imaging and methanol oxidation activity. *Journal of Electroanalytical Chemistry,* **500**, pp. 333-343.

Decourt, B., Lajoie, B., D., R. and Soupa, O., 2014. *The hydrogen-based energy conversion Fact Book*.

Del Colle, V., Souza-Garcia, J., Tremiliosi-Filho, G., Herrero, E. and Feliu, J.M., 2011. Electrochemical and spectroscopic studies of ethanol oxidation on Pt stepped surfaces modified by tin adatoms. *Physical Chemistry Chemical Physics,* **13**, pp. 12163-12172. .

Dicks, A.L. 2012, PEM Fuel Cells: Applications in Comprehensive Renewable Energy, ed. A. Sayigh, Elsevier, Oxford, pp. 203-245.

Domínguez-Crespo, M.A., Ramírez-Meneses, E., Montiel-Palma, V., Torres Huerta, A.M. & Dorantes-Rosales, H. 2009, Synthesis and electrochemical characterization of stabilized nickel nanoparticles. *International Journal of Hydrogen Energy*, **34**, pp. 1664-1676.

Dong, C., Gu, Y., Zhong, M., Li, L., Sezer, K., Ma, M. and Liu, W., 2011. Fabrication of superhydrophobic Cu surfaces with tunable regular micro and random nano-scale structures by hybrid laser texture and chemical etching. *Journal of Materials Processing Technology,* **211**, pp. 1234-1240.

Dong, C., Chen, C., Chen, C. and Hung, C., 2014. Platinum particles supported on mesoporous carbons: fabrication and electrocatalytic performance in methanol-tolerant oxygen-reduction reactions. *Scientific Reports,* **4**, pp. 5790.

Du, B. and TONG, H., 2005. A coverage-dependent study of Pt spontaneously deposited onto Au and Ru surfaces: direct experimental evidence of the ensemble effect for methanol electro-oxidation on Pt. *The Journal of Physical Chemistry B*, **109**, pp. 17775-17780.

Engstfeld, A.K., Klein, J., Brimaud, S. and Behm, R.J., 2015. Electrochemical stability and restructuring and its impact on the electro-oxidation of CO: Pt modified Ru(0001) electrodes. *Surface Science*, **631**, pp. 248-257.

Enthaler, S., von Langermann, J. & Schmidt, T., 2010, Carbon dioxide and formic acid- the couple for environmental-friendly hydrogen storage. *Energy & Environmental Science*, **3**, pp. 1207-1217.

Esposito, D.V. and Chen, J.G., 2011. Monolayer platinum supported on tungsten carbides as low-cost electrocatalysts: opportunities and limitations. *Energy & Environmental Science*, **4**, pp. 3900-3912.

Esposito, D.V., Hunt, S.T., Kimmel, Y.C. and Chen, J.G., 2012. A new class of electrocatalysts for hydrogen production from water electrolysis: metal monolayers supported on low-cost transition metal carbides. *Journal of the American Chemical Society*, **134**, pp. 3025-3033.

Flórez-Montaño, J., García, G., Rodríguez, J.L., Pastor, E., Cappellari, P. and Planes, G.A., 2015. On the design of Pt based catalysts. Combining porous architecture with surface modification by Sn for electrocatalytic activity enhancement. *Journal of Power Sources*, **282**, pp. 34-44.

Franaszczuk, K. and Sobkowski, J., 1992. The influence of ruthenium adatoms on the oxidation of chemisorbed species of methanol on a platinum electrode by a radiochemical method. *Journal of Electroanalytical Chemistry*, **327**, pp. 235-245.

Franceschini, E.A., Planes, G.A., Williams, F.J., Soler-Illia, G.J.A.A. and Corti, H.R., 2011. Mesoporous Pt and Pt/Ru alloy electrocatalysts for methanol oxidation. *Journal of Power Sources*, **196**, pp. 1723-1729.

Friedl, J. and StimminG, U., 2013. Model catalyst studies on hydrogen and ethanol oxidation for fuel cells. *Electrochimica Acta*, **101**, pp. 41-58.

Garcia, G. and Koper, M.T.M., 2008. Stripping voltammetry of carbon monoxide oxidation on stepped platinum single-crystal electrodes in alkaline solution. *Physical Chemistry Chemical Physics*, **10**, pp. 3802-3811.

Giddey, S., Badwal, S.P.S., Kulkarni, A. & Munnings, C., 2012, A comprehensive review of direct carbon fuel cell technology. *Progress in Energy and Combustion Science*, **38**, pp. 360-399.

Gong, M., Li, Y., Wang, H., Liang, Y., Wu, J.Z., Zhou, J., Wang, J., Regier, T., Wei, F. and Dai, H., 2013. An advanced Ni@Fe layered double hydroxide electrocatalyst for water oxidation. *Journal of the American Chemical Society*, **135**, pp. 8452-8455.

Greeley, J., Jaramillo, T.F., Bonde, J., Chorkendorff, I. and Norskov, J.K., 2006. Computational high-throughput screening of electrocatalytic materials for hydrogen evolution. *Natural Material*, **5**, pp. 909-913.

Guo, D. and Ding, Y., 2012. Porous Nanostructured Metals for Electrocatalysis. *Electroanalysis*, **24**, pp. 2035-2043.

Hu, Y.H. 2010, Advances in CO_2 conversion and utilization, ACS Symposium Series. American Chemical Society. Washington DC; **1056**.

Huang, J., MA, R., Huang, T., Zhang, A. & Huang, W. 2011, Carbon dioxide reforming of methane over Ni/Mo/SBA-15-La_2O_3 catalyst: Its characterization and catalytic performance. *Journal of Natural Gas Chemistry*, **20**, pp. 465-470.

Jakšić, M.M., 2000. Hypo–hyper-d-electronic interactive nature of synergism in catalysis and electrocatalysis for hydrogen reactions. *Electrochimica Acta*, **45**, pp. 4085-4099.

Jiang, J. and Kucernak, A., 2009. Synthesis of highly active nanostructured PtRu electrocatalyst with three-dimensional mesoporous silica template. *Electrochemistry Communications*, **11**, pp. 623-626.

Jiang, J. and Kucernak, A., 2003. Electrooxidation of small organic molecules on mesoporous precious metal catalysts: II: CO and methanol on platinum–ruthenium alloy. *Journal of Electroanalytical Chemistry*, **543**, pp. 187-199.

Jiang, K., Zhang, H., Zou, S. & Cai, W. 2014, Electrocatalysis of formic acid on palladium and platinum surfaces: from fundamental mechanisms to fuel cell applications. *Physical Chemistry Chemical Physics*, **16**, pp. 20360-20376.

Jiang, Q., Lu, H.M., AND Zhao, M., 2004. Modelling of surface energies of elemental crystals. *Journal of Physics: Condensed Matter*, **16**, pp. 521.

Jin, K., Park, J., Lee, J., Yang, K.D., Pradhan, G.K., Sim, U., Jeong, D., Jang, H.L., Park, S., Kim, D., Sung, N., Kim, S.H., Han, S. and Nam, K.T., 2014. Hydrated Manganese (II) Phosphate ($Mn_3(PO_4)_2{\cdot}3H_2O$) as a Water Oxidation Catalyst. *Journal of the American Chemical Society*, **136**, pp. 7435-7443.

Jung, N., Chung, D.Y., Ryu, J., Yoo, S.J. and Sung, Y., 2014. Pt-based nanoarchitecture and catalyst design for fuel cell applications. *Nano Today*, **9**, pp. 433-456.

Kamarudin, M.Z.F., Kamarudin, S.K., Masdar, M.S. and Daud, W.R.W., 2013. Review: Direct ethanol fuel cells. *International Journal of Hydrogen Energy*, **38**, pp. 9438-9453.

Kelly, T.G., Lee, K.X. and Chen, J.G., 2014. Pt-modified molybdenum carbide for the hydrogen evolution reaction: From model surfaces to powder electrocatalysts. *Journal of Power Sources*, **271**, pp. 76-81.

Kim, S., Zhang, T., Park, J., Rhee, C. and Ryu, H., 2012. Particle size effect: Ru-modified Pt nanoparticles toward methanol oxidation. *Bulletin of the Korean Chemical Society*, **33**, pp. 3331-3337.

Kitahara, T., Sugawara, A., Sano, H. and Mizutani, G., 2003. Anisotropic optical second-harmonic generation from the Au nanowire array on the NaCl(110) template. *Applied Surface Science,* **219**, pp. 271-275.

Knutson, T.L., Bollinger, M.L. and Smyrl, W.H., 2008. Mesoporous microspheres of Pt and Pt/Ru formed by electrodeposition: Characterization of high surface area. *Journal of the Electrochemical Society,* **155**, pp. F17-F21.

Kopitkovas, G., Lippert, T., David, C., Wokaun, A. and Gobrecht, J., 2003. Fabrication of micro-optical elements in quartz by laser induced backside wet etching. *Microelectronic Engineering,* **67–68**, pp. 438-444.

Kunze, J. and Stimming, U., 2009. Electrochemical versus heat-engine energy technology: A tribute to wilhelm ostwald´s visionary statements. *Angewandte Chemie International Edition,* **48**, pp. 9230-9237.

Lebedeva, N.P., Koper, M.T.M., Feliu, J.M. and van Santen, R.A., 2000. The effect of the cooling atmosphere in the preparation of flame-annealed Pt(111) electrodes on CO adlayer oxidation. *Electrochemistry Communications,* **2**, pp. 487-490.

Lee, J., SeoO, J., Han, K. and Kim, H., 2006. Preparation of low Pt loading electrodes on Nafion (Na^+)-bonded carbon layer with galvanostatic pulses for PEMFC application. *Journal of Power Sources,* **163**, pp. 349-356.

Lee, S., Jung, N., Cho, J., Park, H., Ryu, J., Jang, I., Kim, H., Cho, E., Park, Y., Ham, H.C., Jang, J.H. & Yoo, S.J., 2014, Surface-Rearranged Pd_3Au/C nanocatalysts by using CO-Induced segregation for formic acid oxidation reactions. *ACS Catalysis,* **4**, pp. 2402-2408.

Léger, J., Rousseau, S., Coutanceau, C., Hahn, F. and Lamy, C., 2005. How bimetallic electrocatalysts does work for reactions involved in fuel cells: Example of ethanol oxidation and comparison to methanol. *Electrochimica Acta,* **50**, pp. 5118-5125.

Lehner, M., Tichler, R., Steinmüller, H. and Koppe, M., 2014. *Power-to-gas: technology and business models.* New York: Springer International Publishing.

Li, W. 2010, Electrocatalytic Reduction of CO_2 to Small Organic Molecule Fuels on Metal Catalysts, ACS Symposium Series. American Chemical Society. Washington DC; **1056,** pp. 55-76.

Liang, Y., Li, Y., Wang, H., Zhou, J., Wang, J., Regier, T. and Dai, H., 2011. Co_3O_4 nanocrystals on graphene as a synergistic catalyst for oxygen reduction reaction. *Nature Materials,* **10**, pp. 780-786.

Litster, S. and McLean, G., 2004. PEM fuel cell electrodes. *Journal of Power Sources,* **130**, pp. 61-76.

Liu, H., Tian, N., Brandon, M.P., Zhou, Z., Lin, J., Hardacre, C., Lin, W. and Sun, S., 2012. Tetrahexahedral Pt nanocrystal catalysts decorated with Ru adatoms and their enhanced activity in methanol electrooxidation. *ACS Catalysis,* **2**, pp. 708-715.

Lizcano-Valbuena, W.H., Paganin, V.A., Leite, C.A.P., Galembeck, F. and González, E.R., 2003. Catalysts for DMFC: Relation between morphology and electrochemical performance. *Electrochimica Acta,* **48**, pp. 3869-3878.

Lizcano-Valbuena, W.H., De Azevedo, D.C. and González, E.R., 2004. Supported metal nanoparticles as electrocatalysts for low-temperature fuel cells. *Electrochimica Acta,* **49**, pp. 1289-1295.

Ma, T.Y., Dai, S., Jaroniec, M. and Qiao, S.Z., 2014. Graphitic carbon nitride nanosheet/carbon nanotube three-dimensional porous composites as high-performance oxygen evolution electrocatalysts. *Angewandte Chemie,* **126**, pp. 7409-7413.

Ma, T.Y., Dai, S., Jaroniec, M. and Qiao, S.Z., 2014. Metallic organic framework derived hybrid Co_3O_4-Carbon porous nanowire arrays as reversible oxygen evolution electrodes. *Journal of the American Chemical Society,* **136**, pp. 13925-13931.

Maiyalagan, T., Wang, X. & Manthiram, A. 2014, Highly active Pd and Pd-Au nanoparticles supported on functionalized graphene nanoplatelets for enhanced formic acid oxidation. *RSC Advances,* **4**, pp. 4028-4033.

Mahapatra, S.S., Dutta, A. and Datta, J., 2011. Temperature dependence on methanol oxidation and product formation on Pt and Pd modified Pt electrodes in alkaline medium. *International Journal of Hydrogen Energy,* **36**, pp. 14873-14883.

Mao, S., Wen, Z., Huang, T., Hou, Y. and Chen, J., 2014. High-performance bi-functional electrocatalysts of 3D crumpled graphene-cobalt oxide nanohybrids for oxygen reduction and evolution reactions. *Energy & Environmental Science,* **7**, pp. 609-616.

Michalak, W.D., Krier, J.M., Alayoglu, S., Shin, J., An, K., Komvopoulos, K., Liu, Z. and Somorjai, G.A., 2014. CO oxidation on PtSn nanoparticle catalysts occurs at the interface of Pt and Sn oxide domains formed under reaction conditions. *Journal of Catalysis,* **312**, pp. 17-25.

Mielenz, J.R., 2001. Ethanol production from biomass: Technology and commercialization status. *Current opinion in microbiology,* **4**, pp. 324-329.

Moghaddam, R.B. and Pickup, P.G., 2012. Support effects on the oxidation of ethanol at Pt nanoparticles. *Electrochimica Acta,* **65**, pp. 210-215.

Moliner, R., Suelves, I., Lázaro, M.J. and Moreno, O., 2005. Thermocatalytic decomposition of methane over activated carbons: Influence of textural properties and surface chemistry. *International Journal of Hydrogen Energy,* **30**, pp. 293-300.

Motoo, S. and Watanabe, M., 1976. Electrocatalysis by Sn and Ge ad-atoms. *Journal of Electroanalytical Chemistry and Interfacial Electrochemistry,* **69**, pp. 429-431.

Motoo, S., Shibata, M. and Watanabe, M., 1980. Electrocatalysis by ad-atoms: Part VI. Enhancement of CO oxidation on Pt(subs) and Pt-Au(subs) electrodes by Sn ad-atoms. *Journal of Electroanalytical Chemistry and Interfacial Electrochemistry,* **110**, pp. 103-109.

Motoo, S. and Watanabe, M., 1980. Electrocatalysis by ad-atoms: Part VII. Enhancement of CO oxidation on platinum by As ad-atoms. *Journal of Electroanalytical Chemistry and Interfacial Electrochemistry,* **111**, pp. 261-268.

Nagle, L.C. and Rohan, J.F., 2008. Aligned carbon nanotube–Pt composite fuel cell catalyst by template electrodeposition. *Journal of Power Sources,* **185**, pp. 411-418.

Nørskov, J.K., Bligaard, T., Logadottira, A., Kitchin, J.R., Chen, J.G., Pandelov, S. and STIMMING, U., 2005. Trends in the Exchange Current for Hydrogen Evolution. *Journal of the Electrochemical Society,* **152**, pp. J23-J26.

Oh, Y. & Hu, X. 2013, Organic molecules as mediators and catalysts for photocatalytic and electrocatalytic CO_2 reduction. *Chemical Society Reviews,* **42**, pp. 2253-2261.

Otero, J., Sese, J., Michaus, I., Santa-Maria, M., Guelbenzu, E., Irusta, S., Carrilero, I. and Arruebo, M., 2014. Sulphonated polyether ether ketone diaphragms used in commercial scale alkaline water electrolysis. *Journal of Power Sources,* **247**, pp. 967-974.

Perales-Rondán, J.V., Ferre-Vilaplana, A., Feliu, J.M. and Herrero, E., 2014. Oxidation mechanism of formic acid on the bismuth adatom-modified Pt(111) surface. *Journal of the American Chemical Society,* **136**, pp. 13110-13113.

Pérez-Rodríguez, S., Corengia, M., García, G., Zinola, C.F., Lázaro, M.J. & Pastor, E. 2012. Gas diffusion electrodes for methanol electrooxidation studied by a new DEMS configuration: Influence of the diffusion layer. *International Journal of Hydrogen Energy,* **37**, pp. 7141-7151.

Peterson, A.A. & Nørskov, J.K., 2012. Activity descriptors for CO_2 electroreduction to methane on transition-metal catalysts. *The Journal of Physical Chemistry Letters*, **3**, pp. 251-258.

Plana, D., Florez-Montaño, J., Celorrio, V., Pastor, E. & Fermin, D.J., 2013. Tuning CO_2 electroreduction efficiency at Pd shells on Au nanocores. *Chemical Communications,* **49**, pp. 10962-10964.

Podlovchenko, B.I., Kolyadko, E.A. & Lu, S., 1994. Electroreduction of carbon dioxide on palladium electrodes at potentials higher than the reversible hydrogen potential. *Journal of Electroanalytical Chemistry,* **373**, pp. 185-187.

Qiao, J., Liu, Y., Hong, F. & Zhang, J., 2014. A review of catalysts for the electroreduction of carbon dioxide to produce low-carbon fuels. *Chemical Society Reviews*, **43**, pp. 631-675.

Raj, I.A. and Vasu, K.I., 1990. Transition metal-based hydrogen electrodes in alkaline solution â€” electrocatalysis on nickel based binary alloy coatings. *Journal of Applied Electrochemistry,* **20**, pp. 32-38.

Rommal, H.E.G. and Morgan, P.J., 1988. The role of absorbed hydrogen on the Voltage-Time behavior of nickel cathodes in hydrogen evolution. *Journal of the Electrochemical Society,* **135**, pp. 343-346.

Sharaf, O.Z. and Orhan, M.F., 2014. An overview of fuel cell technology: Fundamentals and applications. *Renewable and Sustainable Energy Reviews,* **32**, pp. 810-853.

Shen, L., Che, Q., Li, H. and Zhang, X., 2014. Mesoporous $NiCo_2O_4$ nanowire arrays grown on carbon textiles as binder-free flexible electrodes for energy storage. *Advanced Functional Materials,* **24**, pp. 2630-2637.

SIEMENS, 2015-last update, **Hydrogen from Electrolysis: The Most Versatile Fuel**. Available: https://www.siemens.com/innovation/en/home/pictures-of-the-future/energy-and-efficiency/smart-grids-and-energy-storage-electrolyzers-energy-storage-for-the-future.html [08/01, 2015].

Sims, C.M., Ponce, A.A., Gaskell, K.J. and Eichhorn, B.W., 2015. CO tolerance of Pt and PtSn intermetallic electrocatalysts on synthetically modified reduced graphene oxide supports. *Dalton Transactions,* **44**, pp. 977-987.

Soares, D.M., Teschke, O. and Torriani, I., 1992. Hydride effect on the kinetics of the hydrogen evolution reaction on nickel cathodes in alkaline media. *Journal of the Electrochemical Society,* **139**, pp. 98-105.

Strbac, S., Johnston, C.M., Lu, G.Q., Crown, A. and Wieckowski, A., 2004. In situ STM study of nanosized Ru and Os islands spontaneously deposited on Pt(111) and Au(111) electrodes. *Surface Science,* **573**, pp. 80-99.

Suzuki, T., Miyata, H., Noma, T. and Kuroda, K., 2008. Platinum thin film consisting of well-aligned nanowires and its optical behavior. *The Journal of Physical Chemistry C,* **112**, pp. 1831-1836.

Tian, G., Zhao, M., Yu, D., Kong, X., Huang, J., Zhang, Q. and Wei, F., 2014. nitrogen-doped graphene/carbon nanotube hybrids: In situ formation on bifunctional catalysts and their superior electrocatalytic activity for oxygen evolution/reduction reaction. *Small,* **10**, pp. 2251-2259.

Tiwari, J.N., Pan, F., Tiwari, R.,N. and Nandi, S.K., 2008. Facile synthesis of continuous Pt island networks and their electrochemical properties for methanol electrooxidation. *Chemical Communications,* **48**, pp. 6516-6518.

Tripkovic, V., 2015. First principles study of (Cd, Hg, In, Tl, Sn, Pb, As, Sb, Bi, Se) modified Pt(111), Pt(100) and Pt(211) electrodes as CO oxidation catalysts. *Electrochimica Acta,* **168**, pp. 370-378.

Tsai, M., Yeh, T. and Tsai, C., 2006. An improved electrodeposition technique for preparing platinum and platinum–ruthenium nanoparticles on carbon nanotubes directly grown on carbon cloth for methanol oxidation. *Electrochemistry Communications,* **8**, pp. 1445-1452.

Ulleberg, Ø., 2003. Modeling of advanced alkaline electrolyzers: A system simulation approach. *International Journal of Hydrogen Energy,* **28**, pp. 21-33.

Ursúa, A., Sanchis, P. and Marroyo, L., 2013. Electric conditioning and efficiency of hydrogen production systems and their integration with renewable energies In: L. GANDIA, G. ARZAMENDI and P. DIÉGUEZ, eds, *Renewable hydrogen technologies.* Amsterdam: Elsevier.

Velázquez-Palenzuela, A., Brillas, E., Arias, C., Centellas, F., Garrido, J.A., Rodríguez, R.M. and Cabot, P., 2013. Structural analysis of carbon-supported Ru-decorated Pt nanoparticles synthesized using forced deposition and catalytic performance toward CO, methanol, and ethanol electro-oxidation. *Journal of Catalysis,* **298**, pp. 112-121.

Velev, O.D., Tessier, P.M., Lenhoff, A.M. and Kaler, E.W., 1999. Materials: A class of porous metallic nanostructures. *Nature,* **401**, pp. 548-548.

Vidal-Iglesias, F., López-Cudero, A., Solla-Gullón, J., Aldaz, A. and Feliu, J., 2012. Pd-modified shape-controlled Pt nanoparticles towards formic acid electrooxidation. *Electrocatalysis,* **3**, pp. 313-323.

Vidal-Iglesias, F.J., Solla-Gullón, J., Herrero, E., Aldaz, A. and Feliu, J.M., 2010. Pd adatom decorated (100) preferentially oriented Pt nanoparticles for formic acid electrooxidation. *Angewandte Chemie International Edition,* **49**, pp. 6998-7001.

Vieltstich, W., Lamm, A. and Gastaiger, H.A., 2003. *Handbook of fuel cells: Fundamentals, Technology and Applications.* Chichester: John Wiley & Sons.

WAlcarius, A., 2013. Mesoporous materials and electrochemistry. *Chemical Society Reviews,* **42**, pp. 4098-4140.

Walcarius, A. and Kuhn, A., 2008. Ordered porous thin films in electrochemical analysis. *TrAC Trends in Analytical Chemistry,* **27**, pp. 593-603.

Wang, H. and Abruña, H.D., 2015. Origin of multiple peaks in the potentiodynamic oxidation of CO adlayers on Pt and Ru-modified Pt electrodes. *The Journal of Physical Chemistry Letters,* **6**, pp. 1899-1906.

Wang, K., Wu, H., Meng, Y. and Wei, Z., 2014. Conducting polymer nanowire arrays for high performance supercapacitors. *Small,* **10**, pp. 14-31.

Wang, M., Li, Y., Xie, Z., Liu, C. and Yeung, E.S., 2010. Fabrication of large-scale one-dimensional Au nanochain and nanowire networks by interfacial self-assembly. *Materials Chemistry and Physics,* **119**, pp. 153-157.

Wang, Y., Xing, G., Han, Z.J., Shi, Y., Wong, J.I., Huang, Z.X., Ostrikov, K.(. and YANG, H.Y., 2014. Pre-lithiation of onion-like carbon/MoS_2 nano-urchin anodes for high-performance rechargeable lithium ion batteries. *Nanoscale,* **6**, pp. 8884-8890.

Wang, Y., Zhang, G., Xu, W., Wan, P., Lu, Z., Li, Y. and Sun, X., 2014. A 3D nanoporous Ni/Mo electrocatalyst with negligible overpotential for alkaline hydrogen evolution. *ChemElectroChem,* **1**, pp. 1138-1144.

Waszczuk, P., Solla-Gullón, J., Kim, H-., Tong, Y.Y., Montiel, V., Aldaz, A. and Wieckowski, A., 2001. Methanol electrooxidation on platinum/ruthenium nanoparticle catalysts. *Journal of Catalysis,* **203**, pp. 1-6.

Wei, Z.D., Li, L.L., Luo, Y.H., Yan, C., Sun, C.X., Yin, G.Z. and Shen, P.K., 2006. Electrooxidation of methanol on upd-Ru and upd-Sn modified Pt electrodes. *The Journal of Physical Chemistry B,* **110**, pp. 26055-26061.

Wu, Y.N., Liao, S.J., Su, Y.L., Zeng, J.H. and Dang, D., 2010. Enhancement of anodic oxidation of formic acid on palladium decorated Pt/C catalyst. *Journal of Power Sources,* **195**, pp. 6459-6462.

Xin, S., Guo, Y. and Wan, L., 2012. Nanocarbon networks for advanced rechargeable lithium batteries. *Accounts of Chemical Research,* **45**, pp. 1759-1769.

Xu, Y. and Zhang, B., 2014. Recent advances in porous Pt-based nanostructures: synthesis and electrochemical applications. *Chemical Society Reviews,* **43**, pp. 2439-2450.

Yaroslavtsev, A.B., Dobrovolsky, Y.A., Shaglaeva, N.S., Frolova, L.A., Gerasimova, E.V. and Sanginov, E.A., 2012. Nanostructured materials for low-temperature fuel cells. *Russian Chemical Reviews,* **81**, pp. 191.

Zhao, D., Xu, M.W., Zhou, W., Zhang, J. and Li, H.L., 2008. Preparation of ordered mesoporous nickel oxide film electrodes via lyotropic liquid crystal templated electrodeposition route. *Electrochimica Acta,* **53**, pp. 2699-2705.

Zhong, Y., Xu, C., Kong, L. and Li, H., 2008. Synthesis and high catalytic properties of mesoporous Pt nanowire array by novel conjunct template method. *Applied Surface Science,* **255**, pp. 3388-3393.

Zielińska-Jurek, A. and Hupka, J., 2014. Preparation and characterization of Pt/Pd-modified titanium dioxide nanoparticles for visible light irradiation. *Catalysis Today,* **230**, pp. 181-187.

2. OBJETIVOS

El objetivo central de esta Tesis Doctoral es la síntesis y caracterización de nuevos materiales electrocatalíticos que incrementen la eficiencia energética de las celdas de combustible de membrana de electrolito polimérico y de los electrolizadores en la obtención de combustibles (hidrógeno y biocombustibles).

Los objetivos específicos establecidos para su consecución han sido:

1. Síntesis de catalizadores de Pt mesoporosos (MPPt) y su modificación superficial con adátomos de Ru (MPPt/Ru) y Sn (MPPt/Sn).

2. Síntesis de nanodiscos de Ni y NiMo soportados sobre óxido de grafeno reducido.

3. Caracterización fisicoquímica de los materiales sintetizados mediante técnicas de microscopía de barrido con sonda (microscopía de efecto túnel (STM) y microscopía de fuerza atómica (AFM)), microscopía de transmisión electrónica (TEM), por difracción de rayos X (XRD) y las espectroscopías fotoelectrónica de rayos X (XPS), de dispersión de rayos X (EDS) y espectroscopía Raman.

4. Mejora y optimización del espectrómetro de masas diferencial electroquímico para el estudio de catalizadores no soportados.

5. Estudio mediante técnicas electroquímicas y espectroelectroquímicas de la influencia de la geometría, de la naturaleza química de la superficie catalítica y del efecto del soporte en la oxidación de metanol y etanol sobre MPPt, MPPt/Ru, mesoporoso de Pt y Ru codepositados (MPPtR) y una aleación de PtRu soportada sobre carbón comercial.

6. Estudio electroquímico y espectroelectroquímico de la actividad catalítica de MPPt/Sn para la oxidación de metanol y determinación de la influencia del Sn en el mecanismo de reacción.

7. Estudio espectroelectroquímico de estructuras núcleo-cubierta de Au-Pd (*core-shell*, Au@Pd) para determinar la influencia electrónica del núcleo de Au sobre la superficie para la oxidación de CO y HCOOH.

8. Estudio de la eficiencia faradaica para la reducción de CO_2 sobre nanoestructuras bimetálicas Au@Pd.

9. Estudio electroquímico de la generación de hidrógeno sobre composites de grafeno con Ni y NiMo en medio alcalino.

3. METODOLOGÍA

En este capítulo se provee información de los reactivos y disoluciones utilizadas, de los diferentes métodos de preparación de los materiales catalíticos, y también de las técnicas utilizadas para la caracterización físico-química. Además, se describen las técnicas electroquímicas y espectroelectroquímicas, estas últimas desarrolladas en el Grupo de Investigación "Ciencia de Superficies y Electrocatálisis" (GCSE) de la ULL.

3.1 REACTIVOS Y DISOLUCIONES

Todas las disoluciones se prepararon usando agua ultra pura obtenida de un sistema Milli-Q® Advantage A10 (Merck Millipore) con una resistencia especifica de 18,2 MΩ cm y 2 ppb de materia orgánica total. La tabla 4.1 recoge el conjunto de reactivos y gases empleados en el desarrollo experimental de esta Tesis.

Tabla 4.1. Lista de reactivos y gases.

Nombre	**Fórmula**	**Compañía**	**Pureza**
Ácido fórmico	CH_2O_2	Merck	98-100 % p.a.
Ácido hexacloroplatínico	H_2PtCl_6	Sigma-Aldrich	8 %
Ácido perclórico	$HClO_4$	Merck	60 % p.a.
Ácido sulfúrico	H_2SO_4	Merck Suprapur	95-97 %
Argón	Ar	Air Liquide	99,998 %
Cloruro de níquel(II) hexahidratado	$NiCl_2 \cdot 6H_2O$	Sigma-Aldrich	> 98 % p.a.
Cloruro de paladio	$PdCl_2$	Sigma-Aldrich	99 %
Cloruro de rutenio(III) hidratado	$RuCl_3 \cdot xH_2O$	Sigma-Aldrich	45-55 % Ru
Etanol	CH_3CH_2OH	Merck	99,9 % p.a.
Éter cetil polioxietileno, Brij®10	$C_{16}H_{33}(OCH_2CH_2)_{10}OH$	Fluka	99 %
Etilenglicol	$C_2H_6O_2$	Sigma-Aldrich	99,9 %
Grafito	C	Sigma-Adrich	
Heptamolibdato de amonio tetrahidratado	$(NH_4)_6Mo_7O_{24} \cdot 4H_2O$	Sigma-Aldrich	
Mezcla Hidrógeno/Nitrógeno	$5\%H_2$-$95\%N_2$	Air Liquide	
Hidróxido de amonio	NH_4OH	Merck	20 %
Hidróxido sódico	NaOH	Sigma-Aldrich	99,99 %
Metanol	CH_3OH	Merck	99,9 % p.a.
Monóxido de carbono	CO	Air Liquide	99,997 %
Nafion®	-	Sigma-Aldrich	5 %

Nombre	**Fórmula**	**Compañía**	**Pureza**
Nitrógeno	N_2	Carburos metálicos	99,999 %
Permanganato de potasio	$KMnO_4$	Panreac	99,0 %
Sulfato de estaño(II)	$SnSO_4$	Sigma-Aldrich	98 %

Las siguientes disoluciones se han utilizado como electrolitos de fondo en los estudios electroquímicos:

- Ácido sulfúrico 0,5 M.
- Ácido perclórico 0,1 M.
- Hidróxido sódico 0,1 M.

Las disoluciones de los alcoholes se prepararon desoxigenando previamente la correspondiente disolución del electrolito de fondo con nitrógeno o argón. Se han utilizado:

- Disolución 1,0 M de metanol y 0,5 M de ácido sulfúrico.
- Disoluciones 0,01 M, 0,05 M, 0,1 M, 0,5 M y 1,0 M de etanol y 0,5 M de ácido sulfúrico.

La modificación superficial del electrodo de Pt mesoporoso (MPPt) con adátomos de Ru y Sn se realizó usando las siguientes disoluciones:

- Disolución 4,0 mM de cloruro de rutenio(III) y 0,1 M de ácido perclórico.
- Disolución 0,5 mM de sulfato de estaño(II) y 0,5 M de ácido sulfúrico.

3.2 PREPARACIÓN DE ELECTRODOS NANOESTRUCTURADOS NO SOPORTADOS

3.2.1 Síntesis de catalizadores de Pt mesoporoso

El Pt mesoporoso (MPPt) se obtiene por electrodeposición de una mezcla 1:1 del surfactante Brij®10 y H_2PtCl_6, a una temperatura de 60 ºC, sobre una superficie de Au con un diámetro aproximado de 1 mm previamente pulida. El electrodo de Au se pone en contacto con la disolución manteniendo un potencial aplicado de 0,85 V. Posteriormente, se aplica un salto de potencial a 0,15 V durante un tiempo de 600 s. A continuación, el electrodo se lava varias veces con abundante agua ultra pura caliente con el objeto de eliminar el surfactante y quede sólo el material nanoestructurado de Pt.

En el caso de los electrodos de PtRu mesoporoso (MPPtRu) la electrodeposición se llevó a cabo con un salto de potencial desde 0,85 a 0,05 V durante 300 s, en disoluciones de composición 1:0,5:0,5 del surfactante, la sal de platino (H_2PtCl_6) y la sal metálica de rutenio ($RuCl_3$) a 60 ºC.

3.2.2 Modificación superficial de Pt mesoporoso con adátomos de Ru, Sn y Pd

3.2.2.1 Modificación espontánea con Ru

La modificación de la superficie de los electrodos de MPPt con Ru se realizó mediante el siguiente procedimiento:

1. Durante 30 min se sumerge el electrodo MPPt en una disolución 4,0 mM de $RuCl_3$ y 0,1 M de $HClO_4$, manteniendo una configuración tipo menisco y dejando el potencial a circuito abierto.
2. Se retira el electrodo y se eliminan los restos de la disolución del interior de los poros mediante un lavado con agua ultra pura.

3. A continuación se realiza la activación de la superficie del electrodo en $HClO_4$ 0,1 M mediante la técnica de voltamperometría cíclica, a una velocidad de 0,05 V s^{-1}, entre 0,05 y 0,55 V como límites inferior y superior de potencial, hasta obtener una respuesta reproducible. Los potenciales indicados están referidos a un electrodo reversible de hidrógeno (ERH).
4. Seguidamente se registra el perfil voltamperométrico en H_2SO_4 0,5 M a la velocidad de 0,02 V s^{-1}, entre 0,05 y 0,85 V (vs. ERH), hasta obtener una respuesta reproducible de la superficie de Pt modificada por Ru.
5. Lavado con agua ultra pura.

Este procedimiento se aplica reiteradamente hasta obtener las condiciones óptimas en las que el electrodo modificado se comporta mejor frente a la oxidación de metanol (normalmente 3 ciclos).

La figura 4.1 muestra cómo varía el voltamperograma cíclico del electrodo de MPPt en ácido perclórico 0,1 M después de sucesivas modificaciones con Ru a temperatura ambiente. Se puede apreciar claramente la disminución de los picos correspondientes a la adsorción/desorción de hidrógeno junto con el incremento de la corriente en la región 0,40-0,80 V por la presencia de los adátomos depositados sobre la estructura mesoporosa.

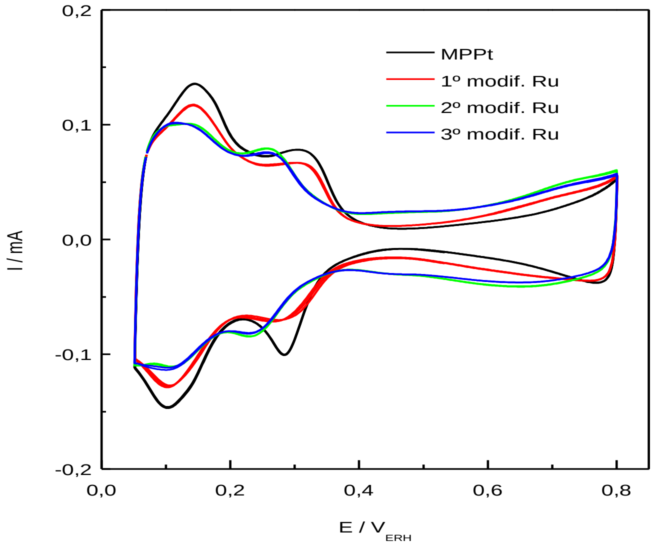

Figura 4.1. Voltamperogramas cíclicos obtenidos en una disolución 0,1 M de $HClO_4$, a una velocidad de barrido de 0,02 Vs^{-1}, con un electrodo de MPPt y después de tres modificaciones sucesivas con Ru (MPPt/Ru).

El cubrimiento relativo de Ru en la superficie (θ_{Metal}) puede calcularse fácilmente al comparar la carga en la región de adsorción de hidrógeno, antes y después de la modificación superficial de la superficie de Pt mesoporoso con Ru [Cramm, 1997], mediante la siguiente ecuación:

$$\theta_{Metal} = \frac{Q_0^H - Q_{Metal}^H}{Q_0^H} \qquad (4.1)$$

Donde, Q_0^H es la carga total de hidrógeno desorbido de la superficie de Pt y Q_{Metal}^H es la carga total de hidrógeno desorbido desde la superficie de Pt modificada con Ru.

La composición superficial encontrada para los electrodos de Pt mesoporoso con la tercera modificación de adátomos de Ru (MPPt/Ru) corresponde al recubrimiento de un 40 % de Ru. La elección de este grado de recubrimiento se basa en el supuesto de que esta superficie presente unos potenciales de oxidación del CO_{ad} similares a los encontrados para las aleaciones convencionales de Pt-Ru soportadas sobre carbón con esta composición [García, 2011; Jusys, 2002].

3.2.2.2 Modificación espontánea con Sn

La modificación superficial de la estructura mesoporosa de Pt con adátomos de Sn se consigue sumergiendo el electrodo, a circuito abierto, en una disolución 0,5 mM en $SnSO_4$ y 0,5 M en H_2SO_4 recién preparada para evitar la oxidación autocatalitica de Sn^{2+} a Sn^{4+} debido al oxígeno disuelto [(Wei, 2006)]. El recubrimiento relativo del Sn depositado sobre la superficie de MPPt puede calcularse de manera similar que para el Ru, mediante la ecuación (4.1).

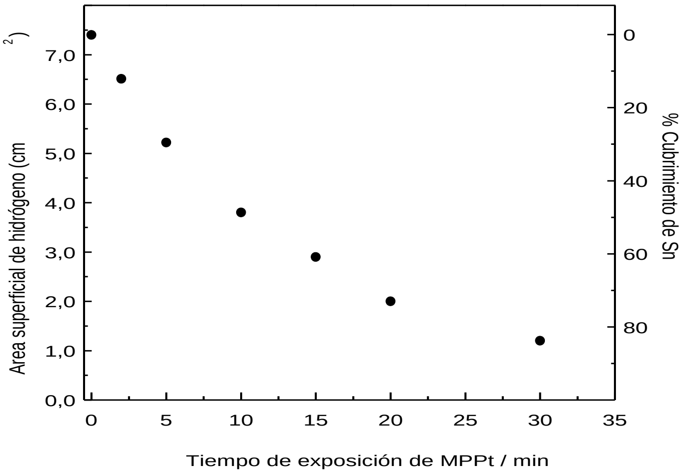

Figura 4.2. Área de superficie de Pt calculada a partir de la región de adsorción/desorción de hidrógeno (eje Y izquierdo); y porcentaje de cubrimiento de Sn a diferentes tiempos de adsorción (eje Y derecho) *vs.* tiempo de inmersión en la disolución del precursor metálico.

La figura 4.2 muestra la variación del grado de recubrimiento de la superficie del MPPt con el tiempo de inmersión en la disolución del precursor; se observa que en los primeros 15 min es cuando ocurre el cambio más sigificativo en el recubrimiento de Sn, alcanzando aproximadamente un 60 %. A tiempos mayores no hay una gran variación en la cantidad de Sn que se deposita. Por lo que se consideró que este estudio se limitara a tres modificaciones que equivalen a 15 min de exposición del electrodo en contacto con la disolución y corresponden a un recubrimiento aproximado del 60 %.

La obtención de MPPt modificado con Sn se realizó aplicando tres ciclos del siguiente procedimiento para obtener un recubrimiento aproximado del 60%:

1. Inmersión del electrodo durante 5 min en la disolución del precursor metálico, en una configuración tipo menisco y a circuito abierto.
2. Lavado con agua ultra pura.
3. Activación de la superficie del electrodo en una disolución de H_2SO_4 0,5 M mediante la técnica de voltamperometría cíclica, a la velocidad de 0,05 V s^{-1} entre 0,05 y 0,55 V (vs. ERH) como límite inferior y superior de potencial, hasta obtener una respuesta reproducible.
4. Seguidamente se registra el perfil voltamperométrico en H_2SO_4 0,5 M a la velocidad de 0,10 V s^{-1}, entre 0,05 y 0,85 V (vs. ERH), hasta obtener un voltamperograma cíclico reproducible de la superficie de Pt modificada por Sn.
5. Lavado con agua ultra pura.

3.3 PREPARACIÓN DE NANOESTRUCTURAS PARA EL ALMACEAMIENTO O GENERACIÓN DE HIDRÓGENO

3.3.1 Síntesis de nanodiscos de Ni y NiMo soportados en óxido de grafeno reducido (RGO)

3.3.1.1 Síntesis de óxido de grafeno

El óxido de grafeno (GO) se preparó modificando el método de Hummer [Hummers, 1958], con el fin de utilizar menos agentes oxidantes que puedan contaminar el producto final.

A un matraz Erlenmeyer que contiene 1,0 g de grafito, y que se encuentra sumergido en un baño de hielo, se adicionan 30 mL de H_2SO_4 concentrado. La mezcla se deja en agitación magnética durante 1 h para conseguir una buena dispersión. A continuación se adicionan lentamente 3,5 g de $KMnO_4$, manteniendo la agitación y el baño frío durante 1 h. Pasado ese tiempo, el matraz con la mezcla se retira del baño de hielo, se diluye con 50 mL de agua ultra pura y, posteriormente, se deja agitando durante 1 h a 35 ºC obteniéndose una disolución de color verde. A continuación la temperatura se incrementa hasta 98 ºC, se deja 30 min en agitación y, luego, se adicionan lentamente 200 mL de agua ultra pura seguido de 1,25 mL de H_2O_2 al 30 % manteniendo la agitación durante otros 30 min. Finalmente, el óxido de grafeno se obtiene por varios lavados con agua ultra pura y centrifugados. Cuando el pH del sobrenadante esté cerca de 7, el precipitado se dispersa con un mínimo de agua y se seca a 60 ºC en estufa.

3.3.1.2 Síntesis de Ni/RGO y NixMo1-x/RGO (0 ≤ x ≤1)

Las nanoestructuras de Ni y NiMo soportadas sobre RGO se sintetizaron siguiendo un método similar al utilizado por McKone *et al.* [McKone, 2013]. El control de la relación atómica se realizó mediante el uso de la relación molar correspondiente de las sales metálicas. La síntesis de los diferentes catalizadores involucra la dispersión por medio de ultrasonido de 0,150 g de GO en 5 mL de agua ultra pura, seguido de la adición de los precursores metálicos ($NiCl_2 \cdot 6H_2O$ y $(NH_4)_6Mo_7O_{24} \cdot 4H_2O$). Una vez se ha dispersado la mezcla se adicionan 3 mL de NH_4OH al 20 % a la disolución y se deja en agitación magnética por 1 h. Luego se añaden 45 mL de etilenglicol y se mantiene la agitación durante varias horas (16-18 h) a temperatura ambiente. Posteriormente la mezcla se calienta hasta ebullición (alrededor de 180-200 ºC) manteniendo la agitación. Cuando la disolución empieza a hervir, el recipiente se retira y la disolución se transfiere a los tubos para centrifugar mientras todavía está caliente. La suspensión se centrifuga a 3.000 rpm por 10 min. El precipitado obtenido se lava y centrifuga tres o cuatro veces con agua ultra pura, y una vez con acetona. Finalmente el precipitado se transfiere a un vidrio reloj y se seca en estufa a 60 ºC.

Una vez seco, el precipitado se traspasa a una barquilla de cerámica, y se introduce en un horno tubular para realizar el tratamiento térmico reductor durante 1 h a 450 ºC, bajo un flujo de 100 mL min^{-1} de H_2 al 5 %. Este tratamiento permite la completa reducción del NiO a Ni metálico y del GO a RGO, tal y como se ilustra en la figura 4.3. Durante el tratamiento térmico la muestra se calienta primero con una rampa de temperatura de 5 ºC min^{-1} hasta llegar a 200 ºC, donde se mantiene por 30 min para secar la muestra, y posteriormente continua hasta alcanzar la temperatura de carbonización correspondiente.

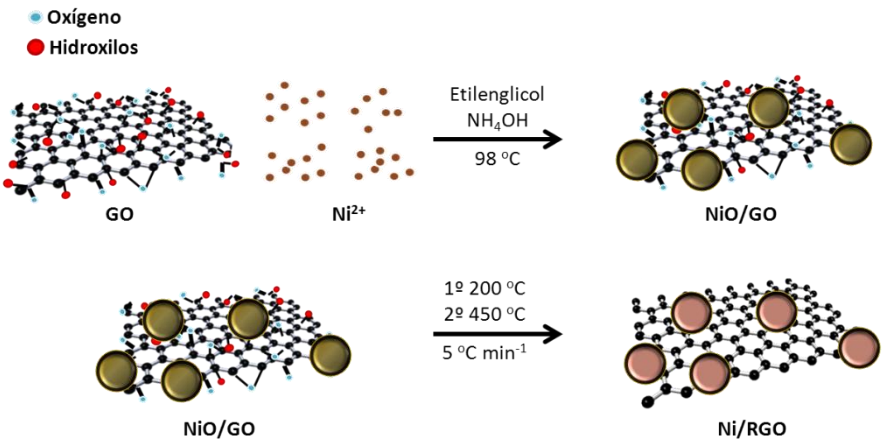

Figura 4.3. Esquema de la síntesis de nanodiscos de Ni soportados sobre RGO

3.3.2 Síntesis de nanoestructuras bimetálicas tipo *core-shell* de Au@Pd (CS)

Las nanopartículas de Au recubiertas por Pd, tipo core-shell (CS), empleadas en este trabajo fueron sintetizadas y caracterizadas por el *Bristol Electrochemistry Group*, dirigido por el Dr. David Fermín de la Universidad de Bristol (Reino Unido).

Las nanopartículas de Au-Pd (CS) fueron sintetizadas por la reducción de H_2PdCl_4 sobre partículas de Au de alrededor de 19 nm en presencia de ácido ascórbico de acuerdo al método de Montes *et al.* [Montes, 2011]. El tamaño del espesor de la capa externa de Pd se obtuvo mediante el control de la cantidad añadida de una disolución H_2PdCl_4 0,1 M a 50 mL de una disolución de nanopartículas de Au, colocadas en un baño de hielo y bajo agitación magnética. Posteriormente, se adiciona gota a gota un exceso (6 mL) de ácido L-ascórbico (0,1 M) para evitar la formación de nanopartículas de Pd aisladas.

Para obtener este catalizador soportado en carbón, a las disoluciones de Au@Pd (CS) se les añade la cantidad específica de carbón necesaria para que resulte una carga metálica del 20 % peso. La mezcla se mantiene en agitación magnética durante 48 h. Finalmente, el material se filtra, se lava con agua Milli-Q y se seca a 60 ºC en estufa.

3.4 CARACTERIZACIÓN POR TÉCNICAS FISICOQUÍMICAS

La caracterización fisicoquímica de los catalizadores preparados y especialmente su caracterización superficial, resultan fundamentales para poder relacionar el comportamiento catalítico de los materiales sintetizados con su naturaleza, estructura y propiedades fisicoquímicas. Se intenta así establecer una relación estructura - composición - actividad electrocatalítica. Las principales técnicas utilizadas en el desarrollo de esta Tesis están en el Servicio General de Apoyo a la Investigación (SEGAI) de la ULL y se describen a continuación.

3.4.1 Microscopía de efecto túnel (STM)

La microscopía de efecto túnel (STM) fue desarrollada por Binnig y Rohrer en el año 1981 [Binnig, 1982], siendo galardonados en 1986 con el premio Nobel de Física por esta contribución. La técnica STM permite caracterizar cuantitativamente la complejidad morfológica de las superficies observadas e, incluso, permite “ver” uno a uno los átomos de la superficie. Su principio de operación se basa en el establecimiento y medida de la corriente túnel entre una punta afilada acabada idealmente en un solo átomo y una muestra conductora. Desde el punto de vista de la mecánica clásica, un electrón no puede superar una barrera de potencial superior a su energía. Sin embargo, según la mecánica cuántica, los electrones no tienen definida una posición precisa, sino una densidad de probabilidad. Esto provoca que en ciertos sistemas esta densidad de probabilidad se extienda hasta el otro lado de una barrera de potencial. Por tanto, el electrón puede atravesar la barrera y contribuir a generar una intensidad eléctrica. Esta intensidad se denomina intensidad de efecto túnel y es el parámetro de control que nos permite obtener la topografía de la superficie. En un microscopio de efecto túnel la sonda es una punta conductora lo más afilada posible. Durante las medidas microscópicas, la punta no toca la muestra, sino que se queda a una distancia equivalente a un par de átomos (del orden de angstroms) de la superficie. La diferencia de potencial generada entre la muestra y la punta provoca una corriente de efecto túnel, que es muy sensible tanto a la distancia, como a la diferencia de potencial generada. El parámetro de medida es, por tanto, la "intensidad de corriente túnel". De esta manera y mientras la punta barre la superficie, un mecanismo electrónico de retroalimentación mide la corriente de efecto túnel y mantiene la punta a una distancia constante sobre los átomos de la superficie o, alternativamente, la intensidad se mantiene constante y lo que se mide es la altura. Este movimiento es leído y procesado por el ordenador, obteniéndose así una imagen tridimensional de la superficie. La resolución espacial de las imágenes obtenidas por STM depende críticamente del potencial seleccionado, así como de la naturaleza de la punta y de la superficie (muestra), haciendo necesario un conocimiento y control meticuloso del potencial aplicado (voltaje bias) y de la naturaleza de la punta (sonda) para la adecuada caracterización de las muestras.

Los análisis por microscopía de efecto túnel (STM) se realizaron con un microscopio nanoscopio IIIa de Digital Instrument (Veeco), operando en el modo de corriente constante al aire, ex situ. Se emplearon para ello puntas de Pt-Ir. Se utilizaron valores de corriente túnel entre 0,25 – 1,00 nA y entre 0,1 – 1,0 V de potencial bias. Las velocidades de barrido fueron generalmente bajas, del orden de 0,5-1 Hz. Se tomaron imágenes de la superficie de la muestra desde 5 x 5 nm^2 hasta 10 x 10 μm^2. La superficie mesoporosa para este análisis fue electrodepositada a un potencial de 0,15 V durante 0,5 y 1 s sobre una placa de Au (111) sumergida en una disolución compuesta del surfactante y la sal de platino, tal y como se mencionó en el apartado 3.2.1

3.4.2 Microscopía de fuerzas atómicas (AFM)

En el microscopio de fuerza atómica una punta afilada situada en el extremo de una micropalanca flexible (cantiléver), recorre la superficie de una muestra manteniendo constante una pequeña fuerza de interacción, a diferencia del STM que depende de la conducción eléctrica. Las fuerzas de interacción se generan cuando la punta y la muestra están suficientemente cerca, y pueden ser debidas a fuerzas de diferente naturaleza a nivel atómico, tales como van der Waals, electrostáticas, magnéticas, capilares, de fricción, etc. El AFM fue desarrollado por G. Binnig y colaboradores [Binnig, 1986] y permite medir fuerzas en el rango del piconewton.

La obtención de un mapa topográfico de la superficie de una muestra determinada, se puede realizar mediante la detección de una fuerza atómica que se genera cuando la punta del cantiléver se acerca lo suficiente a la superficie de la muestra. La pequeña flexión de la micropalanca que obedece la ley de Hooke se registra mediante un haz láser reflejado en su parte posterior. Un sistema auxiliar piezoeléctrico desplaza la muestra tridimensionalmente, mientras que la punta recorre ordenadamente la superficie.

Las imágenes de AFM presentadas en esta Tesis se realizaron en un microscopio Nanoscope IIIa de Digital Instrument (Veeco), ubicado en las instalaciones del SEGAI. Las medidas se realizaron utilizando un modo "tapping" a una velocidad de barrido de 1 Hz con una punta de silicona grabada (TAP150A, 126-169 KHz y 5 N/m). La calibración del equipo se realizó con un grafito pirolítico altamente ordenado (HOPG) y con los escalones monoatómicos que se encuentran en una placa de Au (111).

3.4.3 Dispersión de energía de rayos X (EDX)

Esta técnica utiliza los rayos X emitidos por la muestra durante el bombardeo con un haz de electrones, para la identificación y cuantificación elemental de la composición de las muestras en superficie que se observan en microscopía electrónica. Así, cuando el haz incidente de electrones excita un electrón de una capa interna expulsándolo de su órbita, uno de los electrones de un nivel de energía superior rellena el hueco dejado por el electrón saliente emitiendo un fotón de rayos X. El microscopio electrónico dispone de un detector semiconductor que caracteriza los fotones de rayos X según sus energías incidentes y registra todo el espectro simultáneamente, lo que le confiere gran velocidad. La energía de los fotones emitidos está directamente relacionada con el número atómico del elemento emisor, y por tanto, la información que se puede obtener de la muestra será, por una parte, el elemento que los está produciendo (análisis cualitativo), y por otra, la cantidad relativa de cada elemento (análisis cuantitativo) a partir del número de fotones emitido de cada energía [Bertin, 1978].

La composición de los electrocatalizadores se determinó por energía dispersiva de rayos X (EDX) mediante un microscopio electrónico de barrido de 3,5 nm de resolución, marca Jeol JSM 6300, con un microanalizador de energías dispersivas de Rayos X Oxford Instruments Microanalysis Group 6699 ATW.

3.4.4 Microscopía de transmisión de electrones (TEM)

En 1932, Max Knoll y Ernest Ruska construyen en Alemania el primer microscopio electrónico de transmisión, comercializado en 1939 por Siemens Corporation. Esta microscopía emplea las interacciones de los electrones con la muestra para producir imágenes y patrones de difracción que se utilizan para analizar el material a escala atómica [Kanellopoulos, 2011]. El TEM puede analizar la señal de los electrones incidentes, los electrones dispersados y los electrones difractados, permitiendo trabajar en diversas técnicas y obtener información en imagen y/o análisis elemental. Así, es posible hacer un análisis de la composición química de materiales y proporcionar una caracterización estructural (morfología, tamaño de grano, grado de cristalinidad, identificación de fases de cristales, etc.). Una de sus limitaciones es la preparación de muestras, ya que deben ser transparentes a los electrones y se deben transmitir suficientes electrones para poder formar una imagen de fácil interpretación.

En el TEM, un haz de electrones pasa por la muestra y produce una imagen de la misma a través del haz transmitido. Existen diferentes modos de formación de la imagen: si la imagen se forma a partir del haz transmitido, que no ha sufrido dispersión, entonces la imagen del objeto es oscura sobre un fondo brillante. Si por el contrario, se utilizan los electrones dispersados, en este caso la imagen aparece brillante sobre un fondo oscuro. Por ello estas dos técnicas se denominan formación de imagen en campo claro y en campo oscuro, respectivamente. La primera es la más utilizada. Los microscopios de gran resolución (tres lentes generadoras de imagen), son capaces de ampliar la imagen hasta 500.000 veces y tienen poder de resolución de fracciones del nanómetro.

El microscopio de transmisión utilizado para observar las nanoestructuras depositadas sobre el óxido de grafeno reducido fue JEOL JEM 2100 de 200 kV, ubicado en el Servicio de Microscopía Electrónica, SEGAI-ULL.

3.4.5 Difracción de rayos X (XRD)

Es una técnica especialmente útil en el seguimiento de cambios estructurales, identificación y medida de tamaño de cristal de las fases cristalinas en un material. Para ello, se emplea una radiación con una longitud de onda comparable a la distancia interatómica [Jenkins, 2012], permitiendo el estudio de la estructura de los componentes cristalinos presentes en las muestras con cierto grado de periodicidad en la disposición tridimensional de sus átomos o iones constituyentes. De acuerdo con la ley de Bragg [Surynarayana, 1996], al incidir un haz monocromático de rayos X sobre un monocristal ordenado, se producen interferencias constructivas con concordancia de fase en ciertas direcciones privilegiadas del haz difractado, que definen los valores de los distintos ángulos de Bragg, cuya posición se considera como "huella de identidad" del sólido ordenado. La técnica de difracción en monocristal proporciona la información necesaria para resolver la estructura de cristales relativamente grandes.

Sin embargo, los catalizadores heterogéneos suelen consistir en fases microcristalinas, por lo que mucha información difractada se encuentra fuertemente solapada, siendo necesario recurrir a la técnica de difracción por el método convencional de polvo (Debye-Scherrer) [Perego, 1998]. Es posible obtener información sobre el tamaño de cristal gracias al método Rietveld [Rietveld, 1967], así como también cuantificar el tamaño medio de los cristales (d) presentes en una muestra en polvo, en relación a la anchura del correspondiente pico de difracción a mitad de altura (B) de las líneas del difractograma, por medio de la ecuación de Debye-Scherrer:

$$d = \frac{0.9 * \lambda}{B_{2\theta} * cos\theta_{max}} \tag{4.2}$$

En esta ecuación, θ es la posición angular del máximo de la línea de difracción y λ la longitud de onda de la radiación empleada. Esta expresión supone que el único factor que afecta a la extensión angular de la reflexión es el tamaño del cristal, es decir, los picos de difracción muy estrechos se corresponden con partículas grandes y cristalinas, mientras que los picos ensanchados lo hacen con partículas pequeñas o amorfas, donde el número de planos paralelos disponibles es insuficiente para obtener una línea de difracción aguda. No obstante, otros factores como la desalineación del difractómetro, una fuente de rayos X no monocromática, o la no idealidad de los cristales (tensiones y deformaciones cristalinas), contribuyen también a este ensanchamiento.

Los difractogramas de rayos X (DRX) de los electrocatalizadores fueron obtenidos con un difractómetro Panalytical X´Pert utilizando un haz de Cu-Kα operando a 40 kV y 30 mA, en el Servicio Integrado de Difracción de Rayos X, SEGAI-ULL.

3.4.6 Espectroscopia de fotoelectrónica de rayos X (XPS)

Esta técnica permite dilucidar el estado de oxidación y el entorno químico de un determinado átomo, dependiendo de la molécula de la cual forma parte, basándose en el efecto fotoeléctrico [Watts, 2003]. Un fotón elimina un electrón de un material cuando posee una energía mayor que la energía de enlace del electrón con los electrones adyacentes; el exceso de energía le confiere al electrón saliente una determinada energía cinética. La energía cinética (E_k) del fotoelectrón expulsado se mide por medio de un espectrómetro fotoelectrónico y viene dada por la ley de Einstein $E_k = h\nu - E_b$, donde E_k es la cantidad de energía medida en el experimento, E_b es la energía de enlace del electrón en un nivel particular energético y $h\nu$ es la energía de la radiación incidente. Si el fotón incidente tiene energía suficiente, se pueden arrancar electrones de diferentes niveles energéticos, de forma que se obtiene un espectro que muestra todos los niveles de energía accesibles y la distribución de la energía cinética de los fotoelectrones.

El espectro fotoelectrónico reproduce, de manera bastante exacta, la estructura electrónica de un elemento, teniendo en cuenta que todos los electrones con una energía de enlace menor a la energía del fotón irradiado aparecerán en dicho espectro. La energía de enlace de los electrones en los niveles energéticos más internos es característica de cada átomo y varía según la interacción electrostática con otros electrones, el potencial de atracción del núcleo y el entorno del átomo [Watts, 2003]. Por lo que esta técnica permite determinar no sólo la composición química de la superficie del material sino también el estado de oxidación de los átomos que la conforman.

El equipo utilizado en esta Tesis Doctoral fue un espectrómetro ESCALAB 250 equipado con un ánodo dual de Al-Mg, usando una radiación monocromatizada de Al Kα (*hv* = 1486,6 eV) con un tamaño de spot de 650 µm. Los espectros fueron registrados en modo de energía de analizador constante (CAE), con un *pass energy* de 20 eV y con una resolución de energía de alrededor 0,1 eV. Todas las medidas se realizaron en una cámara de ultra alto vacío a una presión menor de 9,0 $\cdot 10^{-9}$ mbar, permitiendo que el fotoelectrón expulsado interactúe con las moléculas de gas.

3.4.7 Espectroscopia Raman

El fenómeno de dispersión inelástica de la luz fue postulado por primera vez por Smekal en 1923 y observado experimentalmente en 1928 por Raman y Krishnan. Desde entonces, el fenómeno ha sido referido como espectroscopia Raman [Smith, 2005].

La espectroscopía Raman es una técnica fotónica de alta resolución que proporciona en pocos segundos información química y estructural de casi cualquier compuesto orgánico o inorgánico, permitiendo así su identificación. El análisis mediante espectroscopia Raman se basa en el examen de la luz dispersada por un material al incidir sobre él un haz de luz monocromático. Una pequeña porción de la luz es dispersada inelásticamente experimentando ligeros cambios de frecuencia, característicos del material analizado e independiente de la frecuencia de la luz incidente. Se trata de una técnica de análisis no destructiva, que se realiza directamente sobre el material a analizar sin ningún tipo de preparación especial.

Los análisis se realizaron en un equipo de espectroscopia Raman modelo RENISHAW "*Invis reflex*" con un microscopio confocal Leica DM, perteneciente al departamento de Química Física de la Universidad de Santiago de Compostela. El espectro fue obtenido usando una fuente de excitación de iones de Ar (514 nm) bajo una potencia mínima de láser (0,5 mW) para evitar el calentamiento inducido de la muestra.

3.5 CARACTERIZACIÓN POR TÉCNICAS ELECTROQUÍMICAS

Entre las muchas aplicaciones de las técnicas electroquímicas están el estudio de la reactividad de especies en disolución y la caracterización de las especies adsorbidas en la superficie del electrodo de trabajo.

La instrumentación electroquímica utilizada consiste en una celda electroquímica en su configuración de tres electrodos y un potenciostato, que se describen a continuación.

3.5.1 Potenciostato

Se han utilizado los potenciostato-galvanostato AUTOLAB (Eco Chemie) PGSTAT302 y PGSTAT30, que permiten controlar el potencial del electrodo de trabajo, con respecto al electrodo de referencia, y medir la respuesta de corriente eléctrica que circula por él.

3.5.2 La celda electroquímica

La figura 4.4 muestra una de las celdas electroquímicas utilizadas. Se trata de una celda de vidrio de doble pared, acoplable a un termostato, y que en la parte superior posee las bocas esmeriladas para colocar el electrodo de trabajo, el de referencia, el contraelectrodo, las piezas que permiten la entrada de disoluciones y el borboteo de gases, además de una trampa para la salida de éstos. En la parte inferior de la celda existe una llave que permite la salida de la disolución de su interior.

La caracterización electroquímica de especies adsorbidas requiere el uso de la celda electroquímica en su configuración de flujo, por lo que es necesario acoplarle los recipientes que contienen las disoluciones de la muestra a analizar y del electrolito de fondo (ver figura 4.4). Estos recipientes están provistos de una entrada de gas para purgar con argón o nitrógeno las disoluciones que contienen, además de un sistema de llaves que regula la entrada de estas disoluciones a la celda. Con esta disposición, y usando la llave situada en la parte inferior de la celda, es posible realizar el cambio de disolución existente en su interior, procurando que en todo momento el electrodo de trabajo esté en contacto con la disolución y, por tanto, manteniendo el control sobre el potencial.

Figura 4.4. Celda electroquímica de flujo con el recipiente que contiene el electrolito.

3.5.3 Electrodo de referencia y electrodo auxiliar

El electrodo de referencia consistió en un electrodo reversible de hidrógeno (ERH), preparado en un tubo de vidrio sellado por un extremo, con un alambre de Pt en su interior y relleno de la disolución de electrolito soporte. Previamente a cada experiencia, el hidrógeno se genera en el interior del tubo de vidrio mediante la realización de una electrolisis. En su disposición en la celda electroquímica, el electrodo de referencia se introduce en un capilar de Luggin, que lo acerca al electrodo de trabajo. Todos los potenciales recogidos en esta Tesis Doctoral están referidos al ERH.

El electrodo auxiliar o contraelectrodo utilizado en las medidas electroquímicas fue una barra de carbón vítreo con una elevada área superficial, mientras que en la preparación de los electrodos MPPt se utilizó una lámina de Pt platinizado de 4 cm^2.

3.5.4 Electrodos soportados sobre carbón

Los electrodos de trabajo con catalizadores soportados para PEMFC y DAFC se prepararon a partir de los diferentes materiales electrocatalíticos mediante la técnica de electrodo de capa ultrafina [Schmidt, 1998]. Una alícuota (20 μL) de una mezcla homogénea de 2,0 mg del electrocatalizador en polvo, 500 μL de agua Milli-Q y 15 μL de Nafion®, se depositó sobre una superficie de carbón vítreo pulida (un disco con 0,28 cm^2 de área geométrica), y se secó en atmósfera de argón o nitrógeno antes de su utilización.

3.5.5 Electrodos nanoestructurados no soportados

Para el estudio de los electrodos nanoestructurados no soportados, los catalizadores mesoporosos han sido electrodepositados sobre un electrodo de Au policristalino pulido a espejo con un diámetro aproximado de 0,7 mm.

3.5.6 Aspectos teóricos de las técnicas electroquímicas aplicadas

3.5.6.1 Voltamperometría cíclica

El término voltamperometría se usa para clasificar al grupo de técnicas electroanalíticas en las que se mide la corriente que fluye a través de la celda electroquímica mientras se varía el potencial aplicado a los electrodos. La voltamperometría cíclica es una de las técnicas de caracterización electroquímica que puede aportar más información con un dispositivo experimental relativamente sencillo. Consiste en variar el potencial del electrodo de trabajo (WE) con el tiempo, entre dos límites, superior e inferior, a la vez que se registra la corriente que circula a través de este electrodo.

Cuando el barrido se inicia hacia potenciales positivos ($0 < t < \tau$), la variación del potencial con el tiempo se expresa mediante la siguiente ecuación:

$$E = E_i + vt \tag{4.4}$$

y para el barrido de retorno hacia potenciales negativos ($t > \tau$), como:

$$E = E_i + v\tau - vt \tag{4.5}$$

Siendo E_i el potencial inicial, v la velocidad de barrido de potencial ($v = dE/dt$), t el tiempo transcurrido, y τ el tiempo de inversión del potencial. En un gráfico se representa como (figura 4.5).

El barrido de potencial se puede realizar a distintas velocidades, cubriendo diferentes intervalos de potencial. La elección de estas variables depende de la respuesta cinética del sistema electroquímico. En ciertas condiciones de perturbación, con determinados procesos electroquímicos, se puede lograr un verdadero estado estacionario. A medida que aumenta la velocidad de barrido, disminuye la influencia de los procesos de transporte de materia que condicionan la respuesta estacionaria del sistema, y se ponen de manifiesto los procesos de transferencia de carga. En consecuencia, este método es útil para estudiar los procesos de oxidación, reducción, electroadsorción y electrodesorción que ocurren en la interfaz.

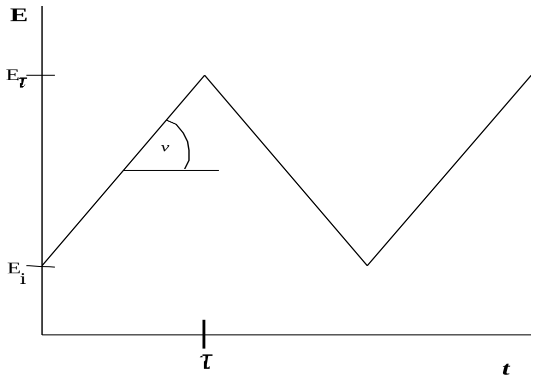

Figura 4.5. Programa de potencial en función del tiempo correspondiente a la voltamperometría cíclica.

El perfil corriente-potencial que se obtiene se denomina voltamperograma cíclico (VC) y depende de la naturaleza de la interfaz electroquímica. Aplicando diferentes programas de potencial es posible obtener información acerca de los procesos que tienen lugar sobre la superficie del electrodo de trabajo en diferentes regiones de potencial [Bard, 1980].

3.5.6.2 Cronoamperometría

Mediante esta técnica se registra la variación de la corriente en función del tiempo durante la perturbación del sistema con un salto de potencial. Básicamente el experimento comienza de un potencial inicial donde generalmente no ocurre ninguna reacción faradaíca y por tanto, no circula corriente en el sistema. Posteriormente, se pasa instantáneamente a otro potencial donde la corriente corresponde al límite difusional y obedece la ecuación de Cottrell [Bard, 1980]:

$$i_d\ t = \frac{nFD_0^{\frac{1}{2}}C_0}{\pi^{\frac{1}{2}}t^{\frac{1}{2}}} \qquad (4.6)$$

Donde $i_d\ t$ es la corriente limitada por difusión de la especie electroactiva hacia el electrodo a un tiempo t, n es el número de electrones involucrados en la reacción electroquímica, D_0 corresponde al coeficiente de difusión de la especie electroactiva y C_0^* es la concentración de la especie en el seno de la disolución. La aplicación del salto de potencial hace que la concentración de la especie activa en la superficie disminuya rápidamente a cero, y es reemplazada por la existente en zonas próximas del seno de la disolución; a partir de ese momento se produce una variación del perfil de concentración en función del tiempo y en función de la distancia al electrodo (figura 4.6).

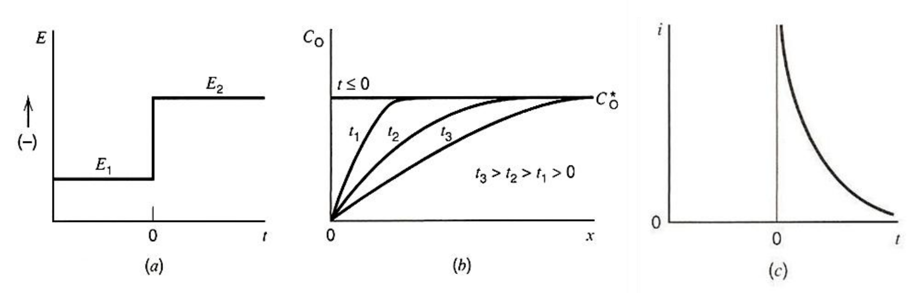

Figura 4.6. Perfiles de concentración de la especie oxidada para diferentes tiempos durante un mismo experimento; (b) variación de la corriente en función del tiempo.

3.5.7 Aspectos experimentales de las técnicas de caracterización electroquímica

Una vez montado el sistema de la celda electroquímica de flujo (figura 4.4) con el correspondiente electrodo de referencia y contraelectrodo, se introduce la disolución del electrolito de fondo desde su correspondiente recipiente, a la vez que se hace pasar el gas inerte para eliminar el oxígeno la disolución y de todo el sistema de la celda. El electrodo de trabajo recién preparado, como se indica en el apartado 3.5.3 o en el 3.5.4 según proceda, se coloca en la boca central de la celda.

Antes de cada experimento la superficie del electrodo de trabajo se activa en la disolución del electrolito soporte mediante la voltamperometría cíclica, aplicando una velocidad de barrido de potencial 0,10 V s^{-1} entre un límite de potencial inferior de 0,05 V, que corresponde al inicio de la evolución de hidrógeno, y un límite de potencial superior de 0,80 V para evitar la pérdida de material electrocatalítico, ya que a valores más altos se solubilizan los óxidos metálicos. Durante este tratamiento el electrolito de fondo se reemplaza varias veces, con el objeto de obtener un perfil reproducible y que indique la ausencia de impurezas.

En los estudios de electrooxidación del analito por voltamperometría cíclica se aplican estos mismos límites de potencial, y en los estudios de electroreducción el límite de potencial superior se fija en 0,4 V, que corresponde a la zona de la doble capa eléctrica.

Las temperaturas a las cuales se realizaron los experimentos fueron 25,0 ± 0,1 ºC y 60,0 ± 0,1 ºC que se controlaron por medio de un termostato P- Selecta®.

3.5.7.1 Estudio de la oxidación del CO adsorbido

Después de la activación de la superficie del electrodo de trabajo, se fija el potencial al que se va a realizar el experimento de adsorción (E_{ad}), que en todas las medidas fue E_{ad} = 0,07 V. A continuación, se hace borbotear el CO en la disolución del electrolito de fondo presente en la celda durante un tiempo de adsorción mínimo (t_{ad}) de 10 min, asegurando de esta manera que los adsorbatos formados alcancen el máximo recubrimiento posible de la superficie del electrodo de trabajo. Pasado ese tiempo, se elimina el CO de la disolución mediante el lavado con una cantidad considerable de disolución de electrolito de fondo y el borboteo de gas inerte en la disolución de la celda. Finalmente, se aplica la voltamperometría cíclica iniciando un barrido hacia valores positivos de potencial (a 0,01 ó 0,02 V s^{-1}), hasta alcanzar el potencial de inversión de 0,85 – 0,95 V. De esta manera se obtienen los VCs correspondientes a la oxidación de los residuos del CO formados sobre la superficie del catalizador a 0,07 V.

3.5.7.2 Estudio con alcohol en disolución

Una vez activado el electrodo, comprobado el estado de la superficie y haber realizado la caracterización por adsorbatos de CO, se fija el potencial del electrodo de trabajo a 0,05 V y se introduce en la celda la disolución del alcohol correspondiente a estudiar, previamente preparada en el electrolito soporte que se ha desoxigenado con anterioridad. Seguidamente se realizan dos tipos de estudios:

- Estudio voltamperométrico en la disolución de alcohol

Se inicia un barrido hacia potenciales positivos, a una velocidad de 0,01 V s^{-1} hasta un potencial de inversión de 0,85 V, registrándose el VC correspondiente. A partir del perfil de corriente obtenido se pueden obtener los valores de potencial a los que comienza la oxidación del alcohol, así como los potenciales de pico de las diferentes contribuciones presentes en el VC.

- Estudio cronoamperométrico en la disolución de metanol

Partiendo del potencial inicial aplicado impuesto al electrodo, se aplica un salto a un potencial final comprendido entre 0,50 y 0,65 V, registrándose la respuesta de la corriente con el tiempo. Se han seleccionado esos potenciales finales ya que son próximos al potencial que presenta una DAFC en funcionamiento. Es interesante observar la respuesta en densidad de corriente de los diferentes catalizadores, con el fin de determinar quienes presentan una mayor eficiencia.

El procedimiento utilizado para el estudio de la oxidación de ácido fórmico es similar al realizado para los alcoholes.

3.5.7.3 Estudio para la reacción de evolución de hidrógeno (HER)

Los experimentos para el estudio de la HER se realizaron en una disolución recién preparada de NaOH 0,1 M previamente desoxigenada. La ventana de potencial de trabajo fue de 0,10 V a -0,50 V a una velocidad de barrido de 0,001 V s^{-1}. Esta velocidad permite simular las condiciones de estado estacionario necesarias para los estudios cinéticos.

3.5.7.4 Estudio para la electroreducción de CO_2

Las medidas para el estudio de electroreducción de CO_2 sobre las nanoestructuras Au@Pd se llevaron a cabo en una disolución de Na_2SO_4 0,1 M a pH = 4, ya sea purgada con Ar o saturada con CO_2. Para evaluar tanto los procesos de oxidación como de reducción sobre la superficie de Pd, los límites de potencial inferior y superior utilizados fueron -1,20 y 0,9 V respectivamente, y la velocidad de barrido de potencial 0,02 V s^{-1}. Para observar la formación de productos y el efecto del hidrógeno durante la reducción de CO_2, los límites aplicados fueron 0,15 y -1,0 V y la velocidad de barrido 0,005 V s^{-1}.

3.6 CARACTERIZACIÓN POR TÉCNICAS ESPECTROELECTRQUÍMICAS

3.6.1 Aspectos teóricos de las técnicas espectroelectroquímicas

3.6.1.1 Espectroscopia de infrarrojo por transformada de Fourier in-situ

La espectroscopia de infrarrojo por transformada de Fourier in-situ (FTIRS) es actualmente una metodología fundamental para la resolución de los problemas relacionados con la catálisis de los procesos electródicos. En esta técnica, la adquisición de todo el espectro se realiza de forma simultánea, lo cual contribuye a que la medida sea rápida y eficaz.

Si consideramos la reflexión en una superficie plana metálica perfectamente pulida (a modo de simplificación, no se contempla la presencia de la disolución), el campo eléctrico complejo en la fase incidente, que resulta de la suma de los vectores eléctricos de los haces incidente y reflejado [Greenler, 1966], depende del estado de polarización de la luz y del ángulo de incidencia (figura 4.7). Esto se debe a que la radiación reflejada sufre un cambio de fase diferente en función del estado de polarización de la luz. Para la radiación perpendicular al plano de incidencia (luz polarizada s) este cambio de fase es de aproximadamente 180º para todos los ángulos de incidencia, mientras que para la polarización paralela al plano de incidencia (luz polarizada p), el cambio de fase depende del ángulo de incidencia y varía entre 60º y 90º. De aquí se derivan dos consecuencias: (a) la dependencia de la intensidad de la banda con el ángulo de incidencia; y (b) la introducción de la regla de selección de la superficie.

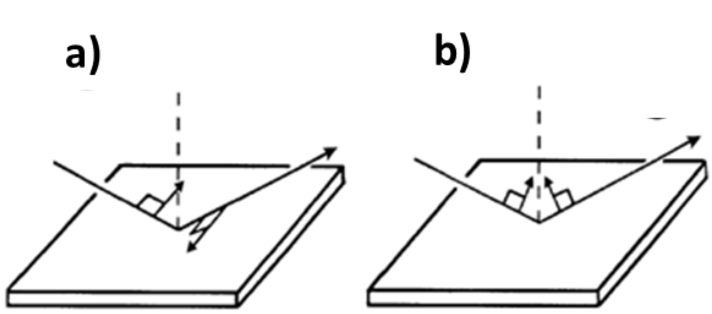

Figura 4.7. Reflexión de luz s (perpendicular) y p (paralela) sobre una superficie conductora.

La intensidad de una señal en el espectro es la medida de la disipación de la energía electromagnética por el medio absorbente a una determinada longitud de onda, y en estas condiciones, el cambio en el flujo de energía es proporcional al campo cuadrático medio [Hansen, 1968]. Supongamos un sistema compuesto por una monocapa de adsorbato sobre la superficie metálica del electrodo. En estas condiciones, la absorción de la radiación infrarroja es el resultado de la interacción del campo eléctrico de la luz incidente con los dipolos eléctricos de las moléculas adsorbidas y con los electrones de la superficie metálica. En consecuencia, la intensidad de absorción viene dada por las propiedades eléctricas del metal. Entonces, la absorción Δ se obtiene a partir de normalizar la diferencia entre la reflectividad en presencia (R) y en ausencia (R_0) de la especie que absorbe radiación:

$$\Delta = \frac{R_0 - R}{R_0} \qquad (4.7)$$

La intensidad de la banda depende del ángulo de incidencia, y por tanto la luz polarizada “s” no interacciona con las moléculas adsorbidas o muy cercanas a la superficie del electrodo, siendo nula la información obtenida respecto a las especies adsorbidas, y sólo será activa a las especies en la disolución. Por otra parte, la luz polarizada “p” será activa tanto a unas como a otras. Además, se obtiene que la intensidad de absorción de la radiación depende del ángulo de incidencia y es máxima para ángulos rasantes en el caso de una interface metal/aire.

La regla de selección de la superficie establece que el cambio del campo eléctrico de la onda estacionaria, que representa la disipación de energía, varía con la distancia al metal de forma senoidal en el caso de la luz "s" y cosenoidal para la radiación "p". Por ello, la luz polarizada "s" no interacciona con los dipolos superficiales y empieza a ser activa al alejarse de la superficie. Por otro lado, la luz polarizada "p" sí interacciona con los dipolos superficiales, es más, el máximo de intensidad del campo eléctrico ocurre en la superficie metálica y disminuye al alejarse, siendo igual al de la luz "s" a una distancia aproximada de 2,5 µm para una interface metal/aire.

Luego, si tenemos en cuenta que la interacción de la radiación únicamente puede tener lugar con aquellos dipolos que presentan la misma dirección del campo eléctrico incidente, podemos concluir que sólo los dipolos perpendiculares a la superficie van a ser activos en la espectroscopia de absorción-reflexión. De esta manera, sólo aquellos modos vibracionales que impliquen cambios en la componente perpendicular a la superficie del momento del dipolo serán activos en el infrarrojo. En el caso de un sistema electroquímico, (sistema real), la aplicación de estos principios implican, al menos, introducir variaciones en el índice de refracción debido a la presencia de una capa delgada de electrolito así como de una ventana transparente a la radiación infrarroja, no obstante, la dependencia es similar.

3.6.1.2 Espectroscopia de masas diferencial electroquímico (DEMS)

La espectrometría de masas está basada en la obtención de iones a partir de moléculas en fase gaseosa, que son posteriormente separados de acuerdo con su masa y su carga, y finalmente se detectan por medio de un dispositivo adecuado. Un espectro de masas será, en consecuencia, una información bidimensional que representa un parámetro relacionado con la abundancia de los diferentes tipos de iones en función de la relación masa/carga de cada uno de ellos.

Cuando el espectrómetro de masas se acopla a una celda electroquímica, esta técnica se denomina espectrometría de masas diferencial electroquímica (DEMS). El hecho de disponer de una celda electroquímica conectada a un espectrómetro de masas permite detectar los productos e intermediarios gaseosos y volátiles generados en los procesos electroquímicos, con una gran sensibilidad en un corto tiempo de respuesta. El análisis instantáneo de las sustancias que se generan durante su producción en una celda electroquímica constituye el vínculo directo entre la corriente que circula y la reacción que tiene lugar en el electrodo [Abd-El-Latif, 2010; Baltruschat, 2004; Baltruschat 1999].

La posibilidad de identificar los productos de una reacción electroquímica conectando una celda electroquímica a un espectrómetro de masas fue sugerida por primera vez por Bruckenstein y Gadde en 1971 [Bruckenstein, 1971], pero fueron Wolter y Heitbaum en 1984 quienes llevaron a cabo el avance más importante de la técnica mediante el uso de un sistema diferencial de vacío empleando dos cámaras con una bomba turbomolecular cada una [Wolter, 1984]. En la primera cámara se eliminan la mayoría de los gases que entran en el espectrómetro, y sólo una pequeña parte llegan a la segunda cámara donde está el analizador, en la que se alcanza una presión inferior a 10^{-5} mbar.

Otra mejora consistió en utilizar electrodos porosos de metales nobles, obtenidos al depositar una capa delgada de una suspensión de finas partículas del metal sobre una membrana hidrófoba de teflón. De esta manera se puede realizar la espectrometría de masas diferencial, en la que se consigue no sólo que las sustancias lleguen rápidamente a la cámara de ionización del espectrómetro, sino que además, apenas se detecten, sean eliminadas del sistema con el fin de evitar la acumulación de productos que impediría su detección diferencial. Esta detección se realiza con una gran sensibilidad, ya que prácticamente todas las especies producidas se analizan. La velocidad de formación de los productos es proporcional a la intensidad de masa en un amplio intervalo de operación, de tal manera que la señal de masa detecta, casi simultáneamente, cualquier cambio rápido en la velocidad de formación [Abd-El-Latif, 2010; Wolter, 1984].

Esta detección se realiza con una gran sensibilidad, pero la velocidad de barrido a la que se puede realizar la voltamperometría cíclica acoplada para que la detección sea *on-line*, queda limitada por el recorrido de las especies a través de la membrana y las cámaras de vacío hasta el detector. En este trabajo la velocidad de barrido utilizada para los estudios de DEMS es de 5 $mV \cdot s^{-1}$.

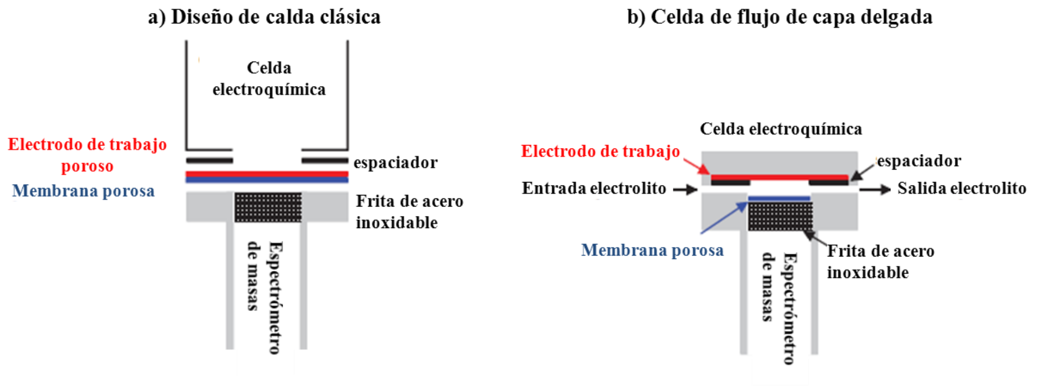

Figura 4.8. Ilustración de a) El diseño convencional de una celda DEMS, y b) La celda de flujo de capa delgada. Tomado de [Oberacher, 2015].

En la figura 4.8a se muestra un esquema de la interface de una celda DEMS convencional. El electrodo de trabajo está directamente conectado a la interface de membrana porosa y se prepara mediante el depósito de una capa del electrocatalizador bien sea por "*sputtering*" o por el recubrimiento con una laca que contiene pequeñas partículas metálicas. Aunque este diseño se caracteriza por tener un tiempo de respuesta rápida (< 1 s) y elevada eficiencia de colección, su configuración no permite un buen transporte de masa lo que conlleva a un agotamiento de los reactantes volátiles en la superficie, y por tanto, materiales que generen altas corrientes como los electrodos masivos no pueden utilizarse. La figura 4.8b corresponde a una configuración de celda de capa delgada desarrollada por Hartung & Baltruschat, [Hartung, 1990; Oberacher, 2015]; para utilizar electrodos lisos o cristalinos. El electrodo de trabajo está separado de la membrana de interface por medio de una capa delgada formada por el electrolito. Los productos de reacción se transportan por difusión desde el electrodo hasta la membrana, lo cual incrementa el tiempo de respuesta (2-3 s) y reduce la colección de datos bajo condiciones de flujo continuo. La celda electroquímica de capa delgada desarrollada por Planes *et al.* [Planes, 2007] permite que el electrodo de trabajo (soportado o no soportado) se coloque próximo a la membrana obteniendo una mayor flexibilidad en cuanto a los sistemas que se pueden estudiar, además de utilizar cantidades de catalizador mucho menores que en las anteriores configuraciones utilizadas en la bibliografía.

3.6.2 Aspectos experimentales de las técnicas de caracterización espectroelectroquímica

3.6.2.1 Espectroscopia de infrarrojo por transformada de Fourier in-situ

La espectroscopia FTIR in situ se utilizó para el estudio superficial de la oxidación de CO adsorbido y de ácido fórmico sobre catalizadores de Pt mesoporoso sin modificar y modificados con adátomos de Pd, y para las partículas con superficie de Pd tipo core-shell.

El espectrofotómetro utilizado es de la casa Bruker, modelo Vector 22, equipado con una fuente láser He/Ne, un detector de MCT (mercurio cadmio teluro) y un polarizador constituido por una rejilla de 0,12 µm de ancho de aluminio sobre un sustrato de talio (KRS-5), el cual permite trabajar con luz polarizada paralela (p) y perpendicular (s) al plano de incidencia.

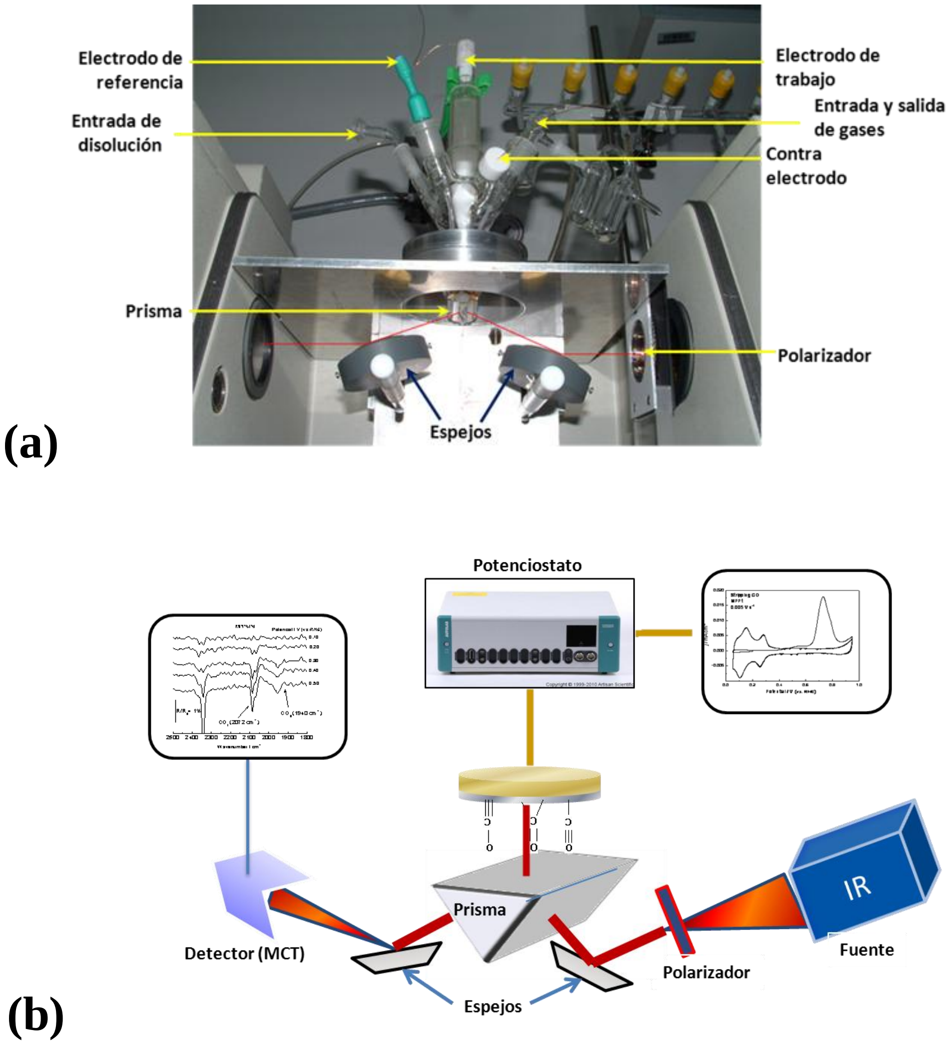

Figura 4.9. a) Montaje de la celda espectroelectroquímica de flujo y los espejos en el sistema de FTIRS, y b) Esquema del funcionamiento de los espejos y el prisma que permiten direccionar el haz hacia la superficie del electrodo.

La figura 4.9 muestra la celda de flujo (4.9a) y el esquema del sistema de espejos utilizados para las medidas en este trabajo (4.9b). Se dispone de un sistema de desviación del haz de radiación, compuesto por dos espejos de oro, que permite que la celda electroquímica se sitúe verticalmente sobre la cámara de muestra del espectrofotómetro de IR, manteniendo el ángulo de incidencia de la radiación sobre la superficie del electrodo próximo al valor óptimo. La plataforma de sustentación de la celda se fija al soporte de los espejos, de forma que se evita el ajuste de la óptica en cada medida. Posee una tapa especialmente diseñada que permite el sellado de la cámara para que pueda ser purgada de vapor de agua y dióxido de carbono, dejando a la celda espectroelectroquímica totalmente accesible en cualquier momento.

El fondo de la celda se cierra con un prisma, el cual debe ser transparente a la radiación infrarroja y resistente a los electrolitos que se utilizan en las medidas electroquímicas. En este estudio se ha empleado un prisma de CaF_2 que permite trabajar entre 4.000 y 1.000 cm^{-1}.

La utilización de una celda de flujo permite el estudio de reacciones con cambio de disolución bajo control del potencial. Esta característica es muy útil para investigar la adsorción irreversible de especies orgánicas. En la parte lateral de la celda existe una boca donde se introduce el contra-electrodo, mientras que en la parte superior se encuentran las demás. Estas bocas se utilizan para la entrada de disolución de muestra o del electrolito soporte, otra para la entrada del gas inerte, para el electrodo de referencia, para la salida de disolución y la central para el electrodo de trabajo. Esta última boca consiste en un tubo de 5 cm de alto con la superficie interna esmerilada, y es donde se introduce el émbolo que contiene al electrodo de trabajo. De esta manera, presionando contra el prisma situado en la parte inferior de la celda es posible conseguir una capa delgada de disolución y así poder realizar la adquisición de los espectros en cada experimento.

Cada espectro FTIR obtenido corresponde al promedio resultante de 128 barridos de frecuencia, que se obtienen con una resolución de 8 cm^{-1}. El procedimiento utilizado para obtener una serie de espectros a diferentes valores de potencial consiste en saturar la superficie catalítica con CO manteniendo un potencial de adsorción de E_{ad} = 0,20 V (vs. ERH). Posteriormente, después de eliminar el exceso de gas que se encuentra en la disolución, el electrodo de trabajo se aproxima a la ventana prismática del fondo de la celda, originando una configuración de capa delgada. En estas condiciones se toma el espectro de referencia, R_0. A continuación se aplican saltos de potencial de 0,05 V hasta llegar a 0,95 - 1,00 V, con el fin de oxidar sucesivamente el CO adsorbido sobre la superficie del catalizador, adquiriendo a cada potencial los correspondientes espectros IR. Al comparar el espectro obtenido a cada potencial con el espectro referencia, $\Delta R/R_0$, resultan una serie de bandas negativas y positivas que corresponden respectivamente a la formación y al consumo de especies en la superficie. Adicionalmente, también se pueden registrar bandas bipolares que se generan por la variación de la frecuencia de vibración de la especie con el potencial aplicado

3.6.2.2 Espectrometría de masas diferencial electroquímica

En este trabajo, se utilizaron dos tipos de configuración DEMS para el estudio espectroelectroquímico. Inicialmente, se empleó una configuración que combina el diseño convencional DEMS con la celda de flujo. La celda electroquímica se acopló a un espectrómetro de masas Pfeiffer-Vacuum (Figura 4.10), el cual contiene el detector Prisma QMS 200 que permite la adquisición simultánea de hasta 72 señales masa/carga (m/z). Sin embargo, durante la medida es conveniente registrar solo dos señales para obtener una buena señal/ruido.

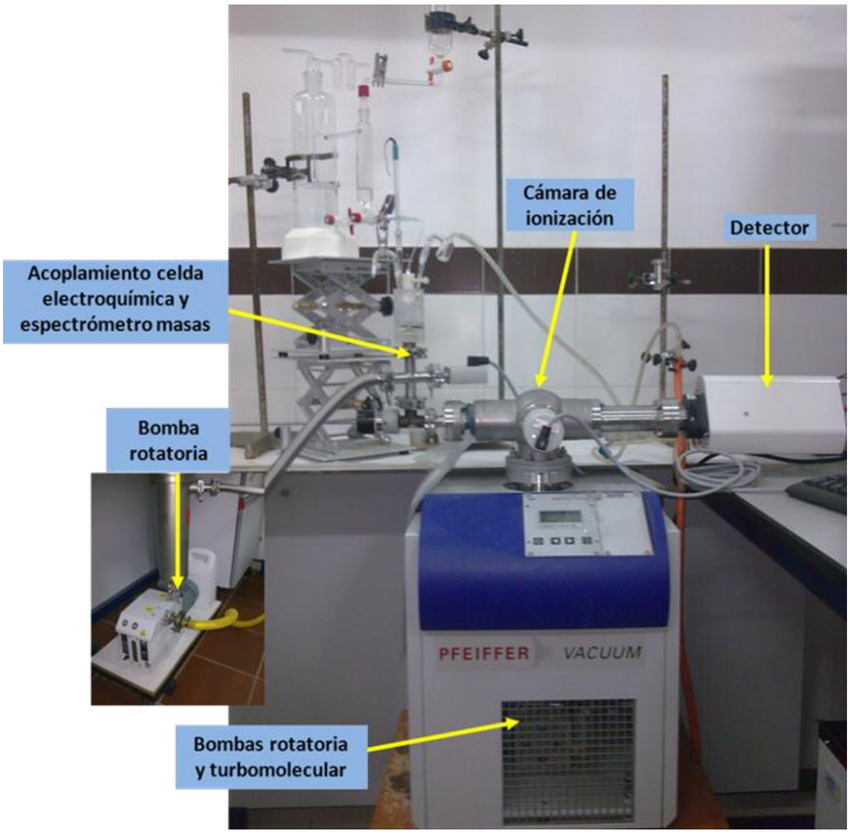

Figura 4.10. Sistema electroquímico acoplado a un espectrómetro de masas diferencial (DEMS).

La celda electroquímica está acoplada a una cámara del espectrómetro dónde existe una presión del orden de 10^{-3} mbar, que se consigue con una bomba de vacío rotativa, y está separada por una válvula micrométrica de una segunda cámara, dónde la presión es del orden de 10^{-8} mbar, la cual se obtiene con una bomba de vacío turbomolecular. En esta segunda cámara también se encuentra otra bomba de vacío rotativa, que en el instante en que se enciende el equipo proporciona la presión necesaria (10^{-2} mbar) para que la bomba turbomolecular pueda encenderse. La apertura de la válvula micrométrica se gira cuidadosamente para lograr ajustar la presión de la cámara a 5×10^{-6} mbar. La diferencia de presión entre las dos cámara permite que los productos gaseosos y/o volátiles procedentes de la celda electroquímica sean dirigidos hacia la segunda cámara, dónde se produce su ionización y su detección (en una copa de Faraday) gracias a un cuádrupolo que deja pasar aquellos iones con la relación masa/carga deseada.

Se utilizó una celda hecha de plexiglas de 50 mL de capacidad, donde es posible utilizar electrodos porosos y su esquema se muestra en la figura 4.11. En la parte inferior se encuentra una membrana hidrófoba de teflón (Scimat Ltd., 200/40/60), que es la interface entre la celda electroquímica y el espectrómetro de masas y es permeable a los productos gaseosos y/o volátiles generados durante la reacción electroquímica. La membrana se coloca sobre una pieza de acero poroso, cuya misión es dar la estabilidad mecánica necesaria para el sistema de vacío. El sellado entre la celda y la entrada del espectrómetro se consigue con un anillo de vitón.

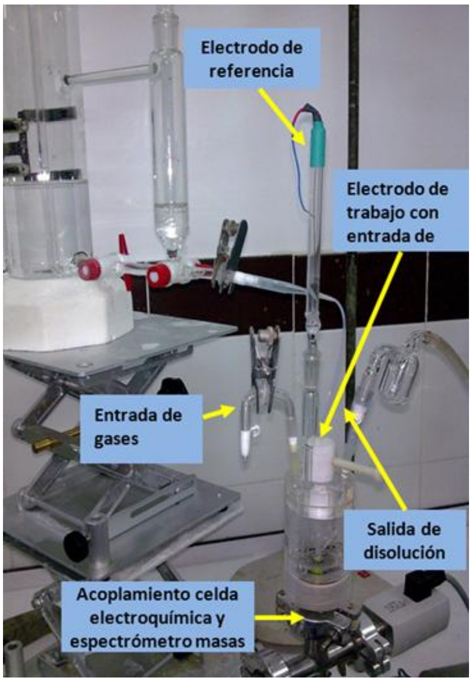

Figura 4.11. Montaje de la celda electroquímica de flujo en el DEMS.

La Figura 4.12 muestra un esquema de la celda que permite el flujo constante de electrolito en el interior de la capa delgada, debido a la existencia de un orificio en el centro del electrodo, que se conecta con los recipientes del disolvente y del metanol mediante un tubo de teflón (A). El electrodo dispone de un cuerpo cónico de polipropileno en su reverso (M) y se une a un vástago de vidrio (C) por medio del tubo de alimentación de teflón, que le otorga cierta flexibilidad y permite así un mejor acoplamiento a la membrana de teflón situado en la parte inferior de la celda. Por el interior del vástago de vidrio pasa el tubo de teflón y un alambre de Au de 0,5 mm de diámetro que sirve de contacto eléctrico con el electrodo (B).

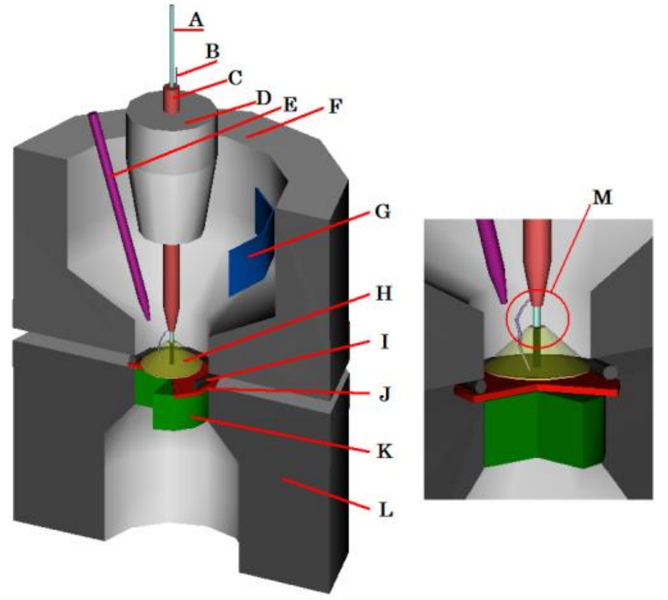

Figura 4.12. Esquema de la celda de flujo utilizada en las experiencias de DEMS.

El conjunto de electrodo/vástago se desliza por el interior de un cuerpo de teflón (D) que se acopla al centro de la tapa de la celda electroquímica. Esto posibilita un ajuste preciso en el eje vertical y por tanto de la distancia que separa la cara inferior (H) (la única electroquímicamente activa del electrodo) de la membrana de teflón (J) que forma la interface, conformando la celda de flujo de capa delgada. La tapa de la celda dispone de las bocas u orificios alrededor del electrodo de trabajo para los restantes componentes de la celda: el electrodo de referencia de hidrógeno (E), el contraelectrodo (G), el tubo de vidrio para la salida de la disolución, la entrada y salida de gases.

La temperatura de trabajo se controla por medio de un flujo de agua termostatada a través de un circuito externo que envuelve la celda y permite conseguir la temperatura de trabajo deseada. El flujo del electrolito es controlado por medio de las llaves de los recipientes que contienen el electrolito.

La segunda configuración DEMS utilizada en este trabajo, también ha sido desarrollada por el Grupo de Ciencia de Superficies y Electrocatálisis de la ULL. En esta nueva configuración la sonda de un espectrómetro de masas comercial Omnistar Pfeiffer-Vacuum (detector Prisma QMS 200) es adaptada al electrodo de trabajo a través de un orificio en el centro. La sonda contiene en su extremo una membrana de teflón que actúa de interface entre la disolución y el vacío del espectrómetro de masas como se aprecia en la figura 4.13. Esta disposición permite utilizar una celda electroquímica convencional con todos sus accesorios, y requiere el uso de la configuración menisco en el electrodo de trabajo durante las medidas para concentrar las especies en la entrada de la sonda.

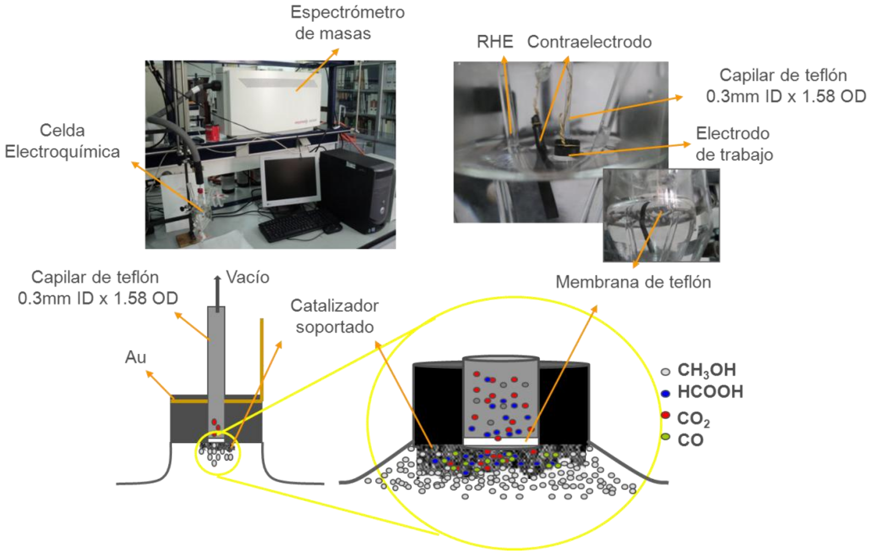

Figura 4.13. Espectrómetro de masas comercial acoplado a una celda electroquímica y configuración del electrodo de trabajo para un catalizador soportado.

En el caso de la configuración para sistemas no soportados (figura 4.14), el capilar se introduce en una punta de pipeta y la superficie del electrodo se acerca a la membrana para formar una capa delgada. Debido a que este último ajuste es manual, se corre el riesgo de que la distancia entre membrana y electrodo no sea siempre la misma, y por tanto es necesario comprobar que las señales de la corriente iónica (m/z) y la corriente voltamperométrica no estén desfasadas previamente a la realización del experimento correspondiente.

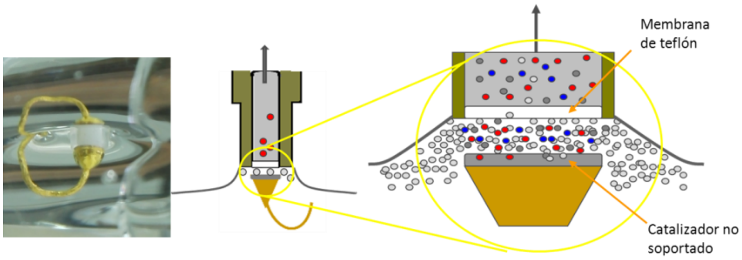

Figura 4.14. Configuración del electrodo de trabajo para un catalizador no soportado.

Bibliografía

Abd-El-Latif, A.A., Mostafa, E., Huxter, S., Attard, G. & Baltruschat, H., 2010. Electrooxidation of ethanol at polycrystalline and platinum stepped single crystals: A study by differential electrochemical mass spectrometry. *Electrochimica Acta*, **55**, pp. 7951-7960.

Baltruschat, H., 1999. In *Interfacial Electrochemistry: Theory, Experiment and Applications*, eds. A. Wieckowski & M. Dekker,New York, pp. 577.

Baltruschat, H., 2004. Differential electrochemical mass spectrometry. *Journal of the American Society for Mass Spectrometry*, **15**, pp. 1693-1706.

Bard, A.J. & Faulkner, L.R. 1980, *Electrochemicals Methods*, John Wiley a& Sons Inc., New York.

Bertin, E. 1978, "Energy-DispersiveX-ray Spectrometry" in *Introduction to X-ray Spectrometric Analysis* Springer US, pp. 231-253.

Binnig, G., Quate, C.F. & Gerber, C., 1986. Atomic Force Microscope. *Physical Review Letters*, **56**, pp. 930-933.

Binnig, G., Rohrer, H., Gerber, C. & Weibel, E., 1982, Surface studies by scanning tunneling microscopy. *Physical Review Letters,* **49**, pp. 57-61.

Bruckenstein, S. & Gadde, R.R., 1971. Use of a porous electrode for in situ mass spectrometric determination of volatile electrode reaction products. *Journal of the American Chemical Society,* **93**, pp. 793-794.

Cramm, S., Friedrich, K.A., Geyzers, K-, Stimming, U. & Vogel, R., 1997. Surface structural and chemical characterization of Pt/Ru composite electrodes: A combined study by XPS, STM and IR spectroscopy. *Fresenius' journal of analytical chemistry,* **358**, pp. 189-192.

García, G., Florez-Montaño, J., Hernandez-Creus, A., Pastor, E. & Planes, G.A., 2011. Methanol electrooxidation at mesoporous Pt and Pt–Ru electrodes: A comparative study with carbon supported materials. *Journal of Power Sources,* **196**, pp. 2979-2986.

Greenler, R.G., 1966. Infrared Study of Adsorbed Molecules on Metal Surfaces by Reflection Techniques. *The Journal of Chemical Physics,* **44**, pp. 310.

Hansen, W.N., 1968. Electric fields produced by the propagation of plane coherent electromagnetic radiation in a stratified medium. *Journal of the Optical Society of America,* **58**, pp. 380-388.

Hartung, T. & Baltruschat, H., 1990. Differential electrochemical mass spectrometry using smooth electrodes: adsorption and hydrogen/deuterium exchange reactions of benzene on platinum. *Langmuir,* **6**, pp. 953-957.

Hummers, W.S. & Offeman, R.E., 1958. Preparation of Graphitic Oxide. *Journal of the American Chemical Society,* **80**, pp. 1339-1339.

Jenkins, R. and Snyder, R., 2012. *Introduction to X-ray powder diffractometry,* 267th edn, John Wiley & Sons.

Jusys, Z., Kaiser, J. & Behm, R.J., 2002. Composition and activity of high surface area PtRu catalysts towards adsorbed CO and methanol electrooxidation—: A DEMS study. *Electrochimica Acta,* **47**, pp. 3693-3706.

Kanellopoulos, N., 2011. *Nanoporous materials: Advanced techniques for characterization, modeling, and processing,* Taylor & Francis US.

McKone, J.R., Sadtler, B.F., Werlang, C.A., Lewis, N.S. & Gray, H.B., 2013. NiMo nanopowders for efficient electrochemical hydrogen evolution. *ACS Catalysis,* **3**, pp. 166-169.

Montes, d.O., Kumarakuru, H., Cherns, D. & Fermín, D.J., 2011. Hydrogen adsorption at strained Pd nanoshells. *The Journal of Physical Chemistry C,* **115**, pp. 10489-10496.

Oberacher, H., Pitterl, F., Erb, R. & Plattner, S., 2015. Mass spectrometric methods for monitoring redox processes in electrochemical cells. *Mass spectrometry reviews,* **34**, pp. 64-92.

Perego, G., 1998. Characterization of heterogeneous catalysts by X-ray diffraction techniques. *Catalysis Today,* **41**, pp. 251-259.

Planes, G.A., García, G. & Pastor, E., 2007. High performance mesoporous Pt electrode for methanol electrooxidation. A DEMS study. *Electrochemistry Communications,* **9**, pp. 839-844.

Rietveld, H.M., 1967. Line profiles of neutron powder-diffraction peaks for structure refinement. *Acta Crystallographica,* **22**, pp. 151-152.

Schmidt, T.J., Gasteiger, H.A., Stäb, G.D., Urban, P.M., Kolb, D.M. & Behm, R.J., 1998. Characterization of High-Surface-Area Electrocatalysts Using a Rotating Disk Electrode Configuration. *Journal of the Electrochemical Society*, **145**, pp. 2354-2358.

Smith, W. E. and G. Dent, G., 2005. Introduction, Basic Theory and Principles in *Modern Raman Spectroscopy – A Practical Approach* John Wiley & Sons, pp. 1-21.

Surynarayana, C. and Norton, G. 1996, *X-Ray Diffraction: A practical Approach,* Plenum Press, New York.

Vidal-Iglesias, F., Lopez-Cudero, A., Solla-Gullón, J., Aldaz, A. & Feliu, J., 2012. Pd-modified shape-controlled Pt nanoparticles towards formic acid electrooxidation. *Electrocatalysis,* **3**, pp. 313-323.

Vidal-Iglesias, F.J., Solla-Gullón, J., Herrero, E., Aldaz, A. & Feliu, J.M., 2010. Pd adatom decorated (100) preferentially oriented pt nanoparticles for formic acid electrooxidation. *Angewandte Chemie International Edition,* **49**, pp. 6998-7001.

Watts, J.F. & Wolstenholme, J. 2003, *An introduction to surface analysis by XPS and AES,* John Wiley & Sons, Chichester.

Wei, Z.D., Li, L.L., Luo, Y.H., Yan, C., Sun, C.X., Yin, G.Z. & Shen, P.K., 2006. Electrooxidation of methanol on upd-Ru and upd-Sn modified Pt electrodes. *The Journal of Physical Chemistry B,* **110**, pp. 26055-26061.

Wolter, O. & Heitbaum, J., 1984. Differential Electrochemical Mass Spectroscopy (DEMS): A new method for the study of electrode processes. *Berichte der Bunsengesellschaft für physikalische Chemie,* **88**, pp. 2-6.

4. RESULTADOS Y DISCUSIÓN

Como se ha descrito anteriormente, los sistemas electroquímicos como las pilas de combustible y los electrolizadores son una excelente alternativa para complementar un sistema energético basado en energías más limpias, que permita satisfacer las exigencias de los dispositivos electrónicos que tienden a ser cada vez más pequeños. Para ello, es necesario el desarrollo de micro y nanoestructuras organizadas, que tengan un coste aceptable y el mismo rendimiento energético que los catalizadores que se utilizan convencionalmente (nanopartículas de Pt y aleaciones de este metal soportadas sobre carbón). Hay que tener en cuenta que estas nuevas estructuras deben cumplir ciertas características que permitan que las reacciones electroquímicas puedan llevarse a cabo de manera eficiente. En el caso de las micropilas de combustible, uno de las principales requisitos que debe poseer un catalizador es tener una elevada superficie electroquímicamente activa con un mínimo de volumen.

En este sentido, los catalizadores mesoporosos de Pt no soportados cumplen perfectamente con esta premisa, y además, su estructura les confiere una gran cantidad de sitios activos con bajo número de coordinación (escalones, bordes, esquinas, islas) que facilitan la formación de especies oxigenadas que ayudan a la oxidación del CO [Esterle, 2010]. El monóxido de carbono actúa como “veneno” catalítico y se forma como intermediario en la reacción de oxidación de alcoholes, aldehídos y ácidos, como el metanol, el etanol o el ácido fórmico.

La oxidación electroquímica de metanol hasta CO_2 ocurre mediante un mecanismo que involucra dos reacciones paralelas. La primera ocurre a través de intermediarios fuertemente adsorbidos (principalmente CO_{ad}), mientras que en la segunda participan especies débilmente adsorbidas que pueden producir derivados parcialmente oxidados como el formaldehído o el ácido fórmico [Cohen, 2007; Wang, 2007]. De acuerdo con estudios previos desarrollados por el Grupo de Investigación [Planes, 2007], la mayor producción, y por tanto, la mayor eficiencia de conversión a CO_2 se favorece con la formación de CO adsorbido en sistemas con difusión restringida, como es el caso de los catalizadores soportados en carbón, donde los productos solubles (como el formaldehído y el ácido fórmico) pueden interactuar con la superficie una vez formados y re-adsorberse. Sin embargo, este hecho genera un efecto de competencia entre las moléculas de metanol y los productos parcialmente oxidados por los sitios de reacción en el interior del catalizador, lo que ocasiona una disminución en la corriente. Por tanto, se puede concluir que los electrodos con difusión restringida incrementan las cantidades relativas de ácido fórmico y formaldehido en el interior del catalizador debido a la dificultad de que estas moléculas dejen la estructura porosa, obstruyendo el flujo en el interior del catalizador y evitando que el metanol llegue a los centros catalíticos [Baena-Moncada, 2014].

En el caso de la oxidación de etanol sobre Pt mesoporoso en medio ácido, la reacción no es completa y las principales especies formadas son el acetaldehído y el ácido acético, produciéndose cantidades mucho menores de CO_2 . Debido a que el mecanismo de reacción es mucho más complejo, el efecto de la morfología y la estructura del material sobre las diferentes vías de reacción que condicionan las diferentes especies que se producen, juega un papel muy importante a la hora de evaluar la densidad de corriente generada en el sistema [Braunchweig, 2013].

A diferencia de las aleaciones que normalmente se utilizan en los catalizadores soportados sobre materiales carbonosos, los catalizadores mesoporosos de Pt modificados con otro metal (M) por deposición espontánea, mejoran la actividad electrocatalítica hacia la electrooxidación de metanol respecto a las aleaciones de Pt-M convencionales. Esta mejora se debe principalmente a la capacidad que tienen algunos metales de promover la oxidación de CO_{ad} y algunos alcoholes mediante la participación en el proceso de oxidación de especies oxigenadas, que se adsorben sobre la superficie de estos metales a potenciales más bajos que sobre el Pt.

Otro tipo de nanoestructuras bimetálicas que han llamado la atención en los últimos años son las nanopartículas tipo "*core-shell*" (nucleo-cubierta), las cuales pueden variar su actividad catalítica mediante el crecimiento controlado de las capas delgadas ("*shells"*) sobre la partícula metálica que actúa de sustrato (*"core"*). La reactividad de este tipo de sistemas se racionaliza en términos de efectos electrónicos y geométricos conocidos como "*strain*" o tensión, los cuales pueden alterar la posición del centro de la banda *d* del metal [Strasser, 2010, Santos, 2010]. La formación de capas de Pd sobre un sustrato de Au ha sido de gran interés, particularmente en reacciones de evolución/oxidación de hidrógeno y oxidación de ácido fórmico, donde se ha mostrado que el sustrato de Au en el núcleo de la partícula puede tener un efecto apreciable sobre la actividad catalítica de las capas de Pd [Bonnefont, 2013; Quaino, 2011; Kibler, 2005; Lee, 2008; Ruvinsky, 2008].

Experimentalmente se ha demostrado una fuerte dependencia de la oxidación de CO_{ad} sobre capas de Pd con la estructura del sustrato de Au [Ruvinsky, 2008; El-Aziz, Kibler 2002; Kuo, 2013]. Así, estudios basados en estructuras núcleo-cubierta de Au@Pd han presentado que la tensión de las capas de Pd es menor cuando se incrementa el tamaño de la capa de 1 a 10 nm, lo que afecta directamente a la adsorción y la oxidación del CO [Montes, 2011; Montes, 2012]. Aunque esta tendencia es menos evidente para la oxidación electroquímica de CO cuando estas nanoestructuras están soportadas en carbón, conocer este efecto en más detalle puede ayudar a entender las diferencias de reactividad en función del espesor de la capa de Pd durante la oxidación de ácido fórmico.

Este efecto no sólo tiene influencia en los procesos de oxidación sino también a los de reducción. En el caso de la reducción de CO_2 [Qin, 2014; Lee, 2014], se ha reportado que la eficiencia faradaíca está limitada por la velocidad de la reacción de evolución de hidrógeno HER. Sin embargo, esta eficiencia puede cambiar mediante el control del espesor de la capa externa de Pd que se encuentra sobre el sustrato de Au [Bonnefont, 2013; Quaino, 2011].

Recientemente, con el desarrollo de membranas alcalinas para las pilas de combustible, la electrolisis basada en pilas tipo PEM tiene gran interés debido a que permite utilizar electrocatalizadores no-nobles como los materiales basados en Ni, que son mucho más baratos. En estos dispositivos, la dispersión del catalizador y la conductividad del soporte son factores de gran importancia. Comparados con otros materiales carbonosos, los materiales basados en grafeno presentas ventajas como un área superficial elevada [Li, 2008], excelente conductividad [Geim, 2007], única estructura con planos basales grafitizados y, a diferencia del grafeno, se pueden obtener por métodos más económicos. En este tipo de soportes se facilita el acceso del electrolito hacia la superficie catalítica, que se produce más rápidamente al disminuir en gran medida los efectos de difusión que ocurren en otro tipo de soportes carbonosos. Más aún, la integración de nanopartículas metálicas con capas de grafeno evita la formación de agregados de partículas más grandes con elevada energía superficial, lo que permite una muy buena actividad electroquímica.

En base a todo lo expuesto, la presente Tesis Doctoral abarca un estudio de las reacciones electrocatalíticas, tanto de oxidación como de reducción, que suceden en sistemas electroquímicos para generar o almacenar energía. Para ello se han sintetizado y caracterizado 3 tipos de materiales nanoestructurados: metales mesoporosos, nanopartículas núcleo-cubierta soportadas y materiales grafénicos. Los resultados obtenidos han dado lugar a una serie de trabajos que se pueden dividir en dos grupos. El primero de ellos lo forman cuatro publicaciones que corresponden al estudio de la oxidación de combustibles para pilas tipo PEM. Para ello se procedió a la síntesis y caracterización de catalizadores mesoporosos de base Pt para la electrooxidación de alcoholes como el metanol y etanol; y a la evaluación electroquímica de catalizadores tipo "*core-shell*" (Au@Pd) para la oxidación de ácido fórmico. En estos catalizadores se pudo determinar el efecto estructural, morfológico y en algunos casos electrónico, hacia la oxidación de CO (como sustancia modelo) y los diferentes tipos de combustibles (metanol, etanol y ácido fórmico).

El segundo grupo lo constituyen dos trabajos en los que abordan procesos de reducción. En el primero se estudia como varía la eficiencia de electroreducción de CO_2 con el grosor de las capas de Pd en las nanopartículas de Au@Pd. Mientras que en el segundo se sintetizan y se caracterizan catalizadores basados en grafeno para la reacción de evolución de hidrógeno en medio alcalino.

A continuación, se expondrán los logros más relevantes de las investigaciones realizadas en la presente Tesis Doctoral.

4.1 CATALIZADORES PARA LA ELECTROOXIDACIÓN DE COMBUSTIBLES ALTERNATIVOS

4.1.1. Electrooxidación de metanol en electrodos de Pt y PtRu mesoporoso. Un estudio comparativo con materiales soportados en carbón. *Methanol electrooxidation at mesoporous Pt and Pt–Ru electrodes: A comparative study with carbon supported materials.* Journal of Power Sources, **2011**, 196, p. 2979-2986.

Los catalizadores mesoporosos de Pt (MPPt) y de Pt-Ru (MPPtRu) se obtuvieron por la electrorreducción de los correspondientes precursores en presencia de un surfactante. Al comparar la actividad catalítica hacia la oxidación de metanol de estos catalizadores y el MPPt/Ru (preparado por deposición espontanea de Ru sobre MPPt) con el PtRu/C, se observó que las estructuras monolíticas mesoporosas, en especial el MPPt/Ru, son más activas y presentan mayor densidad de corriente que el catalizador soportado.

Utilizando la espectrometría de masas diferencial electroquímica con celda de flujo de capa delgada (TLFC-DEMS), se demostró que la mayor actividad del catalizador MPPt/Ru está relacionada con el arreglo de su estructura porosa, la cual permite la difusión de las especies parcialmente oxidadas como el ácido fórmico y el formaldehido durante la reacción. Esto evita que estas especies reaccionen de nuevo para generar CO_{ad} y ocupen sitios catalíticamente activos que puedan estar disponibles para que reaccionen otras moléculas de metanol. La figura 5.1.1 describe el modelo propuesto para los catalizadores con difusión restringida, como el PtRu/C, y sin difusión restringida, como ocurre en los catalizadores mesoporosos.

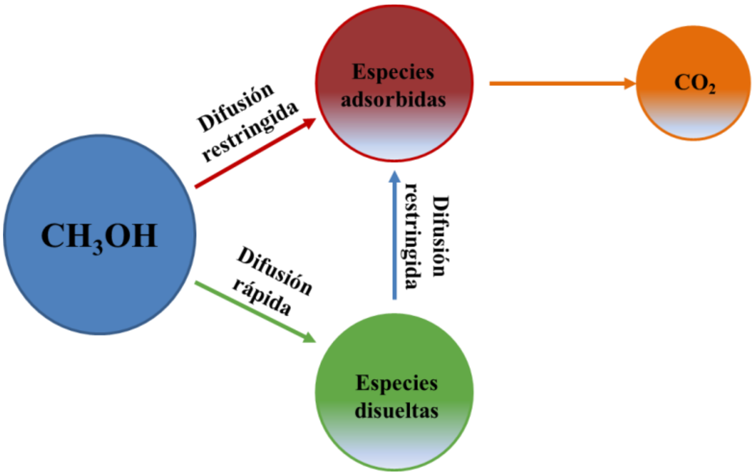

Figura 4.1.1. Modelo del mecanismo de oxidación de metanol en catalizadores con difusión restringida y en los catalizadores mesoporosos.

4.1.2. Acerca del diseño de catalizadores basados en Pt. Arquitectura porosa combinada con la modificación superficial con Sn para mejorar la actividad electrocatalitica.

On the design of Pt based catalysts. Combining porous architecture with surface modification by Sn for electrocatalytic activity enhancement. Journal of Power Sources, **2015**, 282, p. 34-44.

Como se mencionó en el trabajo anterior, los catalizadores MPPt pueden prepararse por un procedimiento simple de manera *in situ*. En este trabajo se estudió la actividad electroquímica del MPPt modificado con adátomos de Sn (MPPt/Sn) hacia la oxidación de CO_{ad} y metanol. Los resultados a 25 y 60 ºC se compararon con el catalizador comercial de PtSn/C (3:1). La presencia de Sn sobre la superficie mejora la electrooxidación de CO_{ad} y metanol debido a la presencia de átomos oxofílicos de Sn (identificados por XPS) ubicados en la superficie de la estructura mesoporosa.

Se observó que la velocidad de los procesos catalíticos aumenta con la temperatura y el potencial aplicado. Así, los mejores resultados se obtuvieron con el catalizador MPPt/Sn a potenciales bajos y temperatura alta. El análisis por espectrometría de masas diferencia electroquímica DEMS (figura 5.1.2), reveló que a potenciales elevados se producen densidades de corriente altas debido a la formación de productos intermedios, principalmente formaldehído en lugar de ácido fórmico, con el consiguiente decrecimiento de la eficiencia de conversión de metanol a CO_2.

Por otro lado, se observó una vez más que la difusión de los productos intermedios es más rápida en las estructuras mesoporosas, que permiten que el "*turn-over*" o reutilización de sitios activos para la reacción sea mayor, y de esta forma, la corriente faradaica sea elevada. Asimismo, la alta conversión a CO_2 en el catalizador comercial se asocia a una difusión lenta de los reactivos en la estructura porosa del soporte carbonoso, lo que conlleva bajas densidades de corriente.

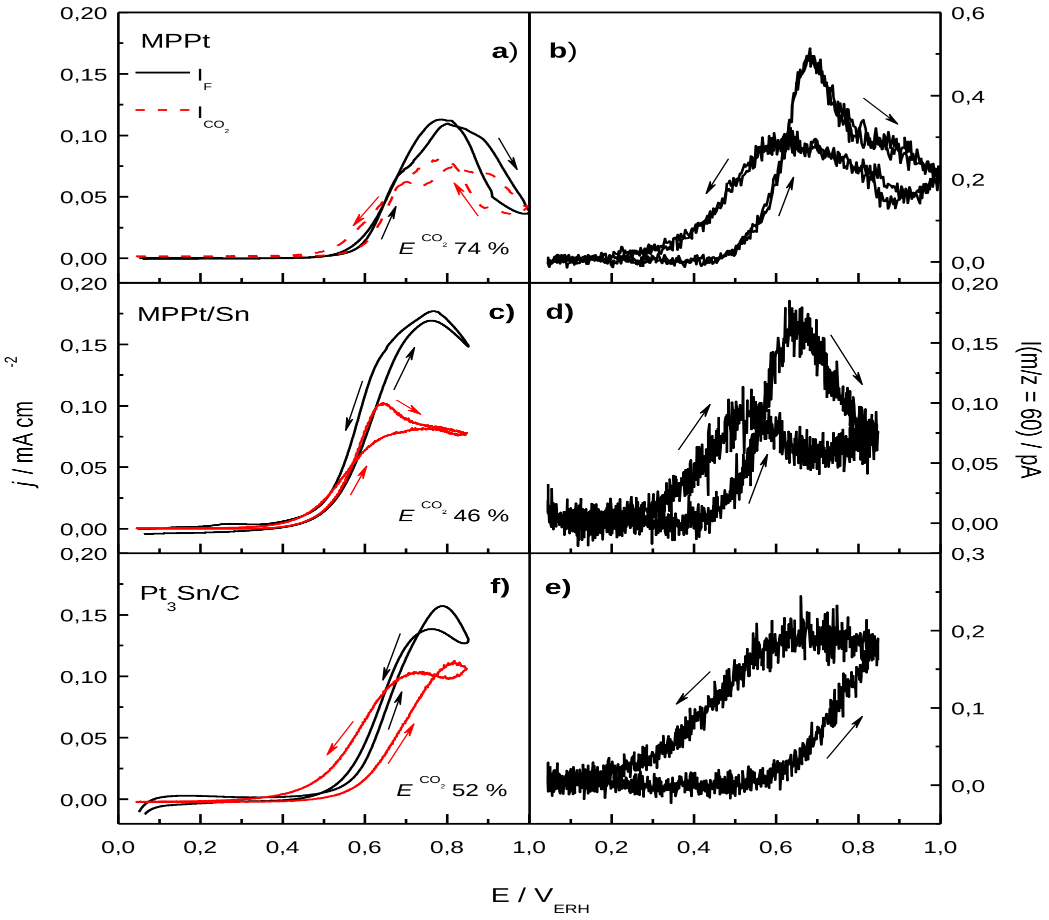

Figura 4.1.2. Voltamperogramas y masogramas cíclicos para la oxidación de metanol sobre los catalizadores MPPt (arriba), MPPt/Sn (θ_{Sn} = 0,60) (centro) and Pt_3Sn/C (abajo) en una disolución CH_3OH 0,1 M + H_2SO_4 0,5 M a 25 ºC. v = 0,002 V s^{-1}. Paneles en la izquierda: corriente faradaíca experimental (línea negra) y obtenida a partir el CO_2 producido (línea roja). Paneles de la derecha: $HCOOCH_3$ (señal masa/carga = 60) formado por la reacción de condensación entre metanol y ácido fórmico.

5.1.3. Estudio en medio ácido de la electrooxidación de etanol sobre un electrodo de Pt mesoporoso mediante una nueva configuración de espectrometría de masas electroquímica.

Mechanism of ethanol electrooxidation on mesoporous Pt electrode in acidic medium studied by a novel electrochemical mass spectrometry set-up. Electrochimica Acta, enviado, ELECTACTA-S-1505905.

En este trabajo se estudió el comportamiento electroquímico de catalizadores de platino mesoporoso nanoestructurado (MPPt) hacia la reacción de electrooxidación del etanol en función de la concentración del alcohol. Para ello, se utilizaron las técnicas de voltamperometría cíclica y la cronoamperometría combinadas con una nueva configuración de un espectrómetro de masas electroquímico, el cual permite una elevada sensibilidad de detección con pequeñas cantidades del catalizador.

El resultado principal indica que al aumentar la concentración de etanol se incrementa la formación de acetaldehído y ácido acético, y la formación de CO_2 se mantiene constante. Por consiguiente, la mayor eficiencia de conversión de etanol hasta CO_2 (~11 %) se obtuvo con la concentración de alcohol más baja (etanol 0,01 M) y a un potencial de 0,60 V.

La detección de las fracciones iónicas de diferentes especies como metano (señal masa/carga (m/z) = 15) y acetato de etilo (m/z = 43, 61, 73 y 88), en combinación con el análisis cinético realizado mediante curvas de Tafel, permitió establecer que el paso determinante de la reacción electroquímica es la formación de grupos OH_{ad} y proponer el mecanismo de reacción presentado en la figura 5.1.3.

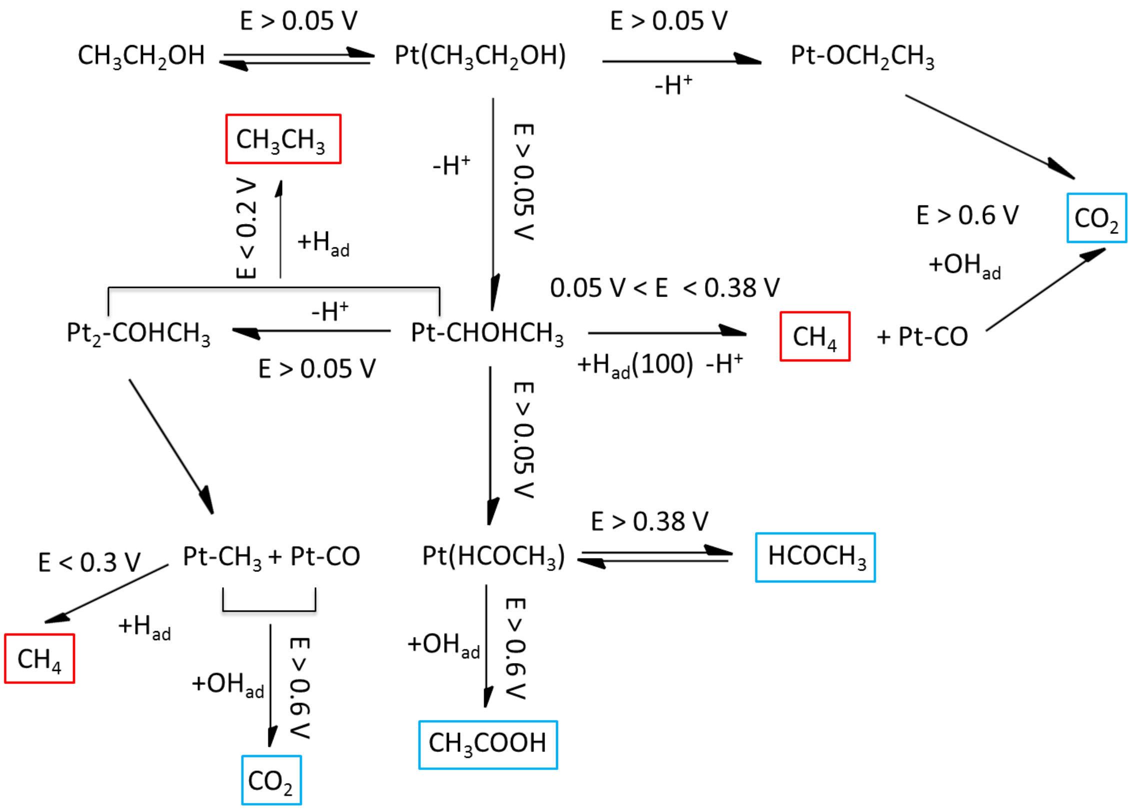

Figura 4.1.3. Esquema de las principales vías de reacción del etanol sobre electrodos de Pt mesoporoso en medio ácido.

4.1.4. Evidencia espectroscópica del efecto electrónico del núcelo sobre la electrooxidación de CO y HCOOH en estructuras núcleo-cubierta de Au-Pd.

Spectroscopic evidences of core electronic effects on CO and HCOOH electrooxidation at Au-Pd core-shells. En preparación.

El estudio espectroscópico de la electrooxidación de CO y el ácido fórmico sobre estructuras núcleo-cubierta de Au@Pd soportadas en negro de carbón, de aproximadamente 1 nm (CS1/C) y 10 nm (CS10/C) de espesor, se realizó aplicando la espectrometría de masas diferencial electroquímica (DEMS) y la espectroscopia de infrarrojo por transformada de Fourier (FTIRS) *in situ* combinada con la voltamperometría cíclica. De este modo, se detectaron *in situ* los intermedios generados durante el proceso de oxidación en estas estructuras, y a su vez, se estableció la influencia del espesor de la capa externa de Pd y la existencia de un efecto electrónico ocasionado por el núcleo de Au.

Se encontró que el incremento de capas de Pd no sólo afecta al inicio del potencial de electrooxidación, al desplazarlo a valores más negativos, sino que también tiene influencia sobre la adsorción del CO y el OH. Adicionalmente, de acuerdo a los resultados de FTIRS, se pudo establecer la formación de especies formiato, $HCOO_{ad}$, como intermedio en la oxidación del ácido fórmico a CO_2 en nanoestructuras de Au@Pd, siendo la desprotonación hasta CO_2 más rápida sobre el catalizador CS10/C que sobre el CS1/C. El análisis por espectrosocopía fotoelectrónica de rayos X (XPS) permitió determinar una mayor contribución de especies Pd (IV) sobre el primero, promoviendo la oxidación a potenciales menores.

En base a estos resultados, se concluye que el efecto electrónico del núcleo de Au sobre la superficie de Pd puede ser controlado por medio del espesor de la capa de este último, y como consecuencia, es posible modificar el mecanismo de una reacción en la dirección deseada.

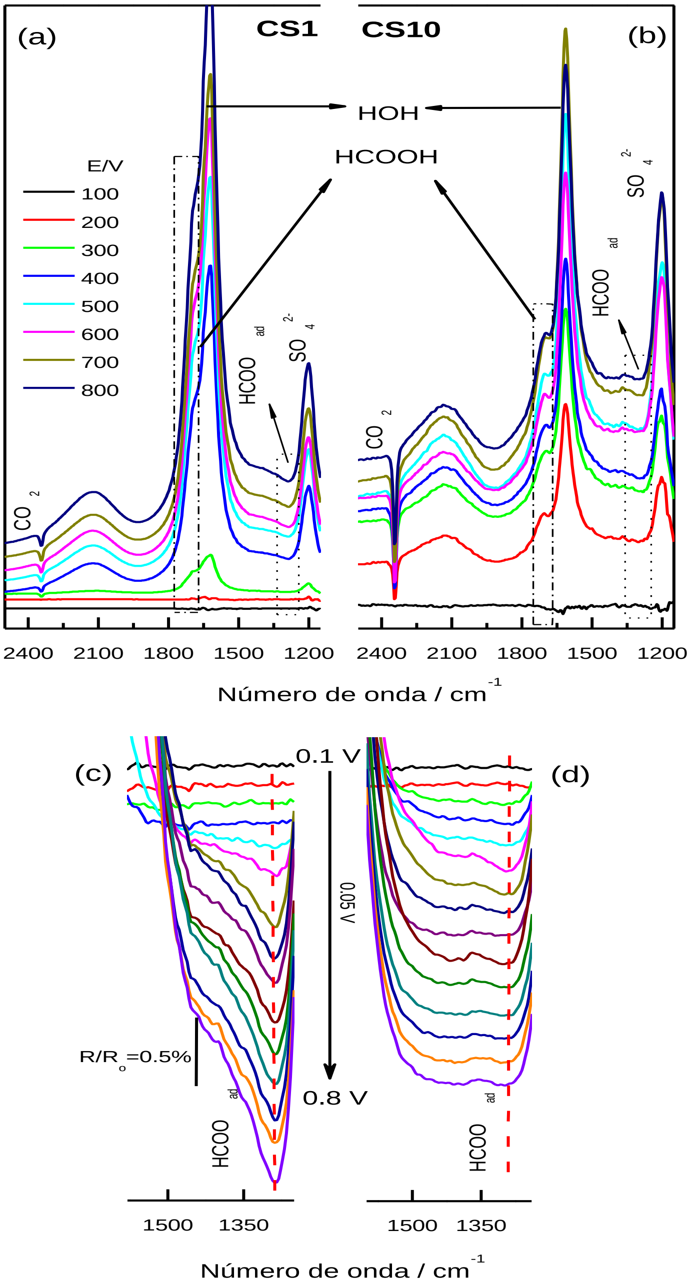

Figura 4.1.4. Espectros FTIR *In situ* registrados durante la electrooxidación de ácido fórmico en una disolución de HCOOH 0.1 M + H_2SO_4 0.5 M sobre los catalizadores (a) CS1/C (izquierda) y (b) CS10/C (derecha). (c) and (d) muestran los espectros correspondientes a la banda $HCOO_{ad}$ registrados en la región entre 1250-1600 cm^{-1} durante la electrooxidación de ácido fórmico sobre los catalizadores CS1/C y CS10/C respectivamente. El potencial fue cambiado con saltos de 0.05 V en dirección positiva desde 0.05 V (potencial de referencia) hasta 1.20 V. Cada espectro se registró con 128 scans, 8 cm^{-1}.

4.2 CATALIZADORES PARA OBTENER COMBUSTIBLES ALTERNATIVOS MEDIANTE PROCESOS DE ELECTROREDUCCIÓN

4.2.1 Ajuste de la eficiencia de electroreducción de CO_2 en capas de Pd sobre nanonúcleos de Au. *Tuning CO_2 electroreduction efficiency at Pd shells on Au nanocores*. Chemical Communications, **2013**, 49, p. 10962-10964.

En este trabajo se establece por primera vez que la eficiencia faradaica obtenida durante la electrorreducción de CO_2 se ve afectada de manera considerable por el espesor de las nanocapas (*nanoshells*) de Pd que envuelven a las nanopartículas de Au (*core*). Mediante DEMS se determinó la relación entre la evolución de hidrógeno y la reducción de CO_2. En la figura 5.2.1 se puede observar las imágenes TEM de las nanopartículas tipo *"core-shell"* de Au-Pd con un diámetro del centro (o corazón) de Au de 19,3 ± 1,0 nm y espesor de las capas externas de Pd de 1,3 y 9,9 ± 1,0 nm, las cuales se denominan como CS1 y CS10, respectivamente.

Los resultados electroquímicos junto con los obtenidos por el DEMS muestran claramente que el catalizador CS1 presenta sobrepotenciales más bajos para la reducción de CO_2 que el CS10. El análisis cuantitativo de la señal m/z = 2 indica que la adsorción de hidrógeno y la evolución del mismo juega un papel fundamental en la reactividad de las nanocapas de Pd.

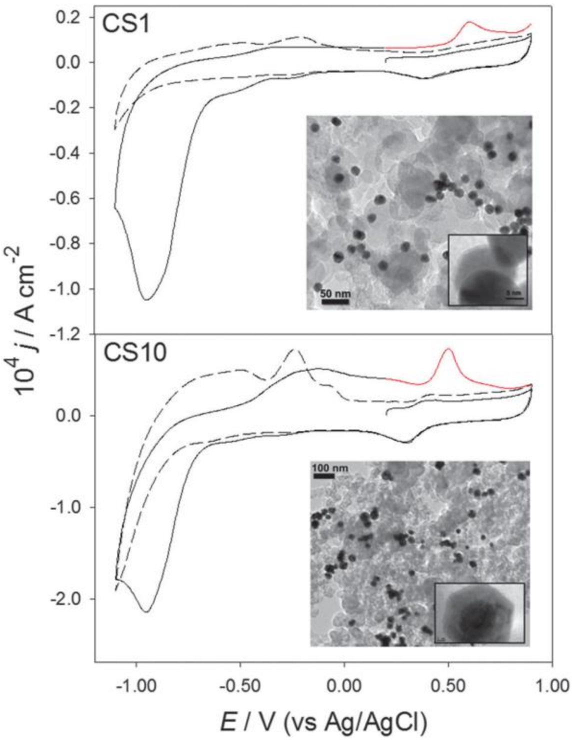

Figura 4.2.1 Voltamperogramas cíclicos (VCs) de los catalizadores nanoestructurados tipo core-shell CS1 y CS10 soportados en carbón Vulcan, obtenidos a una velocidad de barrido de potencial de 0,02 V s^{-1} en una disolución de Na_2SO_4 0,1 M con pH = 4. La línea segmentada corresponde a los experimentos realizados en la disolución saturada con Ar; en la disolución saturada en CO_2, se muestra el primer VC con una línea continua negra, y parte del segundo ciclo con una línea roja.

4.2.2. Nanoestructuras de Ni y NiMo soportadas sobre oxido de grafeno reducido con elevada actividad para la reaccion de evolución de hidrógeno.

Ni and NiMo nanostructures supported on reduced graphene oxide with enhanced activity towards the hydrogen evolution reaction. En preparación.

La electrolisis alcalina presenta la ventaja de poder utilizar materiales no-nobles como electrocatalizadores. Las mejoras que han experimentado estos dispositivos han permitido que se utilicen materiales basados en Ni, los cuales son estables en medio alcalino y exhiben una actividad relativamente alta para la reacción de evolución de hidrógeno (HER).

En este trabajo, se prepararon nanodiscos de Ni y Ni_xMo_{1-x} soportados sobre óxido de grafeno reducido (RGO). La estructura de los materiales sintetizados fue caracterizada por diferentes técnicas de rayos X, espectroscopía Raman y técnicas de microscopía. Mediante microscopía de fuerza atómica (AFM) se pudo identificar el crecimiento de nanodiscos con un diámetro promedio de 13 nm y una altura de 3-5 átomos (figura 5.2.2). Los experimentos electroquímicos demostraron que la electroactividad de estos materiales hacia la HER es elevada, siendo el catalizador de NiMo/RGO el que presenta potenciales de producción más cercanos a 0,0 V. Mediante la espectrometría de masas diferencia electroquímica se pudo detectar simultáneamente la corriente faradaica y la corriente iónica debida a la producción de H_2. Estos resultados permiten establecer que las corrientes generadas no están asociadas a otros procesos de reducción (como la reducción de óxidos de Mo o Ni) que ocurren en paralelo a la HER, sino que sólo corresponde a la producción hidrógeno.

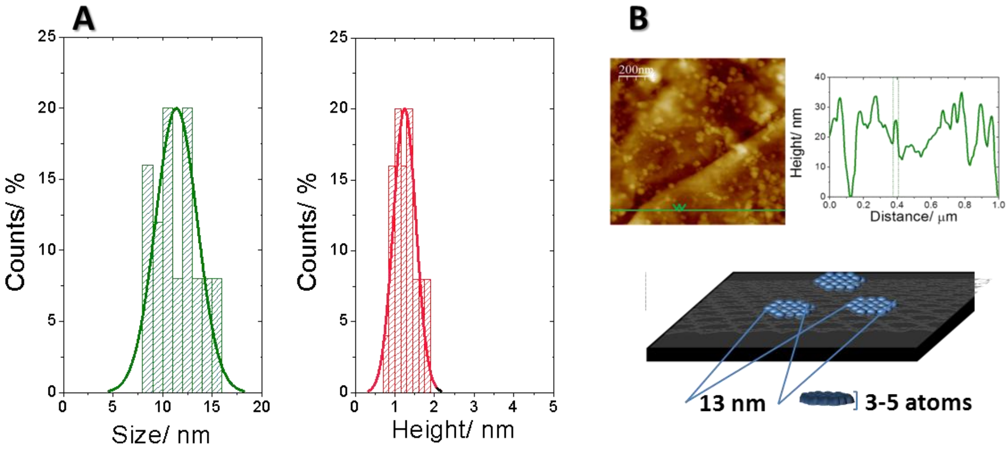

Figura 4.2.2. (A) Histograma de la distribución del tamaño de las partículas de Ni a partir de las medidas de AFM. (B) Imagen de AFM y perfil de profundidad (arriba). Esquema de los nanodiscos de Ni/RGO a partir de las imágenes AFM.

Bibliografia

Baena-Moncada, A.M., Coneo-Rodríguez, R., Calderón, J.C., Flórez-Montaño, J., Barbero, C.A., Planes, G.A., Rodríguez, J.L. & Pastor, E. 2014. Macroporous carbon as support for PtRu catalysts. *International Journal of Hydrogen Energy,* **39**, pp. 3964-3969.

Bonnefont, A., Simonov, A.N., Pronkin, S.N., Gerasimov, E.Y., Pyrjaev, P.A., Parmon, V.N. and Savinova, E.R. 2013. Hydrogen electrooxidation on PdAu supported nanoparticles: An experimental RDE and kinetic modeling study. *Catalysis Today,* **202**, pp. 70-78.

Braunchweig, B., Hibbitts, D., Neurock, M. & Wieckowski, A. 2013. Electrocatalysis: A direct alcohol fuel cell and surface science perspective. *Catalysis Today,* **202**, pp. 197-209.

Cohen, J.L., Volpe, D.J. & Abruna, H.D. 2007. Electrochemical determination of activation energies for methanol oxidation on polycrystalline platinum in acidic and alkaline electrolytes. *Physical Chemistry Chemical Physics,* **9**, pp. 49-77.

El-Aziz, A.M. & Kibler, L.A. 2002. Influence of steps on the electrochemical oxidation of CO adlayers on Pd(111) and on Pd films electrodeposited onto Au(111). *Journal of Electroanalytical Chemistry,* **534**, pp. 107-114.

Esterle, T.F., Russell, A.E. & Bartlett, P.N. 2010. Study of carbon monoxide oxidation on mesoporous platinum. *ChemPhysChem,* **11**, pp. 2896-2905.

Geim, A.K. & Novoselov, K.S. 2007. The rise of graphene. *Nature Material,* **6**, pp. 183-191.

Kibler, L.A., El-Aziz, A.M., Hoyer, R. & Kolb, D.M. 2005. Tuning reaction rates by lateral strain in a palladium monolayer. *Angewandte Chemie International Edition,* **44**, pp. 2080-2084.

Kuo, C., Lamontagne, L.K., Brodsky, C.N., Chou, L., Zhuang, J., Sneed, B.T., Sheehan, M.K. & Tsung, C. 2013. The effect of lattice strain on the catalytic properties of Pd nanocrystals. *ChemSusChem,* **6**, pp. 1993-2000.

Lee, S., Jung, N., Cho, J., Park, H., Ryu, J., Jang, I., Kim, H., Cho, E., Park, Y., Ham, H.C., Jang, J.H. & Yoo, S.J. 2014. Surface-rearranged Pd_3Au/C nanocatalysts by using CO-induced segregation for formic acid oxidation reactions. *ACS Catalysis,* **4**, pp. 2402-2408.

Lee, Y.W., Kim, N.H., Lee, K.Y., Kwon, K., Kim, M. & Han, S.W. 2008. Synthesis and characterization of flower-shaped porous Au@Pd alloy nanoparticles. *The Journal of Physical Chemistry C,* **112**, pp. 6717-6722.

Li, D., Muller, M.B., Gilje, S., Kaner, R.B. & Wallace, G.G. 2008. Processable aqueous dispersions of graphene nanosheets. *Nature Nano,* **3**, pp. 101-105.

Montes, d.O., Kumarakuru, H., Cherns, D. & Fermín, D.J. 2011. Hydrogen adsorption at strained Pd nanoshells. *The Journal of Physical Chemistry C,* **115**, pp. 10489-10496.

Montes, d.O., Plana, D., Celorrio, V., Lazaro, M.J. & Fermín, D.J. 2012. Electrocatalytic properties of strained Pd nanoshells at au nanostructures: CO and HCOOH oxidation. *The Journal of Physical Chemistry C*,**116**, pp. 692-699.

Planes, G.A., García, G. & Pastor, E. 2007. High performance mesoporous Pt electrode for methanol electrooxidation. A DEMS study. *Electrochemistry Communications*, **9**, pp. 839-844.

Qin, Y., Wang, J., Wu, Y. & Wang, L. 2014. Improved hydrogen production from formic acid under ambient conditions using a PdAu catalyst on a graphene nanosheets-carbon black support. *RSC Advances, 4*, pp. 30068-30073.

Quaino, P., Santos, E., Wolfschmidt, H., Montero, M.A. & Stimming, U. 2011. Theory meets experiment: Electrocatalysis of hydrogen oxidation/evolution at Pd–Au nanostructures. *Catalysis Today,* **177**, pp. 55-63.

Ruvinsky, P.S., Pronkin, S.N., Zaikovskii, V.I., Bernhardt, P. & Savinova, E.R. 2008. On the enhanced electrocatalytic activity of Pd overlayers on carbon-supported gold particles in hydrogen electrooxidation. *Physical Chemistry Chemical Physics,* **10**, pp. 6665-6676.

Santos, E., Quaino, P. & Schmickler, W. 2010. On the electrocatalysis of nanostructures: Monolayers of a foreign atom (Pd) on different substrates M(111). *Electrochimica Acta,* **55**, pp. 4346-4352.

Strasser, P., Koh, S., Anniyev, T., Greeley, J., More, K., Yu, C., Liu, Z., Kaya, S., Nordlund, D., Ogasawara, H., Toney, M.F. & Nilsson, A. 2010. Lattice-strain control of the activity in dealloyed core@shell fuel cell catalysts", *Nature Chemistry,* **2**, pp. 454-460.

Wang, H. & Baltruschat, H. 2007. DEMS study on methanol oxidation at poly- and monocrystalline platinum electrodes: The effect of anion, temperature, surface structure, Ru adatom, and potential. *The Journal of Physical Chemistry C,* **111**, pp. 7038-7048.

5. CONCLUSIONS/CONCLUSIONES

CONCLUSIONES

5.1 CATALIZADORES PARA LA ELECTROOXIDACIÓN DE COMBUSTIBLES ALTERNATIVOS

1. Se sintetizaron catalizadores monolíticos no soportados por el método de electrorreducción en presencia de un surfactante no iónico, para uso en micropilas de combustible que trabajan a bajas temperaturas. En concreto, se prepararon de manera rápida y eficiente electrodos de Pt y PtRu con estructura mesoporosa (MPPt y MPPtRu, respectivamente), no soportados, y se modificaron los MPPt con adátomos de Ru y Sn (MPPt/Ru y MPPt/Sn).
2. Se observó que estos materiales presentan áreas electroquímicas elevadas, del mismo orden de magnitud que los materiales soportados, y pueden ofrecer mejores actividades hacia la electrooxidación de metanol que los catalizadores soportados sobre carbón.
3. De acuerdo a los resultados obtenidos por espectrometría de masas diferencial electroquímica (DEMS), los electrodos con estructura mesoporosa permiten que el flujo de los productos parcialmente oxidados generados durante la electrooxidación de metanol (formaldehído y ácido fórmico) ocurra con mayor facilidad, y por tanto, su readsorción sea poco probable.
4. En el estudio comparativo de la electrooxidación del metanol sobre MPPt/Ru, MPPtRu y PtRu soportado sobre carbón comercial (E-TEK), los mejores resultados se obtuvieron con el mesoporoso de Pt modificado con Ru, probablemente por la mayor disponibilidad de los adátomos, siendo más reactivos frente a la oxidación del CO_{ad}. Además, los estudios de DEMS de estos catalizadores a 2 temperaturas (25 y 60 ºC) permitieron establecer que no hay una relación directa entre las

densidades de corriente y las eficiencias a CO_2. Así, los electrodos mesoporosos de PtRu presentaron densidades de corriente mayores que el comercial PtRu E-TEK y menores eficiencias de conversión a CO_2.

5. En el caso del MPPt/Sn la electrooxidación de CO y metanol comienza a potenciales más negativos debido a la presencia de átomos de Sn oxófilicos situados en la superficie. El Sn promueve la disociación de agua pero no adsorbe CO, y por tanto, el "*turnover*" o número de veces que un sitio activo puede ser utilizado, mejora. Como consecuencia, el mecanismo bifuncional se lleva a cabo mediante especies de óxidos de estaño capaces de generar especies oxigenadas (OH) a potenciales más bajos que el Pt. Además, el incremento en la corriente faradaica a altos potenciales respecto al resto de catalizadores, se debe a la formación de productos parcialmente oxidados, principalmente formaldehido, con el subsecuente decrecimiento de la eficiencia de conversión a CO_2.
6. Tanto en los experimentos con Pt-Ru como en los de Pt-Sn, la velocidad del proceso electrocatalítico aumenta con el incremento de la temperatura y el potencial aplicado. Por tanto, los mejores resultados se obtuvieron con el catalizador MPPt/Sn al presentar los menores potenciales de electrooxidación a 60 ºC.
7. La cinética y el mecanismo de la electrooxidación de etanol sobre MPPt fue investigado por medio de la combinación de técnicas electroquímicas con una nueva y versátil configuración de la espectrometría de masas electroquímica. Se observó que la fuerte competencia entre la desorción de hidrogeno y la adsorción de etanol a potenciales menores de 0,38 V *vs* RHE durante el primer ciclo voltamperométrico, conlleva a la formación de CH_4 y CO. A potenciales superiores a 0,60 V *vs* RHE comienza la oxidación total a CO_2 y parcial a acetaldehído y ácido acético. En el

barrido negativo de potencial se detectó la producción de metano y etano a potenciales inferiores a 0,20 V *vs* RHE.

8. El hecho de que la producción de CO_2 no se modifique con la concentración de etanol implica que se trata de un fenómeno superficial relacionado con las especies adsorbidas. Lo mismo sucede con la formación de metano y etano. Por otra parte, se demuestra que el aumento de la corriente faradaíca con la concentración de etanol está asociado a un incremento de la formación de acetaldehído y ácido acético, siendo estas reacciones la principal contribución a la densidad de corriente. Este resultado justifica que el paso determinante de la velocidad sea la formación de OH_{ad} y las bajas eficiencias de conversión a CO_2 (□ 11%) obtenidas.
9. Se estableció la influencia del espesor de la capa de Pd y el efecto electrónico del núcleo de Au en estructuras tipo núcleo-cubierta (*core-shell*) soportadas en carbón Vulcan XC-72R (Au@Pd/C), sobre la oxidación electroquímica de CO_{ad} y ácido fórmico, empleando dos catalizadores con espesor aproximado de 1 y 10 nm (CS1/C y CS10/C, respectivamente).
10. En el caso de la oxidación del CO adsorbido, se confirmó mediante técnicas espectroelectroquímicas (DEMS y espectroscopía de infrarrojo por transformada de Fourier, FTIRS *in situ*), que el potencial de comienzo de la oxidación del CO_{ad} es más positivo a medida que decrece el espesor de la capa de Pd. Los estudios de FTIRS sugieren que la electrooxidación de CO_{ad} a CO_2 tiene lugar por vías diferentes en el catalizador CS10/C y en el CS1/C. En el primer caso el proceso ocurre mediante la formación de especies OH_{ads}, mientras que en el catalizador CS1/C posiblemente sucede con la formación de especies carboxílicas $COOH_{ads}$. El análisis de los experimentos de FTIRS y la composición superficial determinada por espectroscopía fotoelectrónica de rayos X (XPS), permiten confirmar la existencia

de un efecto electrónico inducido por el núcleo de Au sobre la cubierta de Pd, que evita la retro-donación de electrones desde el Pd hacia el CO, lo que debilita la interacción Pd-CO en el catalizador CS1/C. En el caso del catalizador CS10/C, su comportamiento es parecido al de un electrodo de Pd masivo al contener un mayor número de nanocapas de Pd.

11. En relación a la oxidación del ácido fórmico, los estudios de DEMS y FTIRS confirmaron que el único producto formado en ambos catalizadores es el CO_2. De acuerdo con ello, se estimaron por DEMS eficiencias de conversión cercanas al 100 %, mientras que en los espectros de FTIRS no se presentaron bandas asociadas a la formación de CO_{ad} durante la oxidación, por lo que podría pensarse que sólo existe la vía directa de oxidación. Sin embargo, en los espectros del catalizador CS1/C se aprecia claramente la banda asociada a especies formiato $HCOO_{ad}$, lo que indica que esta especie adsorbida interviene en el proceso de electrooxidación del ácido fórmico. El hecho de que no se detecte en el catalizador CS10/C puede explicarse en base a un efecto electrónico causado por el Au sobre la superficie de Pd, que induce una adsorción más fuerte sobre el catalizador CS1/C haciendo la desprotonación del $HCOO_{ad}$ hasta CO_2 más rápida sobre el catalizador CS10/C.
12. Esos resultados han demostrado que los efectos electrónicos del núcleo sobre la superficie de la cubierta pueden ser controlados por el espesor de la capa y, en consecuencia, el mecanismo de reacción se puede modificar en la dirección deseada.

5.2 CATALIZADORES PARA OBTENER COMBUSTIBLES ALTERNATIVOS MEDIANTE PROCESOS DE ELECTROREDUCCIÓN

13. Por primera vez se logró estudiar la electroreducción de CO_2 sobre una partícula tipo núcleo-cubierta de Au-Pd mediante DEMS y determinar cómo afecta el espesor de las nanocapas de Pd a la eficiencia faradaica del proceso. Los resultados muestran que el catalizador con un espesor de 1 nm (CS1/C) presenta sobrepotenciales más bajos para la reducción de CO_2 que el catalizador con un espesor de 10 nm (CS10/C). El análisis cuantitativo de la señal de masas para la evolución de hidrógeno indica que la adsorción de hidrógeno y la evolución del mismo juega un papel fundamental en la reactividad de las nanocapas de Pd.
14. Se preparó óxido de grafeno reducido (RGO) para utilizarlo como soporte en catalizadores con aplicación en dispositivos electroquímicos. Asimismo, se sintetizaron satisfactoriamente mediante reducción con etilenglicol y posterior tratamiento térmico en atmósfera reductora, nanoestructuras de Ni y NiMo soportadas sobre RGO. La caracterización fisicoquímica confirma la formación de nanodiscos de Ni(111) de aproximadamente 20-30 nm de diámetro y de 3-5 átomos de altura, que crecen sobre el RGO, y sugiere la formación de capas de MoO_3 amorfo sobre la superficie del Ni.
15. Las técnicas electroquímicas muestran que la presencia de Mo incrementa la actividad electrocatalítica del material hacia la reacción de evolución de hidrógeno (HER), siendo los catalizadores con mayor contenido de Mo los materiales más activos. La corriente iónica registrada por DEMS permitió confirmar que la corriente faradaica de reducción obtenida corresponde a la HER diferenciándola del resto de procesos de reducción (como puede ser la reducción de óxidos) que ocurren en la misma ventana de potencial.

CONCLUSIONS

5.1 CATALYSTS FOR ALTERNATIVE FUEL ELECTROOXIDATION

1. Unsupported monolithic anodic catalysts were synthesized using the electroreduction method in the presence of a non-ionic surfactant, to be applied in micro fuel cells operating at low temperatures. In fact, Pt and PtRu unsupported mesoporous electrodes (MPPt and MPPtRu, respectively) as well as MPPt modified with Ru and Sn adatoms (MPPt/Ru and MPPt/Sn) were prepared fast and efficiently.
2. It was observed that these materials present high electroactive areas, of the same order of magnitude than supported catalysts, but can offer better performances towards methanol electrooxidation.
3. According to differential electrochemical mass spectrometry (DEMS) results, mesoporous electrodes allow the easily flow of partially oxidized products from methanol electrooxidation (e.g. formaldehyde and formic acid) avoiding their readsorption and further oxidation to CO_2.
4. Comparison of methanol electrooxidation at MPPt/Ru, MPPtRu and carbon supported PtRu alloy, has shown that the best results were obtained with the mesoporous material modified with Ru, probably because of the higher adatoms availability being more reactive towards CO_{ad} oxidation. Moreover, DEMS data have allowed establishing the conversion efficiency of these catalysts to CO_2 at two temperatures (25 and 60 ° C). It was observed that there is no direct relationship between current densities and efficiencies to CO_2. Thus, the mesoporous PtRu electrodes showed higher current densities than the commercial E-TEK PtRu material but lower CO_2 conversion efficiencies.
5. In the case of CO and methanol electrooxidation at MPPt/Sn, the onset potential

occured at more negative potentials due to the presence of Sn oxophilic atoms located on an open surface structure. Sn promotes the water dissociation but does not adsorb CO, and therefore, the turnover rate of the fuel is increased. Consequently, the bifunctional mechanism takes place by the Sn oxides which generate OH species at lower potentials than Pt. Moreover, the increase in the faradaic current at high potentials for this catalyst is related to the formation of partially oxidized intermediates, mainly formaldehyde, with the subsequent decrease in the CO_2 conversion efficiency.

6. For both Pt-Ru and Pt-Sn materials, the rate of the electrocatalytic process increased with the temperature and the applied potential. Accordingly, the best results were obtained with the MPPt/Sn catalyst as it presented the lowest electrooxidation potentials at 60 ºC.
7. A deep fundamental study devoted to establish the reaction mechanism and the kinetic for the ethanol oxidation on MPPt was performed by combining electrochemical techniques with a new electrochemical mass spectrometry set-up. Methane formation on MPPt in parallel to CO_{ad} production during the positive scan at potentials below 0.38 V is reported for the first time. This result is of paramount importance since new insights in the ethanol oxidation reaction are revealed. At potentials more positive than 0.60 V commences the complete oxidation of ethanol to CO_2 and the partial oxidation to acetaldehyde and acetic acid. During the negative potential scan, methane and ethane were detected below 0.20 V.
8. CO_2 production remains constant with ethanol concentration indicating that adsorbed species are involved in this process. The same occurs with methane and ethane production. On the other hand, it is proved that the increase in the faradaic current density with the increment of ethanol concentration is associated to the

formation of acetaldehyde and acetic acid, being these reactions the main contribution to the faradaic current density. This result justifies the low CO_2 conversion efficiencies (~11%) and that the rate-determining step is the OH_{ad} formation.

9. The influence of the Pd thickness and the Au electronic effect on the surface in core-shell structures supported on carbon (Au@Pd/C) towards the electrochemical oxidation of CO_{ad} and formic acid were established studying 1 nm and 10 nm Pd-shell catalysts (CS1/C and CS10/C, respectively).
10. In the case of CO_{ad} oxidation, DEMS and *in situ* Fourier transform infrared spectroscopy (FTIRS) studies have confirmed that the onset potential for CO_{ad} electrooxidation shifts positively as the Pd thickness decreases. Additionally, OH_{ad} was detected only in the 10 nm Pd-shell (CS10/C) catalyst, indicating a stronger water interaction which acts as the source of OH_{ads} species co-adsorbed with the CO adlayer, while the CO oxidation on the 1 nm Pd-shell (CS1/C) catalyst possibly occurs through the formation of the carboxylic species $COOH_{ads}$ as a short-life intermediate. FTIR analysis and surface composition of Pd species at CS nanostructures determined by XPS confirmed the existence of an electronic effect induced by Au on the Pd nanoshells that avoid the electro back-donation from Pd to CO and as consequence, the Pd-CO interaction in the CS1/C catalysts is weakened. In the case of the CS10 catalysts instead, it contains a larger number of Pd nanoshells and the particle tends to resemble the electronic behavior of Pd bulk.
11. Concerning the formic acid electrooxidation at these materials, DEMS and FTIRS confirmed that the sole oxidation product was the CO_2 and accordingly, conversion efficiencies around 100 % were obtained (as expected). No bands associated to CO_{ad} were observed in FTIR spectra. However, a formate signal was detected in the

infrared spectra in the case of CS1/C, suggesting again that an electronic effect caused by Au core on the Pd overlayer happens inducing a stronger adsorption of $HCOO_{ad}$ species on the catalyst with 1 nm Pd nanoshell than on the 10 nm one. In agreement, the deprotonation of $HCOO_{ad}$ on CS10/C seems to be faster than on CS1/C.

12. These results demonstrate that core electronic effects on the shell surface can be controlled by the thickness of the overlayers, and accordingly, the reaction mechanism modified in the desired direction.

5.2 CATALYSTS FOR OBTAIN ALTERNATIVE FUEL THROUGH ELECTROREDUCTION PROCESS

13. A remarkable thickness dependence of the faradaic efficiency for CO_2 electroreduction at Pd nanoshells on Au cores is reported for the first time and analized by DEMS. Results showed that CS1/C catalyst exhibits lower overpotential for CO_2 reduction than CS10/C. Quantitative DEMS analysis of the hydrogen evolution signal indicates that hydrogen adsorption and evolution play an important role in the reactivity of Pd nanoshells.
14. Reduced graphene oxide (RGO) was prepared to be used as catalyst support for electrochemical devices. Moreover, Ni and Ni_xMo_{1-x} nanodisks supported on RGO were obtained by reduction with ethylene glycol followed by a heat treatment in reductive atmosphere. Physicochemical characterization confirmed the formation of Ni(111) nanodisks of 20-30 nm dia and 3-5 nm height on the RGO and the formation of amorphous MoO_3 on the Ni surface.
15. Electrochemical techniques showed that the presence of Mo in the composite results

in an increase in the electrocatalytic activity towards the hydrogen evolution reaction (HER) when compared to pure Ni composite, being the most actives ones. the catalysts with the highest Mo content. DEMS allowed establishing that the faradaic reduction current recorded corresponds to the HER and not to other reduction process occurring in the same potential window (as oxide reduction reactions).

6. ANEXO I (Publicaciones de la Tesis)

Journal of Power Sources 196 (2011) 2979–2986

Contents lists available at ScienceDirect

Journal of Power Sources

journal homepage: www.elsevier.com/locate/jpowsour

Methanol electrooxidation at mesoporous Pt and Pt–Ru electrodes: A comparative study with carbon supported materials

Gonzalo García[a], Jonathan Florez-Montaño[a], Alberto Hernandez-Creus[a], Elena Pastor[a,*], Gabriel A. Planes[b,**]

[a] Departamento de Química Física, Instituto Universitario de Materiales y Nanotecnología, Universidad de La Laguna, Astrofísico F. Sánchez s/n, 38071 La Laguna, Tenerife, Spain
[b] Departamento de Química, Universidad Nacional de Río Cuarto, Agencia Postal 3, 5800 Río Cuarto, Argentina

ARTICLE INFO

Article history:
Received 1 August 2010
Received in revised form
27 September 2010
Accepted 7 November 2010
Available online 24 November 2010

Keywords:
Mesoporous materials
Micro fuel cells
PtRu
DEMS
Methanol electrooxidation
CO electrooxidation

ABSTRACT

The electrochemical behaviour of fuel cell catalysts (mesoporous Pt (MPPt), MPPtRu, MPPt modified by adsorbed Ru (MPPt/Ru) and carbon supported PtRu alloy) was studied using the thin layer flow cell differential electrochemical mass spectrometry (TLFC-DEMS) technique. The catalysts present high catalytic activity towards the methanol oxidation reaction (MOR), being the PtRu/C electrode the least active for MOR, while MPPt/Ru presents higher current densities for this reaction than MPPtRu. The results suggest that the diffusion properties obtained in the porous structure of the MP electrodes and the surface atomic arrangement in the electrode are the main reasons for the higher catalytic activity achieved. Finally, TLFC-DEMS was proved to be a powerful technique which evaluates and correlates the CO_2 efficiency with the catalytic activity and the porous structure of the catalysts.

1. Introduction

The employ of liquid fuel, such as methanol, as source of hydrogen offers some advantages respect to hydrogen fuel cell (PEMFC), especially on handling, storage, power density and transport [1]. These advantages allow the use of direct methanol fuel cell (DMFC) in portable electronic devices, but their performance is limited by several problems, like kinetic restraints, methanol cross-over from the anode to the cathode side through the membrane, and continuous poisoning of the catalysts due to the presence of intermediates generated in the methanol oxidation reaction (MOR) [1–3].

At present, PtRu catalysts are the most active for methanol oxidation [2]. Different electrode systems, such as electrochemical deposited Ru on Pt, bulk PtRu alloys and electrodeposited PtRu alloys, have been investigated extensively [4–9]. These studies have demonstrated that the presence of Ru on the electrode surface catalyses the oxidation of CO species, and consequently, enhances the electrocatalytic activity for methanol oxidation and other fuels.

Recently, the appearance of a new series of nanostructured metallic catalysts developed by soft templating has originated an attractive alternative to the traditional methods to obtain mesoporous (MP) electrodes. In this way, combining the soft template technique with electrochemistry is possible to obtain catalysts with high performance at the anodes and cathodes of fuel cells. These electrodes are especially interesting because they include in situ construction capabilities and accurate tailoring of the final porous structures [10,11]. In fact, during the last years the use of these MP materials as electrodes for methanol electrooxidation has been tested successfully [12–14].

On the other hand, Pt surface has been broadly modified by spontaneous deposition of metal adatoms (Pt/M) of diverse nature [15]. It was reported that Ru adatoms improve twice the catalytic activity against conventional PtRu alloys [16] during methanol electrooxidation. At the present, the catalytic activity of the catalysts has been attributed mainly to facts related to the chemical nature of the surface, such as improved water activation, appropriated crystallographic planes on metal surface, or parallel pathways [12,14,17,18].

Based on data provided by DEMS analysis, a new concept in the reaction mechanism of fuel cell catalysts was first proposed by Wang et al. [19,20] and later explored by Jusys et al. [21]. In this model, the fuel cell electrode can be considered as formed by a highly dispersed catalyst into a porous matrix, each active site may undergo to a particular condition for the access to reactants and products and sub-products release. Recently, we have studied the

---

* Corresponding author. Tel.: +34 922 319071; fax: +34 922 318002.
** Corresponding author: Tel.: +54 358 4676111; fax: +54 358 4676233.
E-mail addresses: epastor@ull.es (E. Pastor), gplanes@exa.unrc.edu.ar (G.A. Planes).

0378-7753/$ – see front matter © 2010 Elsevier B.V. All rights reserved.
doi:10.1016/j.jpowsour.2010.11.085

methanol oxidation on mesoporous Pt (MPPt) by thin layer flow cell differential electrochemical mass spectrometry (TLFC-DEMS) [14]. It was concluded that, under restricted diffusion of the soluble products (i.e. formic acid and formaldehyde), as occurs in real carbon supported catalysts, these products can readsorb and interact again with the catalytic surface, increasing the CO_2 efficiency. However, the current density diminishes.

In the present work we extend our previous analysis to more diverse systems in order to know the factors (i.e. geometry, chemical nature of the catalytic surface and support effect) that influence the observed electrode behaviour. In this way, diverse catalysts were studied, such as mesoporous electrodeposited Pt (MPPt), MPPt modified by adsorbed Ru (MPPt/Ru), MP coelectrodeposited Pt and Ru (MPPtRu) and carbon supported PtRu alloy (PtRu/C, 20 wt.% E-TEK). All of them were analysed towards CO and MOR by TLFC-DEMS at different temperatures. By means of quantitative DEMS analysis, the relationship between CO_2 yield and current density for all catalysts was evaluated. Additionally, the influence of the temperature, roughness factor, electrode materials and diffusion conditions for methanol oxidation was established.

2. Experimental

2.1. Electrode preparation

Mesoporous Pt electrodes were obtained by electrochemical reduction of a mixture of aqueous hexachloroplatinic acid (8%) and octaethyleneglycol monohexadecyl ether ($C_{16}EO_8$) (50% weight fraction) onto a DEMS Au disk electrode (φ = 7 mm) at 60 °C and 0.15 V. Typically, after 10 min of Pt^{4+} reduction, a charge of 749 mC cm^{-2} was passed during the deposition onto a Au substrate, resulting in a mesoporous Pt layer containing 1.04×10^{-4} g of Pt (assuming 75% efficiency). Then, the electrode was left in distilled water for 48 h, to let the surfactant be completely removed from porous structure. For MPPtRu electrodeposition, the aqueous fraction was composed of hexachloroplatinic acid (8%) and $RuCl_3$ in 1/1 metal ratio.

The surface modification by Ru adatoms was obtained in the following way: a MPPt electrode was immersed in 2 mM $RuCl_3$ + 0.1 M $HClO_4$ aged solution for 30 min with the purpose to facilitate the Ru dispersion inside the porous structure. After that, the electrode was rinsed with water, and finally transferred to an electrochemical cell containing 1 M $HClO_4$ (H_2SO_4 solution can not be used during this step due to interferences produced by sulphate co-adsorption). Finally, the electrode was cycled between 0.05 and 0.50 V to reduce the adsorbed Ru precursor to metallic Ru. The whole procedure was repeated three times.

In the studies of the carbon supported PtRu/C catalyst, the working electrode consists of a certain amount of the PtRu/C powder (20 wt.% metal supported on Vulcan XC-72, ETEK) deposited as a thin layer over a glassy carbon disc (ϕ = 7 mm). For this purpose, an aqueous suspension of 4.0 mg ml^{-1} of the PtRu/C catalyst was prepared by ultrasonically dispersing it in 15 μl of Nafion (5 wt.% Aldrich) and pure water. An aliquot (20 μl) of the dispersed suspension was pipetted onto the glassy carbon surface and dried at ambient temperature under Ar atmosphere.

2.2. Physicochemical characterization

X-ray diffraction (XRD) patterns of the electrocatalysts were obtained using a universal diffractometer Carl Zeiss-Jena, URD-6, equipped with a Cu Kα radiation (λ = 0.15406 nm) generated at 45 kV and 40 mA. The real content of Pt and Pt–Ru in the electrocatalysts and the Pt to Ru ratio were determined by energy dispersive X-ray (EDX) technique coupled to a scanning electron microscopy Jeol JEMMod. 1010 with a silicon detector with Bewindowand applying 20 keV, while a scanning tunneling microscope (STM) from Nanoscope IIE, Digital Instrument was used to achieve surface images of the catalysts.

2.3. Electrochemical measurements

A high surface area carbon rod was used as a counter electrode and a reversible hydrogen electrode (RHE) in the supporting electrolyte was employed as reference electrode. All potentials in the text are referred to this electrode. Electrochemical measurements were performed with a computer-controlled HEKA potentiostat–galvanostat (PG 310). All experiments were carried out in a thermostatized electrochemical flow cell using a three-electrode configuration. The cell allows the exchange of the solution holding the potential control on the working electrode. Argon (N50) was used to deoxygenate all solutions and CO (N47) was employed for the adsorption experiences. Sulphuric acid and methanol (Merck, p.a.) were used for the preparation of the base electrolyte solution (1 M H_2SO_4) and methanol solution (1 M) in the base electrolyte.

In this work, currents are expressed as current densities J (A cm^{-2}), calculated from the measured current I (A) and the real electroactive area S (cm^2). S was estimated from the CO stripping from the relation $S = Q^{CO_2}/(n \times 210)$, where Q^{CO_2} is the charge obtained from the integration of the current recorded in the cyclic voltammogram for the stripping of CO_{ad} formed at $E_{ad} = 0.07$ V; n is the electrons exchanged in the oxidation reaction of CO to CO_2 ($n = 2$) and 210 μC cm^{-2} is the charge involved in a one electron per surface Pt atom reaction (linear configuration of adsorbed CO and full coverage are assumed).

2.4. TLFC-DEMS setup

This cell design permits the use of electrodes prepared by different methods under flow conditions (flow rate in the present communication: 0.4 ml min^{-1}). In addition, gaseous species produced on the electroactive surface can be followed on-line by mass spectrometry. Volatile species generated at the electrode evaporate at the pores of the membrane into the vacuum and are detected by the mass spectrometer with a time constant of ca. 1 s. This time constant is small enough to allow mass spectrometric cyclic voltammograms (MSCVs) for selected mass-to-charge ratios (m/z) to be recorded in parallel to cyclic voltammograms (CVs) at a scan rate of 0.02 V s^{-1}. A more detailed picture of the cell design is described in a previous communication [14].

2.5. TLFC-DEMS calibration

The calculation of the efficiency for methanol conversion to CO_2 by DEMS requires a previous determination of the m/z = 44 calibration constant (K^{CO_2}). This constant correlates the number of CO_2 molecules generated on the electrode surface (through the faradaic charge) with the portion of this molecules captured by the mass spectrometer (proportional to m/z = 44 ion current). K^{CO_2} has to be determined before each experiment because it depends of several variables (membrane–electrode gap, flow rate, temperature and pressure in the mass vacuum line) and it has to be fixed during the experience.

The calibration constant is calculated as follow: faradaic ($Q_f^{CO_2}$) and ionic m/z = 44 ($Q_i^{CO_2}$) charges were calculated from CO stripping and related according to equation:

$$K^{CO_2} = \left[2 \frac{Q_i^{CO_2}}{Q_f^{CO_2}} \right] \tag{1}$$

Then, the current efficiency E for methanol electrooxidation to CO_2 is determined from the subsequent equation:

$$E^{CO_2} = \frac{6Q_i^{CO_2}}{K^{CO_2}Q_f^T} \qquad (2)$$

where Q_f^T is the charge associated to all faradaic processes occurring at the surface during methanol electroxidation (obtained from the cyclic voltammogram) and $Q_f^{CO_2}$ is the charge associated to the m/z = 44 signal recorded during the MOR.

3. Results

3.1. Mesoporous Pt production and characterization

The insert of Fig. 1 shows the current transient corresponding to the Pt salt reduction onto a Au electrode. Following an initial sharp peak due to the high Pt^{4+} abundances close to the electrode surface, a continuous decrease in the current was observed. A constant response was verified after a few seconds, in the mass transfer controlled region (see the double insert including the Cottrell representation).

Several potential cycles (not shown) between 0.05 and 0.90 V in acid media were required to clean the surface from residual adsorbed surfactant molecules. After that, the cyclic voltammograms for a MPPt electrode recorded at 0.20 V s^{-1} in 1 M H_2SO_4 (Fig. 1) shows neither residual current due to impurities nor diffusion complications.

At the macroscopic level, the surface looks as a smooth and shining metallic Pt layer. However, in the nanoscopic scale, the appearance is related to the quantity of catalyst deposited. At the initial stage, a uniform layer of metal characterized by small grooves produced by the liquid crystal patterning (Fig. 2A) is visible. Finally, metallic spheroids [22] are produced once the process begins to be controlled by diffusion (Fig. 2B). Note that the small metal clusters present in Fig. 2B are the initial stage for bigger nanospheres, visible at the image background.

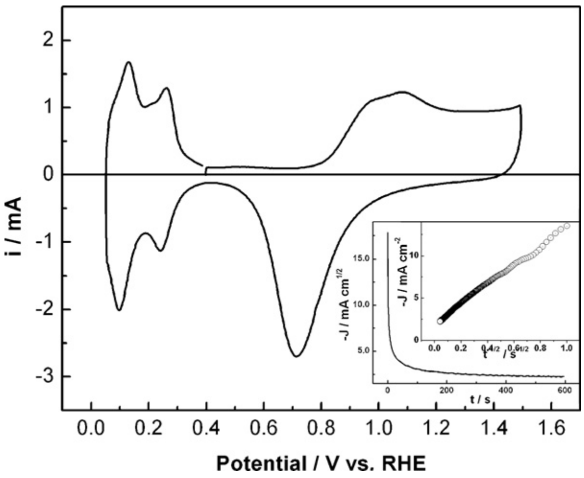

Fig. 1. Principal: Cyclic voltammogram for a MPPt electrode in 1 M H_2SO_4 at 0.2 V s^{-1}. Insert*:* Current transient during Pt deposition at 0.15 V_{RHE}. Double insert*:* Cottrell representation for the current recorded during Pt reduction at 60 °C.

The EDX analysis carried out over MPPt/Ru and MPPtRu samples shown compositions of 5% and 40% of Ru, respectively. However, it must be considered that the EDX sampling extends a few micro metre inside metal structure, where Ru is not present in the case of MPPt/Ru electrodes. This induces a sub-estimation of the Ru adatoms present at the surface of MPPt/Ru.

Fig. 3 shows the XRD patterns of the gold substrate as well as MPPt/Ru and MPPtRu electrocatalysts supported on gold. All the the sample show the typical peaks of the fcc structure of Pt (i.e. the planes (1 1 1), (2 0 0), (2 2 0), (3 1 1) and (2 2 2)) and those related to the gold substrate. These five peaks in the MPPtRu diffractogram are

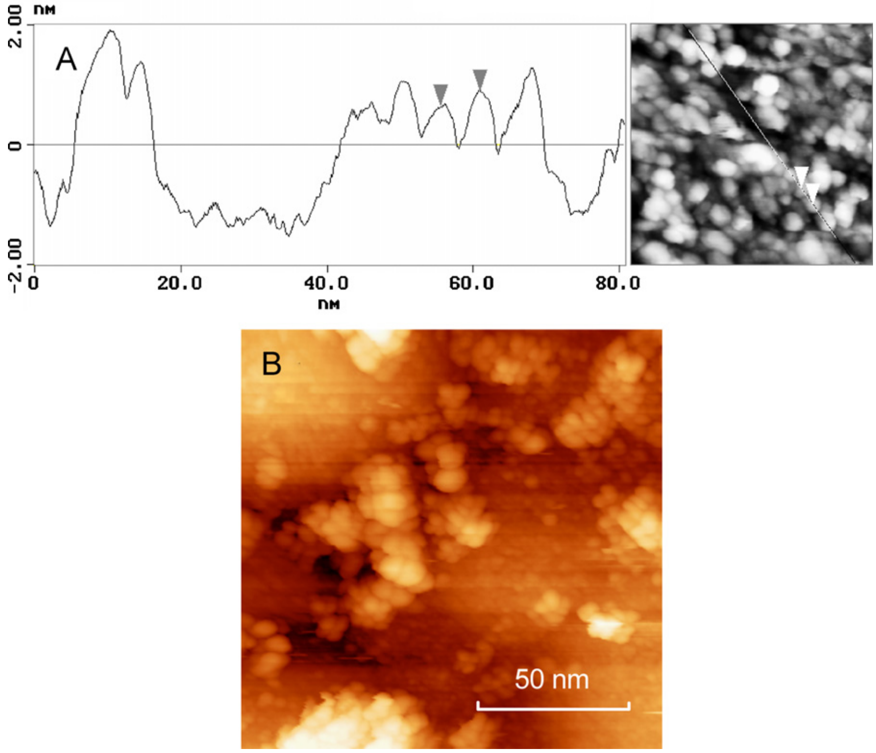

Fig. 2. (A) STM image (right) and the corresponding cross section analysis (left) at the initial stage of MPPtRu electrodeposition. (B) STM image of electrodeposited MPPt at the end of deposition (750 mC cm^{-2}). Nanoscope IIE, Digital Instrument.

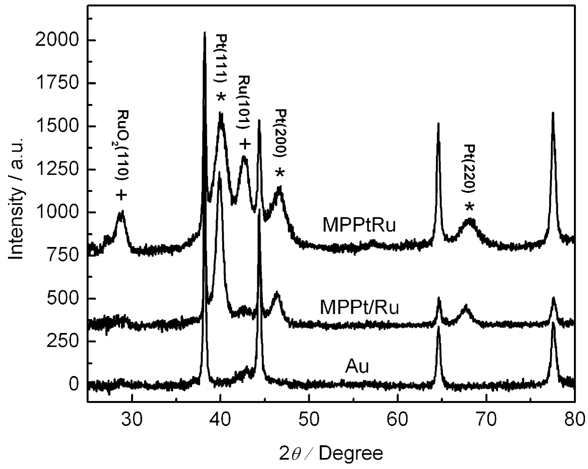

Fig. 3. XRD patterns of MPPt/Ru, MPPtRu and Au substrate samples. Main diffraction peaks related to Ru (+) and Pt (*) crystalline structure.

slightly shifted to higher angles with respect to the corresponding peaks in MPPt spectrum (not shown), indicating a small contraction of the lattice and possible alloy formation. Nevertheless, the MPPtRu electrode develops a large peak at ca. 42.7° related to the hexagonal structure of metallic Ru, while for the MPPt/Ru catalyst the same but smaller signal can be perceived. In addition, the MPPtRu material develops peaks at ca. 28° and 57° related to Ru oxides. Therefore, a metallic alloy formation is unlikely for MPPt/Ru due to the presence of pure metallic Ru and its oxides, but it cannot completely ruled out for MPPtRu.

3.2. CO electrooxidation

CO stripping experiments were performed in order to characterize the catalyst surface. The oxidation of a CO_{ad} monolayer gives useful information about the catalytic activity of the electrode and offers a safety way to estimate the final electroactive area before and after the surface modification with metallic adatoms (i.e. Ru).

Fig. 4 compares the stripping voltammetry observed for a CO saturated electrode for the three different catalysts (MPPtRu, MPPt/Ru and PtRu/C) at two temperatures (25 °C and 60 °C) at a scan rate of 20 mV s^{-1}. CO stripping voltammograms were obtained after bubbling CO through the cell for 10 min while keeping the electrode in the bulk of the solution at 0.07 V, followed by argon purging for 20 min to remove the excess of CO.

The CO stripping voltammograms depicted in the upper panel (Fig. 4A) were recorded with the MPPt/Ru surface. The modification of the MPPt surface with Ru atoms involved three exposition time of the electrode in the Ru solution followed by a stabilization procedure. After this procedure, the CO oxidation peak position shifts from 0.75 V_{RHE} at the MPPt electrode [14,23] to 0.56 V_{RHE} at the MPPt/Ru catalyst at 25 °C. A further exposition to Ru solution results in a displacement of the CO oxidation peak towards more positive potentials (not shown). A great shift to more negative potentials of the onset as well as the peak potential for the CO oxidation is observed with the increase of the temperature. In fact, the peak potential shifts from 0.55 V at 25 °C to 0.41 V at 60 °C, while the onset moves from 0.37 V at 25 °C to 0.23 V at 60 °C. Also, it is important to note the asymmetry of the peaks: they present a fast current increase followed by long current tail.

Fig. 4B shows the CO electrooxidation on the MPPtRu catalyst at two different temperatures. The peak potential decreases from 0.53 V at 25 °C to 0.43 V at 60 °C, while the onset moves from 0.36 V at 25 °C to 0.28 V at 60 °C. Interestingly, in this case the CO oxidation reaction presents a very symmetric peak at both temperatures.

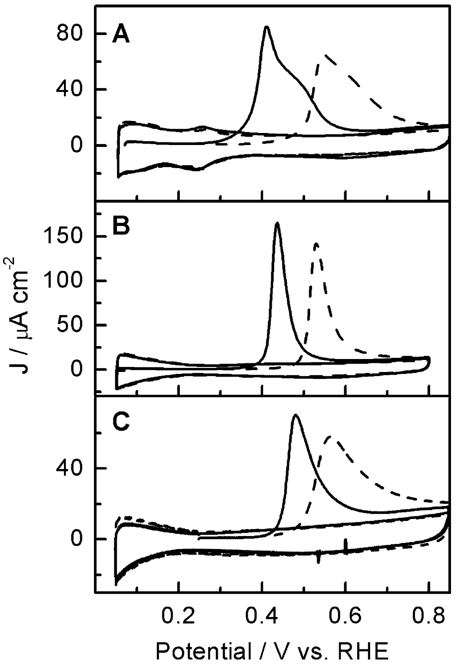

Fig. 4. CO stripping on MPPt/Ru (A), MPPtRu (B) and PtRu/C (C) electrodes. ν = 0.02 V s^{-1}, 1 M H_2SO_4, 25 °C (- - - -) and 60 °C (—).

The lower panel of Fig. 4 displays the stripping voltammograms recorded with the commercial catalyst (PtRu/C) at the selected temperatures. The peak potential at 25 and 60 °C are located at 0.56 V_{RHE} and 0.48 V_{RHE} respectively; while no substantial dependence of the onset for the CO oxidation (~0.4 V_{RHE}) with temperature was observed for this catalyst. In addition, the shape of the CO oxidation peak turns to be more symmetric while the temperature increases.

In order to obtain more detailed information on the symmetry of the CO oxidation peak on the Pt catalysts, similar experiments were performed using perchloric acid. Fig. 5 compares CO stripping curves of MPPt/Ru recorded in 0.1 M $HClO_4$ with MPPt/Ru and MPPtRu in 0.1 M H_2SO_4 at 25 °C. It is remarkable the similarity of the CO stripping voltammograms for MPPt/Ru in 0.1 M $HClO_4$ and MPPtRu in 0.1 M H_2SO_4. The CO stripping voltammogram recorded with the catalyst modified with Ru on the surface presents a symmetric CO oxidation peak in perchloric acid (solid line) contrasting with the behaviour in sulphuric acid (dotted line). It is well known that sulphate adsorbs strongly on Pt surface [24], so the observed current tail in sulphuric acid has to be attributed to sulphate adsorption on the catalyst surface, which difficult the CO diffusion towards the most catalytic site. Interestingly, the MPPtRu catalyst (dashed line) seems to be not affected by sulphate species, pointing out the different surface structure obtained with diverse methodology (i.e. Ru adsorption and Ru co-deposition), which may affect any surface reaction. In fact, it is well know that metal oxides on the surface inhibit the adsorption of sulphate species [25] and it was proved by the XRD analysis that the MPPtRu electrode contains large amounts of Ru oxides.

3.3. Methanol electrooxidation

The electrode activity towards methanol electrooxidation was evaluated by cyclic voltammetry in 1 M CH_3OH + 1 M H_2SO_4 solution at 25 and 60 °C. The CVs (solid line) and the corresponding mass signals for CO_2 (m/z = 44) and formic acid (followed through methylformate formation, m/z = 60) during methanol electrooxidation at 25 °C can be seen in Fig. 6 for all MP electrodes. Also, it is

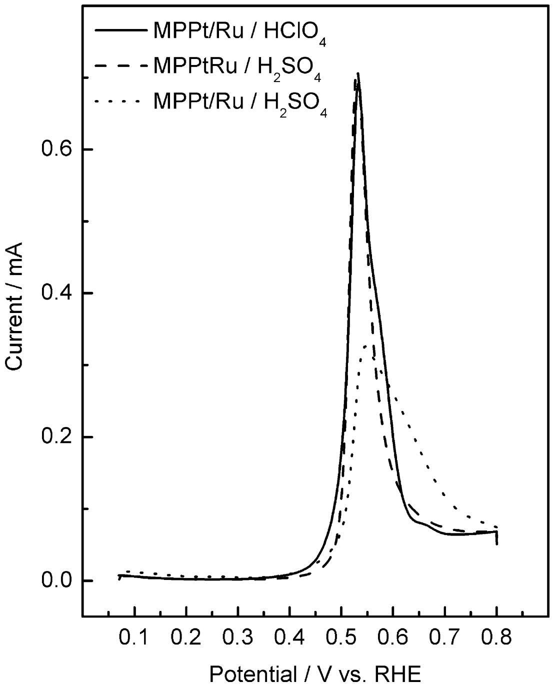

Fig. 5. CO stripping on MPPt/Ru (—) in 0.1 M $HClO_4$ and MPPt/Ru (. . .) and MPPtRu (– – – –) in 0.1 M H_2SO_4. $\nu = 0.02\,V\,s^{-1}$, 25 °C.

included the faradic current expected for 100% efficient conversion of methanol to CO_2 calculated from the m/z = 44 signals after the calibration procedure (dashed line). The difference in area between experimental (solid curve) and theoretical (dashed curve) currents is the extra charge associated with the formation of different products than CO_2 (formic acid can be indirectly detected by DEMS, but not formaldehyde). The presence of formic acid and its dependence with the applied potential can be visualized in the lower panel of Fig. 6.

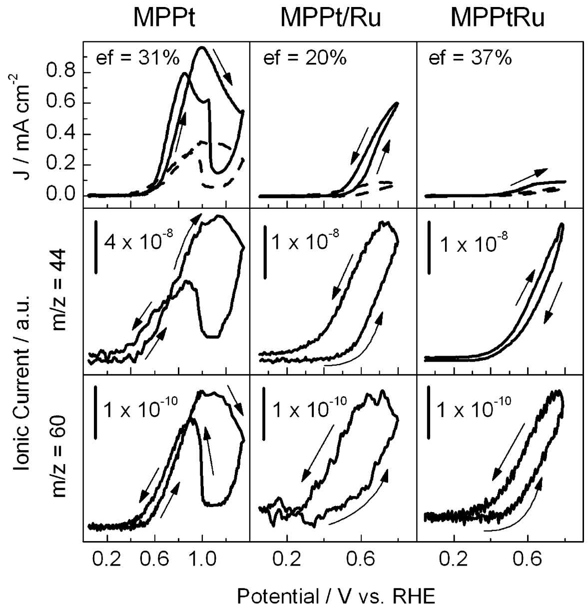

Fig. 6. CVs and MSCVs for CO_2 (m/z = 44) and HCO_2H (m/z = 60) formed during methanol electrooxidation on MPPt (left), MPPt/Ru (center) and MPPtRu (right). Faradaic current (—) and current calculated from CO_2 signal (m/z = 44) (– – – –). $\nu = 0.02\,V\,s^{-1}$, 1 M CH_3OH + 1 M H_2SO_4. T = 25 °C.

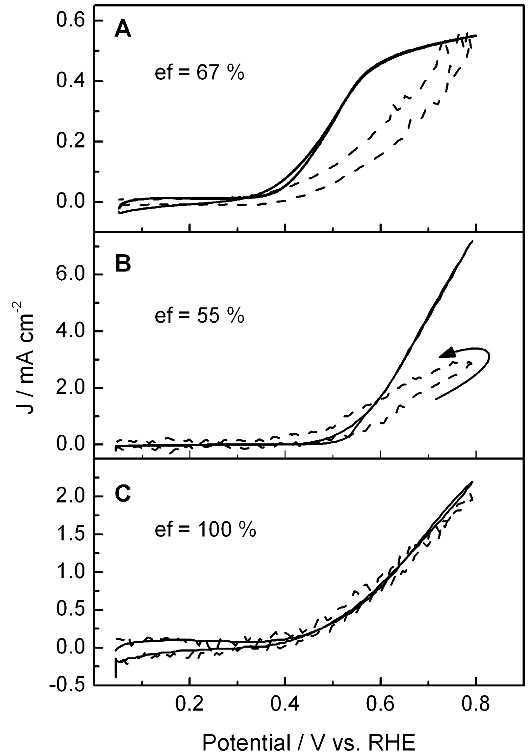

Fig. 7. CVs for (A) MPPtRu, (B) MPPt/Ru and (C) PtRu/C E-TEK. Faradaic current (—) and current calculated from CO_2 signal (m/z = 44) (– – – –). $\nu = 0.02\,V\,s^{-1}$, 1 M CH_3OH + 1 M H_2SO_4. T = 60 °C.

The same analysis has been carried out at 60 °C. Fig. 7 shows the CVs in 1 M CH_3OH + 1 M H_2SO_4 solution at 60 °C (solid line) and the faradic current expected for 100% efficient conversion of methanol to CO_2 calculated from the m/z = 44 signals (dashed line), for the MPPtRu and MPPt/Ru electrodes and the carbon supported PtRu (E-TEK) catalyst. The signals for the ionic masses are omitted for clarity.

A more reliable way to test the catalysts aptness for fuel cell applications involves chronoamperometric measurement of surface activity ($A\,cm^{-2}$) for methanol oxidation. The response of each electrode to a potential step from 0.05 V (a potential where methanol adsorption and oxidation are negligible) to 0.55 V (a potential similar to that achieved during operation conditions in a fuel cell) can be observed in Fig. 8. Commercial carbon supported PtRu catalyst was also tested for the sake of comparison.

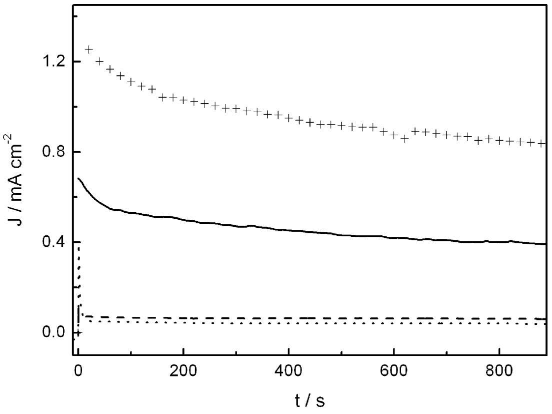

Fig. 8. Current transients for methanol electrooxidation on MPPt (. . .), MPPt/Ru (+++), MPPtRu (—) and PtRu/C E-TEK (– – – –) at 0.55 V_{RHE}. 1 M CH_3OH/1 M H_2SO_4. T = 60 °C.

4. Discussion

Fig. 4 shows the CO stripping experiences for each catalyst. The MPPt/Ru catalyst presents the best behaviour towards CO oxidation, with the lowest onset for CO oxidation at 0.23 V_{RHE} at 60 °C. This value is clearly more negative than the observed for the other catalysts at the same temperature. This material presents a noticeable shift in the peak potential for CO oxidation as result of Ru oxides formation at $E > 0.20\,V_{RHE}$. Consequently, the peak potential for CO_{ad} oxidation shifts to more negatives values for the Ru modified surface. Note that the onset for CO oxidation at MPPt/Ru electrodes at 25 °C occurs roughly at the same potential that the pre-peak observed during the CO oxidation at MPPt surface [14,23]. In addition, this electrode also shows an accentuated dependence of the onset for the CO oxidation reaction with the temperature, as well a marked broadening of the CO stripping peak after Ru deposition which was related to sulphate adsorption. The later is supported by previous investigations, in which similar electrochemical behaviour was observed with different Ru coverages (obtained by spontaneous deposition) on nanoparticles and smooth Pt [15,16]. However, for the extremely concave and irregular surface of MPPt (pore diameter ~3 nm) it is more difficult to extrapolate results. Due to the mesoporous morphology and small pore size, an accurate characterization of the Ru-modified MPPt will require a significant effort, and it will be the subject of further works.

On the other hand, the electrodeposition process used for MPPtRu synthesis seems to outcome in a more homogeneous metallic composition (bulk and surface), but with high Ru oxides coverage. Also, this surface presents an unique almost symmetric oxidation peak during CO stripping, which is characteristic of a fast CO diffusion on the surface towards the most active site. It is remarkable that the morphology of the MPPt/Ru and MPPtRu electrodes is similar but their metallic composition and atomic arrangement in the surface are totally different. Consequently, the catalytic activity towards the CO oxidation seems to be similar when the experiment is carried out in perchloric acid, but totally different when the effect of anion co-adsorption (i.e. sulphate species) is present. Once more, the difference during the CO oxidation in sulphuric acid between both Ru-based catalysts may be addressed principally to the presence of Ru oxides species on the MPPt/Ru surface.

In agreement with the literature [26,27], the CO stripping voltammogram recorded at carbon supported PtRu catalyst at 25 °C (Fig. 4C) presents a wide oxidation peak at 0.56 V_{RHE} with an onset located at ca. 0.38 V_{RHE}, in which its position is independent with the temperature.

In all cases, an increase of temperature result in a clear peak shift to more negative values, demonstrating an improved condition for CO elimination from the catalyst surface.

Fig. 6 compares the MOR for each electrode at 25 °C. It is evident that Ru modifies the electrode behaviour at $E < 0.6\,V_{RHE}$, where Pt–OH abundance at the surface is extremely low. The influence of the foreign metal (i.e. Ru) extends up to 0.7 V_{RHE}, where Ru-based catalysts show a near two-folded current density. At higher overpotenitials ($E > 0.75\,V_{RHE}$), the differences in catalytic activities descend due to the contribution of Pt–OH species to the bifunctional mechanism [8,28–30].

The CO_2 conversion efficiency (as average for a forward–backward scan) is in all cases lower than 40%, in agree with previous reported TLFC analysis for mesoporous catalysts [14]. The complete electrooxidation of methanol involves six electrons and gives CO_2 as final product. However, the low methanol conversion to CO_2 observed here involves the production of appreciable quantities of other reaction intermediates, such as formaldehyde and formic acid (Fig. 6C), which are formed in some fraction in the catalysts surface as consequence of partial alcohol oxidation (two and four electrons respectively).

The effect of increase the temperature reaction up to 60 °C (Fig. 7), results in a noticeable change of methanol conversion to CO_2 for all MP electrodes, reaching to 67% for the MPPtRu and 55% for the MPPt/Ru catalysts. Note, however, that CO_2 conversion for MP electrodes is far lower than verified for PtRu/C catalyst (100%). Additionally, PtRu/C shows the lowest surface activity (0.05 mA cm^{-2}) when it is compared with MPPtRu (0.38 mA cm^{-2}) and MPPt/Ru (0.42 mA cm^{-2}) at 0.55 V_{RHE}.

Fig. 8 shows the transients for methanol electrooxidation on all the catalysts at 0.55 V_{RHE}. It is remarkable that, considering the value of the stationary current, the catalytic activity for methanol oxidation at MPPt/Ru (0.82 mA cm^{-2}) is more than twice higher than the observed at MPPtRu catalyst (0.38 mA cm^{-2}). A two folded relationship in current density was reported by Waszczuk et al. [16] using nanoparticles as catalysts. They compared Pt nanoparticles decorated with ruthenium, and 1:1 PtRu alloy nanoparticles. We believe that the additional improvement observed in the present work could be related to the existence of especially active Ru surface states originated during Ru island formation [15] over an extremely curved surface, as was discussed above for the CO stripping, i.e. the morphology structure is similar in our MP electrodes but the distribution of the Ru atoms at the surface is different, which provides diverse properties such as stronger sulphate species adsorption and higher catalytic activity towards the MOR. Moreover, the difference in catalytic activity towards the methanol oxidation reaction may be related not only to Ru atomic distribution on the surface but also to the surface chemistry that is different for both Ru-based catalysts. It is well known that the presence of Pt and Ru oxides on the surface does not favour the dehydrogenation step[2].

In a general terms, the current density for MPPtRu (0.38 mA cm^{-2}) is in reasonable agree with that reported in ref [14] (~0.3 mA cm^{-2}), in particular considering that the synthesis parameters employed here, such as salts concentration, temperature and applied potential, are quite different. In the present work, the MP catalysts deposition occurs at higher overpotentials in the presence of low metal salt concentration. This combination produces high porosity and irregular surface (Fig. 2B). The latter is a relevant factor, because it generates a novel catalyst with a combined porous structure. The large gaps between the mesoporous Pt spheroids operate interconnecting all the MP structure, which turns into appropriates channels for mass transport inside the monolithic electrode. Even more, these gaps offers a suitable link between the inner and external surface.

However, the real dimension of the catalytic enhancement becomes clear when MPPt/Ru catalyst is compared with the carbon supported PtRu catalyst. The difference in the catalytic activity towards the methanol oxidation is more than one order of magnitude, being 0.82 mA cm^{-2} and 63 μA cm^{-2} for MPPt/Ru and PtRu/C, respectively (Fig. 8).

In order to check the proposed effect described in our previous report [14], in which the diffusion conditions are related to the catalytic activity, special care is necessary to prevent dissimilarity on catalysts load, especially for PtRu/C. For this reason a similar electroactive area and roughness factor are required for all catalysts, though the carbon supported catalyst seems to undergo restricted mass transport. In this context, the DEMS analyses depicted in the Figs. 6 and 7 support this idea, in which a real dependence between CO_2 production and electrode morphology is observed, being the diffusion of the intermediates (i.e. formic acid and formaldehyde) on the electrode surface the principal responsible for this fact. Moreover, this conclusion is supported by the

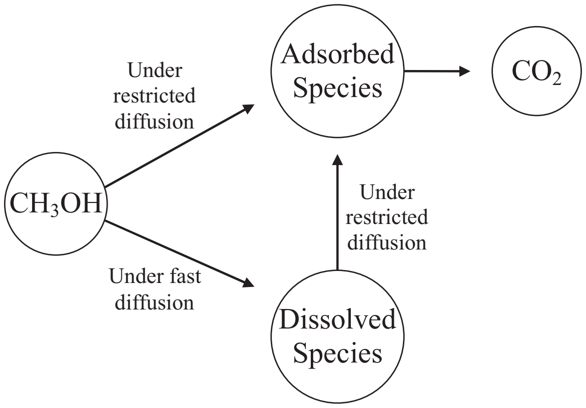

Scheme 1. Mechanism for methanol electrooxidation on mesoporous electrodes.

ratio between higher current densities with lower CO_2 conversion efficiency. It is clearly observable that MP catalysts develop higher current densities and lower efficiency for methanol conversion to CO_2 (~60%) than carbon supported Pt [14] and PtRu electrodes (~100%), in good agreement with our previous results [14]. Jusys et al. [21] found a similar effect on products distribution, keeping inalterable the inert porous matrix but offering more adsorption possibilities by increasing the metal load for carbon supported catalysts.

Scheme 1 depicts the proposed model for methanol electrooxidation. The production of CO_2 (and therefore the CO_2 efficiency) is related to the formation of adsorbed CO or other adsorbed species not detailed. Thus, an increase in CO_2 efficiency has to be accompanied by consumption of adsorbed intermediates (i.e. adsorbed CO). Then, under restricted diffusion, the soluble by-products (i.e. formaldehyde and formic acid) can interact again with the surface and readsorb. As a consequence, the amount of adsorbed CO increases during the complete oxidation process, and accordingly, the CO_2 efficiency. However, the current density diminishes.

Moreover, the restricted diffusion emphasizes the competitive effects for reactions sites onto inner porous surface between methanol molecules and partially oxidized by-products. Finally, it is observed that electrodes with restricted diffusion increase the relative quantities of formic acid and formaldehyde due to the difficulty of these molecules to leave out of the porous structure, obstructing in this way the free pore-replenishment by methanol.

5. Conclusions

Complete procedures to obtain MPPtRu and MPPt/Ru catalysts were developed. The electrodes obtained in this way have shown to be highly efficient for methanol oxidation. The least active catalyst for methanol oxidation is the PtRu/C electrode, while the unsupported MPPt/Ru catalyst is more active than the MPPtRu one.

It was observed that an electrode properly structured and modified, such as a monolithic catalyst electrode, can offers better performance towards methanol electrooxidation than a traditional carbon supported catalysts which have higher specific areas.

Results can be understood taking into account the especially accessible porous structure of mesoporous electrodes produced by electrochemical reduction under mass transfer controlled regimen. In the resulting structure, the possibility of readsorption of partially oxidized products is low. As a consequence, the surface coverage by adsorbed CO decreases and the turnover frequency increases during methanol oxidation. The high current developed at mesoporous catalysts during the methanol oxidation is originated in a first stage by a fast CO elimination due principally by the second metal (i.e. Ru) which provides sites that promotes the OH formation at more negative potentials than Pt. After that, the reaction is mainly enhanced by the existence of alternative paths for methanol electrooxidation to formic acid and formaldehyde, which do not involves the formation of adsorbed CO. In addition, it was observed a better performance for the MPPt/Ru than the MPPtRu towards the methanol oxidation, which was suggested to be due to a surface factor: absence of Ru oxides and a better surface atomic arrangement on the MPPt/Ru surface.

TLFC-DEMS has demonstrated to be an appropriate technique for the determination of reaction products during methanol electrooxidation at MP and carbon supported catalysts. With the aid of DEMS calibration, it is possible to evaluate the efficiency for CO_2 conversion and correlate it with the porous characteristics of the catalyst.

The results obtained in the present work support the idea that the porous architecture is an important factor for the observed electrode behaviour. This factor is crucial and has a relative importance comparable to the chemical nature of the surface. Due to the high porosity of real fuel cell electrodes, results in the present paper can be of importance for the application of the developed materials in this type of systems. Consequently, further works in the field are necessary.

Catalysts easily produced as MPPtRu and MPPt/Ru electrodes have good possibilities to be used in special applications (i.e. micro fuel cells), where high catalysts surface load and scale factors make the in situ construction an essential issue [31].

Acknowledgments

Authors thank the MICINN for financial support (project MAT2008-06631-C03-02) and the AECID for sustaining the cooperation between both universities (PCI A/025292/09). J.F. acknowledges ACIISI (Gobierno de Canarias) for the predoctoral fellowship.

References

[1] X. Ren, P. Zelenay, S. Thomas, J. Davey, S. Gottesfeld, J. Power Sources 86 (2000) 111.
[2] A.S. Aricò, S. Srinivasan, V. Antonucci, Fuel Cells 1 (2001) 133.
[3] B. Gurau, E.S. Smotkin, J. Power Sources 112 (2002) 3339.
[4] G. García, J.A. Silva-Chong, O. Guillén-Villafuerte, J.L. Rodríguez, E.R. González, E. Pastor, Catal. Today 116 (2006) 415.
[5] G. García, V. Baglio, A. Stassi, E. Pastor, V. Antonucci, A.S. Aricò, J. Solid State Electrochem. 11 (2007) 1229.
[6] C.E. Lee, S.H. Bergens, J. Phys. Chem. B 102 (1998) 193.
[7] W.F. Lin, M.S. Zei, M. Eiswirth, G. Erh, T. Iwasita, W. Vielstich, J. Phys. Chem. 103 (1999) 6968.
[8] H.A. Gasteiger, N. Markovic, P.N. Ross Jr., E. Cairns, J. Phys. Chem. 98 (1994) 617.
[9] Z. Jusys, H. Massong, H. Baltruschat, J. Electrochem. Soc. 146 (1999) 1093.
[10] G.S. Attard, P.N. Bartlett, N.R.B. Coleman, J.M. Elliot, J.R. Owen, J.H. Wang, Science 278 (1997) 838.
[11] J.M. Elliot, G.S. Attard, P.N. Bartlett, N.R.B. Coleman, P.A.S. Merckel, J.R. Owen, Chem. Mater. 11 (1999) 3602.
[12] J. Jiang, A. Kucernak, J. Electroanal. Chem. 533 (2002) 153.
[13] J. Jiang, A. Kucernak, Chem. Eng. J 93 (2003) 81.
[14] G.A. Planes, G. García, E. Pastor, Electrochem. Commun. 9 (2007) 839.
[15] A. Crown, C. Johnston, A. Wieckowski, Surf. Sci. 506 (2002) L268.
[16] P. Waszczuk, J. Solla-Gullón, H.S. Kim, Y.Y. Tong, V. Montiel, A. Aldaz, A. Wieckowski, J. Catal. 203 (2001) 1.
[17] A. Rodes, J. Clavilier, J.M. Orts, J.M. Feliu, A. Aldaz, J. Electroanal. Chem. 338 (1–2) (1992) 317.
[18] M.T.M. Koper, J. Electroanal. Chem. 574 (2) (2005) 375.
[19] H. Wang, C. Wingender, H. Baltruschat, M. Lopez, M.T. Reetz, J. Electroanal. Chem. 509 (2001) 163.
[20] H. Wang, T. Loffler, H. Baltruschat, J. Appl. Electrochem. 31 (7) (2001) 759.
[21] Z. Jusys, J. Kaiser, R.J. Behm, Langmuir 19 (2003) 6759.
[22] J. Jiang, A. Kucernak, Chem. Mater. 16 (2004) 1362.
[23] G. García, M.M. Bruno, G.A. Planes, J.L. Rodriguez, C.A. Barbero, E. Pastor, Phys. Chem. Chem. Phys. 10 (2008) 6677.
[24] A. Kolics, A. Wieckowski, J. Phys. Chem. B 105 (2001) 2588.

[25] F.C. Nart, T. Iwasita, J. Electroanal. Chem. 308 (1991) 277.
[26] Z. Jusys, T.J. Schmidt, L. Dubau, K. Lasch, L. Jörissen, J. Garche, R.J. Behm, J. Power Sources 105 (2002) 297.
[27] S. Pasupathil, V. Tricoli, J. Solid State Electrochem. 12 (2008) 1093.
[28] C. Roth, A.J. Papworth, I. Hussain, R.J. Nichols, D.J. Schiffrin, J. Electroanal. Chem. 581 (2005) 79.
[29] L.L. Mickelson, C. Friesen, J. Am. Chem. Soc. 131 (2009) 14879.
[30] M. Watanabe, S. Motoo, J. Electroanal. Chem. 60 (1975) 267.
[31] Toshiba at the CeBIT Electronics Fair in Hanover, August 2003.

Journal of Power Sources 282 (2015) 34–44

Contents lists available at ScienceDirect

Journal of Power Sources

journal homepage: www.elsevier.com/locate/jpowsour

On the design of Pt based catalysts. Combining porous architecture with surface modification by Sn for electrocatalytic activity enhancement

Jonathan Flórez-Montaño [a], Gonzalo García [a], José L. Rodríguez [a], Elena Pastor [a], *, Paula Cappellari [b], Gabriel A. Planes [b]

[a] Instituto Universitario de Materiales y Nanotecnología, Universidad de La Laguna, Astrofísico F. Sánchez s/n, 38071 La Laguna, Tenerife, Spain
[b] Departamento de Química, Universidad Nacional de Río Cuarto, Agencia Postal 3, 5800 Río Cuarto, Argentina

HIGHLIGHTS

- Mesoporous Pt material (MPPt) was successfully modified by Sn adatoms (MPPt/Sn).
- The CO tolerance was evaluated at MPPt, MPPt/Sn and commercial Pt_3Sn/C catalysts.
- The catalytic activity toward methanol oxidation for all electrodes was evaluated.
- CO and methanol oxidation reactions were studied at 25 and 60 °C by DEMS.
- Energy conversion efficiency from methanol to CO_2 for all catalysts was calculated.

GRAPHICAL ABSTRACT

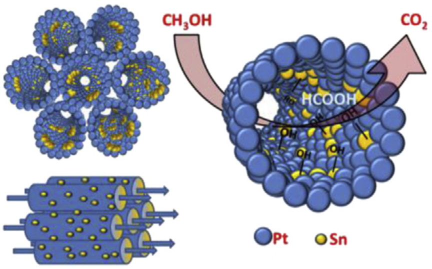

ARTICLE INFO

Article history:
Received 16 October 2014
Received in revised form
2 January 2015
Accepted 4 February 2015
Available online 7 February 2015

Keywords:
DMFC
DEMS
Mesoporous electrodes
CO oxidation
Methanol oxidation
Pt-based materials

ABSTRACT

Metallic mesoporous (MP) catalysts with large surface area can be obtained *in-situ*, in a single step, by electrochemical reduction. In this work, the electrochemical behavior of MPPt and Sn modified mesoporous Pt (MPPt/Sn) was studied and compared with commercial carbon supported PtSn alloy (3:1). The electrochemical activity toward carbon monoxide and methanol oxidation reactions were evaluated by cyclic voltammetry and chronoamperometry, whereas X-ray photoelectron spectroscopy was used to determine the surface composition and oxidation state of the atoms in the top layers of the catalysts. The analysis of methanol conversion to CO_2 was performed with aid of differential electrochemical mass spectrometry (DEMS). Results reveal a better performance of the MPPt/Sn, which shows higher current density and energy conversion efficiency of fuel to CO_2 than conventional carbon supported PtSn alloy (3:1).

1. Introduction

Direct methanol fuel cells (DMFC) are devices that produce energy from an electrochemical reaction. Main differences

---

* Corresponding author.
E-mail address: epastor@ull.edu.es (E. Pastor).

http://dx.doi.org/10.1016/j.jpowsour.2015.02.018
0378-7753/

between DMFC and conventional batteries are the use of a liquid combustible, continuous operating capability and high thermodynamic efficiency limit [1]. Thus, DMFC have been proposed as suitable power devices for mobile applications. All the advantages mentioned before, allows envisage the DMFC technology like a suitable transition to a completely clean energy generation [2–4].

Conversely, some serious weaknesses delay the commercial utilization of DMFC. One of the most important difficulties is the cost of the novel metal required for the electrocatalytic process used at both electrodes (mainly Pt and some of its alloys) [5–8]. Also kinetic restrictions must be overcome for a better metal utilization at the cathode (oxygen reduction reaction, ORR) [9–11], Additionally, a better performance of the anode becomes necessary. With these purposes, the use of lower noble metal loading with high surface accessibility and low poisoning of the active sites by reaction intermediates (i.e. CO, HCHO, HCOOH) is required [12].

The economic problem associated to the catalysts production is an important reason, but not the only one, for build-up nanostructured electrodes. Since electrochemical processes are almost of superficial nature, the fabrication of nanostructured catalysts presents the most powerful approach for the production of small electrodes with high surface area and low metal loading [13,14]. However, this approach introduces some intrinsic difficulties like metallic surface stability in the nanometer scale, and mass transport requirements for reactants and products [15].

There are different ways to prepare practical catalysts for DMFC [16,17]. Generally catalysts utilized as electrodes in PEM fuel cells comprise noble metal nanoparticles supported on high surface carbon (e.g. Pt/C, Pt–Ru/C, etc.). The most widespread route to synthesize this kind of catalysts involves the chemical reduction of the precious metal after its impregnation onto the catalyst support [16–21]. While various synthetic approaches were intended, the design of well-defined mesoporous catalysts persist as one of the most promising objectives [16].

During the last decade, some publications have focused on the study of unsupported electrodes (e.g. mesoporous metal catalysts) [22–25]. In this context, metallic mesoporous (MP) catalysts are interesting because they can be obtained *in-situ* by chemical or electrochemical reduction of the metal cations present in the aqueous phase of a liquid crystalline solution. Usually, this single process renders thin electrodes with high surface area, with the additional advantage that their architecture can be easily tuned by adjusting of the synthesis parameters (i.e. the porous radio can be adjusted by the choice of the appropriated surfactant, and additional porosity can be introduced by the selection of the applied potential). The resulting catalysts possess an extremely concave mesoporous surface, and this characteristic may, by itself, affect the CO electrooxidation reaction [26].

On the other hand, the search for more active surfaces has led to surface modification by adatoms (Pt/M) of diverse nature. Consequently, the Pt surface has been broadly modified by spontaneous deposition of metal [23,26–28]. This approach is even more interesting when combined with mesoporous Pt surface.

For this reasons, in the present work MPPt surfaces were modified by Sn adatoms (MPPt/Sn) and employed in order to understand the effect of mesoporous surface modification by oxophilic atoms toward the methanol electrooxidation reaction. Consequently, the electrochemical properties of the synthesized MPPt/Sn electrodes were examined by the CO and methanol oxidation reactions and compared with a commercial catalyst (Pt_3Sn/C, E-TEK). In addition, *in situ* differential electrochemical mass spectroscopy (DEMS) measurements were carried out with the aim to quantify the CH_3OH conversion to CO_2.

2. Experimental

2.1. Physicochemical characterization

The XPS characterization of the samples was performed in a UHV chamber (base pressure $< 5 \times 10^{-9}$mbar), equipped with a double anode X-ray source (Omicron) and a hemispherical electronanalyzer (VG Scienta). All XPS measurements were performed at room temperature, using non-monochromatic Mg–K radiation (h = 1253.6 eV) and a pass energy of 50 eV and 20 eV for the survey and high-resolution spectra, respectively.

2.2. Electrochemical measurements

A thermostatized three electrodes electrochemical cell was used to realize the analysis at 25 and 60 °C. This electrochemical cell allows solution exchange holding the potential control on the working electrode. For the study of CO tolerance a 0.5 M H_2SO_4 solution was used, while that for the methanol oxidation reaction a 0.5 M H_2SO_4 + 0.1 M CH_3OH solution was utilized at both temperatures. The cell includes a carbon as counter electrode and a reference hydrogen electrode (RHE) in the electrolyte. All potentials in this work are given against the RHE. Electrochemical measurements were performed with a PC Autolab potentiostat-galvanostat. All reagents were analytical grade. Argon (N50) was bubbled through the solution to avoid dissolved oxygen. CO (N47) was employed for the adsorption experiences. In this work, currents are expressed as current densities J (A cm^{-2}), calculated from the measured current I (A) and the real electroactive area S. The electroactive area S was estimated from the CO stripping experiences. With this purpose, CO was bubbled for 10 min at 0.2 V vs. RHE and subsequently argon for 30 min was used to degas the solution during 30 min. After that, the potential was scanned from the adsorption potential down to 0.05 V (so the hydrogen adsorption region can be checked) and then up to 0.90 V, and three consecutive cycles were recorded at 0.005 V s^{-1}. First cycle corresponds to the CO_{ads} electrooxidation, while the second and third cycles show the background voltammogram, indicating that all adsorbed carbon monoxide was completely removed from the catalyst surface.

2.3. DEMS setup

The gaseous species produced on the electro-active surface can be followed on-line by mass spectrometry. For detection of the ion current during mass spectrometric measurement, Quadstar™ 422-software (Pfeiffer-vacumm Thermostar) was used. The setup allows the detection of the ion current for each m/z separately. A conventional electrochemical cell was used and the meniscus configuration was adopted. The working electrode surface is placed very close (~micrometers) to a Teflon capillary, which is connected directly to the vacuum of the mass spectrometer. Details of the setup can be found elsewhere [29].

2.4. DEMS calibration

The calculation of the efficiency for methanol conversion to CO_2 by DEMS requires a previous determination of the $m/z = 44$ calibration constant (K^{CO_2}). This constant correlates the number of CO_2 molecules generated on the electrode surface (through the faradaic charge) with the portion of this molecules captured by the mass spectrometer (proportional to $m/z = 44$ ion current). K^{CO_2} has to be determined before each experiment because it depends of several variables (membrane-electrode gap, flow rate, temperature and pressure in the mass vacuum line). The calibration constant is calculated as follow: faradaic ($Q_f^{CO_2}$) and ionic $m/z = 44$ ($Q_i^{CO_2}$)

charges were calculated from CO stripping and related according to equation:

$$K^{CO_2} = 2\frac{Q_i^{CO_2}}{Q_f^{CO_2}} \tag{1}$$

Then, the current efficiency E for methanol electrooxidation to CO_2 is determined from the subsequent equation:

$$E^{CO_2} = \frac{6*Q_i^{CO_2}}{K^{CO_2}*Q_f^T} \tag{2}$$

where Q_f^T is the charge associated to all faradaic processes at the surface.

Cyclic voltammograms (CVs) and mass spectrometry cyclic voltammograms (MSCVs) for CO_{ads} and methanol at MP electrodes in sulphuric acid were recorded at 5 and 2 mV s^{-1}. Current transients (CTs) and mass spectrometry current transients (MSCTs) for methanol oxidation at MP electrodes in sulphuric acid were recorded at 0.55 and 0.65 V.

2.5. Working electrode preparation

Mesoporous Pt electrodes were obtained by electrochemical reduction of a mixture of aqueous hexachloroplatinic acid (8%) and octaethylene glycol monohexadecyl ether ($C_{16}EO_8$) (50% weight fraction) onto a DEMS Au disk electrode (Ø = 1 mm) at 60 °C and 0.15 V. Typically, after 10 min of Pt^{+4} reduction a charge of 724 mC cm^{-2} was deposited onto Au substrate, resulting in a mesoporous Pt layer containing 1.94×10^{-4} g of Pt (assuming 75% efficiency). Then, the electrode was leaved in distilled water for 48 h, to let the surfactant be completely removed from the porous structure. The surface modification by Sn adatoms was obtained in the following way: an MP Pt electrode was immersed in 0.5 mM $SnSO_4$/0.5 M H_2SO_4 fresh solution for 5 min. This last step facilities the Sn dispersion inside the porous structure. After that, the electrode was rinsed with water, and finally transferred to an electrochemical cell containing 0.5 M H_2SO_4. Finally, the electrode was cycled between 0.05 and 0.50 V to reduce the adsorbed Sn precursor to metallic Sn. The last procedure was repeated as many times necessary.

For studies of the carbon-supported Pt_3Sn/C E-TEK catalyst, the working electrode consists of a certain amount of the Pt_3Sn/C powder (20 wt. % metal supported on Vulcan XC-72, ETEK) deposited as a thin layer over a glassy carbon disc (Ø = 7 mm). For this purpose, an aqueous suspension of 1.0 mg mL^{-1} of the Pt_3Sn/C catalyst was prepared by ultrasonic dispersion of 2.0 mg of the Pt_3Sn/C catalyst in 15 μL of Nafion (5 wt. % Aldrich) and pure water (0.5 mL). An aliquot (10 μL) of the dispersed suspension was pipetted on a glassy carbon surface (7 mm diameter) and dried at ambient temperature under Ar atmosphere.

3. Results and discussion

3.1. MPPt catalyst modified by Sn adatoms

Fig. 1 shows the variation of the hydrogen adsorption/desorption area and the Sn coverage degree for different Sn adsorption times (in several exposition steps, the time is expressed accumulatively). Each step involves the introduction of the MPPt working electrode into a Sn solution for 5 min and a subsequent electrochemical reduction. The degree of Sn coverage was calculated using the following equation [30–34].

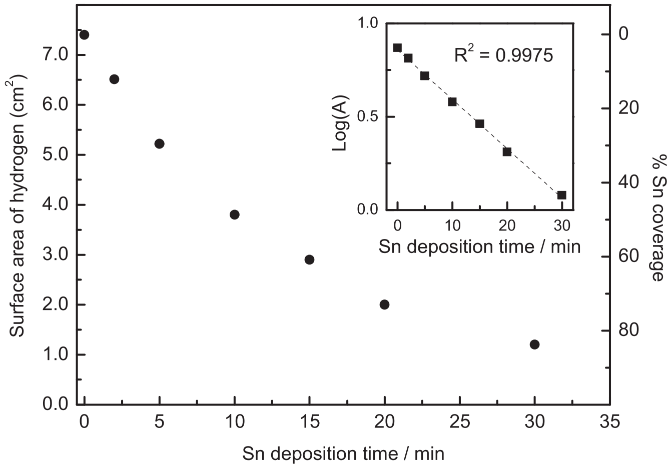

Fig. 1. Pt surface area calculated from the hydrogen adsorption/desorption region (left Y-axis), and Sn coverage percentage at different adsorption times (right Y-axis) vs adsorption time. Inset: Logarithmic behavior of the deposition current.

$$\theta_{Sn} = \frac{Q_H^b - Q_H^a}{Q_H^b} \tag{3}$$

Q_H^a is the electrical charge for the MPPt/Sn, evaluated from cyclic voltammetry in the potential region between 0.05 and 0.40 V_{HRE}, and Q_H^b is the electric charge for the MPPt at the same potential region. A close inspection of Fig. 1 reveals that the most significant change in the Sn coverage occurs between 5 and 15 min. The inset graph shows that the Sn deposition process follows an exponential behavior. The slope points out that, for each Sn deposition step, the available (Sn-free) Pt surface is reduced about 20%. Additionally, no substantial increment in the charge is observed for longer Sn deposition time, indicating that the process operates self-poisoning the Pt surface, as was early reported by Gupta et al. [35]. Considering that in the present case only a small change occurs for more than three deposition steps, the study is limited to 15 min that corresponds to $\theta_{Sn} = 0.60$. In this sense, it was reported high activity towards methanol oxidation with similar nominal value of Sn modified Pt catalysts in acidic media [36].

The cyclic voltammograms for MPPt and MPPt/Sn electrodes in sulphuric acid solution are given in Fig. 2. The black line corresponds to the current response for the unmodified MPPt material, in which is well visible the hydrogen adsorption/desorption (H_a/H_d) region between 0.05 and 0.4 V. At potentials above 0.4 V, a non-faradaic process is observed along the double layer region (between 0.4 and 0.8 V). Finally, the slight increment of the anodic current at $E > 0.8$ V indicates the formation of oxygenated species onto the Pt surface, i.e. the onset potential for Pt oxides formation. The effect of the Sn adatoms on the MPPt surface (red, green and blue lines) is noticeable by the charge fall in the H_a/H_d region, especially in the sites related with (100) and (110) surface orientations [37]. Additionally, it is observed a new contribution at ca. 0.73 V, corresponding to the onset for the Sn oxidation process. Also, it can be discerned that as the Sn coverage rises with the successive exposition steps, the Sn oxide redox couple around 0.75 and 0.62 V is notoriously increased. As was described above, the surface blocking effect by Sn adatoms in the H_a/H_d region will be used later to estimate the Sn coverage (θ_{Sn}) [34,35].

All these results are consistent with those reported previously by other authors for PtSn alloys [19], carbon supported PtSn nanoparticles [20] and Pt single crystal structures modified by Sn [21,34]. The double layer broadening has usually been attributed to

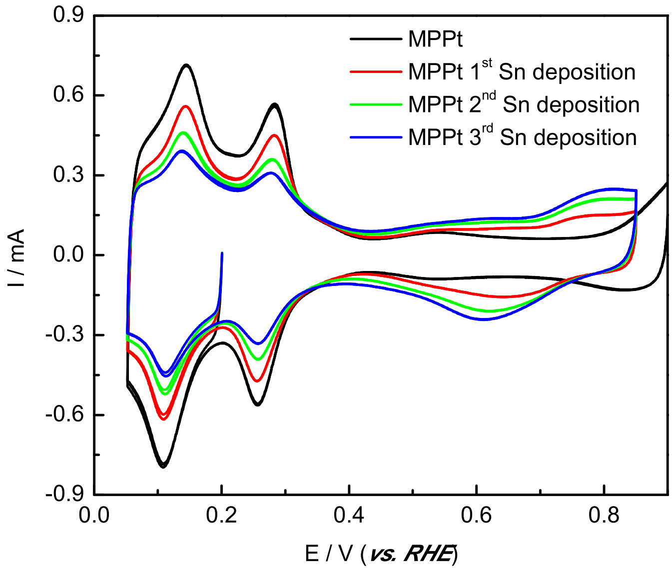

Fig. 2. Cyclic voltammograms obtained for MPPt and MPPt/Sn catalysts in 0.5 M H_2SO_4 solution at a scan rate of 100 mV s^{-1} and 25 °C.

H_2O activation on Sn and/or SnO_2 species, while the anodic peak around 0.7 V is associated to Sn oxide (SnO_2) formation from the dissociation of H_2O on the metallic surface [30–32,35].

The application of techniques as Energy Dispersive X-Ray Spectroscopy (EDX) or X-Ray Diffraction (XRD) for the detection of Sn in the sample is not possible as the amount of Sn is very small (the surface is covered only by ad-atoms of Sn) and it is not present in a crystalline form. For this reason, the surface constituent phase of the MPPt and MPPt/Sn ($\theta_{Sn} = 0.60$) materials were further studied by XPS analysis which is more appropriated as a surface sensitive technique. Fig. 3A displays the Pt 4f XPS spectra that contain two peaks corresponding to the Pt $4f_{7/2}$ and Pt $4f_{5/2}$ states. Each peak was deconvoluted and associated to three different Pt oxidation states (Pt^0, Pt^{2+} and a small contribution of Pt^{4+}).

MPPt develops a $4f_{7/2}$ signal that can be correlated to three curves peaked at 71.0, 72.1 and 73.3 eV, which are attributed to Pt^0, Pt^{2+} (PtO and $Pt(OH)_2$-like species) and Pt^{4+}, respectively [39,40]. On the other hand, MPPt/Sn spectra (Fig. 3B) shows similar signals than MPPt, but at small shift of B.E. toward higher values can be discerned, i.e. Pt^0, Pt^{2+} and Pt^{4+} curves appear centered at 71.0, 72.5 and 73.8 eV, respectively. However, the most important finding is the change in their relative area that is associated to the amount of the species in the catalyst surface (Table 1). The Sn 3d signal of the MPPt/Sn was also deconvoluted into two distinguishable doublets (Fig. 3C) with different intensities. In this context, the $3d_{5/2}$ peaks at 484.6 and 486.5 eV are attributed to metallic Sn^0 and SnO_2 species [30,40].

Table 1 shows that MPt/Sn catalyst surface is almost composed by Sn and Pt species in the oxide (SnO_2) and metallic (Pt^0) states, respectively. The last is caused by electronegativity differences between Pt and Sn, leading to a charge transfer from the less electronegative Sn to the more electronegative Pt.

Furthermore, the spectra developed by the modified material after three Sn deposition steps reveals a surface atomic ratio of Pt:Sn of 40:60, which is in total agreement with the calculated by the charge decrease in the hydrogen adsorption/desorption potential region. In this context, it is important to remind that both XPS and cyclic voltammetry are surface sensitive techniques, and this is the reason for the excellent correlation.

Therefore, it can be extracted from these results that the catalyst surface is mainly formed by metallic Pt and SnO_2 located mainly on Pt sites with (110) and (100) orientations, in addition to rather similar mass percent composition of both elements [40].

3.2. CO stripping

The oxidative desorption of a CO monolayer adsorbed on a catalyst surface (denoted here as CO stripping) is an important tool for surface characterization. Since adsorbed CO is a strong catalyst poison and it is a reaction intermediate during, for example, the methanol and formic acid electrooxidation reaction, its removal is a key factor to be investigated [23,24]. Furthermore, the CO stripping is a powerful technique for the study of the surface morphology and structure. In addition, CO stripping is a convenient method to obtain an accurate estimation of the electroactive surface area [26,41].

The left side of Fig. 4 (panels denoted as A, C and E) shows CO stripping experiments for MPPt, MPPt/Sn ($\theta_{Sn} = 0.60$) and commercial Pt_3Sn/C E-TEK electrodes recorded at two different temperatures (25 and 60 °C) in 0.5 M H_2SO_4 at 5 mV s^{-1}. It is observed that for all catalysts the onset and peak potentials for CO oxidation reaction shift toward more negative values with the increment of the temperature. However, some differences between them can be found. MPPt material develops an onset potential at ca. 0.45 V_{RHE} and a smooth anodic wave (or pre-peak) centered at ca. 0.55 V_{RHE} that is followed by a sharp anodic peak at 0.7 V_{RHE} at 25 °C. The rise of the temperature shifts all these features about 0.1 V towards more negative potentials.

In contrast, MPPt/Sn catalyst with $\theta_{Sn} = 0.60$ presents the onset potential for the CO stripping at much lower values (0.23 V_{RHE}) than MPPt at 25 °C. Additionally, the CO stripping profile recorded at 25 °C for MPPt/Sn electrode develops two well-defined anodic peaks centered at ca. 0.4 (denoted as I) and 0.67 V_{RHE} (denoted as II). These results are consistent with those reported by other authors in the literature [30–36,38], in which a Sn promoter effect was observed. In fact, Sn is capable to promote the oxidation of adsorbed CO [42,43] with the aid of adsorbed oxygenated species (i.e. OH species), which are produced at lower potentials than Pt. The increasing of the temperature to 60 °C does not shift the onset and peak potential developed at 0.4 V (I) but increases the faradaic charge in this potential region. Additionally, it is observed a current charge diminution and a shift to lower potentials of the second anodic peak (II) with the rise of the temperature. These results indicate the existence of sites with different catalytic activity towards the CO oxidation reaction at MPPt/Sn, and suggest a CO surface diffusion from the least (II) to the most (I) active sites, which increases with the temperature [44].

On the other hand, CO_{ad} oxidation on commercial Pt_3Sn/C electrode shows a broad anodic peak with an onset and peak potential at ca. 0.25 and 0.75 V, respectively. It is noticeable the higher value of the CO peak potential developed by the commercial Pt_3Sn/C catalyst in comparison with the MPPt and MPPt/Sn materials. Similar to the observed for both MP electrodes, the CO peak potential for the Pt_3Sn/C shifts negatively with the increment of the temperature.

Results are consistent with an enhancement of the water activation process (adsorbed oxygenated species formation) due to the introduction of Sn and the rise of the temperature, which affect the CO electrooxidation by means of the bi-functional mechanism [31–36,42]. Nevertheless, small contribution from electronic effect cannot be discarded.

The recorded mass spectrometric cyclic voltammograms (MSCVs) related to CO_2 formation ($m/z = 44$) for each material are given at the right side of Fig. 4 (panels denoted as B, D and F). This figure clearly shows a close correlation between faradaic and ionic

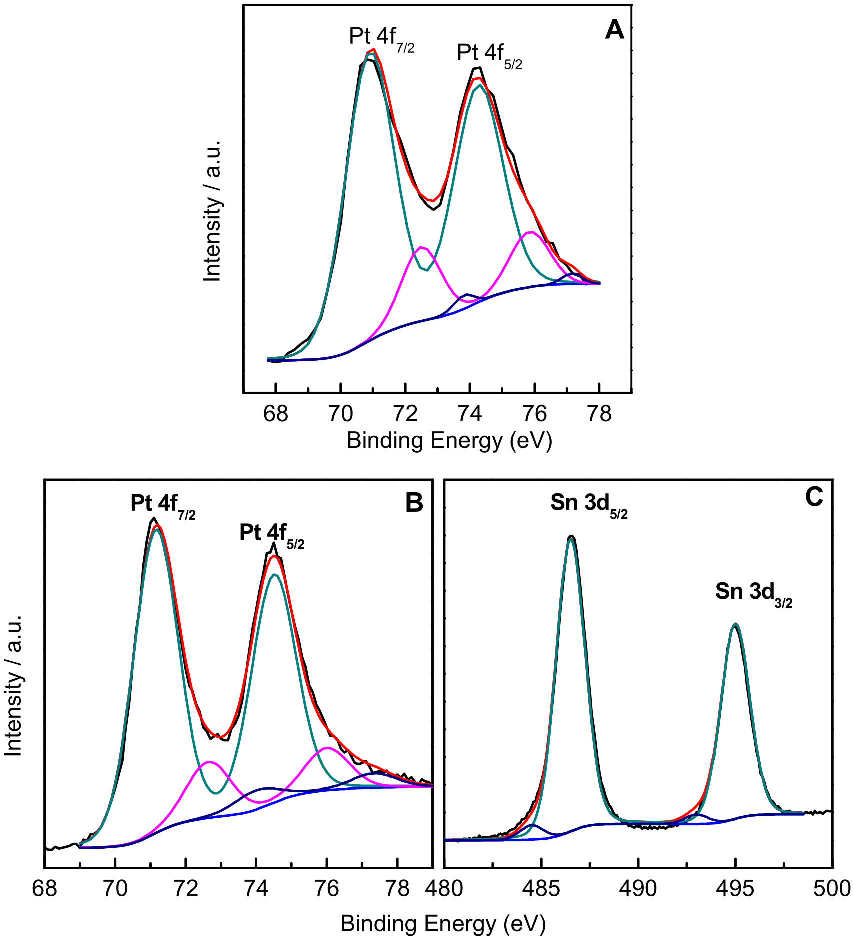

Fig. 3. Pt 4f XPS spectra for MPPt (A) and MPPt/Sn ($\theta_{Sn} = 0.60$) (B). Sn 3d XPS spectra for MPPt/Sn ($\theta_{Sn} = 0.60$) (C).

Table 1
XPS results for MPPt/Sn electrode.

Catalyst	$Pt_{species}$	Pt $4f_{7/2}$/eV (%at.)	$Sn_{species}$	Sn $3d_{5/2}$/eV)	Pt:Sn (%at.)	Pt:Sn (%wt.)
MPPt	Pt(0)	70.9 (67)	Sn(0)	–	–	–
	Pt(II)	71.9 (26)	Sn(IV)	–		
	Pt(IV)	73.1 (7)				
MPPt/Sn	Pt(0)	71.0 (80)	Sn(0)	484.4 (4)	40:60	51:49
($\theta_{Sn} = 0.60$)	Pt(II)	72.5 (14)	Sn(IV)	486.3 (96)		
	Pt(IV)	73.8 (5)				

currents, pointing out that the CO_{ad} oxidation reaction occurs in the 0.2–0.95 V_{RHE} potential range. Even more, due to the absence of interference associated to the double layer charging, oxide formation or other reaction different to CO_2 formation, the MSCV allows a better determination of the onset potential for the CO_{ad} oxidation reaction. In this context, the ionic current signal $m/z = 44$ rises at more negative potentials (a shift close to 0.06 V can be discerned) than that observed for the faradaic current. Moreover, by means of MSCV, the onset potential for the CO_2 production at MPPt/Sn electrode is detected at 0.2 V_{RHE}. The last value is lower than that observed by *in-situ* FTIRS utilized in a potentiostatic mode [45]. Furthermore, it is observed that the CO tolerance increases in the following way: MPPt << Pt_3Sn/C < MPPt/Sn. This order is not only confirmed by the onset potential for CO_{ad} oxidation reaction, but also by the increment of the $m/z = 44$ signal at more negative potentials. In other words, ionic current developed at 0.4 V is higher on MPPt/Sn than on Pt_3Sn/C material. In this context, Sn oxides deposited on mesoporous metallic Pt sites appear to be relevant for an enhanced activity towards the CO oxidation reaction.

On the other hand, a clear anodic peak (I) appears for the CO oxidation onto MPPt/Sn, which is absent for carbon supported PtSn, while the anodic contribution (II) occurs at more negative potentials for MPPt/Sn catalyst in comparison with the commercial catalyst. The first anodic peak (I) is related to high abundance of reactive sites. In this sense, low-coordinated Sn atoms, which can be presented as kink or step on the Pt surface, are reactive sites that may promote the formation of oxygenated species onto the surface (Sn–OH and SnO_2) at lower potentials than conventional PtSn alloys [45,46]. In this sense, it is well documented that CO stripping on Pt basal planes is more reactive on open than close-packed surfaces in acidic media [37], i.e. surface sites with (110) and (100) orientations are more reactive than that with (111) sites. Therefore, the higher CO tolerance can be associated to facile water dissociation on Pt open surfaces. As was discussed above and observed at Fig. 2, Sn adatoms as SnO_2 species (see XPS analysis at Table 1) are mainly deposited on MPPt sites with (110) and (100) orientations. Moreover, CO does not adsorb on Sn surfaces and consequently the formation of adsorbed oxygenated species (OH) is assured. The last does not occur on Ru-based materials (e.g. PtRu), in which CO_{ad} and water dissociation (OH_{ad} formation) compete for the same adsorption sites. For all the exposed reasons, the onset potential for CO stripping on MPPt/Sn is located at more negative potential when is compared with those experiments performed at

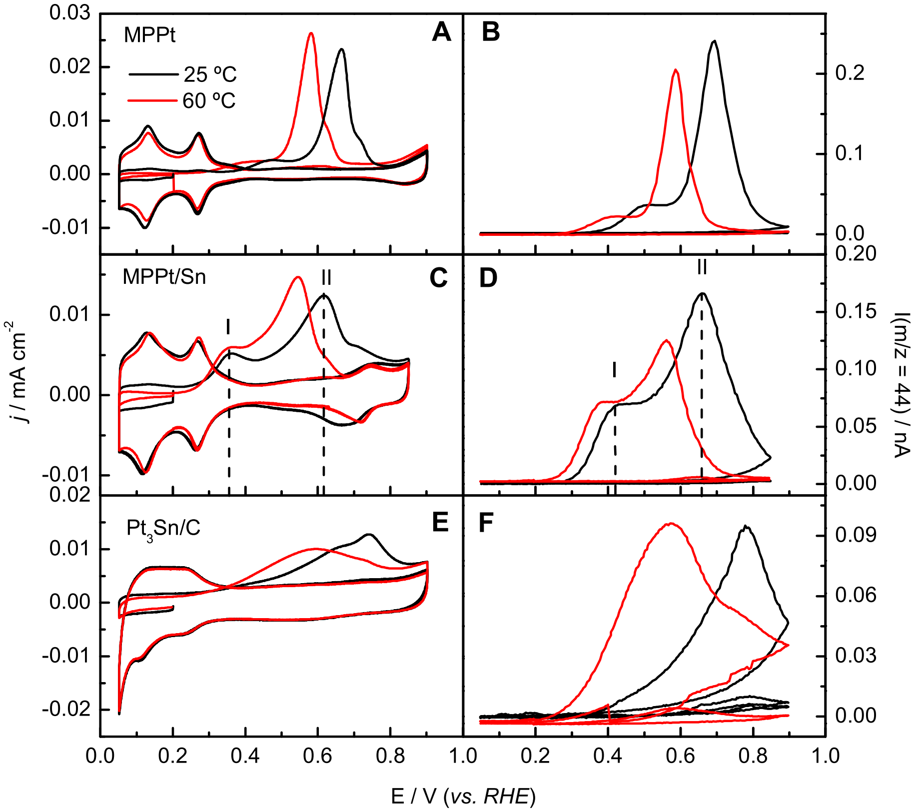

Fig. 4. CVs (left panels) and MSCVs (right panels) for CO_{ad} oxidation on MPPt (A, B); MPPt/Sn ($\theta_{Sn} = 0.60$) (C,D) and commercial Pt_3Sn/C (E, F) in 0.5 M H_2SO_4. Scan rate 5 mV s^{-1}; T = 25 and 60 °C.

MPPtRu, MPPt/Ru and PtRu/C materials [23,24].

3.3. Methanol oxidation on MPPt and MPPt/Sn ($\theta_{Sn} = 0.60$) catalysts

The potentiodynamic oxidation of methanol on MPPt (top panel), MPPt/Sn (middle panel) and Pt_3Sn/C E-TEK (bottom panel) recorded by cyclic voltammetry and DEMS can be seen in Fig. 5. Theoretical faradic currents calculated from the $m/z = 44$ signals after the calibration procedure were included (left panels, red lines). Note that the difference in area between experimental (black curve) and theoretical (red curve) faradaic currents is the extra charge associated with the formation of different products than CO_2 (e.g. formaldehyde and formic acid), and therefore, the CO_2 conversion efficiency can be estimated. Additionally, the ionic current related to methyl formate ($m/z = 60$) that is produced by the condensation reaction of methanol and formic acid, is depicted in the right panels of Fig. 5. Thus, formic acid production can be followed through this signal.

Interestingly, the onset potentials for faradaic current and formic acid formation are similar for both MPPt and MPPt/Sn. However, the peak potential for formic acid production (right panels) appears at more negative potentials than those observed for the faradaic current (black lines, left panels) at these electrodes. The last indicates that a by-side product such as formaldehyde is favored at high potentials at mesoporous electrodes. In this sense, it is difficult to distinguish between methanol and formaldehyde ionic signals, since both molecules develop the same m/z signals. On the other hand, the $m/z = 60$ signal for the carbon-supported material develops a completely different profile which can be explained assuming the slow diffusion of formic acid out of the porous structure of the carbon (this diffusion is favored in the mesoporous materials respect to the carbon supported ones as previously shown in Ref. [24]). The current efficiency to CO_2 (as average of the forward and backward scans) is higher for the MPPt (74%) than for the MPPt/Sn materials (46%). Indeed, the CO_2 conversion efficiency increases in the following way: MPPt/Sn < Pt_3Sn/C < MPPt (Table 2), although the experimental faradaic current density shows the opposite trend.

As stated above, the incomplete oxidation of methanol produces by-side reaction products, such as formaldehyde, formic acid and adsorbed reaction intermediates (mainly CO_{ad}). In fact, the decrease in the formation of these soluble side products produces a subsequent increase of the CO_2 conversion current efficiency, but this effect is not necessary accompanied by an increase in the recorded faradaic current density. Thus, the commercial Pt_3Sn/C catalyst develops lower faradaic current density than the MPPt/Sn electrode but higher CO_2 conversion efficiency. Therefore the lower current density can be associated to surface poisoning (blocking effect) by adsorbed species (e.g. adsorbed CO, formaldehyde or formic acid) that further oxidize to carbon dioxide, causing the rise of the energy conversion efficiency. In the same sense, thin catalytic MPPt/Sn films produce higher current densities and lower CO_2 formation than thick films (not shown), as faster diffusion is favored for the former avoiding further reaction of side products on the catalyst surface. Conversely, MPPt catalyst presents the highest CO_2 efficiency and also the most intense signal for formic acid. As will be shown later, this result can only be explained assuming a low production of formaldehyde at this electrode.

The influence of the morphology on the catalytic activity was confirmed comparing the results for the MPPt material with a Pt electrode prepared by electrodeposition following the same

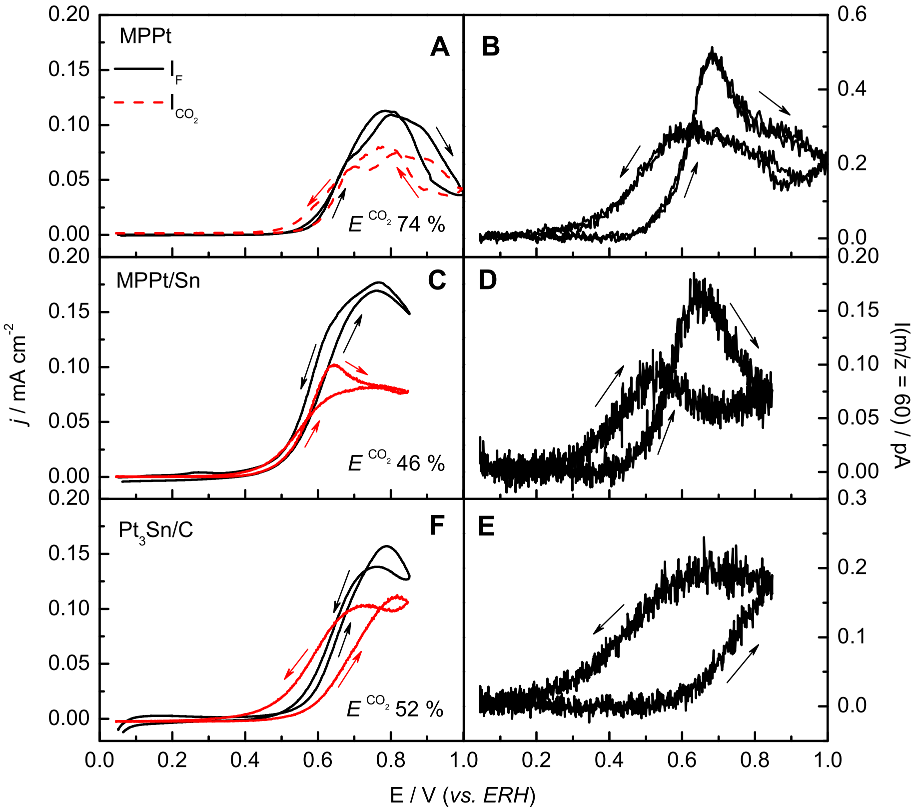

Fig. 5. CVs and MSCVs for methanol oxidation on MPPt (top panels), MPPt/Sn ($\theta_{Sn} = 0.60$) (middle panels) and Pt_3Sn/C (bottom panels) catalysts in 0.1 M CH_3OH + 0.5 M H_2SO_4 at 25 °C. Scan rate = 2 mV s^{-1}. Left panels: experimental (black line) and theoretical (from $m/z = 44$, red line) faradaic currents. Right panels: $HCOOCH_3$ ($m/z = 60$) formed by the condensation reaction of methanol and formic acid. (For interpretation of the references to color in this figure legend, the reader is referred to the web version of this article.)

Table 2
Efficiency conversion from methanol to CO_2 at 25 and 60 °C.

E(mV)	MPPt		MPPt/Sn		PtSn/C	
	Efficiency to CO_2 conversion					
	25 °C	60 °C	25 °C	60 °C	25 °C	60 °C
550[a]	95	100	100	84	96	73
650[a]	65	71	78	68	71	50
E_{total}	74	54	46	59	52	59

E_{total}: Efficiency conversion to CO_2 calculated from CVs.
[a] Efficiency conversion to CO_2 calculated from chronoamperometry.

procedure used for the MPPt but in the absence of surfactant. The cyclic voltammograms (see Supporting Information, Figs. 1S and 2S) show that higher current densities are obtained with the MPPt, concluding that higher activity can be achieved with the mesoporous structure. In concordance with results from Fig. 5 previously discussed, the lower current densities for the electrodeposited Pt are accompanied with a higher efficiency to CO_2 (80% for the electrodeposited Pt in the absence of surfactant and 74% for MPPt at 25 °C).

On the other hand, the chemical nature of the catalytic material appears as an important factor for both, the energy conversion efficiency and the current density. Left panels of Fig. 5 show that the onset potential for methanol oxidation on MPPt/Sn and MPPt electrodes is located at 0.4 and 0.5 V respectively. Both electrodes are smooth surfaces, in which reaction products diffuse in a similar way. However, Sn significantly improves the methanol oxidation reaction but not the CO_2 conversion efficiency at high potentials. Therefore, diverse pathways during the methanol oxidation reaction are operating at both mesoporous surfaces depending on the applied potentials. Actually, Sn deposition on Pt sites with (110) and (100) orientations enhances the CO tolerance and decreases the overpotential needed for the methanol oxidation reaction. Additionally, low production of formic acid is observed on Sn-containing electrodes. Consequently, the low CO_2 conversion efficiency and the high current delivered at $E > 0.60$ V for MPPt/Sn are associated to soluble formaldehyde formation.

Fig. 6 depicts the experimental (top panels) and theoretical (bottom panels) faradaic currents calculated from the CO_2 signal $m/z = 44$ and recorded at 0.55 and 0.65 V (25 °C). It is observed that the experimental faradaic current depends on the catalytic nature of the electrode and increases in the following way: $Pt_3Sn/C < MPPt << MPPt/Sn$, in good agreement with that observed in the potentiodynamic experiments (Fig. 5). Additionally, methanol conversion to CO_2 is almost complete for Pt–Sn catalysts at 0.55 V (Table 2), but decreases at 0.65 V, whereas the faradaic current increases. In this sense, Fig. 5 also displays a CO_2 conversion drop at potentials higher than 0.60 V. Opposite, for MPPt the current density increases with the applied potential and also does the current efficiency for CO_2 production. These results indicate, firstly, that the full methanol oxidation to CO_2 occurs not only through the adsorbed carbon monoxide path: MPPt increases the efficiency to CO_2 with the applied potential whereas decreases at Pt–Sn materials, being the former less tolerant to CO according to Fig. 4. In fact, the formic acid path, presumably by adsorbed formate, contributes also to carbon dioxide formation. The latter is in agreement with infrared results previously published [47–49]. Secondly, considering that formic acid also contributes to CO_2 formation, methanol conversion drop to CO_2 at Pt–Sn materials should be then associated to formaldehyde production instead of formic acid at 0.65 V.

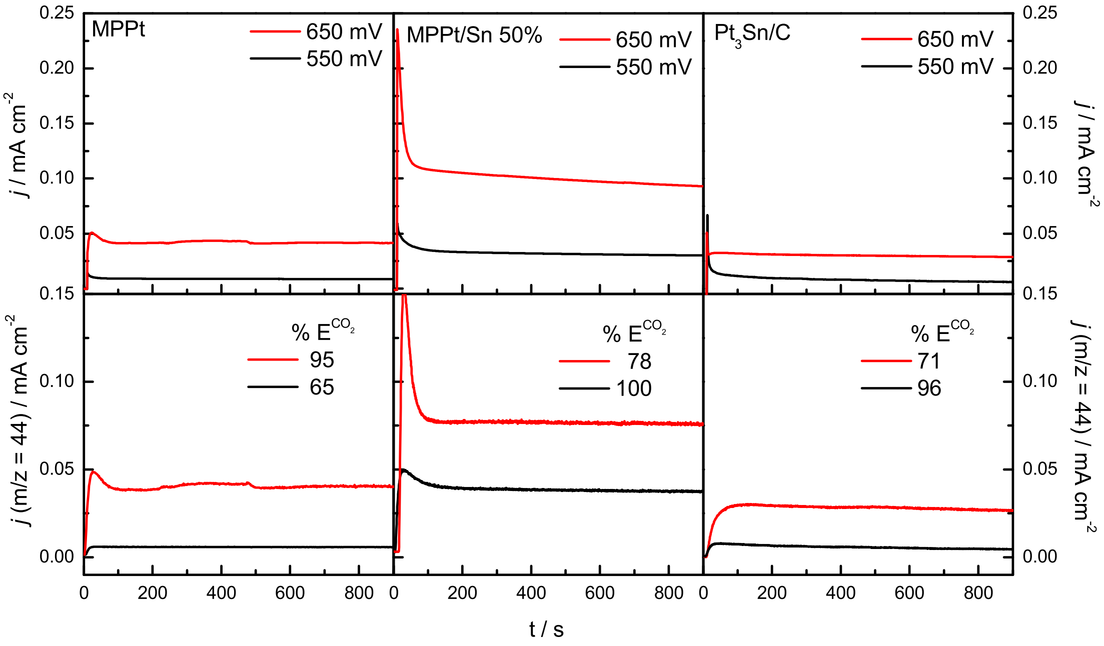

Fig. 6. Current transients for methanol electrooxidation at MPPt (left panels), MPPt/Sn ($\theta_{Sn} = 0.60$) (middle panels) and Pt_3Sn/C (right panels) at 0.55 (red line) and 0.65 V (black line) in 0.1 M CH_3OH + 0.5 M H_2SO_4 at 25 °C. Experimental (top panels) and theoretical (bottom panels) faradaic currents. (For interpretation of the references to color in this figure legend, the reader is referred to the web version of this article.)

The effect of the increment of the temperature up to 60 °C can be seen in Figs. 7 and 8. The curves in Fig. 7 show a raise of the current density for all catalysts with the temperature, being especially noticeable for MPPt/Sn. The onset potential for methanol oxidation at 60 °C remains with a similar trend to that observed at 25 °C, i.e. MPPt/Sn < Pt_3Sn/C < MPPt. Interestingly, the CO_2 conversion

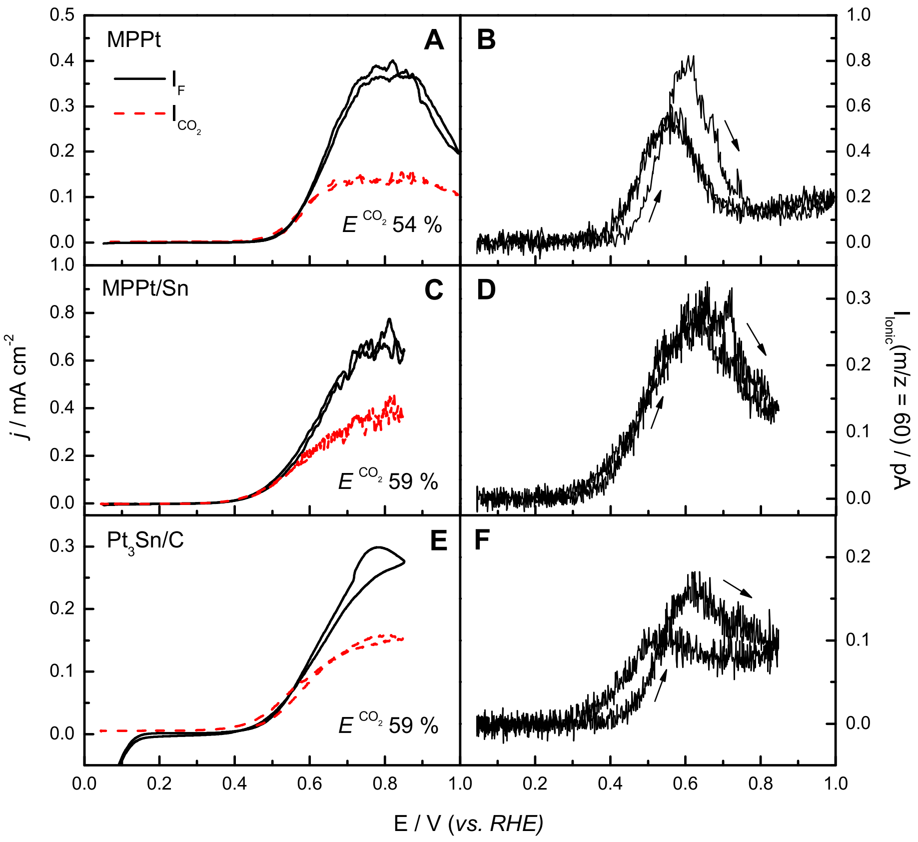

Fig. 7. CVs and MSCVs for methanol oxidation on MPPt (top panels), MPPt/Sn ($\theta_{Sn} = 0.60$) (middle panels) and Pt_3Sn/C (bottom panels) catalysts in 0.1 M CH_3OH + 0.5 M H_2SO_4 at 60 °C. Scan rate = 2 mV s^{-1}. Left panels: experimental (black solid line) and theoretical faradaic (red dash line) currents. Right panels: $HCOOCH_3$ ($m/z = 60$) formed by the condensation reaction of methanol and formic acid. (For interpretation of the references to color in this figure legend, the reader is referred to the web version of this article.)

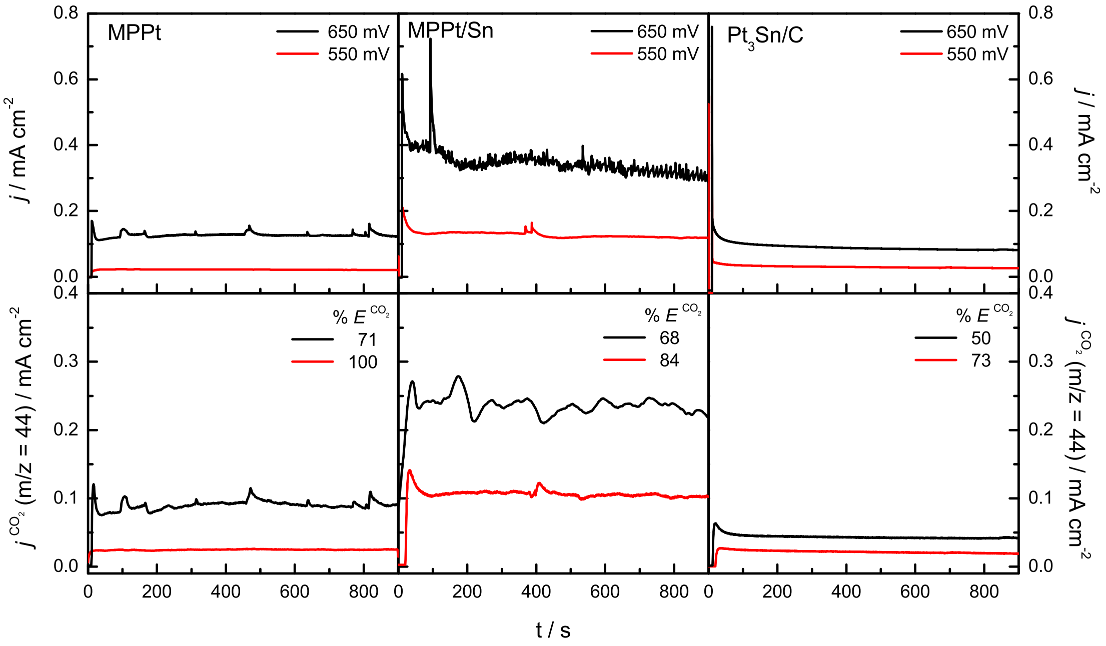

Fig. 8. Current transients for methanol electrooxidation at MPPt (left panels), MPPt/Sn ($\theta_{Sn} = 0.60$) (middle panels) and Pt_3Sn/C (right panels) at 0.55 (red line) and 0.65 V (black line) in 0.1 M CH_3OH + 0.5 M H_2SO_4 at 60 °C. Experimental (top panels) and theoretical (bottom panels) faradaic currents. (For interpretation of the references to color in this figure legend, the reader is referred to the web version of this article.)

efficiency diminishes for MPPt and growths for both electrodes containing Sn with the rise of the temperature (Table 2). Moreover, at 60 °C the intensity for the $m/z = 60$ signal increases notoriously, so the growth in the faradaic current is mainly related to the activation of the formic acid production pathway. It is observed that both ionic peak potentials for this signal (forward and backward scans) become similar in intensities and potential range, especially for the MPPt/Sn catalyst. This effect is explained by the enhancement of the water activation reaction with the rise of the temperature, increasing the kinetic and reversibility of the metallic oxide formation/reduction reaction.

Potentiostatic measurements at 0.55 and 0.65 V for methanol oxidation on all catalysts at 60 °C are depicted in Fig. 8. It can be established the following trend for recorded faradaic currents (upper panels): Pt_3Sn/C < MPPt << MPPt/Sn which also increase with the rise of the temperature, in concordance with the results in the CVs (Fig. 7). As explained before, the increment of the temperature facilitates the water dissociation onto metallic surfaces, and thereby, the CO tolerance. The higher CO_2 conversion occurs at 0.55 V, since the onset for formic acid production shifts to more negative potentials notoriously at 60 °C. Additionally, the presence of Sn onto the mesoporous electrode decreases the onset potential for the $m/z = 60$ signal associated to formic acid formation. Theoretical curves in Fig. 8 (bottom panels) show that at 60 °C the energy conversion efficiency from methanol to carbon dioxide at both applied potentials increases in the following way: $Pt_3Sn/C < < \text{MPPt/Sn} \leq \text{MPPt}$. However, the highest delivered current by the MPPt/Sn suggests that this material presents the best performance toward methanol oxidation reaction. Indeed, it is expected for this catalyst high current density with elevated energy conversion efficiency at lower potentials (e.g. 0.45 V), in which low temperature fuel cells are operative.

Summarizing, the rise of the temperature promotes the water dissociation on metallic surfaces, thus producing an enhancement of both the CO and methanol oxidation reactions. The kinetic of methanol deprotonation process increases with the temperature and the applied potential, and then the formic acid formation is favored, although the current efficiency to CO_2 decreases. Adsorbed CO oxidation reaction is also favored with the temperature by the increment of the water activation process, and it is expected to liberate the surface for a fast methanol replacement. In this context, Sn does not adsorb CO but increases the rate of carbon monoxide removal, appearing as a better promoter than Ru for Pt-based materials. All these parameters (high activity and conversion efficiency to CO_2) suggest a good performance toward methanol oxidation on Pt–Sn based materials at high temperatures and low overpotentials. In this context, Sn atoms adsorbed onto Pt open structures (MPPt/Sn) present higher tolerance than Pt–Sn alloys toward CO.

On the other hand, product (carbon dioxide, formaldehyde and formic acid) diffusion away from the active site is fast on well-structured mesoporous surfaces, and consequently, the turnover rate of methanol at these surfaces is high. Thus, mesoporous electrodes exhibit high faradaic currents during the methanol oxidation reaction; meanwhile the introduction of Sn improves the conversion efficiency to CO_2 [50]. Thus, commercial Pt_3Sn/C catalyst develops elevated conversion efficiency but small current density, which is associated with a low turnover rate of methanol inside the carbon support structure.

4. Conclusions

Methanol oxidation on mesoporous Pt (MPPt) and Sn modified MPPt (MPPt/Sn) with 60% of Sn coverage ($\theta_{Sn} = 0.60$) was studied and compared with commercial carbon supported Pt_3Sn alloy at 25 and 60 °C in acidic media. Reaction intermediates and energy conversion efficiency from methanol to CO_2 were also investigated using a new configuration of the cell differential electrochemical mass spectrometry (DEMS). This setup allowed the use of a conventional electrochemical cell and a meniscus configuration can be adopted [29].

The presence of Sn onto the MPPt surface enhances the CO and methanol electrooxidation at low overpotentials due to the presence of Sn oxophilic atoms situated on an open surface structure. Sn promotes the water dissociation but does not adsorb CO, and therefore the turnover rate of the fuel is accurate. Consequently, the bifunctional mechanism appears to be operative, i.e. oxygenated tin species are able to supply oxygenated species (OH) at lower potentials than Pt, resulting in an enhancement of CO and methanol electrooxidation reactions.

The rate of the electrocatalytic process increases with the temperature and the applied potential. Thus, best performance is obtained with MPPt/Sn catalyst at low potentials and high temperatures. High potentials produce high faradaic currents due to formation of side products mainly as formaldehyde, with the subsequent decrease of the conversion efficiency to CO_2.

Mesoporous structures appear as suitable electrodes to replace carbon supported material in low temperature fuel cells. This appreciation arises from carbon corrosion that produces catalyst dissolution and agglomeration, and consequently loss of fuel cell performance. However, mesoporous materials are stable and possess high electronic conductivity in acidic media. Moreover, the porous structure facilitates the diffusion of soluble products away of the catalysts site, increasing in this way the turnover rate and consequently allowing catalyst active sites reutilization.

Acknowledgments

The authors gratefully acknowledge financial support given by the Spanish MINECO under the project CTQ2011-28913-C02-02 and PRI-AIRBAR-2011-1307 for the cooperation between both groups. P.S.C acknowledges CONICET (Argentine) for the doctoral fellowship. J.F-M. is indebted to the ACIICI (Gobierno de Canarias) for the predoctoral fellowship. G.A. Planes is a permanent research fellow of CONICET.

Appendix A. Supplementary data

Supplementary data related to this article can be found at http://dx.doi.org/10.1016/j.jpowsour.2015.02.018.

References

[1] C. Lamy, A. Lima, V. LeRhun, F. Dlime, C. Coutanceau, J.M. Leger, Recent advances in the development of direct alcohol fuel cells (DAFC), J. Power Sources 105 (2002) 283–296.
[2] R. O'Hayre, S.W. Cha, W. Collela, F.B. Prinz, Fuel Cells Fundamentals, Second ed., Wiley, Hoboken, NJ, 2009.
[3] J. Larminie, A. Dicks, Fuel Cells Systems Explained, Wiley, Hoboken, NJ, 2003.
[4] G. Hoogers, Fuel Cell Technology Handbook, CRC Press, Boca Raton, FL, 2003.
[5] M. Watanabe, S. Motoo, Electrocatalysis by ad-atoms: part II. Enhancement of the oxidation of methanol on platinum by ruthenium ad-atoms, J. Electroanal. Chem. 60 (1975) 267–273.
[6] M. Watanabe, Y. Genjima, K. Turumi, Direct methanol oxidation on platinum electrodes with ruthenium adatoms in hot phosphoric acid, J. Electrochem. Soc. 144 (1997) 423–428.
[7] K.L. Ley, R. Liu, C. Pu, Q. Fan, N. Leyarovska, C. Segre, E.S. Smotkin, Methanol oxidation on single-phase Pt-Ru-Os ternary alloys, J. Electrochem. Soc. 144 (1997) 1543–1548.
[8] M. Götz, H. Wendt, Binary and ternary anode catalyst formulations including the elements W, Sn and Mo for PEMFCs operated on methanol or reformate gas, Electrochim. Acta 43 (1998) 3637–3644.
[9] M. Lefèvre, J.P. Dodelet, Fe-based catalysts for the reduction of oxygen in polymer electrolyte membrane fuel cell conditions: determination of the amount of peroxide released during electroreduction and its influence on the stability of the catalysts, Electrochim. Acta 48 (2003) 2749–2760.
[10] R.W. Reeve, P.A. Christensen, A. Hamnett, S.A. Haydock, S.C. Roy, Methanol tolerant oxygen reduction catalysts based on transition metal sulfides, J. Electrochem. Soc. 145 (1998) 3463–3471.
[11] T.J. Schmidt, U.A. Paulus, H.A. Gasteiger, N. Alonso-Vante, R.J. Behm, Oxygen reduction on $Ru_{1.92}Mo_{0.08}SeO_4$, Ru/carbon, and Pt/carbon in pure and methanol-containing electrolytes, J. Electrochem. Soc. 147 (2000) 2620–2624.
[12] B. Beden, L. Lamy, A. Bewick, K. Kunimatsu, Electrosorption of methanol on a platinum electrode. IR spectroscopic evidence for adsorbed CO species, J. Electroanal. Chem. 121 (1981) 343–347.
[13] S. Sakka, Handbook of Sol-Gel Science and Technology, Kluwer AP, Dordrecht, 2004.
[14] P.K. Jal, S. Patel, B.K. Mishr, Chemical modification of silica surface by immobilization of functional groups for extractive concentration of metal ions, Talanta 62 (2004) 1005–1028.
[15] T.S. Zhao, C. Xu, R. Chen, W.W. Yang, Mass transport phenomena in direct methanol fuel cells, Prog. Energy Combust. Sci. 35 (2009) 275–292.
[16] Y. Tokudome, K. Nakanishi, K. Kanamori, K. Fujita, H. Akamatsu, T. Hanada, Structural characterization of hierarchically porous alumina aerogel and xerogel monoliths, J. Colloid Interface Sci. 338 (2009) 506–513.
[17] W.H. Lizcano-Valbuena, V.A. Paganin, C.A.P. Leite, F. Galembeck, E.R. Gonzalez, Catalysts for DMFC: relation between morphology and electrochemical performance, Electrochim. Acta 48 (2003) 3869–3878.
[18] W.H. Lizcano-Valbuena, D.C. Azevedo, E.R. Gonzalez, Supported metal nanoparticles as electrocatalysts for low-temperature fuel cells, Electrochim. Acta 49 (2004) 1289–1295.
[19] E. Antolini, J.R.C. Salgado, L.G.R.A. Santos, G. Garcia, E.A. Ticcianelli, E. Pastor, E.R. Gonzalez, Carbon supported Pt-Cr alloys as oxygen-reduction catalysts for direct methanol fuel cells, J. Appl. Electrochem. 36 (2006) 355–362.
[20] H. Liu, C. Song, L. Zhang, J. Zhang, H. Wang, D.P. Wilkinson, A review of anode catalysis in the direct methanol fuel cell, J. Power Sources 155 (2006) 95–110.
[21] E. Antolini, Formation of carbon-supported PtM alloys for low temperature fuel cells: a review, Mater. Chem. Phys. 78 (2003) 563–573.
[22] J. Jiang, A. Kucernak, Electrooxidation of small organic molecules on mesoporous precious metal catalysts: II: CO and methanol on platinum–ruthenium alloy, J. Electroanal. Chem. 543 (2003) 187–199.
[23] G.A. Planes, G. García, E. Pastor, High performance mesoporous Pt electrode for methanol electrooxidation. A DEMS study, Electrochem. Commun. 9 (2007) 839–844.
[24] G. García, J. Florez-Montaño, A. Hernandez-Creus, E. Pastor, G.A. Planes, Methanol electrooxidation at mesoporous Pt and Pt–Ru electrodes: a comparative study with carbon supported materials, J. Power Sources 196 (2011) 2979–2986.
[25] A. Kucernak, J. Jiang, Mesoporous platinum as a catalyst for oxygen electroreduction and methanol electrooxidation, Chem. Eng. J. 93 (2003) 81–90.
[26] T.F. Esterle, A.E. Russell, P.N. Bartlett, Study of carbon monoxide oxidation on mesoporous platinum, ChemPhysChem. 11 (2010) 2896–2905.
[27] A. Crown, C. Johnston, A. Wieckowski, Growth of ruthenium islands on Pt (*hkl*) electrodes obtained via repetitive spontaneous deposition, Surf. Sci. 506 (2002) L268–L274.
[28] J.S. Spendelow, P.K. Babu, A. Wieckowski, Electrocatalytic oxidation of carbon monoxide and methanol on platinum surfaces decorated with ruthenium, Curr. Opin. Solid State Mater. Sci. 9 (2005) 37–48.
[29] S. Pérez-Rodríguez, M. Corengia, G. García, C.F. Zinola, M.J. Lázaro, E. Pastor, Gas diffusion electrodes for methanol electrooxidation studied by a new DEMS configuration: influence of the diffusion layer, Int. J. Hydrog. Energy 37 (2012) 7141–7151.
[30] E. Lamy-Pitara, J. Barvier, Platinum modified by electrochemical deposition of adatoms, Appl. Catal. A 149 (1997) 49–87.
[31] H. Massong, S. Tillmann, T. Langkau, E.A. Abd El Meguid, H. Baltruschat, On the influence of tin and bismuth UPD on Pt(111) and Pt(332) on the oxidation of CO, Electrochim. Acta 44 (1998) 1379–1388.
[32] H. Massong, H. Wang, G. Samjeské, H. Baltruschat, The co-catalytic effect of Sn, Ru and Mo decorating steps of Pt (111) vicinal electrode surfaces on the oxidation of CO, Electrochim. Acta 46 (2001) 701–707.
[33] X.Y. Xiao, S. Tillmann, H. Baltruschat, Scanning tunneling microscopy of Sn coadsorbed with Cu and CO on Pt (111) electrodes, Phys. Chem. Chem. Phys. 4 (2002) 4044–4050.
[34] A.A. El-Shafei, M. Eiswirth, Electrochemical activity of Sn-modified Pt single crystal electrodes for ethanol oxidation, Surf. Sci. 604 (2010) 862–867.
[35] S.S. Gupta, S. Singh, J. Datta, Temperature effect on the electrode kinetics of ethanol electro-oxidation on Sn modified Pt catalyst through voltammetry and impedance spectroscopy, Mater. Chem. Phys. 120 (2010) 682–690.
[36] E. Antolini, E.R. Gonzalez, Effect of synthesis method and structural characteristics of Pt–Sn fuel cell catalysts on the electro-oxidation of CH_3OH and CH_3CH_2OH in acid medium, Catal. Today 160 (2011) 28–38.
[37] G. García, M.T.M. Koper, Carbon monoxide oxidation on Pt single crystal electrodes: understanding the catalysis for low temperature fuel cells, ChemPhysChem. 12 (2011) 2064–2072.
[38] S. Stalnionis, L. Tamasauskaite-Tamasiunaite, V. Pautieniene, A. Sudavicius, Z. jusys, Modification of a Pt surface by spontaneous Sn deposition for electrocatalytic applications, J. Solid State Electrochem. 8 (2004) 892–899.
[39] J.F. Moulder, W.F. Stickle, P.E. Sobol, K.D. Bomben, Jill Chastain (Eds.), Handbook of X-ray Photoelectronic Spectroscopy, Perkin-Elmer Corp, Eden Prairie, MN, USA, 1992.
[40] D. Teschner, A. Wootsch, Z. Paál, Preferential CO oxidation in hydrogen (PROX) on unsupported PtSn catalyst, Appl. Catal. A 411–412 (2012) 31–34.
[41] M. Arenz, K.J.J. Mayrhofer, V. Stamenkovic, B.B. Blizanac, T. Tomoyuki, P.N. Ross, N.M. Markovic, The effect of the particle size on the kinetics of CO electrooxidation on high surface area Pt catalysts, J. Am. Chem. Soc. 127 (2005) 6819–6829.
[42] E. Antolini, E.R. González, The electro-oxidation of carbon monoxide, hydrogen/carbon monoxide and methanol in acid medium on Pt-Sn catalysts for low-temperature fuel cells: a comparative review of the effect of Pt-Sn structural characteristics, Electrochim. Acta 56 (2010) 1–14.
[43] D.M. Dos Anjos, F. Hahn, J.M. Léger, K.B. Kokoh, G. Tremiliosi-Filho, Ethanol electrooxidation on Pt-Sn and Pt-Sn-W bulk alloys, J. Braz. Chem. Soc. 19

(2008) 795–799.

[44] O. Guillen-Villafuerte, G. García, R. Guil-Lopez, E. Nieto, J.L. Rodriguez, G. Fierro, E. Pastor, Carbon monoxide and methanol oxidations on Pt/X@ MoO_3/C (X = Mo_2C, MoO_2, Mo^0) electrodes at different temperatures, J. Power Sources 231 (2013) 163–172.

[45] M. Arenz, V. Stamenkovic, B.B. Blizanac, K.J. Mayrhofer, N.M. Markovic, P.N. Ross, Carbon-supported Pt–Sn electrocatalysts for the anodic oxidation of H_2, CO, and H_2/CO mixtures: part II: the structure–activity relationship, J. Catal. 232 (2005) 402–410.

[46] V. Del Colle, J. Souza-García, G. Tremiliosi-Filho, E. Herrero, J.M. Feliu, Electrochemical and spectroscopic studies of ethanol oxidation on Pt stepped surfaces modified by tin adatoms, Phys. Chem. Chem. Phys. 13 (2011) 12163–12172.

[47] A. Cuesta, M. Escudero, B. Lanova, H. Baltruschat, Cyclic voltammetry, ftirs, and dems study of the electrooxidation of carbon monoxide, formic acid, and methanol on cyanide-modified Pt (111) electrodes, Langmuir 25 (2009) 6500–6507.

[48] M. Osawa, K. Komatsu, G. Samjeské, T. Uchida, T. Ikeshoji, A. Cuesta, C. Gutierrez, The role of bridge-bonded adsorbed formate in the electrocatalytic oxidation of formic acid on platinum, Angew. Chem. Int. 50 (2011) 1159–1163.

[49] A. Cuesta, G. Cabello, M. Osawa, C. Gutierrez, Mechanism of the electrocatalytic oxidation of formic acid on metals, ACS Catal. 2 (2012) 728–738.

[50] Y. Ishikawa, M. Sheng Liao, C.R. Cabrera, Oxidation of methanol on platinum, ruthenium and mixed Pt–M metals (M = Ru, Sn): a theoretical study, Surf. Sci. 463 (2000) 66–80.

Elsevier Editorial System(tm) for
Electrochimica Acta
Manuscript Draft

Manuscript Number:

Title: Mechanism of ethanol electrooxidation on mesoporous Pt electrode in acidic medium studied by a novel electrochemical mass spectrometry set-up

Article Type: Research Paper

Keywords: Ethanol electrooxidation; Mesoporous platinum; EC-MS; Carbon dioxide; Fuel cells

Corresponding Author: Dr. Gonzalo García,

Corresponding Author's Institution: La Laguna University

First Author: Jonathan Flórez-Montaño

Order of Authors: Jonathan Flórez-Montaño; Gonzalo García; Olmedo Guillén-Villafuertea; José L Rodríguez; Gabriel A Planes; Elena Pastor

Abstract: The electrochemical behavior and mass spectrometric features for ethanol reactions on nanostructured mesoporous platinum catalysts (MPPt) in 0.5 M H2SO4 were studied for the first time as function of the alcohol concentration. With this purpose, cyclic voltammetry and chronoamperometry techniques were combined with a new configuration of an electrochemical mass spectrometry (EC-MS), which allows high detection sensitivity with low amount of catalysts. Accordingly, a comprehensive study of the reaction mechanism and kinetics of the ethanol oxidation on MPPt in acidic medium was carried out. The water dissociation reaction and the first ethanol dehydrogenation step are proposed to be the rate-determining step (rds) for the complete ethanol oxidation reaction and the acetaldehyde production, respectively. Furthermore, acetaldehyde, acetic acid and CO2 formation were monitored during the ethanol electrooxidation reaction and the energy conversion efficiency from ethanol to CO2 was calculated. Results indicate an increment of by-side products (acetaldehyde and acetic acid) maintaining equal CO2 formation with the rise of the alcohol concentration. Consequently, the highest energy conversion efficiency to CO2 (~11 %) was achieved at 0.6 V with the lowest alcohol concentration employed (0.01 M). Results were analyzed in terms of density and type of active surface sites, applied potential and alcohol concentration.

ULL | Universidad de La Laguna

Departamento de Química Física
Dr. Gonzalo García

A.R. Hillman
Editor in Chief, Electrochimica Acta

La Laguna, 22-10-2015

Dear Prof. A.R. Hillman

I send you herewith the electronic version of the manuscript entitled:

“Mechanism of ethanol electrooxidation on mesoporous Pt electrode in acidic medium studied by a novel electrochemical mass spectrometry set-up”

by the authors:

Jonathan Flórez-Montaño, Gonzalo García, Olmedo Guillén-Villafuerte, José Luis Rodríguez, Gabriel A. Planes, Elena Pastor

To be considered for publication in Electrochimica Acta. This is an original article, unpublished, not being considered for publication elsewhere.

In the present work, the electrochemical behavior and mass spectrometric features for ethanol reactions on nanostructured mesoporous platinum catalysts (MPPt) in 0.5 M H_2SO_4 were studied for the first time as function of the alcohol concentration. With this purpose, cyclic voltammetry and chronoamperometry techniques were combined with a new configuration of an electrochemical mass spectrometry (EC-MS), which allows high detection sensitivity with low amount of catalysts. Accordingly, a comprehensive study of the reaction mechanism and kinetics of the ethanol oxidation on MPPt in acidic medium was carried out. Additionally, a profound applied work related to energy generation throughout the fuel cell technology was carried out and the energy conversion efficiency from ethanol to CO_2 was calculated.

We hope that the manuscript will interest your audience, especially in the fields of Surface Science and Fuel Cell.

Sincerely yours,

Dr. G. García

Suggested referees:

Prof. David Fermin
School of Chemistry, University of Bristol
Office S123, Cantock's Close, Clifton, Bristol BS8 1TS, United Kingdom
Email: david.fermin@bristol.ac.uk

Dr. Vincenzo Baglio
Consiglio Nazionale delle Ricerche -ITAE
Via Salita S. Lucia sopra Contesse 5, 98126 Messina, Italy
E-mail: vincenzo.baglio@itae.cnr.it

Dr. M. Victoria Martínez Huerta
Instituto de Catálisis y Petroleoquímica-CSIC
Marie Curie, 2 Cantoblanco, 28049 Madrid, Spain
E-mail: mmartinez@icp.csic.es

Graphical Abstract (for review)

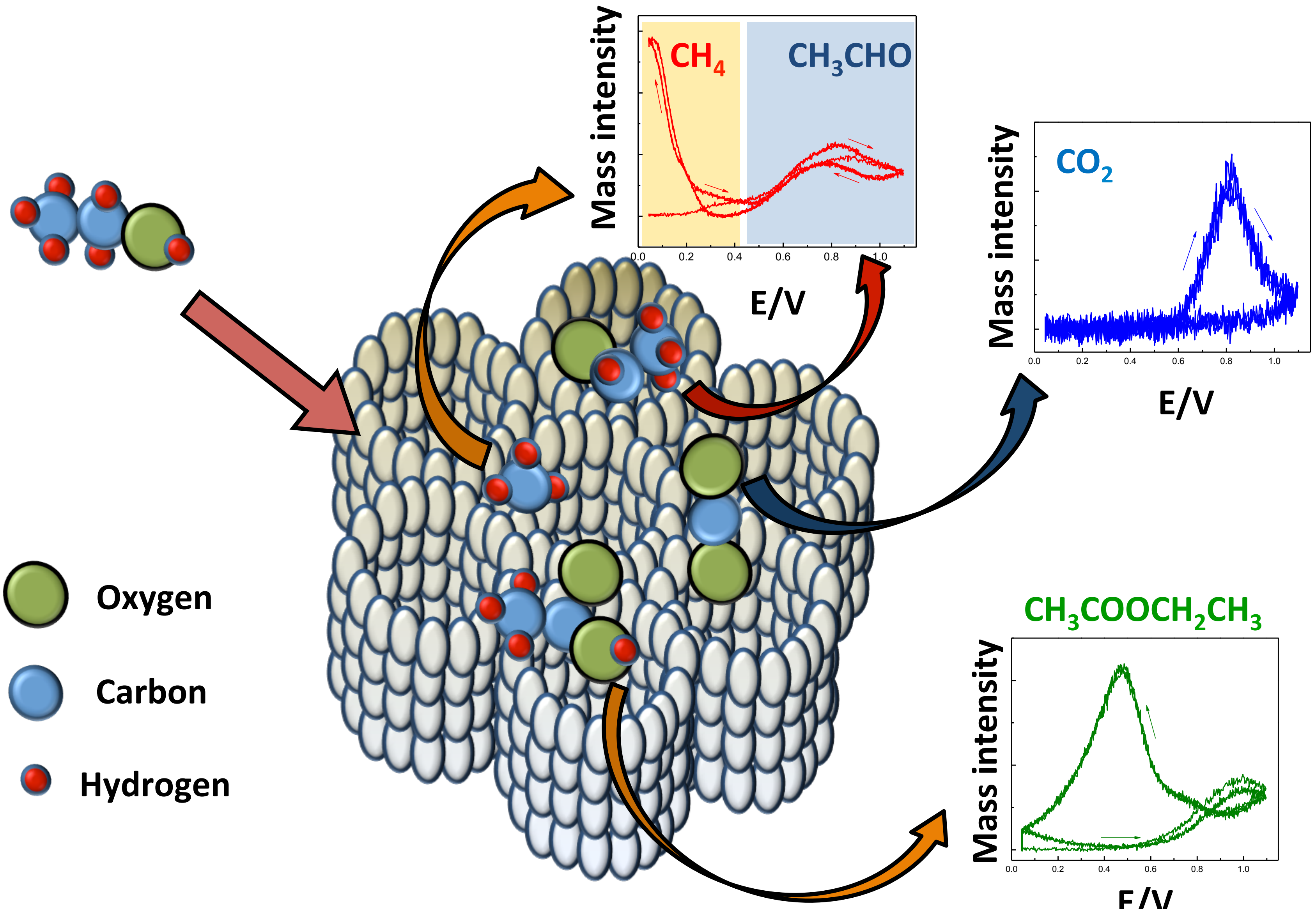

Highlights:

The electrooxidation of ethanol on mesoporous platinum (MPPt) was studied

A new configuration of an electrochemical mass spectrometry (EC-MS) was developed

Methane formation during the positive scan is for the first time reported

A complete study of the reaction mechanism and kinetics of the ethanol oxidation on MPPt was carried out

Energy conversion efficiency from ethanol to CO_2 as function of alcohol concentration was studied

Mechanism of ethanol electrooxidation on mesoporous Pt electrode in acidic medium studied by a novel electrochemical mass spectrometry set-up

Jonathan Flórez-Montaño[a], Gonzalo García[a*], Olmedo Guillén-Villafuerte[a], José Luis Rodríguez[a], Gabriel A. Planes[b], Elena Pastor[a*]

[a]*Instituto de Materiales y Nanotecnología, Universidad de La Laguna, Avda. Astrofísico Francisco Sánchez s/n, 38071 La Laguna, Santa Cruz de Tenerife (Spain).*

[b]*Universidad Nacional de Río Cuarto. Ruta Nac. 36, Km 601, Río Cuarto, Córdoba (Argentina).*

* Corresponding author. Tel.: +34 922 318071; fax: +34 922 318002
E-mail address: ggarcia@ull.edu.es (Gonzalo García).
E-mail address: epastor@ull.edu.es (Elena Pastor).

Abstract

The electrochemical behavior and mass spectrometric features for ethanol reactions on nanostructured mesoporous platinum catalysts (MPPt) in 0.5 M H_2SO_4 were studied for the first time as function of the alcohol concentration. With this purpose, cyclic voltammetry and chronoamperometry techniques were combined with a new configuration of an electrochemical mass spectrometry (EC-MS), which allows high detection sensitivity with low amount of catalysts. Accordingly, a comprehensive study of the reaction mechanism and kinetics of the ethanol oxidation on MPPt in acidic medium was carried out. The water dissociation reaction and the first ethanol dehydrogenation step are proposed to be the rate-determining step (*rds*) for the complete ethanol oxidation reaction and the acetaldehyde production, respectively. Furthermore, acetaldehyde, acetic acid and CO_2 formation were monitored during the ethanol electrooxidation reaction and the energy conversion efficiency from ethanol to CO_2 was calculated. Results indicate an increment of by-side products (acetaldehyde and acetic acid) maintaining equal CO_2 formation with the rise of the alcohol concentration. Consequently, the highest energy conversion efficiency to CO_2 (~11 %) was achieved at 0.6 V with the lowest alcohol concentration employed (0.01 M). Results were analyzed in terms of density and type of active surface sites, applied potential and alcohol concentration.

Keywords: Ethanol electrooxidation, Mesoporous platinum, EC-MS, Carbon dioxide, Fuel cells

1. Introduction

Direct alcohol fuel cells (DAFCs) have attracted considerable interest in recent years because of their potential for portable applications. The main advantage of alcohols as fuel compared to hydrogen is that they are liquid, and therefore, the storage problems are solved. Additionally, the power density of alcohols in terms of energy per volume of fuel is much higher than hydrogen at standard conditions. Since ethanol is the major renewable bio-fuel and less toxic than other alcohols, it appears as a promising liquid fuel for DAFC systems [1-3].

Conventional fuel cell catalysts are mainly composed of metallic nanoparticles (e.g. Pt or Pt alloys) supported on high surface area carbon (e.g. carbon black). The properties of these materials, such as surface area and conductivity, determine the yield of the different electrochemical reactions taking place in DAFCs [4,5], although one of the main drawbacks is the facile catalyst support corrosion under the hard operating conditions. Contrary to conventional catalysts employed in these devices, non-carbon supported mesoporous (MP) metallic nanostructures are easily produced directly onto a conductive material, and therefore compact catalysts with high performance (high catalytic activity and high tolerance toward the corrosion) can be integrated in electronic devices such as micro fuel cells (μFC) and/or direct alcohol micro fuel cells (DAμFC).

Metallic MP catalysts can be synthesized by chemical or electrochemical reduction of metallic salts dissolved in the aqueous domains of a liquid crystal solution [6,7]. Usually, this simple process renders thin and shiny electrodes with high surface area and activity [7]. The MP structure, determined by the porous dimension and porosity degree, is easily tuned by adjusting the synthesis parameters, such as the surfactant, reduction potential and time expended at the applied potential [8]. Usually, the catalysts synthesized contain a porous architecture with an extremely concave MP surface, which strongly affect the CO electrooxidation reaction [9] and improve the catalytic oxidation of the alcohols [10,11].

The full oxidation of ethanol to carbon dioxide has a favorable thermodynamic potential of 0.08 V (vs. RHE), although the efficiency of direct ethanol fuel cells is drastically limited by the formation of partial oxidation products (maintaining intact the carbon-carbon bond, such as acetaldehyde and acetic acid) and strongly adsorbed intermediates [12]. It is accepted that two main paths exist in the overall mechanism of ethanol oxidation at Pt-based electrodes [13]. The first involves the dissociative adsorption of ethanol to produce adsorbed species (CO and CH_x) at low potentials [14-15], whereas the second includes the formation of an adsorbed acetyl species (CH_3CO) that can be further oxidized to acetaldehyde and in presence of adsorbed OH to acetic acid and as a minor extent to carbon dioxide [16].

Pt-based catalysts such as PtSn [17] or PtRu [18] were suggested to enhance the electrocatalytic performance for ethanol electrooxidation with respect to monometallic Pt catalyst. In this sense, it is believed that the use of oxophilic atoms increase the CO tolerance as they enhance the activation of water to form surface hydroxides, which are necessary to oxidize CO and possibly CH_x intermediates by the bifunctional mechanism or electronic effects [19]. In this context, not only foreign elements such as Ru or Sn (i.e. changes in the nature of the material) may produce oxygenated species at low overpotentials, but also Pt atoms located at special sites such as low-coordinated sites are known to easily dissociate water (i.e. effect of the surface geometric structure) [19]. Thus, mesoporous platinum (MPPt) catalysts with extremely high concave structure are expected to produce a synergetic effect during the CO and ethanol oxidation reactions.

The reactivity of ethanol on noble metal electrodes has been the subject of many spectroscopic investigations during the past years. Main identified products by in-situ Fourier transform infrared spectroscopy (FTIRS) [20-22] and on-line differential electrochemical mass spectrometry (DEMS) [23-25] during the ethanol oxidation on Pt in acidic solution were acetaldehyde, acetic acid, adsorbed carbon monoxide and CO_2. DEMS technique has proven to be a useful tool for the study of electrocatalytic processes, in which volatile or gaseous species are involved [21,23,26,27]. In this sense, it appears as an adequate technique to study the reaction mechanisms and the conversion efficiency to final products of the fuel employed in the fuel cell system. Quantitative and qualitative detection of reaction products and intermediates, as well as, the consumption of electroactive species can be easily followed. DEMS experiments showed low CO_2 conversion efficiencies from the ethanol oxidation on carbon-supported Pt catalysts (< 3%) and smooth polycrystalline Pt surfaces (< 2%) [**Error! Bookmark not defined.**,24,27]. The efficiency of ethanol conversion to CO_2 depends on several factors such as an adequate DEMS set-up [28], the catalytic surface structure and nature [29-31], the alcohol concentration [32] and the working temperature [33]. Nevertheless, there is a consensus that the ethanol electrooxidation reaction is not complete and that acetaldehyde and acetic acid are the main responsible for the ca. 30 and 60 % of the delivered faradaic current, respectively [25].

In the current work, ethanol electrooxidation in acidic medium is studied on MPPt catalyst for the first time by a new electrochemical mass spectrometry (EC-MS) configuration. This new set-up allows the use of massive electrodes as well as powder catalysts achieving high sensitivities with low amounts of material, being more versatile than other conventional electrochemical mass spectrometry designs. Reaction intermediates as well as ethanol oxidation products were detected, and the efficiency for ethanol oxidation to CO_2 was achieved for diverse ethanol concentrations.

2. Experiment measurement

2.1 Working electrode preparation. MPPt electrodes were obtained by electrochemical reduction of a mixture of aqueous hexachloroplatinic acid (8%) and octaethylene glycol monohexadecyl ether ($C_{16}EO_8$) (50 % weight fraction) onto an Au disk electrode (Ø = 1mm) at 60 ºC and 0.15 V as have been reported in early publications [6,7]. Structural characterization has been also reported in these works.

2.2 Electrochemical measurements. A thermostated three electrodes electrochemical cell was used to perform the analysis at 25 °C. This cell allows solution exchange under working electrode potential control. A carbon rod was used as counter electrode and a reversible hydrogen electrode (RHE) in the electrolyte as reference electrode. All potentials in this work are given against the RHE. Electrochemical measurements were performed with a PC Autolab potentiostat-galvanostat PGSTAT30.

Experiments were carried out in 0.5 M aqueous sulphuric solutions prepared from high purity reagents (Merck p.a.) and ultra-pure water (Millipore MilliQ gradient A10 system, 18.2 MΩ cm, 2 ppb total organic carbon). Argon (N50) was used to deoxygenate all solutions and CO (N47) to dose CO. CO stripping experiments were obtained after bubbling CO through the cell for 15 min while keeping the MPPt electrode at 0.20 V, followed by argon purging and electrolyte exchange to remove the excess of CO. CO stripping voltammograms were recorded, by first scanning negatively until 0.05 V so that entire hydrogen region was explored, and then scanning positively up to 1.0 V.

The charge involved in the CO oxidation peak was used to determine the electroactive area, assuming a charge of 420 μC cm^{-2} involved in the oxidation of a monolayer of linearly adsorbed CO. Current densities J given in the present paper were calculated with the previously achieved electroactive surface area (ESA).

Potentiodynamic and potentiostatic experiences of ethanol oxidation were performed with several alcohol concentrations (in the range from 0.01 to 1 M). First the working electrode was fixed to 0.05 V and later the alcohol solution was introduced into the electrochemical cell. Next, cyclic voltammograms (CVs) or current transients (CTs) were obtained by sweeping/stepping the potential from 0.05 V to the final oxidation potential.

2.3 EC-MS set-up. Gaseous species produced on the electroactive surface were continuously detected by a new electrochemical mass spectrometry (EC-MS) configuration. The new set-up has the same working principle as the on-line electrochemical mass spectrometry (OLEMS) developed by Koper et al. in the 2006 [34], i.e. no differential pumping is needed during the measurement as only small amount of gas enters to the mass spectrometer. However, there are two main differences between both set-ups: the new EC-MS is handier and easier to build up than OLEMS. Briefly, the analysis system is commercial (Omnistar^{TM}, Pfeiffer) and contains a capillary made of stainless steel as gas inlet, which was replaced by a commercial PTFE capillary (Supelco). The small inlet tip consists of a porous PTFE membrane (Gore-Tex) positioned onto the PTFE capillary and fixed by a PTFE holder (Scheme 1). Thus, the PTFE membrane works as interface between the vacuum of the mass spectrometer and the electrolyte.

The set-up allows the use of massive electrodes such as single crystals and mesoporous materials. It is versatile since the high flexibility of the PTFE capillary allows different arrangements. For example, the inlet tip can be positioned close to the surface of an electrode in hanging meniscus configuration (i.e. OLEMS configuration) or just in the opposite way (see Scheme 1) that allows higher sensitivity and lower response time since volatile species tend to go up. In this context, the new EC-MS system opens new avenues of research that are not only limited to electrochemical experiments. Further information on this set-up is given in [35].

With this EC-MS set-up, mass spectrometry cyclic voltammograms (MSCVs) and mass transients (MST) can be recorded simultaneously with the CVs and CTs, respectively.

2.4 EC-MS calibration. CO_2 and CH_3CHO are produced during the ethanol electrooxidation and both compounds contribute to the signal m/z = 44 ($CO_2^{\cdot+}$ and $CH_3CHO^{\cdot+}$ fragments, respectively). For this reason, the m/z = 22 signal (CO_2^{++}) was used instead of m/z = 44 to follow, distinguish and quantify the amount of CO_2 produced. The current efficiency for ethanol electrooxidation to CO_2 is determined from the subsequent equation (12 electrons per molecule of ethanol):

$$E^{CO_2} = \frac{6Q_i}{K^*_{22} Q_f} \qquad (1)$$

where Q_f and Q_i are the faradaic charge and the ionic charge calculated from the integration of the CVs and mass spectrometric cyclic voltammograms (MSCVs) for m/z = 22, respectively, simultaneously recorded during the ethanol oxidation reaction. The factor 6 is related to the number of electrons required to produce a molecule of CO_2 during the alcohol oxidation. K_{22}^* is the calibration constant for the m/z = 22 signal, which is calculated from a CO stripping experiment through the following expression:

$$K^*_{22} = \frac{2Q_i}{Q_f} \qquad (2)$$

where Q_f and Q_i are the faradaic charge and the ionic charge for m/z = 22, respectively, simultaneously recorded during the oxidation of a monolayer of adsorbed CO (CO_{ad}) to CO_2. The factor 2 is associated to the number of electrons required to produce a molecule of CO_2 during the CO_{ad} oxidation reaction.

3. Results and discussion

3.1 CO stripping

Since adsorbed CO is a strong catalyst poison and it is also a reaction intermediate during the ethanol electrooxidation reaction, its removal from the catalyst surface (denoted as CO stripping) is a key factor to be investigated [10,35]. Furthermore, the CO stripping is a powerful technique for the surface morphology and structure study. In addition, CO stripping is a convenient technique to obtain an accurate estimation of the ESA [9,36].

Figure 1 shows the CO stripping voltammogram and the subsequent CVs recorded for the MPPt catalyst in acidic medium at a scan rate of 5 mV s^{-1} (black lines). Additionally, the MSCVs achieved with ionic currents that are associated to carbon dioxide formation (m/z = 22 and 44) are also depicted in Figure 1. The second CV resembles that previously reported for MPPt surfaces in acidic medium [10]. Thus, the voltammogram shows the presence of reversible current peaks at 0.12 and 0.27 V, which are related to H adsorption/desorption on sites with (110) and (100) orientation, respectively [19]. Additionally, it is clearly observed the onset for the Pt surface oxidation at higher potentials than 0.6 V, which is reduced during the backward scan from 1.0 to 0.6 V.

On the other hand, it is established that the onset potential for the CO oxidation reaction on MPPt catalyst occurs at ca. 0.4 V and that the well-known “pre-peak” appears in this case as an anodic constant current that extends until ca. 0.6 V. The cause of the “pre-peak” has been largely discussed using Pt single crystals in acidic and alkaline media [9,19,30,33,37], and the enhanced catalytic activity toward the CO tolerance was tentatively related to an easily water dissociation on “special sites” such as low-coordinated atoms (atoms situated at border, step, edge, or kink sites), in which the local electronic density is highly altered. Therefore, the charge density under the “pre-peak” region observed at the MPPt catalyst has to be associated to the CO oxidation at very active sites presumably situated onto the concave structure of the electrode. At more positive potentials the complete CO removal occurs developing an anodic peak centered at ca. 0.68 V [9,38]. Then, it is normally accepted that the electrooxidation of adsorbed CO follows a Langmuir–Hinshelwood mechanism, in which the first reaction should be the formation of oxygenated species on the surface [39,40]:

$$\mathrm{Pt} + \mathrm{H_2O} \longrightarrow \mathrm{Pt\text{-}OH} + \mathrm{H^+} + e^- \qquad (1)$$

$$\text{Pt-CO} + \text{Pt-OH} \longrightarrow \text{Pt-COOH} + \text{Pt} \qquad (2)$$

$$\text{Pt-COOH} \longrightarrow CO_2 + H^+ + e^- + \text{Pt} \qquad (3)$$

The signals for m/z = 22 (CO_2^{++}) and m/z = 44 (CO_2^{+}), which are detected at the mass spectrometer, are both associated to the formation of carbon dioxide during the CO_{ad} electrooxidation reaction. Faradaic current can be calculated from the calibration constant for the m/z = 22 (K_{22}^{*}) as was described above (section 2.4). The shift for the main CO_{ad} oxidation peak to higher potentials in the MSCVs can be explained in terms of the impeded diffusion of relatively high amount of CO_2 from the mesoporous structure of the catalyst, which partially delays the detection at the mass spectrometer. However, it is observed that the m/z = 22 and 44 signals decay to zero indicating that all CO_2 produced is detected during the positive-going scan. In this context, the high precision of the new EC-MS set-up allows the detection of the onset potential for the CO oxidation reaction with great exactitude (no shift is expected in the signals at the onset potential as only small amounts of CO_2 are formed and diffusion is not constrained). Thus, from these results it can be concluded that after the correct calibration of the EC-MS system, becomes feasible to study the reaction mechanism and to achieve the ethanol conversion efficiency to CO_2. It is remarkable that a complete on-line detection of the CO stripping (with no shift in the peak potential) is recorded when this configuration is used for the study of carbon supported materials with the same EC-MS (see [35] for more details), so the shift in Figure 1 has to be related to the electrode morphology.

3.2 Ethanol electroreactivity

3.2.1 CVs and MSCVs for MPPt in 0.01 M CH_3CH_2OH + 0.5 M H_2SO_4 solution

Figure 2 shows the first two CVs and the corresponding MSCVs for the m/z = 22 (CO_2^{++}), m/z = 29 (CHO^+) and m/z = 15 (CH_3^+) signals during the electrooxidation of 0.01 M ethanol at the MPPt electrode in acidic media recorded at 2 mV s^{-1}. The signals for m/z = 22 and 29 are related to carbon dioxide and acetaldehyde formation, respectively, while the m/z signal 15 is associated to methane and acetaldehyde production (CH_3^+ fragment from both compounds) at low ($E < 0.5$ V in the forward scan and $E < 0.3$ V in the negative sweep) and high ($E > 0.5$ V in the forward scan and $E > 0.3$ V in the negative sweep) potentials, respectively. The signal for m/z = 15 could be associated to the production of acetaldehyde in the whole potential range, but a close comparison of the MSCVs for m/z = 15 and 29 (the latter only related to acetaldehyde), shows that both MSCVs are similar for E > 0.5 V but at E < 0.5 V the features in the MSCV for m/z = 15 are not present for m/z = 29. Therefore, in this potential range the signal for m/z = 15 has to be related to the formation of a different compound, in this case methane (this difference is even more apparent for 0.1 M ethanol concentration, see Figure 4 middle panels). It is remarkable that methane formation on carbon supported Pt during the forward scan of ethanol electrooxidation in the 0.2-0.5 V potential range has been reported for the first time by our group [35]. As in that case, methane is also produced in the same potential region at MPPt.

It is important to take into account that the ethanol solution was introduced into the cell at a controlled working electrode potential of 0.05 V. Therefore, a competitive adsorption between hydrogen and ethanol is expected during the first potential-going scan from 0.05 V upwards [15,24,27]. A detailed view of the first positive-going scan (Figure 2A) suggests two potential regions, which account for the two main steps of the ethanol oxidation reaction. First, ethanol electrosorption and dehydrogenation steps occur at E < 0.38 V, and the delivered faradaic current in this potential region is related to the hydrogen desorption, ethanol adsorption/dehydrogenation reactions and methane formation. At higher potentials, electrooxidation takes place. A close view of the m/z = 29 and m/z = 15 signals indicate that the onset potentials for acetaldehyde and methane formation are located at 0.38 and 0.2 V, respectively. Moreover, the onset potentials for methane and acetaldehyde coincide with the completion of hydrogen desorption on Pt sites with (110) and (100) orientation, respectively.

In this context, it can be concluded that the dissociative adsorption of ethanol on MPPt at low potentials is not obstructed by the high degree of adsorbed hydrogen, in contrast to what is reported for alcohols on other type of Pt structures [24,26,41-44]. On the other hand, in agreement with previous studies, the results depicted in Figure 2 indicate that breaking of the C-C bond of ethanol molecule can occur at E < 0.5 V and partial oxidation at E > 0.38 V [25]. Other details of the ethanol oxidation reaction mechanism will be described below.

The electrooxidation of ethanol to acetaldehyde is visible at E > 0.38 V (signal for m/z = 29), while the electrooxidation of ethanol fragments (e.g. CO_{ad}) to produce CO_2 (signal for m/z = 22) is apparent at E > 0.5 V. Interestingly all signals (ionic and faradaic currents) develop a peak at ca. 0.8 V, which is close to the onset potential for water dissociation on platinum surface, i.e.

OH_{ad} formation (reaction 1). At potentials higher than 0.8 V, the signal associated to carbon dioxide formation falls to zero, meanwhile the signal related to acetaldehyde decreases. It is well known that alcohol adsorption is inhibited at platinum oxides surface, and consequently, the lower activity toward the ethanol oxidation at these positive potentials is attributed to this fact.

Acetic acid is dissociated in the solution and even being volatile enough, cannot be easily detected by DEMS. However, it can be indirectly followed by the signals m/z = 43, 61 and 73 due to a chemical reaction of the generated acid with ethanol forming the corresponding ester at high ethanol concentrations, as will be discussed in the subsequent section (3.2.3).

During the backward scan, an increment of the faradaic current and acetaldehyde signals (m/z = 15 and 29) is observed between 1.0 and 0.75 V. This behavior is related to surface Pt oxides reduction accompanied with ethanol re-adsorption which finally reacts again. Then, the rate of acetaldehyde formation decreases at $E < 0.75$ V. In addition, the profile of the m/z = 22 signal during the backward scan indicates that almost no carbon dioxide is produced. The last must be associated to negligible C-C bond breaking of the alcohol during the negative-going potential sweep in this potential region. Furthermore, subsequent potentiodynamic cycles for m/z = 22 display the same mass spectrometric profiles, which indicates that equal amount of adsorbed ethanol residues are formed in each cycle. As will be described below, the yield of carbon dioxide is almost independent of ethanol concentration, a fact that can be taken as an indication that CO_2 is mainly produced from the adsorbed species formed on the Pt surface at low potentials.

On the other hand, the MSCV for m/z = 15 (CH_3^+) shows a similar profile to the mass m/z = 29 at $E > 0.5$ V, and therefore, can be ascribed to acetaldehyde production. However, the profile is completely different during the backward scan and subsequent scans at $E < 0.38$ V, in which a strong increment of the m/z = 15 signal is discerned. In this context, the rise of this signal at $E < 0.38$ V is associated to the formation of methane, and consequently, CO_{ad} is expected as adsorbed intermediate from the C-C scission of the ethanol molecule. However, the production of ethane was also observed in this potential region through the signal for m/z = 30 ($C_2H_6^+$) (see later, Figure 6) indicating that C_2-adsorbed species are also formed.

Then, a variety of adsorbed species different and less oxidized than CO_{ad} are present on the catalysts surface, being probably responsible for the low oxidation efficiencies obtained for ethanol electrooxidation to CO_2. According to these results, it is concluded that the m/z = 15 signal follows both acetaldehyde and methane formation on MPPt electrode at higher and lower potentials than 0.3 V, respectively.

3.2.2 CVs and MSCVs for MPPt in 0.01-1.0 M CH_3CH_2OH + 0.5 M H_2SO_4 solutions

In order to study the effect of ethanol concentration during the alcohol oxidation reaction at MPPt electrode, several ethanol solutions were employed. Figure 3 depicts the CVs and MSCVs (m/z = 22 and 44) for the electrooxidation of ethanol (0.01 – 1.0 M) on MPPt in acidic medium. It can be observed a strong increment of the faradaic current and the m/z = 44 signal with the rise of the alcohol concentration. It is noticeable that the m/z = 44 signal can be related to acetaldehyde (CH_3CHO^+) and/or carbon dioxide formation (CO_2^+). However, the m/z = 22 signal, associated only to carbon dioxide production, remains almost constant with the increment of the alcohol concentration. Therefore, the rise of the faradaic current with the ethanol concentration must be related to an increment of by-side reactions, such as acetaldehyde (and acetic acid) production.

In order to confirm the stated above, the ethanol oxidation reaction on MPPt in acidic media was monitored with the mass signals for m/z = 15 and 29 and the alcohol concentration was varied. Figure 4 shows the first two CVs and the corresponding MSCVs for the m/z = 22 (CO_2^{++}), m/z = 15 (CH_3^+) and m/z = 29 (CHO^+) signals during the electrooxidation of three different concentration of ethanol (0.01, 0.1 and 1.0 M) at the MPPt electrode in acidic media recorded at 2 mV s^{-1}. It can be discerned in the CVs that the current density increases and the main anodic peak shifts toward more positive potentials with the rise of alcohol concentration. In this context, the acetaldehyde production (m/z = 29) and the faradaic current follow similar profiles (as well as the signal for m/z = 44 in Figure 3), and it is observed that 10-fold increase in ethanol concentration produces a 10-fold increase of the m/z = 29 signal. The ion current associated to the m/z = 15 signal increases as the m/z = 29 signal at higher potentials than 0.5 V with the rise of the alcohol concentration.

Interestingly, the amount of methane formation (m/z = 15) between 0.2 and 0.45 V during the first forward scan also increases 10-fold with the rise of ethanol concentration from 0.01 to 0.1 M (see Figure 5 for a magnification of the signal in this potential region). However, the intensities of the m/z = 15 signal at E < 0.3 V during the negative sweep and subsequent scans are not (or slightly) affected by the ethanol concentration. The same occurs with the MSCV for m/z = 22. The last behavior indicates that the CH_4 and CO_2 formation, and consequently the C-C bond breaking, is nearly independent of the ethanol concentration after the first positive scan, in agreement with previous results achieved at carbon supported Pt catalysts [25].

The formation of acetic acid from the ethanol oxidation reaction in acidic medium can be followed indirectly, for example by the signal for m/z = 61 ($C_2H_5O_2^+$) (middle panel of Figure 6). As was described above, the dissociation and lower volatility of acetic acid makes impossible its detection by EC-MS and therefore another strategy must be adopted. In this context, it is well known that ethyl acetate ester can be produced from the chemical reaction occurring between ethanol and acetic acid in low pH solutions:

$$CH_3COOH + CH_3CH_2OH \rightleftharpoons CH_3COOCH_2CH_3 + H_2O \qquad (4)$$

Thus, ethyl acetate ester is a volatile molecule that can be identified by EC-MS and the m/z = 43, 61 and 73 signals (the last two in Figure 6) are usual ionic fragments of ethyl acetate to follow during the ethanol oxidation reaction [22,45]. However, the detection time at the mass spectrometer is quite high and an accurate measurement is not possible (see the delay time between the CV and the MSCV). The last is associated to several effects such as the diffusion time from the bulk solution (reaction (4) is not a surface but a bulk solution reaction) to the PTFE membrane, the low permeability of the ethyl acetate ester through the PTFE membrane, as well as, the reaction rate of the equation (4) [**Error! Bookmark not defined.**]. As an equilibrium reaction, it is shifted to the right at high ethanol concentrations. Thus, acetic acid formation can only be indirectly followed by EC-MS at 1.0 M ethanol concentration.

3.2.3 Chronoamperometric studies for MPPt electrode in 0.01-1.0 M CH_3CH_2OH + 0.5 M H_2SO_4 solution. Efficiencies for ethanol conversion to CO_2.

Potentiostatic measurements allow a more precise determination of the conversion efficiency for the ethanol oxidation reaction at relevant voltage values for DAFCs, as the problems associated with the slow diffusion of CO_2 from the MP structure to be detected are avoided if enough recording time is considered. Figure 7 depicts the current transients (CTs) and mass spectrometric current transients (MSCTs) recorded at different applied potentials and several ethanol concentrations in sulphuric acid medium. In agreement with the MSCVs for the m/z = 22 signal (Figures 3 and 4), carbon dioxide formation is not observed in Figure 7 at lower potentials than 0.6 V and its production is almost constant with all ethanol concentrations analyzed. On the other hand, the m/z = 29 signal related to acetaldehyde production increases with the rise of the applied potential and the ethanol concentration, also in good agreement with the voltammetric study described above (Figures 3 and 4). These results confirm that the partial oxidation of ethanol to acetaldehyde (and presumably acetic acid) is the main contribution to the overall faradaic current. On the other hand, it is noticeable the close correlation between faradaic and ionic currents, which indicates the great performance of the novel EC-MS configuration.

Table 1 shows the efficiencies for ethanol conversion to CO_2 (E^{CO2}) calculated for different alcohol concentrations at 0.6 and 0.7 V. In agreement with the potentiostatic and potentiodynamic studies, the highest E^{CO2} (11.1 %) is achieved at 0.6 V with the lowest ethanol concentration utilized (0.01 M), and it decreases with increasing the potential and the rise of alcohol concentration.

3.2.5 Kinetics and reaction mechanism of ethanol electrooxidation at MPPt

In agreement with the results showed above and those in the literature [39,46-50], we are in conditions to give a global description of the ethanol adsorption, oxidation and reduction processes at MPPt electrode. It is well known that saturated alcohol molecules have two reactive sites, the OH group and the α-carbon atom, that can interact with the Pt surface during the adsorption process:

$$\mathrm{Pt + CH_3CH_2OH \rightleftharpoons Pt(CH_3CH_2OH)} \quad (5)$$

$$\mathrm{Pt(CH_3CH_2OH) \longrightarrow Pt\text{-}OCH_2CH_3 + H^+ + e^-} \quad (6)$$

$$\mathrm{Pt(CH_3CH_2OH) \longrightarrow Pt\text{-}CHOHCH_3 + H^+ + e^-} \quad (7)$$

These reactions can be considered the starting steps for the ethanol electrooxidation reaction. These processes occur during the positive scan as soon as free Pt sites are available once hydrogen starts to be desorbed. The ethoxi species Pt-OCH_2CH_3 is relatively stable, whereas the alcohol derivative Pt-$CHOHCH_3$ easily dehydrogenates [15] finally producing acetaldehyde:

$$\mathrm{Pt\text{-}CHOHCH_3 \longrightarrow Pt(HCOCH_3) + H^+ + e^-} \quad (8)$$

$$\mathrm{Pt(HCOCH_3) \rightleftharpoons Pt + HCOCH_3} \quad (9)$$

Both adsorbed ethoxi and alcoholic C_2-intermediates were previously detected at polycrystalline Pt by FTIRS [15,51]. Reactions 7-9 are the main responsible for the delivered current and **acetaldehyde production** at potentials higher than 0.38 V (in the absence of adsorbed hydrogen) and are strongly dependent on the ethanol concentration.

However, during the first positive potential going scan between 0.05 and 0.38 V, it can be assumed that ethanol initially adsorbs at Pt(110) sites as soon as this sites become free of H_{ad} and the alcohol intermediate formed in reaction (7) reacts with H_{ad} still present at (100) sites producing methane:

$$Pt_{100}(H) + Pt\text{-}CHOHCH_3 \longrightarrow Pt\text{-}CO + CH_4 + 2H^+ + 2e^- \qquad (10)$$

This reaction accounts for **methane production** observed **in the first anodic scan in the 0.2-0.4 V potential range** (Figure 5), and as in the case of reactions 7-9, is strongly dependent on ethanol concentration. It is noteworthy that reaction (10) is in agreement with FTIRS experiments in which **adsorbed carbon monoxide** on Pt single crystals was detected at similar potentials [22]. However, FTIRS is not able to detect methane since a change in the dipole moment should occur for a vibration to be infrared active.

On the other hand, if free Pt sites are available, further deprotonation of alcohol species is possible according to:

$$Pt\text{-}CHOHCH_3 + Pt \longrightarrow Pt_2\text{-}COHCH_3 + H^+ + e^- \qquad (11)$$

This new adsorbate cannot be desorbed as acetaldehyde and will be finally oxidized to CO_2 (see Scheme 2) in the positive run. Moreover, further scission of the C-C bond can occur through the reaction:

$$Pt_2\text{-}COHCH_3 \longrightarrow Pt\text{-}CH_3 + Pt\text{-}CO + H^+ + e^- \qquad (12)$$

During the reverse scan, adsorption and deprotonation of ethanol with the formation of species in reaction (11) or (12) can occur as soon as the reduction of Pt oxides takes place, although in this case ethanol adsorption is not limited to Pt(110) sites.

The **production of methane in the hydrogen potential region during the backward scan** (see Figure 4) can be formed with the interaction of the methyl residue formed in reaction (12) with H_{ad}, independently of the Pt surface site structure.

$$\text{Pt-CH}_3 + \text{Pt-H} \longrightarrow \text{CH}_4 \qquad (13)$$

It is remarkable that the yield to methane during the negative-going potential scan is practically independent of the ethanol concentration. The last indicates that methane is mostly produced from the adsorbed species formed on the MPPt electrode in reaction (12).

In addition, it was observed that **carbon dioxide** is mainly **produced during the forward scan**, is practically independent of ethanol concentration and its amount is equal in every potentiodynamic cycle. These facts can be taken as an indication that CO_2 is mainly produced from the adsorbed species (Pt-CH_3 and Pt-CO formed from Pt_2-$COHCH_3$) formed on the MPPt surface. CO_{ad} removal occurs through the reactions (1-3), while the complete oxidation reaction of adsorbed CH_3 species may occur in the following way:

$$\text{Pt-CH}_3 + 2\text{Pt-OH} \longrightarrow \text{CO}_2 + 5\text{H}^+ + 5\text{e}^- + 3\text{Pt} \qquad (14)$$

It is necessary to mention that reaction (14) does not represent the elementary steps of the oxidation of adsorbed CH_3 species, which probably involves a CO-like intermediate [52].

On the other hand, it was proposed in [49] that adsorbed acetaldehyde is responsible for **ethane formation** during the excursion to negative potentials when acetaldehyde was adsorbed on Pt at $E > 0.3$ V. But in that study, ethane was detected only when the applied potential was in the region of hydrogen evolution, other way only methane was detected. Nevertheless, in the current work the onset for ethane production on MPPt is observed at 0.2 V during the negative-going potential scan attaining a maximum at 0.1 V during the forward run. Accordingly, the following reaction appears to be the more suitable for ethane formation in this potential region, in agreement with a previous work on ethanol adsorption [15]:

$Pt_2\text{-}COHCH_3 + 4Pt\text{-}H \longrightarrow CH_3CH_3 + H_2O + 6Pt$ (15)

$Pt\text{-}COHCH_3 + 4Pt\text{-}H \longrightarrow CH_3CH_3 + H_2O + 5Pt$ (16)

Finally, **acetic acid formation** is detected by EC-MS at E > 0.6 V during the forward sweep and also during the reverse scan. Thus, this reaction can be written as a direct reaction of adsorbed acetaldehyde with adsorbed oxygenated species (OH_{ad}) on the metallic substrate:

$Pt(HCOCH_3) + Pt\text{-}OH \longrightarrow CH_3COOH + H^+ + e^- + 2Pt$ (17)

The Scheme 2 will assist in summarizing the principal reaction pathways of the ethanol reactivity on MPPt in acidic media.

Finally, some kinetic information can be obtained from chronoamperometric measurements. Tafel plots (Figure 8) were calculated from stationary faradaic (top panel) and ionic currents (bottom panel) achieved at 300 s during the current-time experiments. The m/z = 15, 29 and 44 signals were acquired in 0.05 M ethanol solution. In order to attain detectable ionic currents, the signal associated to acetic acid (m/z = 61) was obtained in 1 M ethanol solution. Tafel slopes of 120 mV dec^{-1} were achieved for the faradaic currents independently of the ethanol concentration at $E \leq 0.6$ V. Likewise, the m/z = 29 signal related to acetaldehyde formation perfectly match with a Tafel slope of 120 mV dec^{-1} in the same potential range. The signals for m/z = 15 and 44 show slightly higher Tafel slopes (~130 mV dec^{-1}) at $E \leq 0.6$ V and that related to acetic acid production (m/z = 61) develops the highest Tafel slope (140 mV dec^{-1}). The small deviation for the former mass to charge ratios can be associated to the fact that these signals are not only associated to acetaldehyde but also to methane (m/z = 15) and carbon dioxide (m/z = 44), whereas the low accuracy for m/z = 61 (see explanation of reaction 4) appears as the main responsible for this signal.

Therefore, assuming that all faradaic and ionic currents develop similar Tafel slope (~120 mV dec^{-1}) at $E \leq 0.6$ V, the reaction mechanism as well as rate-determining step (*rds*) involved in the ethanol oxidation can be proposed. Indeed, it is noticeable that all signals deviate from the linearity at E = 0.7 V, potential in which the strongly adsorbed ethanol residues (CO and CH_3) can be removed from the Pt surface. Thus, it is expected that ethanol adsorbs dissociatively on the MPPt electrode at low overpotentials leading adsorbed CO and CH_3 fragments on the catalyst surface. These residues are slowly oxidized at lower potentials than 0.6 V, and hence the water dissociation (reaction (1)) appears as the *rds* to fulfill the mechanism reaction for the whole ethanol oxidation reaction [53].

A deeply analysis can be carry out using the ionic currents recorded for m/z = 29 signal which is only related to acetaldehyde. It is important to recall that ethanol dehydrogenation leads acetaldehyde (reactions (7) and (8)) without the need of adsorbed oxygenated species (OH_{ad}). This signal also develops a Tafel slope value of 120 mV dec^{-1}, which must be associated to the first electrochemical step as the *rds.* Thus, equation 7 (the first dehydrogenation step) emerges as the *rds* for the electrochemical production of acetaldehyde species.

4. Conclusions

A new electrochemical mass spectrometry (EC-MS) configuration was developed and applied to different catalysts. It was proved that the novel EC-MS is a valuable and versatile technique with high accuracy and facile to build-up.

A deep fundamental study devoted to establish the reaction mechanism and the kinetics for the ethanol oxidation on MPPt catalyst was successfully investigated by combining electrochemical techniques with the new EC-MS set-up. In this context, methane formation during the positive scan between 0.2 and 0.4 V during the positive-going scan on MPPt is for the first time reported. This result is of paramount importance since new insights of the ethanol oxidation reaction are revealed.

Finally, a profound applied work related to energy generation throughout the fuel cell technology was carried out and the energy conversion efficiency from ethanol to CO_2 was calculated. Main results indicate an increment of by-side products (acetaldehyde and acetic acid) with the rise of the alcohol concentration. Consequently, the highest energy conversion efficiency to CO_2 (~11 %) was achieved at 0.6 V with the lowest alcohol concentration employed (0.01 M).

Acknowledgements

This work has been supported by Fundación Cajacanarias (project BIOGRAF). J. Flórez-Montaño thanks ACIISI (Gobierno de Canarias) for the pre-doctoral fellowship and BIOGRAF for the research contract.

References

[1] E. Antolini, Catalyst for direct ethanol fuel cells, J. Power Sources 170 (2007) 1-12.

[2] C. Lamy, E.M. Belgsir, J.M. Leger, Electrocatalytic oxidation of aliphatic alcohols: Application to the direct alcohol fuel cell (DAFC), J. Appl. Electrochem. 31 (2001) 799-809.

[3] B. Braunchweig, D. Hibbitts, M. Neurock, A. Wieckowski, Electrocatalysis: A direct alcohol fuel cell and surface science perspective, Catal.Today 202 (2013) 197-209.

[4] L. Zhang, W.X. Niu, G.B. Xu,Seed-mediated growth of palladium nanocrystals: The effect of pseudo-halidethiocyanate ions, Nanoscale 3 (2011) 678-682.

[5] Y.W. Lee, S.B. Han, D.Y. Kim, K.W. Park, Monodispersed platinum nanocubes for enhanced electrocatalyticproperties in alcohol electrooxidation, Chem. Commun.47 (2011) 6296-6298.

[6] J.M. Elliott, G.S. Attard, P.N. Bartlett, N.R.B. Coleman, D.A.S. Merckel, J.R. Owen, Nanostructured platinum (HI-ePt) films: Effects of electrodeposition conditions on film properties, Chem. Mater. 11 (1999) 3602-3609.

[7] N. Menzel, E. Ortel, R. Kraehnert, P. Strasser, Electrocatalysis using porous nanostructured materials, ChemPhysChem 13 (2012) 1385-1394.

[8] M.V. Martínez-Huerta; G. García, Fabrication of electrocatalytic nanoparticles and applications to proton exchange membrane fuel cells, in: D.Y.C. Leung, J. Xuan (Eds.), Micro & Nano-Engineering of Fuel Cells (Sustainable Energy Developments), CRC press Taylor and Francis Group, London, 2015. ISBN 0-41564-439-9.

[9] T.F. Esterle, A.E. Russell, P.N. Bartlett, Study of carbon monoxide oxidation on mesoporousplatinum, ChemPhysChem 11 (2010) 2896-2905.

[10] G. A. Planes, G. García, E. Pastor, High performance mesoporous Pt electrode for methanol electrooxidation. A DEMS study, Electrochem.Commun. 9 (2007) 839-844.

[11] H. Wang, C. Wingender, H. Baltruschat, M. Lopez, M.T. Reetz, Methanol oxidation on Pt, PtRu, and colloidal Pt electrocatalysts: A DEMS study of product formation, J. Electroanal. Chem. 509 (2001) 163-169.

[12] H. Wang, H. Abruña, Electrocatalysis of direct alcohol fuel cells: Quantitative DEMS studies fuel cells and hydrogen storage; Bocarsly, A.; Mingos, D. M. P., (Eds.), Springer: Berlin, 2011, 33.

[13] M.T.M. Koper, S.C.S. Lai, E. Herrero, Fuel Cell Catalysis - A Surface Science Approach; M.T.M Koper (Ed.), John Wiley & Son, Inc., Hoboken, New jersey, 2009, pp 192,355.

[14] T. Iwasita, F.C. Nart, Identification of methanol adsorbates on platinum: an in situ FT-IR investigation, J. Electronal. Chem. Interf. Electrochem., 317 (1991) 291-298.

[15] T. Iwasita, E. Pastor, A dems and FTir spectroscopy investigation of adsorbed ethanol on polycrystalline platinum, Electrochim. Acta 39 (1994) 531-537.

[16] J.M. Perez, B. Beden, F. Hahn, A. Aldaz, C. Lamy, “In situ” infrared reflectance spectroscopy study of the early stages of ethanol adsorption at a platinum electrode in acid medium, J. Electronal. Chem. 262 (1989) 251-261.

[17] E. Antolini, E. R. Gonzalez, A simple model to assess the contribution of alloyed and non-alloyed platinum and tin to the ethanol oxidation reaction on Pt–Sn/C catalysts: Application to direct ethanol fuel cell performance,Electrochim. Acta 55 (2010) 6485-6490.

[18] V. Bambagioni, C. Bianchini, A. Marchionni, J. Filippi, F. Vizza, J. Teddy, P. Serp, M. Zhiani, Pd and Pt–Ru anode electrocatalysts supported on multi-walled carbon nanotubes and

their use in passive and active direct alcohol fuel cells with an anion-exchange membrane (alcohol = methanol, ethanol, glycerol), J. Power Sources 190 (2009) 241-251.

[19] G. García, M. T. M. Koper, Carbon Monoxide Oxidation on Pt Single Crystal Electrodes: Understanding the Catalysis for Low Temperature Fuel Cells, ChemPhysChem 12 (2011) 2064-2072.

[20] S.-C. Chang, L.-W.H. Leung, and M.J. Weaver, Metal crystallinity effects in electrocatalysis as probed by real-time FTIR spectroscopy: Electrooxidation of formic acid, methanol, and ethanol on ordered low-index platinum surfaces, J. Phys. Chem. 94 (1990) 6013-6021.

[21] T. Iwasita, B. Rasch, E. Cattaneo, W. Vielstich, A sniftirs study of ethanol on platinum, Electrochim. Acta 34 (1989) 1073-1079.

[22] X.H. Xia, H.-D. Leiss and T. Iwasita, Early stages in the oxidation of ethanol at low index single crystal platinum electrodes, J. Electroanal. Chem. 437 (1997) 233-240.

[23] V.M. Schmidt, R. Ianniello, E. Pastor, S. González, Electrochemical reactivity of ethanol on porous Pt and PtRu: oxidation/reduction reactions in 1 M $HClO_4$, J. Phys. Chem. 100 (1996) 17901-17908.

[24] E. Mostafa, A.A. Abd-El-Latif, R. Ilsley, G. Attard, H. Baltruschat, Quantitative DEMS study of ethanol oxidation: Effect of surfacestructure and Sn surface modification, Phys. Chem. Chem. Phys. 14 (2012) 16115-16129.

[25] H. Wang, Z. Jusys, R.J. Behm, Ethanol electro-oxidation on carbon-supported Pt, PtRu and Pt_3Sn catalysts: A quantitative DEMS study, J. Power Sources154 (2006) 351-359.

[27] J.P.I. De Souza, S.L. Queiroz, K. Bergamaski, E.R. Gonzalez, and F.C. Nart, Electrooxidation of ethanol on Pt, Rh, and PtRh electrodes. A study using DEMS and in-situ FTIR techniques, J. Phys. Chem. B 106 (2002) 9825-9830.

[28] H. Baltruschat, Differential electrochemical mass spectrometry, J. Am. Soc. Mass Spectrom.15 (2004) 1693-1706.

[29] A.A. Abd-El-Latif, E. Mostafa, S. Huxter, G. Attard, H. Baltruschat,Electrooxidation of ethanol at polycrystalline and platinum stepped singlecrystals: A study by differential electrochemical mass spectrometry, Electrochim. Acta 55 (2010) 7951-7960

[30] F. Colmati, G. Tremiliosi-Filho, E.R. Gonzalez, A. Berna, E. Herrero, J.M. Feliu, The role of the steps in the cleavage of the C–C bond during ethanol oxidation on platinum electrodes Phys. Chem. Chem. Phys. 11 (2009) 9114-9123.

[31] S.C.S. Lai, M.T.M. Koper, Electro-oxidation of ethanol and acetaldehyde on platinum single crystal electrodes, Faraday Discuss.140 (2009) 399-416.

[32] D.J. Tarnowski, C. Korzeniewski, Effects of surface step density of the electrochemical oxidation of ethanol to acetic acid, J. Phys. Chem. B 101 (1997) 253-258.

[33] G.A. Camara, T. Iwasita, Parallel pathways of ethanol oxidation: The effect ofethanol concentration, J. Electroanal. Chem. 578 (2005) 315-321.

[34] A.H. Wonders, T.H.M. Housmans, V. Rosca and M.T.M. Koper, On-line mass spectrometry system for measurements at single-crystal electrodes in hanging meniscus configuration, J. Appl. Electrochem., 36 (2006) 1215–1221.

[35] O. Guillén Villafuerte, G. García, J.L. Rodríguez, C. Arévalo, E. Pastor, New insight in the electrochemical oxidation of ethanol on carbon-supported Pt electrode by a novel electrochemical mass spectrometry configuration, Electrochem. Commun., *under revision.*

[36] S. Sun, M. ChojakHalseid, M. Heinen, Z. Jusys, R.J. Behm, Ethanol electrooxidation on a carbon-supported Pt catalyst at elevatedtemperature and pressure: A high-temperature/high-pressure DEMS study, J. Power Sources 190 (2009) 2-13.

[37] G. García, J. Florez-Montaño, A. Hernandez-Creus, E. Pastor, G. A. Planes, Methanol electrooxidation at mesoporous Pt and Pt–Ru electrodes: A comparative study with carbon supported materials, J. Power Sources 196 (2011) 2979-2986.

[38] M. Arenz, K.J.J. Mayrhofer, V. Stamenkovic, B.B. Blizanac, T. Tomoyuki, P.N. Ross, N.M. Markovic,The effect of the particle size on the kinetics of coelectrooxidation on high surface area Pt catalysts, J. Am. Chem. Soc. 127 (2005) 6819-6829.

[39] O. Guillén-Villafuerte, G. García, A. González Orive, B. Anula, A. Hernández-Creus, E. Pastor, Electrochemical characterization of 2D Ptnanoislands, Electrocatal. 2 (2011) 231-241.

[40] R. Gisbert, G. García, M. T.M. Koper, Oxidation of carbon monoxide on poly-oriented and single-crystalline platinumelectrodes over a wide range of pH, Electrochim. Acta 56 (2011) 2443-2449.

[41] S. Gilman, The mechanism of electrochemical oxidation of carbon monoxide and methanol on platinum. II. The ‘reactant-pair” mechanism for electrochemical oxidation of carbon monoxide and methanol, J. Phys. Chem., 68 (1964) 70-80.

[42] J. F. Gomes, K. Bergamaski, M.F.S. Pinto, P.B. Miranda, Reaction intermediates of ethanol electro-oxidation on platinum investigated by SFG spectroscopy, J. Catal., 302 (2013) 67-82.

[43] F. Colmati, E. Antolini, E.R. González, Ethanol oxidation on carbon supported Pt-Sn electrocatalysts prepared by reduction with formic acid, J Electrochem. Soc., 154 (2007) B39-B47.

[44] S. Rousseau, C. Coutanceau, C. Lamy, J.M. Léger, Direct ethanol fuel cell (DEFC): Electrical performances and reaction products distribution under operating conditions with different platinum-based anodes, J. Power Sources, 158 (2006) 18-24.

[45] F. Vigier, C. Coutanceau, F. Hahn, E.M. Belgsir, C. Lamy, On the mechanism of ethanol electro-oxidation on Pt and PtSn catalysts: Electrochemical and in situ IR reflectance spectroscopy studies, J. Electroanal. Chem., 563 (2004) 81-89.

[46] E. Stenhagen, S. Abrahamsson, F.W. McLafferty (Eds.), Atlas of Mass Spectral Data, Interscience, New York, 1969.

[47] E. Pastor, T. Iwasita, D/H exchange of ethanol at platinum electrodes, Electrochim. Acta, 39 (1994) 547-551.

[48] J.L. Rodríguez, E. Pastor, X.H. Xia, T. Iwasita, Reaction intermediates of acetaldehyde oxidation on Pt(111) and Pt(100). An in situ FTIR study, Langmuir 16 (2000) 5479-5486.

[49] J. Silva-Chong, E. Mendez, J.L. Rodriguez, M.C. Arevalo, E. Pastor, Reactivity of acetaldehyde at platinum and rhodium in acidic media. A DEMS study, Electrochim. Acta 47 (2002) 1441–1449.

[50] J.A. Silva-Chong, O. Guillen-Villafuerte, J.L. Rodriguez, E. Pastor, DEMS study on the nature of acetaldehyde adsorbates at Pt and Pd by isotopic labeling, J. Solid State Electrochem., 12 (2008) 517–522.

[51] E. Mendez, J.L. Rodriguez, M.C. Arevalo, E. Pastor, Comparative study of ethanol and acetaldehyde reactivities on rhodium electrodes in acidic media, Langmuir 18 (2002) 763–772.

[52] G. García, J. Silva-Chong, J.L. Rodríguez, E. Pastor, Spectroscopic elucidation of reaction pathways of acetaldehyde on platinum and palladium in acidic media, J. Solid State Electrochem., 18 (2014) 1205–1213.

[53] J. Shin, W.J. Tornquist, C. Korzeniewski, C.S. Hoaglund, Elementary steps in the oxidation and dissociative chemisorption of ethanol on smooth and stepped surface planes of platinum electrodes, Surf. Sci., 364 (1996) 122-130.

[54] S. Fletcher, Tafel slopes from first principles, J. Solid State Electrochem., 13 (2009) 537-549.

Table Captions

Table 1. Efficiency of ethanol conversion to CO_2 (E^{CO2}) at MPPt catalyst recorded at 0.60 and 0.70 V in 0.5 M sulphuric acid solution.

Figure captions:

Scheme 1. The image shows the principal characteristics of the new EC-MS configuration. 1. PTFE capillary, 2. PTFE Cone-shape Tip, 3. Hydrophobic porous PTFE membrane, 4. MPPt electrode, 5. Au wire (electrical contact).

Fig. 1. CO stripping CV and MSCV. Faradaic current density (black) and ionic current density of m/z = 22 and 44 (red and green) registered during the electrooxidation of a CO_{ad} monolayer on MPPt electrode in 0.5 M H_2SO_4. $v = 5$ mV s^{-1}; T = 25 °C.

Fig. 2. Ethanol electrooxidation on MPPt catalyst in 0.01 M ethanol + 0.5 M H_2SO_4. CVs (A) and MSCVs for m/z = 22 (B), m/z = 29 (C) and m/z = 15 (D). $v = 2$ mV s^{-1}; T = 25 °C.

Fig. 3. Ethanol electrooxidation on MPPt in different ethanol concentrations as indicated. CVs (A) and MSCVs for m/z = 22 (B) and m/z = 44 (C) $v = 2$ mV s^{-1}; T = 25 °C. The CO_2^{++} and CO_2^{+} current signals were adjusted by the K_{22}^{*} and K_{44}^{*}, respectively.

Fig. 4. CVs (top panel) and MSCVs (bottom panel: m/z = 15) of ethanol electrooxidation on MPPt in 0.01, 0.1 and 0.5 M ethanol electrooxidation on MPPt in 0.5 M sulphuric acid solution. v = 2 mV s^{-1}; T = 25 °C.

Fig. 5. CVs (top panels) and MSCVs (middle panels: m/z = 22 and 15; bottom panels: m/z = 29) of ethanol electrooxidation on MPPt in 0.01, 0.1 and 1 M ethanol electrooxidation on MPPt in 0.5 M sulphuric acid solution. v = 2 mV s^{-1}; T = 25 °C.

Fig. 6. CVs (top panels) and MSCVs (middle panels: m/z = 30 and 61; bottom panels: m/z = 73) of ethanol electrooxidation on MPPt in 0.01, 0.1 and 1 M ethanol electrooxidation on MPPt in 0.5 M sulphuric acid solution. v = 2 mV s^{-1}; T = 25 °C.

Fig. 7. CTs (A) and MSCTs for m/z = 22 (middle panel) and m/z = 29 (bottom panel) of 0.01, 0.05, 0.1, 0.5, and 1 M ethanol electrooxidation on MPPt in 0.5 M sulphuric acid solution. Potentials steps from 0.05 V to 0.4, 0.5, 0.6 and 0.7 V. T = 25 °C. The CO_2^{++} current signal was adjusted by the K_{22}^{*}.

Scheme 2. Reaction mechanism of the ethanol oxidation on MPPt electrode in acidic medium. Species inside the red and light blue boxes are produced during the backward and forward scans, respectively. Although no indicated for the sake of simplicity, $HCOCH_3$ and CH_3COOH are also formed during the negative-going scan.

Fig. 8. Tafel plots of the CTs (upper panel) and MCTs (bottom panel) on the MPPt electrode.

Table 1.

[EtOH]/mol L^{-1}	**E^{CO2} (0.60 V)**	**E^{CO2} (0.70 V)**
0.01	11.1	9.4
0.05	5.5	4.6
0.10	4.6	3.8
0.50	1.8	1.6
1.00	1.2	1.1

Scheme 1.

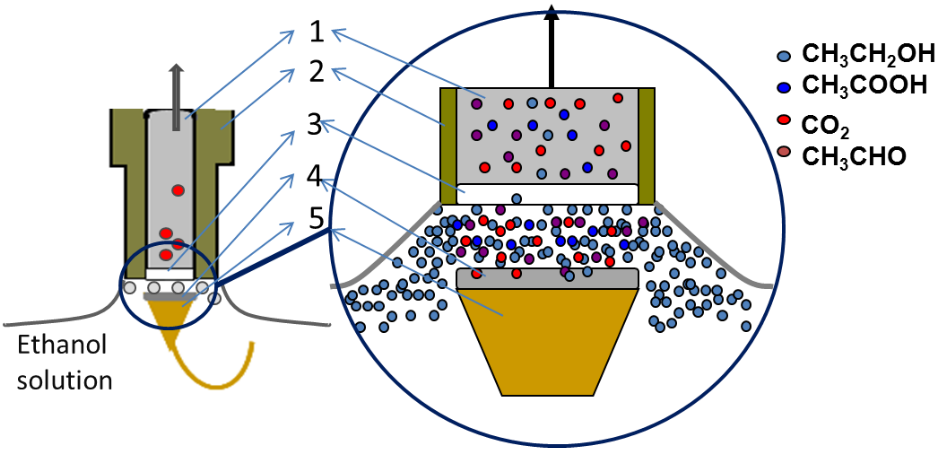

Figure 1.

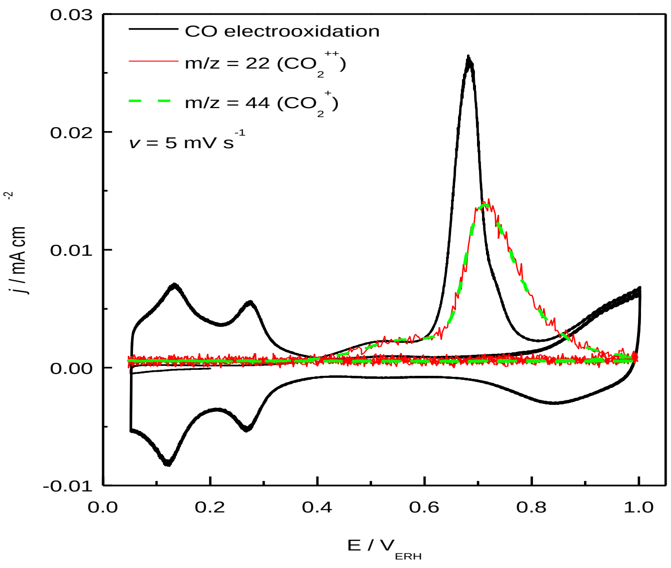
CO electrooxidation
m/z = 22 (CO_2^{++})
m/z = 44 (CO_2^{+})
v = 5 mV s^{-1}
j / mA cm^{-2}
E / V_{ERH}
0.03
0.02
0.01
0.00
-0.01
0.0
0.2
0.4
0.6
0.8
1.0

Figure 2

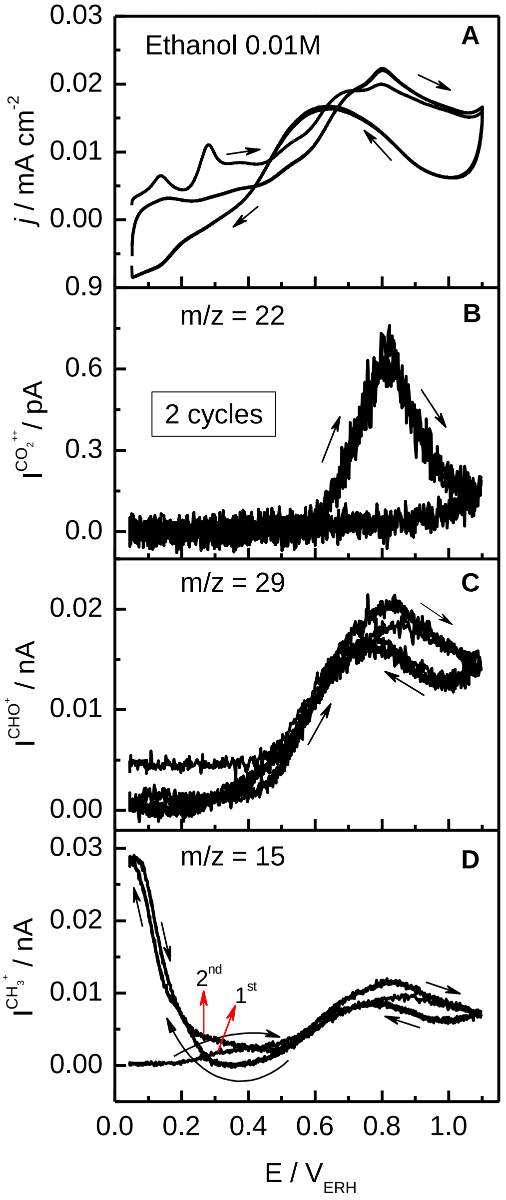
Ethanol 0.01M
A
j / mA cm^{-2}
0.03
0.02
0.01
0.00
m/z = 22
B
2 cycles
$I^{CO_2^{++}}$ / pA
0.9
0.6
0.3
0.0
m/z = 29
C
I^{CHO^+} / nA
0.02
0.01
0.00
m/z = 15
D
$I^{CH_3^+}$ / nA
0.03
0.02
0.01
0.00
2nd
1st
0.0
0.2
0.4
0.6
0.8
1.0
E / V$_{ERH}$

Figure 3

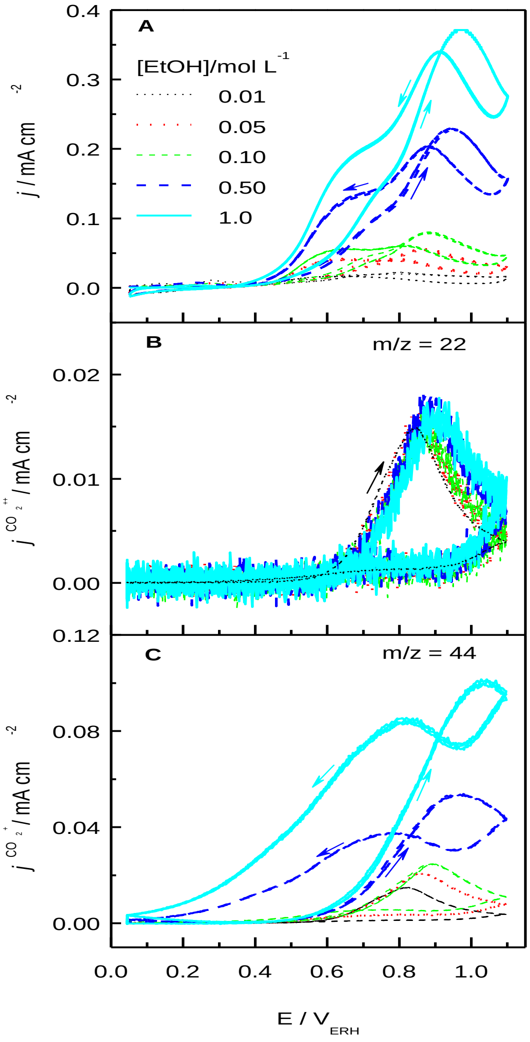
A
[EtOH]/mol L^{-1}
0.01
0.05
0.10
0.50
1.0
j / mA cm^{-2}
0.0
0.1
0.2
0.3
0.4
B
m/z = 22
$j_{CO_2^{++}}$ / mA cm^{-2}
0.00
0.01
0.02
C
m/z = 44
$j_{CO_2^{+}}$ / mA cm^{-2}
0.00
0.04
0.08
0.12
0.0
0.2
0.4
0.6
0.8
1.0
E / V$_{ERH}$

Figure 4

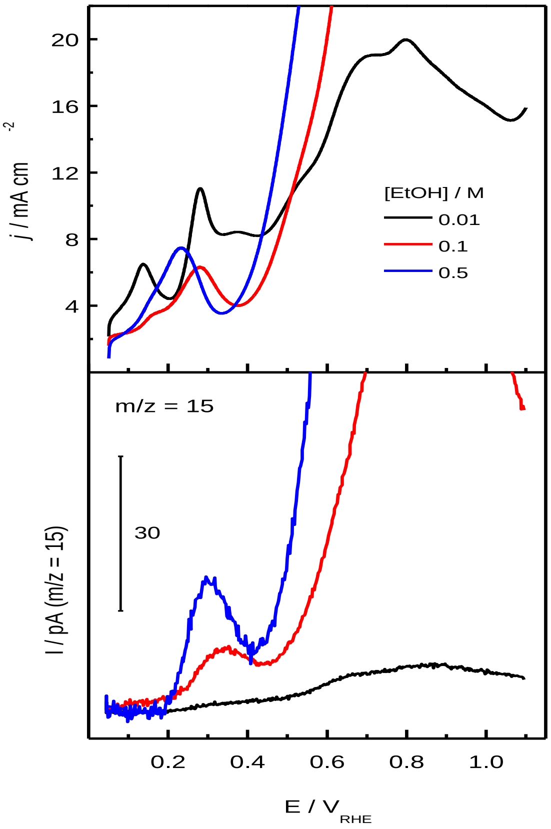
20
16
12
8
4
j / mA cm -2
[EtOH] / M
0.01
0.1
0.5
m/z = 15
30
I / pA (m/z = 15)
0.2
0.4
0.6
0.8
1.0
E / V RHE

Figure 5

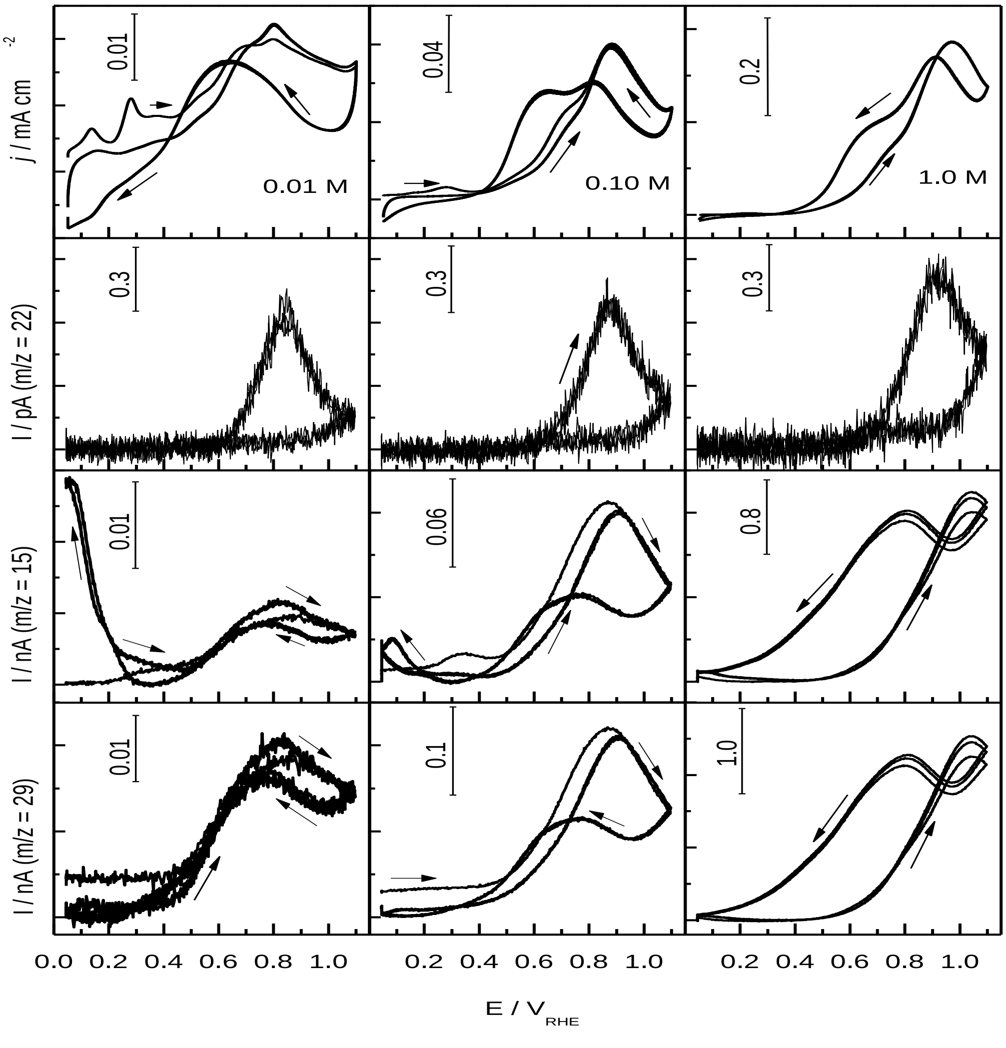
j / mA cm-2
I / pA (m/z = 22)
I / nA (m/z = 15)
I / nA (m/z = 29)
0.01
0.04
0.2
0.01 M
0.10 M
1.0 M
0.3
0.3
0.3
0.01
0.06
0.8
0.01
0.1
1.0
0.0 0.2 0.4 0.6 0.8 1.0
0.2 0.4 0.6 0.8 1.0
0.2 0.4 0.6 0.8 1.0
E / V RHE

Figure 6

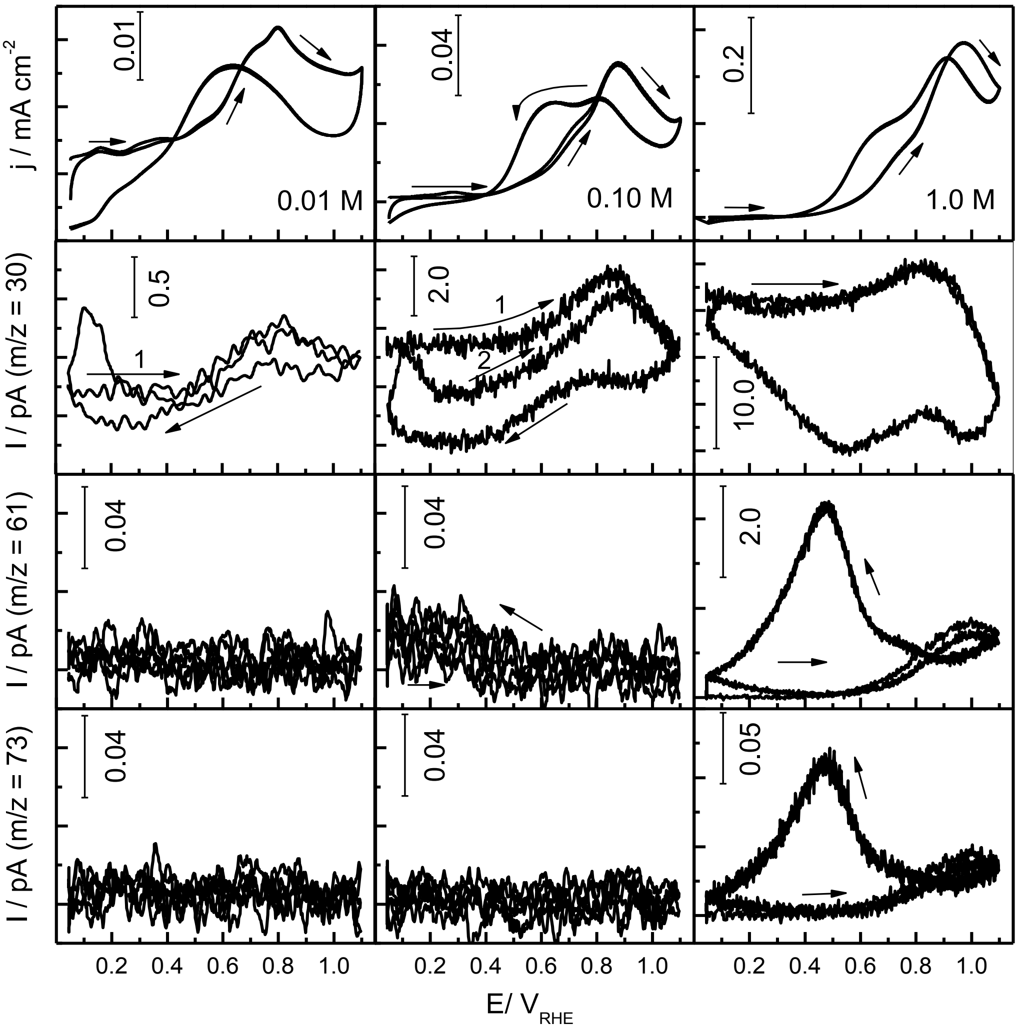

j / mA cm^{-2}
I / pA (m/z = 30)
I / pA (m/z = 61)
I / pA (m/z = 73)
0.01
0.04
0.2
0.01 M
0.10 M
1.0 M
0.5
1
2.0
1
2
10.0
0.04
0.04
2.0
0.04
0.04
0.05
0.2
0.4
0.6
0.8
1.0
E/ V$_{RHE}$

Figure 7

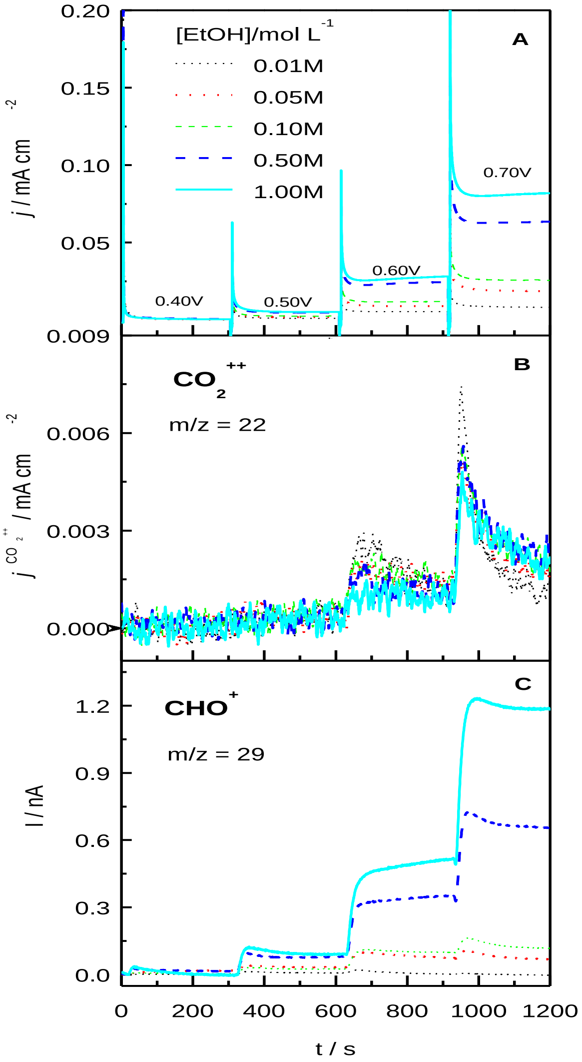
A
[EtOH]/mol L^{-1}
0.01M
0.05M
0.10M
0.50M
1.00M
0.40V
0.50V
0.60V
0.70V
j / mA cm^{-2}
0.20
0.15
0.10
0.05
0.009
B
CO$_2^{++}$
m/z = 22
$j^{CO_2^{++}}$ / mA cm^{-2}
0.006
0.003
0.000
C
CHO$^+$
m/z = 29
I / nA
1.2
0.9
0.6
0.3
0.0
0
200
400
600
800
1000
1200
t / s

Figure 8

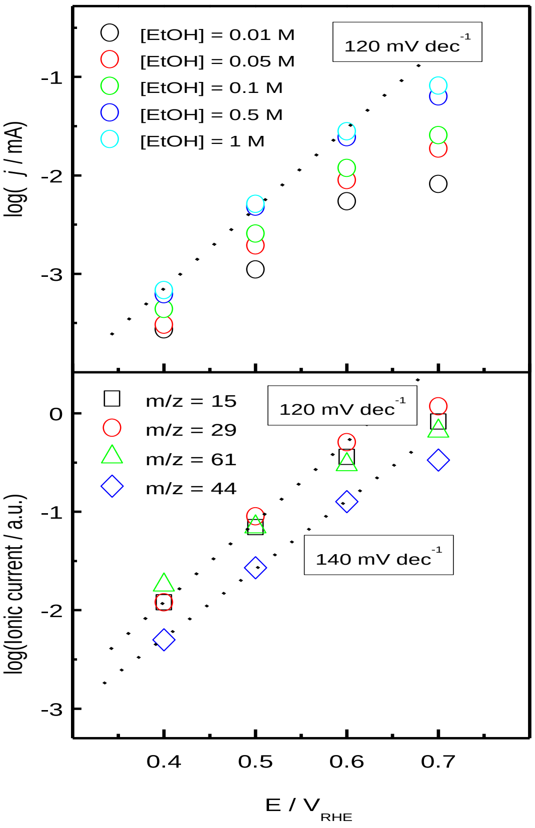
[EtOH] = 0.01 M
[EtOH] = 0.05 M
[EtOH] = 0.1 M
[EtOH] = 0.5 M
[EtOH] = 1 M
120 mV dec^{-1}
log(j / mA)
-1
-2
-3
m/z = 15
m/z = 29
m/z = 61
m/z = 44
120 mV dec^{-1}
140 mV dec^{-1}
log(Ionic current / a.u.)
0
-1
-2
-3
0.4
0.5
0.6
0.7
E / V$_{RHE}$

Scheme 2

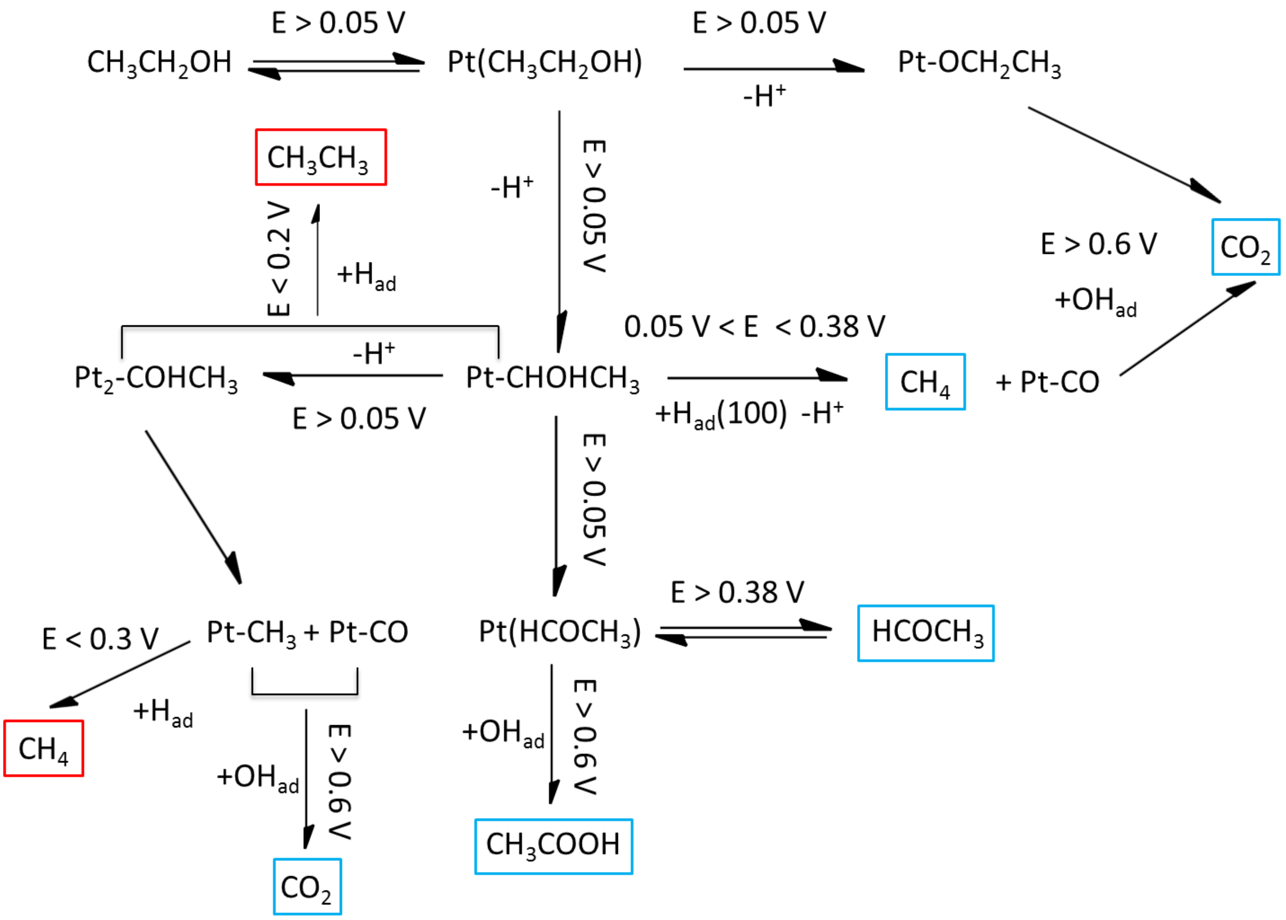
CH_3CH_2OH
$E > 0.05$ V
$Pt(CH_3CH_2OH)$
$E > 0.05$ V
$-H^+$
$Pt-OCH_2CH_3$
CH_3CH_3
$-H^+$
$E > 0.05$ V
$E < 0.2$ V
$+H_{ad}$
$E > 0.6$ V
$+OH_{ad}$
CO_2
$0.05 V < E < 0.38$ V
$Pt_2-COHCH_3$
$-H^+$
$E > 0.05$ V
$Pt-CHOHCH_3$
$+H_{ad}(100)$ $-H^+$
CH_4
$+ Pt-CO$
$E > 0.05$ V
$E > 0.38$ V
$E < 0.3$ V
$Pt-CH_3 + Pt-CO$
$Pt(HCOCH_3)$
$HCOCH_3$
$+H_{ad}$
CH_4
$+OH_{ad}$
$E > 0.6$ V
CO_2
$+OH_{ad}$
$E > 0.6$ V
CH_3COOH

Spectroscopic evidences of core electronic effects on CO and HCOOH electrooxidation at Au-Pd core-shells

Jonathan Flórez-Montaño[‡], *Verónica Celorrio*[†], *Daniela Plana*[†], *David J. Fermín*[†*] *and Elena Pastor*[‡*]

[†]School of Chemistry, University of Bristol, Cantocks Close, Bristol BS8 1TS, UK

[‡]Departamento de Química - UD Química Física, Instituto de Materiales y Nanotecnología, Universidad de La Laguna, Avda. Astrofísico Francisco Sánchez s/n, 38071 Tenerife, Spain

AUTHOR INFORMATION

Corresponding Author

*E-mail: David.Fermin@bristol.ac.uk (D.J.F)

*E-mail: E.Pastor@ull.es (E.P.)

ABSTRACT

The mechanism of electrooxidation of CO and formic acid on Au-Pd core-shells supported on carbon was spectroscopically studied by means of differential electrochemical mass spectrometry (DEMS) and *in situ* Fourier transform infrared spectroscopy (FTIRS) combined with cyclic voltammetry. In this way, the intermediates involved in the oxidation processes at these nanostructures were identified *in situ* and the influence of the thickness of the Pd nanoshells established, confirming the existence of core electronic effects. Thus, not only the onset potential for the electrooxidation shifts to lower values with increasing Pd overlayers, but also the adsorption of both CO and OH is affected. Additionally, according to the FTIR results, it can be concluded that $HCOO_{ad}$ is formed as intermediate in the formic acid oxidation to CO_2 at Au@Pd nanostructures, being its deprotonation to CO_2 faster on the CS10/C catalyst than on the CS1/C material. XPS analysis allows to determine the presence of higher amount of Pd(IV) on the former, promoting the oxidation at lower potentials. Thus, it is demonstrated that core electronic effects on the shell surface can be controlled by the thickness of the overlayers, and accordingly, the reaction mechanism modified in the desired direction.

KEYWORDS Formic acid, Au@Pd core-shells, DEMS, *in situ* FTIRS, electronic effect

INTRODUCTION

Catalytic activity of bimetallic structures can be significantly different from the individual components and can be tuned through the controlled growth of thin films on foreign supports.[1,2] The reactivity of this type of system can be rationalized in terms of electronic and geometric (so called strain) effects, which can alter position of the d-band center.[3,4] Pd overlayers on Au substrates have received significant attention for a variety of catalytic reactions, particularly in the context of the hydrogen evolution/oxidation reactions and formic acid oxidation, where it has been shown that the underlying Au substrate can have significantly effect on the electrocatalytic activity of the Pd layers.[5,6,7,8,9]

A strong dependence on the Au substrate structure has been experimentally demonstrated for the oxidation of CO_{ads} on Pd overlayers.[10,11] while the binding energy has been calculated to be a function of the number of Pd overlayers, with a maximum found at two overlayers.[12] Additional effects on CO oxidation produced by changes in OH adsorption due to structure sensitivity have also been observed.[11,13]

Studies based on Pd nanoshells at Au cores have shown that the effective strain of the Pd overlayers relaxes from 3.5 to 1% as the thickness increases from 1 to 10 nm; this in turn affects the adsorption and oxidation of carbon monoxide.[14,15] Although less obvious trends are electrochemically observed on carbon-supported particles in terms of the oxidation of CO_{ads}, it has been suggested that these effects also contribute towards reactivity differences on both HCOOH oxidation and CO_2 reduction.[13,16,17,18]

In the case of the complete electrooxidation of formic acid to CO_2, the process has been mainly described as an electrochemical reaction in which the formic acid is oxidized through a dual pathway mechanism.[19] Formic acid oxidation at platinum-based catalysts involves a step in which a poisoning intermediate (e.g. CO_{ad}) is formed (indirect pathway).[20] On the other hand, palladium-based catalysts have shown excellent resistance to CO poisoning in such catalytic process[2] and accordingly, no adsorption of CO at low potentials during formic acid oxidation on Pd electrodes was confirmed by infrared reflection absorption spectroscopy (IRAS) studies. Then, the direct pathway was suggested to be the principal route for CO_2 formation at these materials.[21,22] Nevertheless, the mechanism of formic acid oxidation on Pd is still unclear and required further studies, especially on bimetallic catalysts. In this context, several works have reported that Pd−Au electrocatalysts enhance the overall performance of Pd due to a promoting effect of Au[23,24,25,26], and therefore, the Pd to Au ratio plays an important role in the electrocatalytic behavior.[15,24]

In the present paper the electrooxidation of CO and HCOOH on Au@Pd core-shell nanoparticles supported on Vulcan XC-72R has been studied by in-situ Fourier Transform IR Spectroscopy (FTIRS) and differential electrochemical mass spectrometry (DEMS), in order to achieved information on the influence of the Au electronic effects and Pd thickness on the mechanism of formic acid oxidation at these materials.

EXPERIMENTAL METHODS

Preparation of the electrocatalysts. The first step of the synthesis of Au-Pd core-shell (CS) structures involves the preparation of Au nanoparticles, employing trisodium citrate as a reducing and stabilizing agent. Then, Pd was growth onto the Au cores by reduction of H_2PdCl_4 in the presence of ascorbic acid,[1,2] being the Pd thickness controlled by the amount of Pd precursor added. The H_2PdCl_4 solution volume was adjusted in order to control the Pd thicknesses to be 1 and 10 nm. The metallic nanostructures were supported on Vulcan XC-72R (Cabot).[3] A set amount of the

Vulcan XC-72R powder was suspended and stirred during 48 h in controlled amounts of nanoparticle dispersions, calculated to obtain a total metal loading of 20 wt %. The as-prepared carbon-supported nanoparticle powders were filtered, washed with Milli-Q water, and dried at 60 °C overnight. Samples were labelled as CS1/C and CS10/C, when the attempting Pd thicknesses were 1 and 10 nm, respectively.

Characterization of catalysts. The real metal loading was determined by energy dispersive X-ray (EDX) analysis using an Oxford Instruments ISIS 300, coupled to a JEOL JSM 5600LV scanning electron microscope. Transmission electron microscopy (TEM) images were obtained using a JEOL JEM 1200 EX MKI and the image analysis software Soft Imaging Systems GmbH analySIS 3.0.

FTIR and cyclic voltammetry measurements. Electrochemical experiments were carried out in a three-electrode electrochemical cell connected to an Autolab PGstat302N. A high surface area carbon rod was used as counter electrode and a reversible hydrogen electrode (RHE) in the supporting electrolyte was employed as reference electrode. All potentials in the text are referenced to this electrode. The working electrode was prepared by ultrasonically dispersing 2 mg of the electrocatalysts in 0.5 mL of pure water (Millipore) and 15 μl of Nafion. An aliquot of the dispersed suspension was pipetted on the top of the working electrode and dried at ambient temperature. The working electrode supports were glassy carbon electrodes for CO_{ad} stripping technique (7.0 mm diameter) and a gold disk for Fourier transform infrared spectroscopy (10 mm diameter). The experiments were carried out in a 0.5 M sulphuric acid (Merck p.a.) solution prepared with Milli-Q water (Millipore). Fourier transform infrared spectroscopy (FTIRS) experiments were performed with a Bruker Vector 22 spectrometer equipped with a mercury cadmium telluride detector. A small glass flow cell with a CaF_2 prism at its bottom was used. The cell and experimental arrangements have been described in detail elsewhere.[4-5] FTIR spectra were acquired from the average of 128 scans, obtained with 8 cm^{-1} resolution at selected potentials, by applying 0.05 V single potential steps from a reference potential, in the positive going direction. The reflectance ratio R/R_0 was calculated, where R and R_0 are the reflectances measured at the sample and the reference potential, respectively. In this way, positive and negative bands represent the loss and gain of species at the sampling potential, respectively.

DEMS set-up. The gaseous species produced on the electroactive surface can be followed on-line by differential electrochemical mass spectrometry (DEMS). For the detection of the ion current during mass spectrometric measurement, a QuadstarTM 422-software (Pfeiffer-vacumm Thermostar) was used. The set-up allows the detection of the ion current for each m/z separately. A conventional electrochemical cell was used and the meniscus configuration was adopted. The working electrode surface is placed very close (~micrometers) to a Teflon capillary, which is connected directly to the vacuum of the mass spectrometer. Details of the setup can be found elsewhere [27, 28]

DEMS calibration. The calculation of the efficiency for methanol conversion to CO_2 by DEMS requires a previous determination of the m/z = 44 calibration constant (K^{CO_2}). This constant correlates the number of CO_2 molecules generated on the electrode surface (through the faradaic charge) with the portion of this molecules captured by the mass spectrometer (proportional to m/z = 44 ion current). It has to be determined before each experiment because it depends of several variables (membrane-electrode gap, flow rate, temperature and pressure in the mass vacuum line). The calibration constant is calculated as follow: faradaic ($Q_f^{CO_2}$) and ionic m/z = 44 ($Q_i^{CO_2}$) charges were calculated from CO stripping and related according to equation:

$$K^{CO_2} = 2\,\frac{Q_i^{CO_2}}{Q_f^{CO_2}} \qquad (1)$$

Then, the current efficiency E for formic acid electrooxidation to CO_2 is determined from the subsequent equation:

$$E^{CO_2} = \frac{2 * Q_i^{CO_2}}{K^{CO_2} * Q_f^{T}} \qquad (2)$$

where Q_f^T is the charge associated to all faradaic processes at the surface. Further details are given in previous works.[27, 2728]

RESULTS AND DISCUSSION

Physicochemical characterization. Au-Pd core-shell nanoparticles of 1.3 and 9.9 ± 1.0 nm shell thickness (CS1/C and CS10/C, respectively) on 19.3 ± 1.0 nm diameter Au cores were synthesized. They were supported on Vulcan XC-72 aiming for a metal loading of 20 %wt. (15.0 for CS1/10 and 17.5 ± 2.0% for CS10/C). TEM images of the CS nanostructures supported on Vulcan (insets in Figure 1) showed that the nanoparticles were well dispersed in the carbon support, ensuring a high metal dispersion in the catalysts, with very low density of aggregates. A detailed TEM study of shell thickness has been previously published.[13]

CO stripping (cyclic voltammetry and FTIR studies). In previous studies, we have reported that the reactivity of Au-Pd nanostructures towards CO electro-oxidation is not only determined by the composition and structure of the Pd overlayer, but also by the interaction with the support.[13,15,29] Typical cyclic voltammograms for the oxidation of a monolayer of CO adsorbed on VulcanXC-72R at the CS1/C and CS10/C catalyst surfaces are shown in Figure 1.[13] It can be observed that both samples developed a CO stripping peak at around 0.69 V, following the common behavior described in the literature for Pd electrocatalysts,[30,31] and although the peak potential position for CO oxidation is not affected by Pd thickness,[13] the voltammetric profile during CO oxidation is different due to the diverse degree of crystallinity of the Pd shells in the samples.

The broad peak in the CS1/C catalysts suggests a poor crystalline structure of the Pd shell in the nanoparticle, while the sharp peak in the CS10/C material corresponds to the oxidation of a CO monolayer on a crystalline structure rich in Pd. These results agree with previous works.[13,15] A small pre-peak was observed on the CS10/C sample, which has been previously ascribed to the oxidation of CO at defect sites associated with the high surface roughness of these particles.[10,15] Another important parameter concerning the behavior of the catalyst is the onset potential for the CO oxidation to CO_2. This factor is very difficult to be precisely established purely from voltammetric measurements, as other processes occur simultaneously and contribute to the recorded current, such as capacitive contributions from the carbon support. Spectroscopic studies will deal with the solution of this problem.

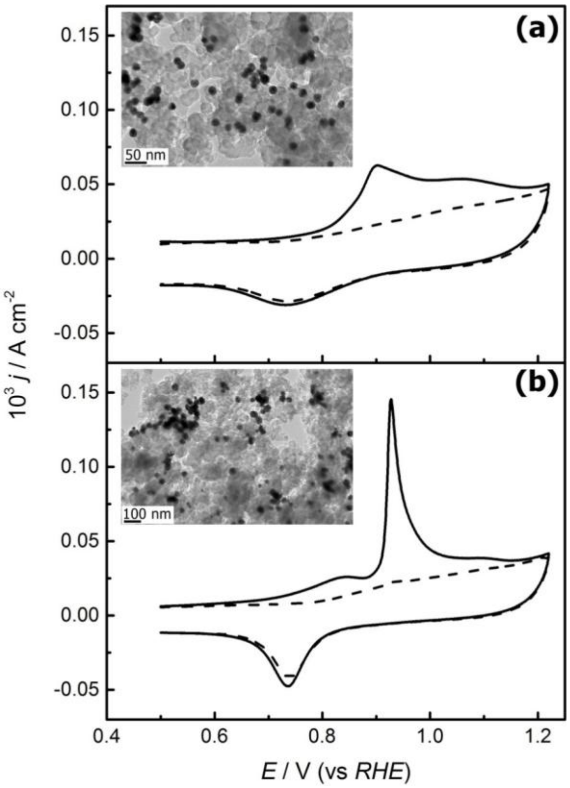

Figure 1. CVs for the oxidative removal of adsorbed CO at CS1/C (a) and CS10/C (b) in 0.5 M H_2SO_4. Adsorption potential = 0.20 V. After adsorption, CO was displaced from solution by argon purging. v = 0.02 V s^{-1}. Insets: TEM images of CS1/C (a) and CS10/C (b) samples.

A series of spectra acquired during the oxidation of an adsorbed CO monolayer (CO_{ad}) and calculated with a reference spectrum obtained at 0.20 V are given in Figure 2. Positive bands in the *in situ* FTIR spectra are related to species present at the reference potential but not at the sample potential. Thus, a signal is observed in both samples that first appears as bipolar around 1970-1920 cm^{-1} and turns positive from 0.80 V up to 1.2 V raising as a positive band at 1962 cm^{-1}, indicating that all CO_{ad} is oxidized. This band is attributed to bridge adsorbed CO (CO_B).[32] The negative band at 2343 cm^{-1} corresponds to the production of CO_2,[32] which is apparent from 0.50 V for CS10/C whereas for CS1/C it does not appear until the potential reaches a value of 0.70 V. This result suggests that although the peak potential for CO oxidation is not affected by Pd thickness, the onset potential shifts positively when Pd thickness decreases.

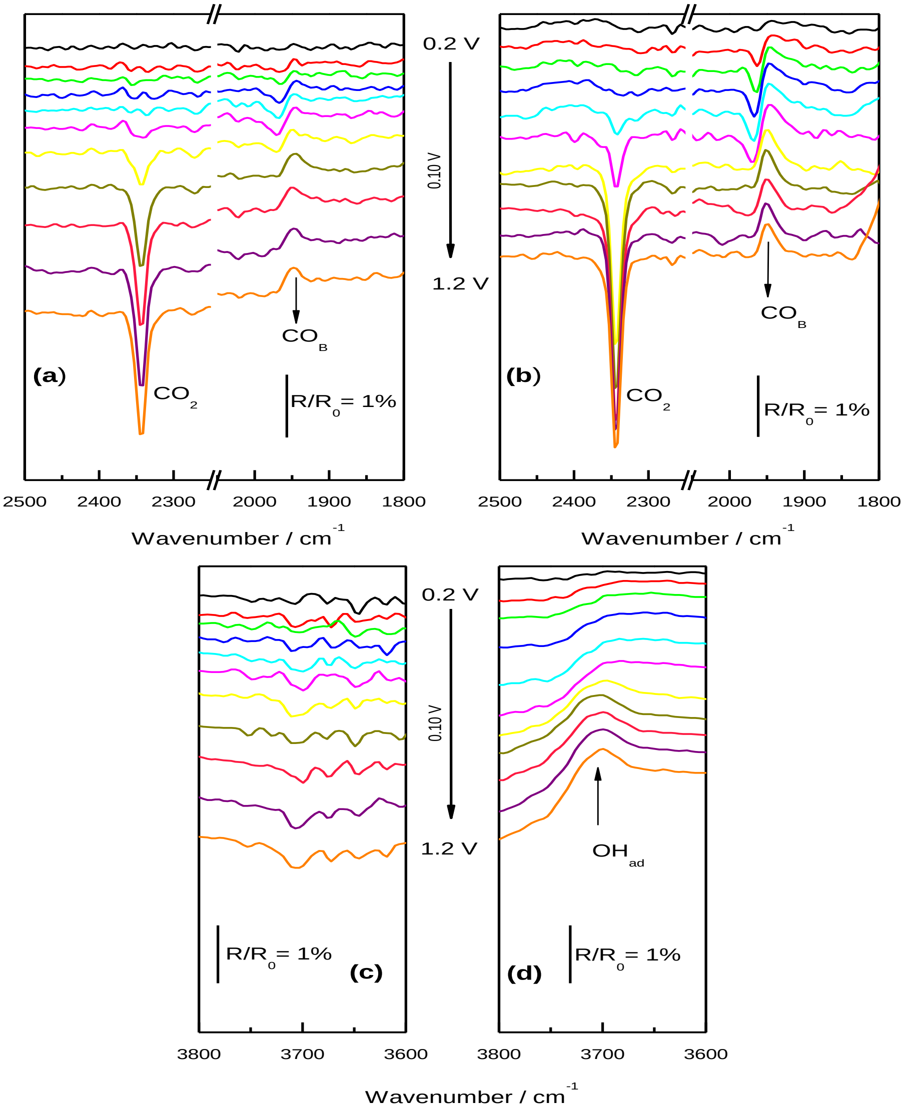

Figure 2. In situ FTIR spectra for the oxidation of CO adsorbed on CS1/C (a) and CS10/C (b) in 0.5 M H_2SO_4. The potential was positively changed from 0.20 V (reference potential) onward in 0.05 V steps up to 1.20 V. 128 scans, 8 cm^{-1} resolution.

A more detailed analysis of the same spectra in the 3800-3600 cm^{-1} region, allows identifying a negative band around 3700 cm^{-1} for CS10/C which is associated to OH_{ad} stretching (Figure 2d),[33,34] in contrast with the spectrum of the CS1/C catalysts where this feature does not appear (Figure 2c). This band describes the OH_{ad} consumption when increasing the applied potential. According to these results, it seems that OH_{ad} species are involved in the CO_{ad} electrooxidation at CS10/C (eq. 4), and therefore, in a first step (eq. 3) water molecules should interact with the Pd surface acting as the source of the OH_{ads} species, similar to what happens with Pd bulk as suggested by Gilman[35]:

$$H_2O + Au@Pd^{10} \rightleftharpoons OH_{ad} + H^+ + e^- \qquad (3)$$

And then this species react with the adsorbed CO yielding CO_2:

$$OH_{ad} + CO_{ad} \longrightarrow CO_2 + H^+ + e^- \qquad (4)$$

On the other hand, FTIR data for CO electrooxidation on CS1/C shows that adsorbed water species as OH_{ad} do not take part in this reaction (Figure 2c). Then, in this case, it is proposed the formation of a carboxylic species $COOH_{ads}$ by direct interaction of CO_{ad} with water.

$$H_2O + CO_{ad} \rightleftharpoons COOH_{ad} + H^+ + e^- \qquad (5)$$

This adsorbate is not stable and decomposes fast to CO_2 (eq. 6) as was proposed previously by other authors [36,37]:

$$COOH_{ad} \longrightarrow CO_2 + H^+ + e^- \qquad (6)$$

A short lifetime and low coverage of this intermediate could justify that cannot be detected spectroscopically. These results are consistent with DFT calculations and other studies related with the CO oxidation on Au, Pt and Pd-Au electrodes, where the differences observed for CO_{ad}

electrooxidation have been qualitatively explained by the position of the d band center for gold in comparison to palladium and platinum.[38,39,40,41]

Following the CO_2 production and CO_B oxidation with the applied potential, the onset potential for CO oxidation can be established. With this purpose, integration of the CO_2 band was easily performed from spectra in Figure 2, but it was not possible to integrate directly the CO_B band due to its bipolar character. It was consequently necessary to change the reference spectrum to one at which no adsorbed CO_B was present on the surface, in order to obtain absolute (not bipolar) bands. In this case, the single bean spectrum acquired at 1.10 V was taken as reference for the calculation of the FTIR spectra and the whole series was reevaluated (see Supporting Information, Figure S1). The integrated band intensities for CO_B and CO_2 at each potential are plotted in Figure 3. For both electrodes, the CO band intensity remains constant in the potential region prior to the onset of formic acid oxidation and decreases as the formation of CO_2 occurs. However, in these curves clear evidences of the different behavior of the materials under investigation can be seen and a shift in CO_2 production of around 100 mV to lower potentials is established for CS10/C, as expected from the cyclic voltammograms in Figure 1.

It is necessary to comment the existence of small differences in the band intensity values (around 10 %) between the two catalysts. Because of the procedures of preparation of the ink and its deposition on the Au electrode used for FTIR studies (see experimental section), it is very difficult to reproduce exactly the same final conditions (same surface reflectivity) even if the procedure for electrode preparation was followed carefully and the same aliquot was deposited each time. Therefore, absolute intensity values are not directly comparable, but the onset potential and the shape of the curves in Figure 3 are not affected by this fact.

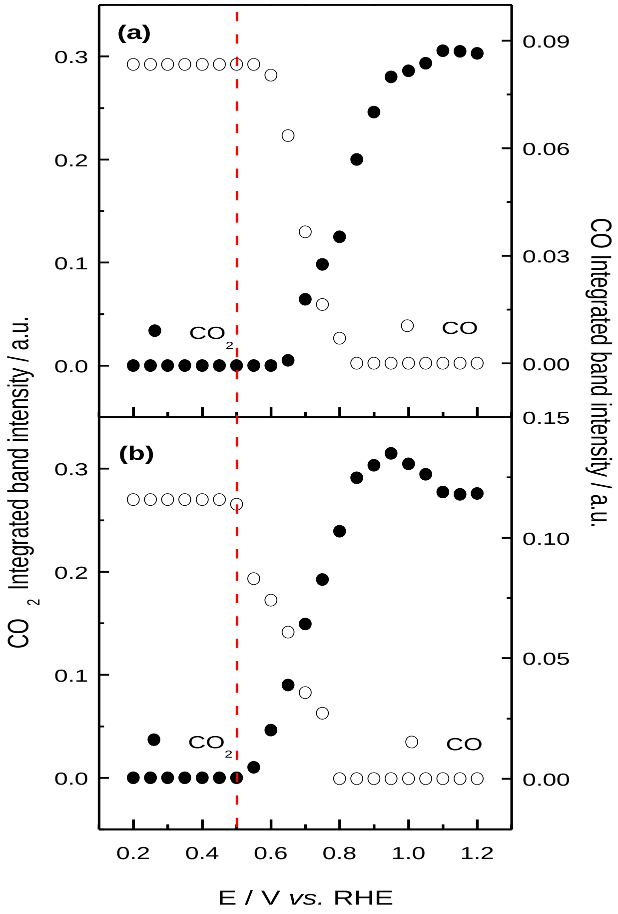

Figure 3. Potential dependence of the integrated band intensity for CO (open circles) and CO_2 (full circles) obtained from CO stripping spectra on CS1/C (a) and CS10/C (b).

Figure 4 shows how the CO_B band center, obtained from Figure S1, shifts with the applied potential for the catalysts studied. The up shift of the band center with the applied potential can be explained on the basis of the metal-CO back-bonding or the perturbation of the vibration frequency in the static electric field of the double layer (the Stark effect), in addition to the effect of the lateral interaction between adsorbed molecules.[42,43]

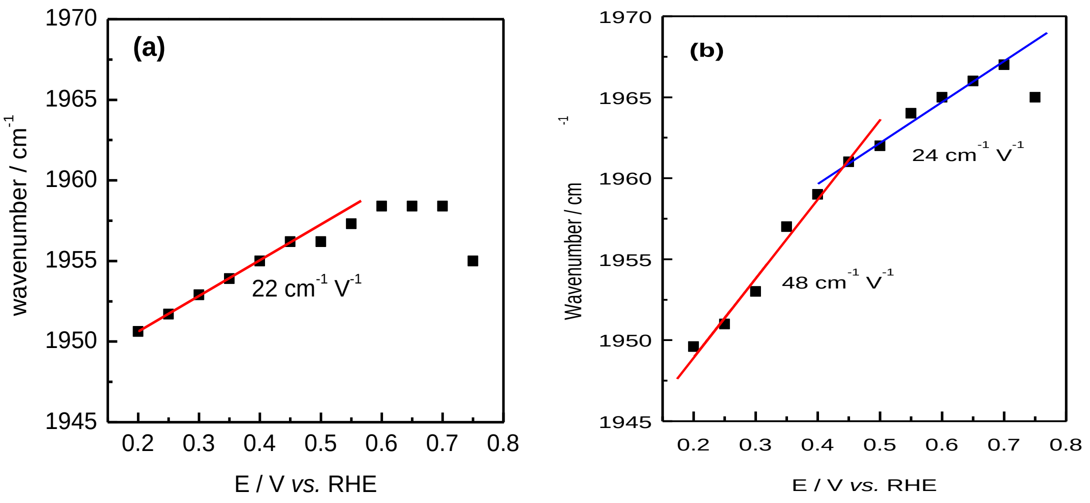

Figure 4. Potential dependence of the C-O stretch wavenumber for CO_{ads} stripping on CS1/C (a) and CS10/C (b).

Firstly, it can be observed that the wavenumbers for CO_{ad} stretch at 0.20 V are similar for both core-shell materials (1951 and 1948 cm^{-1} for CS1 and CS10, respectively). However, big differences are appreciated in the change of the wavenumber with the potential (i.e. *dv/dE*, known as Stark slope). It is observed that between 0.20 and 0.45 V the slope for the CS1/C material is much lower (22 cm^{-1} V^{-1}) than for the CS10/C catalyst (48 cm^{-1} V^{-1}). This fact can be justify considering an electronic effect induced by Au on the Pd nanoshells that avoids the electro back-donation from Pd to CO, and as consequence, the Pd-CO interaction in the CS1/C catalysts is weakened. It must be taken in mind that CO displays a weak adsorption on Au in acid medium.[36] [36,44,45] In the case of the CS10 catalysts instead, it contains a larger number of Pd overlayers and the particle tends to resemble more to Pd bulk,[25,44] strengthening the Pd-CO interaction which corresponds to a higher Stark slope. These results are in agreement with previous studies[46,47,48], where values of 42 and 45 cm^{-1} V^{-1} were obtained for CO_{ad} at Pd bulk and Pd/Pt(110), respectively.

Additionally, in Figure 4 a change in the Stark slope is observed at 0.45 V, i.e. at the onset potential for CO_{ad} oxidation. Thus, a value of 24 cm^{-1} V^{-1} was determined in the 0.45-0.70 V potential range where oxidation takes place. It seems that as soon as the oxidation of adsorbed CO commences, a relaxation of the adsorbate layer takes places decreasing the strength of the interaction with the metal and consequently diminishing the Stark slope in this potential region.

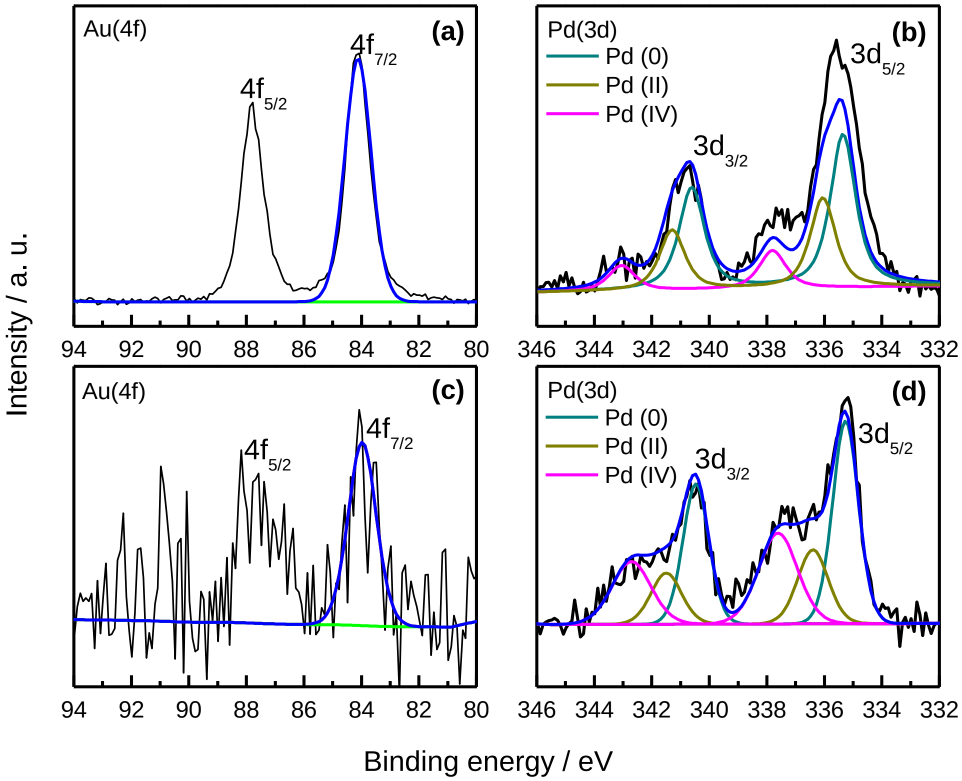

Figure 5. X-ray photoelectron spectra of CS1/C and CS10/C corresponding to Au 4f and Pd 3d transitions. (a, b) CS1 and (c, d) CS10.

In order to identify the electronic effect caused by the Au core on the surface as well as the surface composition, XPS analysis was carried out. The binding energy spectra of Au 4f (Figure 5(a) and (c)) present two peaks at 88 and 84 eV corresponding to the transitions in the Au $4f_{7/2}$ y Au $4f_{5/2}$ orbitals, respectively, which are clearly visible for the CS1/C catalysts but hardly observable for the CS10/C catalysts (with a big noise to signal ratio), confirming the Au vicinity to the surface in the first case. The Au $4f_{7/2}$ peak deconvolution shows that only Au(0) is present in these materials.

On the other hand, the binding energy spectra of Pd 3d are given in Figures 5(b) and (d) showing the transitions associated to the Pd $3d_{3/2}$ and Pd $3d_{5/2}$ orbitals in the binding energy regions 345-339 eV and 339-333 eV, respectively. From the deconvolution of these spectra, three pairs of Pd peaks are found. The peaks close to 340 and 335 eV are attributed to the transitions generated in the $3d_{3/2}$ and $3d_{5/2}$ orbitals for the Pd(0), whereas the second and third pair of peaks, observed ca. 341/336 and 343/338 eV, are related to Pd(II) and Pd(IV), respectively[49]. The blue curves in Figures 5(b) and (d) correspond to the addition of the three pairs of peaks. It is observed that the fitting of this curve with the experimental one is quite bad for the Pd $3d_{5/2}$ transition. This fact can be explained by the presence of a gold signal around 335 eV, which is significant for the CS1/C material. Because of the presence of this contribution, the Pd $3d_{3/2}$ transitions were used for the calculation of the relative abundance of the three possible Pd oxidation states. Table 1 summarizes the results obtained from the XPS study.

For both CS1/C and CS10/C materials, Pd(0) is the predominant oxidation state, although this contribution is higher for the former catalysts. However, significant amounts of oxidized species are also observed being Pd(IV) the main state for CS10/C whereas Pd(II) is the major contribution for CS1/C. The presence of Pt oxides on the surface is justified, in part, by the catalyst exposure to the atmosphere. However, clear differences are observed in the relative abundance of Pd(0), Pd(II) and Pd(IV) for the two core-shell materials. The predominant species in both catalysts is found to be Pd(0), but the relative amount in the CS1/C catalyst is higher than in the CS10/C, probably due to charge transfer from the Au core to the Pd shell. It is remarkable the relative high amount of

Pd(IV) in CS10/C, which seems to be responsible for the trend of this material to adsorb water (eq. 3) and justifies the CO oxidation at more negative potentials respect to CS1/C, as could be observed in the electrochemical results in Figures 1 and 2.

Tabla 1. Electronic and composition parameters from XPS data for CS1/C and CS10/C catalysts

Catalyst	**Pd$_{species}$**	**Pd 3d$_{3/2}$ eV**	**(% at.)**
CS1/C	Pd (0)	340.6	55
	Pd (II)	341.2	31
	Pd (IV)	343.0	14
CS10/C	Pd (0)	340.4	41
	Pd (II)	341.5	24
	Pd (IV)	342.7	35

DEMS and FTIR study of HCOOH electrooxidation. Figure 6 shows the CVs (black lines) and the simultaneously recorded mass spectrometric cyclic voltammogram (MSCVs) for m/z = 44 corresponding to CO_2 (red lines), for the different CS nanostructures supported on Vulcan XC-72R in 0.1 M HCOOH + 0.5 M H_2SO_4. It is observed that only CO_2 was detected during formic acid oxidation and, accordingly, current efficiencies of approx. 100 % were estimated for CO_2 formation. The different CV profiles are possibly due to the electronic effect caused by the underlying Au substrate, which can also influences the nature and amount of intermediates generated during the HCOOH electrooxidation as in the case of CO_{ad}.

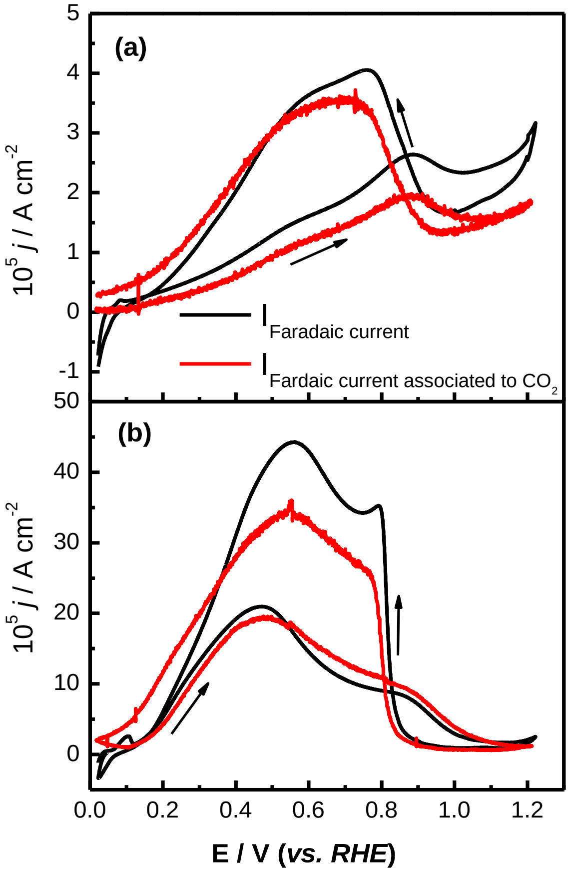

Figure 6. Faradic currents from CVs (black lines) and MSCVs (red lines) for m/z = 44 for the electrodes CS1/C (A) and CS10/C (B); in 0.5 M HCOOH + 0.5 M H_2SO_4. ν = 0.001 V s^{-1}; T = 25 ºC. For details on the conversion of ionic currents from CO_2 in faradaic currents, see Figure 2S in the Supporting Information.

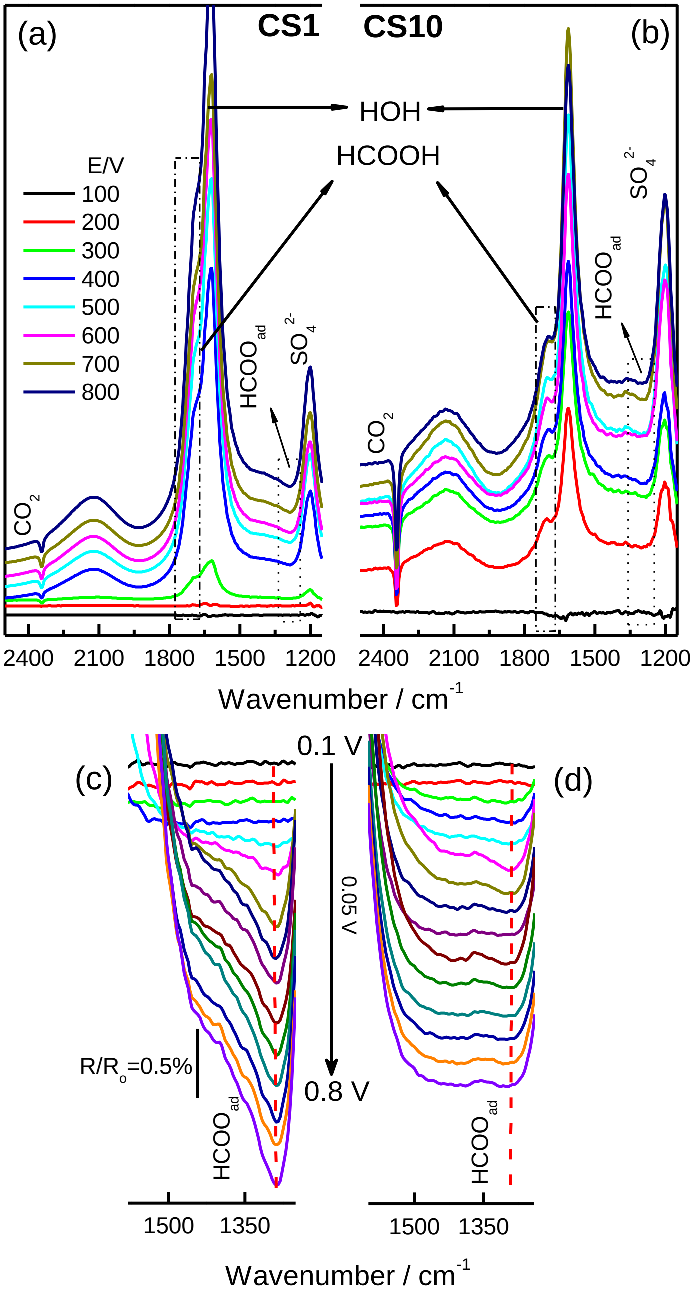

Figure 7. *In situ* FTIR spectra recorded during formic acid electrooxidation on (a) CS1/C (left) and (b) CS10/C (right) catalysts in 0.1 M HCOOH + 0.5 M H_2SO_4. (c) and (d) detail of the 1250-1600 cm^{-1} region for $HCOO_{ad}$ recorded during formic acid electrooxidation on CS1/C and CS10/C catalysts, respectively. The potential was positively changed from 0.05 V (reference potential) onward in 0.05 V steps up to 1.20 V. 128 scans, 8 cm^{-1}.

With the purpose to identify the intermediates formed in the process for both materials, FTIR spectroscopy studies were performed. Figure 7 shows the spectra recorded for the formic acid electrooxidation during positive-going potential steps from 0.05 V (reference potential) onward in 0.05 V steps up to 1.20 V. The spectra exhibit three positive (consumption) bands around 1200, 1620 and 1700 cm^{-1} which corresponds to bisulfate/sulfate anions,[32] water bending and carbonyl vibration from HCOOH, respectively. [22,32,**¡Error! Marcador no definido.**] The negative band located at 2343 cm^{-1} is attributed to the CO_2 formation during the oxidation. In addition, a negative band appears at 1290 cm^{-1} for the CS1/C material that is not present in the case of CS10/C catalyst (see magnification of the spectral region in the Figure 7 (c) and (d)). This feature can be assigned to the presence of $HCOO_{ad}$[50] during formic acid electrooxidation at CS1/C. According to XPS measurements, this effect can be explained assuming that the electronic effect caused by Au core on the Pd surface, induces a stronger adsorption of $HCOO_{ad}$ on CS1 catalysts than on the CS10 (see discussion later). This result agrees with those reported by A. Cuesta *et al.* [45,51]

On the other hand, Miyake *et al.*[46] studied the formic acid electrooxidation on Pd in sulfuric and perchloric acid and they suggested that the absence of the formate adsorption band in perchloric acid is due to the existence of a short-lived intermediate which cannot be detected by IR. Accordingly, in our case, it can be proposed that the voltammetric profile and the low current density for HCOOH oxidation at CS1 are due to the high adsorption barrier for $HCOO_{ad}$ electrooxidation which increases the lived-time of the intermediate. Thus, the electronic effect of the Au core on the Pd shell inducing the presence of lower amounts of Pd oxide, especially Pt(IV), produces that more positive potentials are necessary for the oxidation of the adsorbate to CO_2 (also in the case of COad, higher onset oxidation potential was established for CS1/C from Figures 1 and 2). Accordingly, high current densities are recorded for CS10 at $E < 0.45$ as $HCOO_{ad}$ oxidation to

CO_2 is faster ($HCOO_{ad}$ appears in this case as the short-lived species proposed for oxidation at Pd [41,46,47]) and the intermediate cannot be detected. From this potential upwards, the current density progressively decreases probably because of the concurrence with increasing bi(sulphate) adsorption in this potential region.

According with these results and on the basis of the XPS data from Figure 5 and Table 1, it can be proposed that the difference in the current densities for formic acid electrooxidation on CS1/C and CS10/C catalysts (figure 6) is mainly related with the presence of higher amounts of Pd(IV) for the later. Therefore, the mechanism for formic acid electrooxidation can be described as follows. During the positive going scan, two successive monoelectronic steps are considered. In the first step for both catalysts, HCOOH molecules fast adsorb as formate on the surface through a deprotonation reaction:

$$HCOOH + Au@Pd^{x} \longrightarrow HCOO_{ad} + H^{+} + e^{-} \qquad \text{fast} \qquad (7)$$

This reaction occurs at low potentials and the adsorbate is accumulated on the surface. As mentioned earlier, the second step (eqs. 8 and 9) depends on the oxidation state of the Pd surface.

$$HCOO_{ad} + Au@Pd^{1}(CS1) \longrightarrow CO_2 + H^{+} + e^{-} \qquad \text{slow} \qquad (8)$$

$$HCOO_{ad} + Au@Pd^{10}\ (CS10) \longrightarrow CO_2 + H^{+} + e^{-} \qquad \text{fast} \qquad (9)$$

In this way, on the CS10/C the reaction is fast (eq. 9) as the Pd surface is higher oxidized according to XPS data and the formate formed at low potentials are rapidly oxidized to CO_2 which results in an increase in the current in the CVs (Figure 6). Thus, a current density maximum of 21 A/cm^2 is achieved a 0.45 V. On the contrary, accumulation of the adsorbates occurs on the CS1/C surface catalyst (as demonstrated in the spectra in Figure 7(c)) and the current flow is inhibited attaining a maximum at 0.90 V of 2.6 A/cm^2. Then, more positive potentials are needed in this case for the electrooxidation. For both materials, after the peak the current density slightly decreases (Figure 6) due to the interaction of water with the Pd surface (it should be taken in mind that the formation of Pd surface oxides inhibits the process because the first adsorption step is blocked and consequently the current drops). During the reverse scan, as soon as the oxides are reduced, the reactivation occurs first describing a peak as the surface become free from adsorbates and then decreasing the current density as reaction (7) starts to prevail (Figure 6).

Finally, it is important to mention that during the formic acid electrooxidation, the CO_{ad} formation on both catalysts is not considered because the CO_{ad} was not observed in the FTIR experiments.

CONCLUSIONS

The electrochemical oxidation of CO_{ad} and formic acid on Au@Pd/C nanostructure with different Pd thickness were investigated employing two spectroelectrochemical techniques: differential electrochemical mass spectrometry (DEMS) and *in situ* Fourier transform infrared spectroscopy (FTIRS), combined with cyclic voltammetry. Thus, the electrooxidation mechanism and the intermediates formed were elucidated.

The onset potential for CO stripping exhibited a shift toward more positive potentials as the Pd thickness decreases which was confirmed by FTIR spectra. Additionally, OH_{ad} was detected only in the 10 nm Pd-shell (CS10/C) catalyst, indicating a stronger water interaction which acts as the source of the OH_{ads} species co-adsorbed with the CO adlayer, while the CO oxidation on the 1 nm

Pd-shell (CS1/C) catalyst possibly occurs through the formation of the carboxylic species $COOH_{ads}$ as a short-life intermediate.

FTIR analysis confirmed the existence of an electronic effect induced by Au on the Pd nanoshells that avoid the electro back-donation from Pd to CO and as consequence, the Pd-CO interaction in the CS1/C catalysts is weakened. In the case of the CS10 catalysts instead, it contains a larger number of Pd nanoshells and the particle tends to resemble more the electronic behavior of Pd bulk. This comportment correlates well with the surface composition of Pd species at CS nanostructures determined by XPS.

On the other hand, DEMS and FTIR studies showed that the only product during formic acid oxidation is CO_2. From DEMS current efficiencies around 100 % were estimated (as expected) for CO_2 formation and FTIR spectra have confirmed the absence of CO_{ad} during the process. Moreover, the formate signal in the infrared spectra only observed in the case of CS1/C, suggests again that an electronic effect caused by Au core on the Pd surface has happened, inducing a stronger adsorption of $HCOO_{ad}$ (formate species) on the CS1/C catalyst than on the CS10/C. Accordingly, the deprotonation of $HCOO_{ad}$ on CS1/C is slower than on CS10/C, allowing its detection through FTIRS. XPS analysis permits to determine the presence of higher amount of Pd(IV) on the later, promoting the oxidation at lower potentials.

Thus, it is demonstrated that core electronic effects on the shell surface can be controlled by the thickness of the overlayers, and accordingly, the reaction mechanism modified in the desired direction.

ACKNOWLEDGMENT

VC gratefully acknowledges the UK National Academy by their support through the Newton International Fellows program. EP acknowledges financial support given by the Ministry of Economy and Competitiveness through the Project CTQ2011-28913-C02-02.

ASSOCIATED CONTENT

Supporting Information. Experimental methods . This material is available free of charge via the Internet at http://pubs.acs.org.

AUTHOR INFORMATION

Corresponding Author

*E-mail: David.Fermin@bristol.ac.uk (D.J.F)

*E-mail: E.Pastor@ull.edu.es (E.P.)

REFERENCES

---

(1) Norskov, J. K.; Bligaard, T.; Rossmeisl, J.; Christensen, C. H. *Nat. Chem.* **2009**, 1, 37-46.

(2) Liu, P.; Norskov, J. K. *Phys. Chem. Chem. Phys.* **2001**, 3, 3814-3818.

(3) Strasser, P.; Koh, S.; Anniyev, T.; Greeley, J.; More, K.; Yu, C.; Liu, Z.; Kaya, S.; Nordlund, D.; Ogasawara, H.; Toney, M. F.; Nilsson, A. *Nat. Chem.* **2010**, 2, 454-460.

(4) Santos, E.; Quaino, P.; Schmickler, W. *Electrochim. Acta* **2010**, 55, 4346-4352.

(5) Kibler, L. A.; El-Aziz, A. M.; Hoyer, R.; Kolb, D. M. *Angew. Chem. Int. Ed.* **2005**, 44, 2080-2084.

(6) Bonnefont, A.; Simonov, A. N.; Pronkin, S. N.; Gerasimov, E. Y.; Pyrjaev, P. A.; Parmon, V. N.; Savinova, E. R. *Catal. Today* **2013**, 202, 70-78.

(7) Lee, Y. W.; Kim, N. H.; Lee, K. Y.; Kwon, K.; Kim, M.; Han, S. W. *J. Phys. Chem. C* **2008**, 112, 6717-6722.

(8) Quaino, P.; Santos, E.; Wolfschmidt, H.; Montero, M. A.; Stimming, U. *Catal. Today* **2011**, 177, 55-63.

(9) Ruvinsky, P. S.; Pronkin, S. N.; Zaikovskii, V. I.; Bernhardt, P.; Savinova, E. R. *PhysChemChemPhys.* **2008**, 10, 6665-6676.

(10) El-Aziz, A. M.; Kibler, L. A. *J. Electroanal. Chem.* **2002**, 534, 107-114.

(11) Kuo, C.-H.; Lamontagne, L. K.; Brodsky, C. N.; Chou, L.-Y.; Zhuang, J.; Sneed, B. T.; Sheehan, M. K.; Tsung, C.-K. *ChemSusChem.* **2013**, 6, 1993-2000.

(12) Roudgar, A.; Groß, A. *Phys. Rev. B* **2003**, 67, 033409 (1-4).

---

(13) Celorrio, V.; Montes de Oca, M. G.; Plana, D.; Moliner, R.; Lázaro, M. J.; Fermín, D. J. *J. Phys. Chem. C* **2012**, 116, 6275-6282.

(14) Montes de Oca, M. G.; Kumarakuru, H.; Cherns, D.; Fermín, D. J. *J. Phys. Chem. C* **2011**, 115, 10489-10496.

(15) Montes de Oca, M. G.; Plana, D.; Celorrio, V.; Lazaro, M. J.; Fermín, D. J. *J. Phys. Chem. C* **2011**, 116, 692-699.

(16) Plana, D.; Flórez-Montano, J.; Celorrio, V.; Pastor, E.; Fermin, D. J. *Chem. Commun.* **2013**, 49, 10962-10964.

(17) Qin, Y., Wang, J., Wu, Y. & Wang, L. *RSC Adv.* **2014**, 4, 30068-30073.

(18) Lee, S., Jung, N., Cho, J., Park, H., Ryu, J., Jang, I., Kim, H., Cho, E., Park, Y., Ham, H.C., Jang, J.H. & Yoo, S.J. *ACS Catal.* **2014**, 4, 2402-2408.

(19) Osawa, M., Komatsu, K., Samjeské, G., Uchida, T., Ikeshoji, T., Cuesta, A. & Gutiérrez, C. *Angew. Chem. Int. Ed.* **2011,** 50, 1159-1163.

(20) Rice, C.A. & Wieckowski, A. In *Electrocatalysis in Fuel Cells*, ed.; Chao, M. Eds. Springer-Verlag London, London, 2013; pp. 43-67.

(21) Nishimura, K., Kunimatsu, K., Machida, K. & Enyo, M. *J. Electroanal. Chem. Interf. Electrochem.* **1989**, 260, 181-192.

(22) Cuesta, A., Escudero, M., Lanova, B. & Baltruschat, H. Langmuir, **2009**, 25, 6500-6507.

(23) Maiyalagan, T., Wang, X. & Manthiram, A. *RSC Adv.* **2014**, 4, 4028-4033.

(24) Liu, Y., Wang, L., Wang, G., Deng, C., Wu, B. & Gao, Y. *J. Phys. Chem. C* **2010**, 114, 21417-21422.

(25) Hoshi, N., Kida, K., Nakamura, M., Nakada, M. & Osada, K. *J. Phys. Chem. B* **2006**, 110, 12480-12484.

(26) Chen, M., Kumar, D., Yi, C. & Goodman, D.W. *Science* **2005**, 310, 291-293.

(27) Flórez-Montaño, J.; García, G.; Guillén-Villafuerte, O.; Rodríguez, J. L.; Pastor, E. *Electrochim. Acta*, submitted.

(28) Guillén-Villafuerte, O.; García, G.; Arévalo, C.; Rodríguez, J. L.; Pastor, E., *Electrochem. Commun.*, submitted.

(29) Celorrio, V.; Montes de Oca, M. G.; Plana, D.; Moliner, R.; Fermín, D. J.; Lázaro, M. J. *Int. J. Hydrogen Energ.* **2012**, 37, 7152-7160.

(30) Zhou, W.; Lee, J. Y. *Electrochem. Commun.* **2007**, 9, 1725-1729.

(31) Moore, A.; Celorrio, V.; de Oca, M. M.; Plana, D.; Hongthani, W.; Lazaro, M. J.; Fermin, D. J. *Chem. Commun.* **2011**, 47, 7656-7658.

(32) Iwasita, T.; Nart, F. C. *Prog. Surf. Sci.* **1997**, 55, 271-340.

(33) Yajima, T.; Uchida, H and Watanabe, M. *J. Phys. Chem. B* **2004**, 108, 2654-2659

(34) Panayotov, D. A.; Yates Jr., J. T. *Chem. Phys. Lett.* **2005**, 410, 11–17.

(35) Gilman, S. *J. Phys Chem.* **1964**, 68, 70-80.

(36) Edens, G.J., Hamelin, A. & Weaver, M. J. *J. Phys. Chem.* **1996**, 100, 2322-2329.

(37) Pronkin, S., Hara, M. & Wandlowski, T. *Russ. J. Electrochem.* **2006**, 42, 1177-1192.

(38) Ruban, A., Hammer, B., Stoltze, P., Skriver, H. L. & Nørskov, J. K. *J. Mol. Catal. A: Chemical* **1997**, 115, 421-429.

(39) Hammer, B., Nielsen, O. H. & Nørskov, J. K. *Catal. Lett.* **1997**, 46, 31-35.

(40) Shubina, T. E., Hartnig, C. & Koper, M. T. M. *Phys. Chem. Chem. Phys.* **2004**, 6, 4215-4221.

(41) Roudgar, A. & Groß, A. *J. Electroanal. Chem.* **2003**, 548, 121-130.

(42) Stamenkovic, V.; Chou, K. C.; Somorjai, G. A.; Ross, P. N.; Markovic, N. M. *J. Phys. Chem. B* **2004**, 109, 678-680.

(43) Matthew, N.; Rutger, A. V. S.; Marc, T. M. K. In *Catalysis and Electrocatalysis at Nanoparticle Surfaces*, CRC Press: 2003.

(44) Beltramo, G. L., Shubina, T. E. & Koper, M. T. M. *ChemPhysChem.* **2005**, 6, 2597-2606.

(45) Cuesta, A.; Cabello, G.; Hartl, F. W.; Escudero-Escribano, M.; Vaz-Domíngueza, C.; Kibler, A. K.; Osawa, M.; Gutiérrez, C. *Catal. Today* **2013**, 202, 79– 86.

(46) Park, S.; Xie, Y.; Weaver, M. J. *Langmuir* **2002**, 18, 5792-5798.

(47) Gómez, R., Rodes, A., Pérez, J.M., Feliu, J.M. & Aldaz, A. *Surf. Sci.* **1995**, 327, 202-215.

(48) Jiang, Y., Ding, N. & Sun, S. *J. Electroanal. Chem.* **2004**, vol. 563, no. 1, pp. 15-21.

(49) Wagner, C. D.; Riggs, W. M.; Davis, L. E.; Moulder, J. F. In *Handbook of X-ray Photoelectronic Spectroscopy*, G. E. Muilenberg.; Eds., Perkin-Elmer Corp, Eden Prairie, MN, USA, 1979.

(50) Miyake, H.; Okada, T.; Samjeské, G.; Osawa, M. *Phys. Chem. Chem. Phys.* **2008**, 10, 3662-3669.

(51) Cuesta, A.; Cabello, G.; Osawa, M.; Gutiérrez, C. *ACS Catal.* **2012**, 2, 728–738.

ChemComm

RSC Publishing

COMMUNICATION

View Article Online
View Journal | View Issue

Tuning CO_2 electroreduction efficiency at Pd shells on Au nanocores†

Cite this: *Chem. Commun.*, 2013, **49**, 10962

Received 27th August 2013,
Accepted 11th October 2013

DOI: 10.1039/c3cc46543h

www.rsc.org/chemcomm

Daniela Plana,[a] Jonathan Flórez-Montaño,[b] Veronica Celorrio,[a] Elena Pastor*[b] and David J. Fermín*[a]

The faradaic efficiency of CO_2 electroreduction is significantly affected by the thickness of Pd nanoshells on Au cores. The ratio of hydrogen evolution to CO_2 reduction was determined by differential electrochemical mass spectrometry. Decreasing the Pd shell thickness from 10 to 1 nm leads to a twofold increase in faradaic efficiency.

It is estimated that chemical transformation of carbon dioxide, such as thermo- and electrocatalysis, can reduce CO_2 emissions by 5 to 10%.[1] The electrochemical reduction of CO_2 has attracted considerable attention, particularly using electrodes with high overpotentials for hydrogen evolution, with special emphasis on copper.[2–7] Recent studies have shown that the efficiency can be affected by the presence of copper oxide[8] or the stabilisation of intermediates by the use of molecular systems.[9,10] The mechanisms involved and product selectivity remain to be fully resolved, however. An important limitation is the low solubility of CO_2 in aqueous systems, which leads to slow reduction rates and small molecules as products;[11,12] the use of nanostructured carbon supports for catalytic metallic centres has been suggested to increase local CO_2 concentration.[12,13]

Materials with low hydrogen overpotentials, such as Pt or Pd, have been studied more scarcely, mainly due to the loss of efficiency produced by hydrogen evolution and the self-poisoning phenomena by CO adsorption observed on Pt surfaces. In contrast to other electrocatalytic applications, Pd and Pt have exhibited significantly different behaviour towards CO_2 reduction,[11,14,15] due to differing interactions with adsorbed intermediates, such as CO_{ads} or $COOH_{ads}$, and the presence of absorbed hydrogen in Pd.[14,16,17] On Pd, CO and formic acid have been reported as products at low overpotentials, while a range of alkanes from methane to hexane have been observed at higher potentials.[18,19]

The faradaic efficiency for CO_2 reduction is limited by the rate of the hydrogen evolution reaction (HOR); a process reported to be affected by the thickness of Pd overlayers on Au substrates.[20,21] In this communication, we show for the first time an acute thickness dependence of the CO_2 electroreduction faradaic efficiency at Au–Pd core–shell nanostructures, with values above 90% for shells with thickness of the order of 1 nm. The faradaic efficiency is determined by quantitative analysis of hydrogen generation employing differential electrochemical mass spectrometry (DEMS). The thickness dependence of the effective lattice strain of Pd nanoshells on Au cores and its correlation with hydrogen adsorption–absorption properties, CO tolerance and catalytic activity towards HCOOH oxidation have been investigated in detailed in previous reports.[22–25] Our results clearly show a delicate balance between the adsorption of CO_2 electroreduction intermediates and the rate of HOR.

The preparation and characterisation of the electrocatalysts have been previously described[22,24–26] and are summarised in the ESI.† TEM images of the catalysts are shown as insets in Fig. 1. Au–Pd core–shell nanoparticles of 1.3 and 9.9 ± 1.0 nm shell thickness (CS1 and CS10, respectively) on 19.3 ± 1.0 nm diameter cores were prepared and used to study the influence of Pd thickness on the electrochemical reduction of CO_2. They were attached on carbon supports aiming for an approximate metal loading of 20% (21.1 and 20.2 ± 2.0% for CS1 and CS10, respectively). The effective Pd surface area, used for normalising current responses, was determined in each catalyst by the charge associated with electro-oxidation of a CO monolayer in acid solution (see ESI†).

Fig. 1 shows cyclic voltammograms in CO_2 (full black line) and Ar-saturated (dashed lines) solutions, using CS1 and CS10 supported catalysts. Responses associated with Pd oxide formation and reduction are clearly seen at positive potentials in the absence of CO_2. At negative potentials, signals related to the adsorption, absorption and evolution of hydrogen can be

---

[a] *School of Chemistry, University of Bristol, Cantocks Close, Bristol BS8 1TS, UK. E-mail: david.fermin@bristol.ac.uk; Tel: +44 (0)117 928981*

[b] *Universidad de La Laguna, Dpto. de Química-Física, Instituto de Materiales y Nanotecnología, Avda. Astrofísico Francisco Sánchez s/n, 38071 La Laguna, Spain. E-mail: epastor@ull.es; Tel: +34 92 2318028*

† Electronic supplementary information (ESI) available: Experimental details, as well as determination of *k* values and faradaic efficiency. See DOI: 10.1039/c3cc46543h

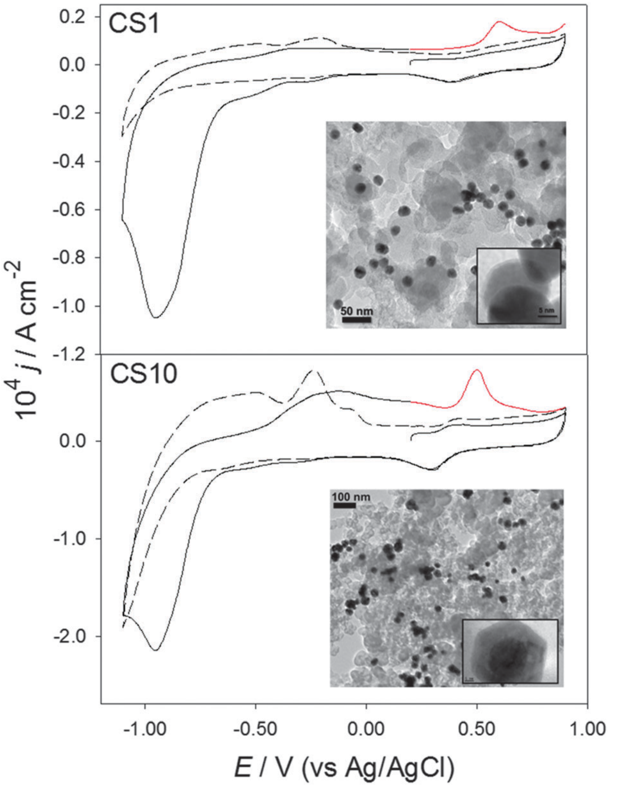

Fig. 1 Cyclic voltammograms at 20 mV s^{-1} in pH 4 0.1 M Na_2SO_4, on Vulcan-supported CS1 and CS10 nanostructures. The dashed lines were performed in Ar-saturated solutions; the full black and red lines show the first and partial second scans in CO_2-saturated solutions, respectively.

observed in the negative going scan, while hydrogen oxidation and desorption are evident on the positive direction. The hydrogen response is significantly larger on the thicker Pd shells (CS10), in agreement with previous studies.[22,25] Upon saturation with CO_2 (full black lines), the Pd oxide signals remain the same, however, a large cathodic current starts at approximately −0.60 V, with a peak observed at −0.95 V (all potentials are quoted *versus* Ag/AgCl). At the peak, the current density is almost an order of magnitude higher than in the absence of CO_2. Two pre-peaks can be seen starting just negative of −0.10 V, particularly on the CS1 sample. The cathodic currents are indicative of CO_2 reduction catalysed by the bi-metallic nanostructures (voltammograms in the absence of metal particles show negligible currents); reduction of CO_2 has been previously observed at similar potentials on bulk Pd surfaces.[15,17]

Upon reversing the scan, the oxidation and desorption of hydrogen are much less significant than in the Ar-saturated solutions, indicating that either hydrogen takes part in CO_2 reduction or that the adsorption sites were blocked by CO_2 or intermediates/products. Additionally, a prominent peak can be seen in the region of Pd oxide formation; this last is due to the oxidation of adsorbed intermediates formed during the reduction of carbon dioxide. The signal has similar shape and appears at the potentials expected for the electro-oxidation of CO_{ads} to CO_2 on this type of catalysts (at the onset of Pd oxide formation, roughly 200 mV more positive than the Pd oxide reduction peak).[24] This response has been ascribed to bridge-bonded CO on Pd bulk surfaces and has recently been reported at thin Pd films on Au substrates.[15,27] The current densities of this peak, as well as that of CO_2 reduction (−0.95 V), are approximately double for CS10 in comparison to CS1.

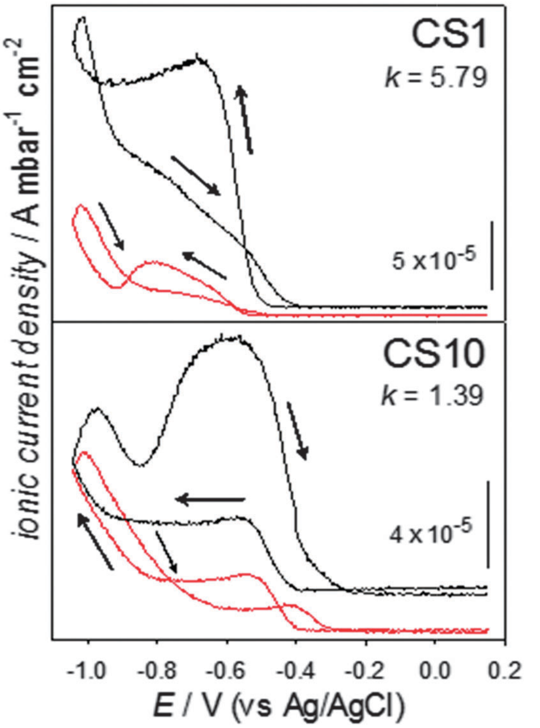

Fig. 2 Mass spectrometric cyclic voltammograms, for the $m/z = 2$ signal, at 5 mV s^{-1}, in Ar- or CO_2-saturated solutions (black and red curves, respectively) using Vulcan-supported CS1 and CS10 nanostructures.

Fig. 2 shows the ionic current density for hydrogen ($m/z = 2$), on CS1 and CS10. Mass spectrometer constant values (k) for the HOR in each catalyst in the set-up used are also presented; their determination is detailed in the ESI.† In the absence of CO_2 (black curves), an initially flat signal begins to rise at potentials close to −0.40 V, with a sharp increase at potentials more negative than −0.80 V, consistent with the electrochemical hydrogen contributions in Fig. 1. Upon scan reversal, clear differences are apparent. For CS1, hydrogen production continues increasing during the first 50 mV and then slowly diminishes with a change in the slope of decrease around −0.90 V, before the signal returns to its original level. For CS10, hydrogen production increases developing a peak at 0.95 V and then a broad contribution around 0.60 V, finally achieving the background level. This second contribution, which is only apparent for the thicker Pd shells, is likely due to hydrogen absorbed in the Pd lattice being expelled.

Significant differences can be observed in the presence of CO_2, clearly indicating that hydrogen processes are affected by the presence and reaction of carbon dioxide. The most notable change is seen in the back scan, where the hydrogen signal sharply decreases in the presence of CO_2. Electrochemical and infrared spectroscopy studies on bulk Pd, have suggested that absorbed hydrogen takes part in CO_2 electroreduction, producing molecules such as HCOOH.[14,16]

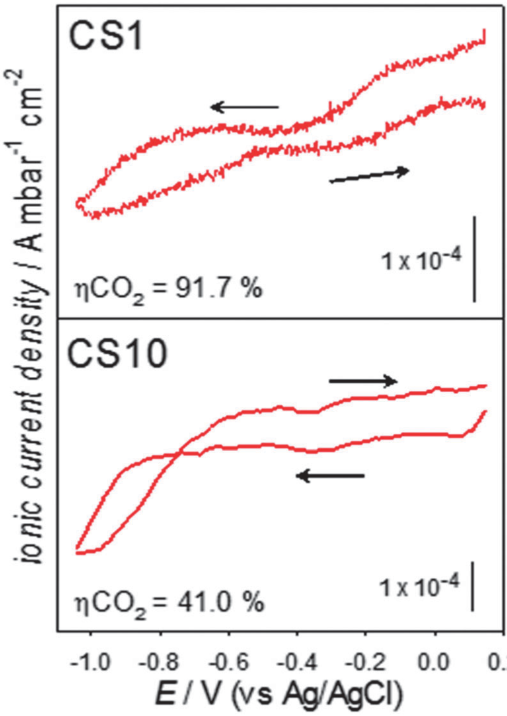

Fig. 3 Mass spectrometric cyclic voltammograms, for the $m/z = 44$ signal, at 5 mV s^{-1}, in CO_2-saturated solutions on the CS1 and CS10 catalysts.

Fig. 3 shows the signal with a charge to mass ratio of 44, indicative of carbon dioxide. A high background signal is obtained on both catalysts, as the system is saturated with CO_2. A decrease in the CO_2 background signal become noticeable from potentials more negative than −0.65 V, which is consistent with onset of CO_2 reduction in Fig. 1 for both samples. It is interesting to note that the current responses between −0.2 and −0.5 V for CS1 (Fig. 1) coincides with a decrease in the CO_2 ionic current (Fig. 3), confirming a lower overpotential for the electroreduction at the CS1 nanostructures.

The faradaic efficiency for CO_2 reduction (ηCO_2), as estimated from integration of the faradaic and ionic current ($m/z = 2$) densities are also indicated in Fig. 3. As discussed in the ESI,† quantitative estimations can be achieved employing the hydrogen signal due to its low background signal and strong potential dependence. On the present conditions, CS1 exhibits a remarkable ηCO_2 above 90% in comparison to the *ca.* 40% observed for CS10. Careful analysis of the trends in Fig. 2 and Fig. S1 (ESI†) suggests the high faradaic efficiency of CS1 particles is related to a strong inhibition of the HOR in the presence of CO_2 rather than higher CO_2 conversion turn-over rate. Similar efficiencies have been obtained employing potential steps at −0.90 and −1.05 V over a timescale of 300 s.

In summary, a remarkable thickness dependence of the faradaic efficiency for CO_2 electroreduction at Pd nanoshells on Au cores is reported for the first time. Electrochemical and DEMS responses clearly show that the CS1 catalyst exhibits lower overpotential for CO_2 reduction than CS10. Quantitative analysis of DEMS responses for $m/z = 2$ indicate that hydrogen absorption and evolution play a fundamental role in the contrasting reactivity of the Pd nanoshells. A key descriptor in this system is the effective lattice strain of the Pd shell, which decreases from 3.5 to less than 1% upon increasing the Pd thickness from *ca.* 1 to 10 nm.[20] For instance, this decrease in lattice strain is responsible for a three-fold increase in the average CO coverage at the Pd shells.[19,21] We believe this trend is responsible for the lower CO_{ads} oxidation current density observed for CS1 in Fig. 1. In this respect, a recent study using Cu overlayers on Pt has shown that lattice strain has a significant effect on carbon dioxide reactivity and selectivity.[28]

The authors thank Dr M. G. Montes de Oca, J. Stephenson and J. A. Jones for their contributions to this project. We acknowledge EPSRC (EP/H046305/1) and Spanish MINECO (CTQ2011-28913-C02-02) for financial support.

Notes and references

1 M. Aresta and A. Dibenedetto, *Catal. Today*, 2004, **98**, 455–462.
2 Y. Hori, O. Koga, H. Yamazaki and T. Matsuo, *Electrochim. Acta*, 1995, **40**, 2617–2622.
3 I. Takahashi, O. Koga, N. Hoshi and Y. Hori, *J. Electroanal. Chem.*, 2002, **533**, 135–143.
4 Y. Hori, H. Konishi, T. Futamura, A. Murata, O. Koga, H. Sakurai and K. Oguma, *Electrochim. Acta*, 2005, **50**, 5354–5369.
5 K. J. P. Schouten, Y. Kwon, C. J. M. van der Ham, Z. Qin and M. T. M. Koper, *Chem. Sci.*, 2011, **2**, 1902–1909.
6 R. Kortlever, K. H. Tan, Y. Kwon and M. T. M. Koper, *J. Solid State Electrochem.*, 2013, **17**, 1843–1849.
7 K. P. Kuhl, E. R. Cave, D. N. Abram and T. F. Jaramillo, *Energy Environ. Sci.*, 2012, **5**, 7050–7059.
8 C. W. Li and M. W. Kanan, *J. Am. Chem. Soc.*, 2012, **134**, 7231–7234.
9 B. A. Rosen, A. Salehi-Khojin, M. R. Thorson, W. Zhu, D. T. Whipple, P. J. A. Kenis and R. I. Masel, *Science*, 2011, **334**, 643–644.
10 J. A. Keith and E. A. Carter, *Chem. Sci.*, 2013, **4**, 1490–1496.
11 M. Spichiger-Ulmann and J. Augustynski, *J. Chem. Soc., Faraday Trans. 1*, 1985, **81**, 713–716.
12 G. Centi and S. Perathoner, *Top. Catal.*, 2009, **52**, 948–961.
13 S. Perez-Rodriguez, G. Garcia, L. Calvillo, V. Celorrio, E. Pastor and M. J. Lazaro, *Int. J. Electrochem.*, 2011, 249804.
14 N. Hoshi, M. Noma, T. Suzuki and Y. Hori, *J. Electroanal. Chem.*, 1997, **421**, 15–18.
15 S. Taguchi, A. Aramata and M. Enyo, *J. Electroanal. Chem.*, 1994, **372**, 161–169.
16 K. Ohkawa, K. Hashimoto, A. Fujishima, Y. Noguchi and S. Nakayama, *J. Electroanal. Chem.*, 1993, **345**, 445–456.
17 D. Kolbe and W. Vielstich, *Electrochim. Acta*, 1996, **41**, 2457–2460.
18 B. I. Podlovchenko, E. A. Kolyadko and S. G. Lu, *J. Electroanal. Chem.*, 1994, **373**, 185–187.
19 M. Azuma, K. Hashimoto, M. Watanabe and T. Sakata, *J. Electroanal. Chem.*, 1990, **294**, 299–303.
20 A. Bonnefont, A. N. Simonov, S. N. Pronkin, E. Y. Gerasimov, P. A. Pyrjaev, V. N. Parmon and E. R. Savinova, *Catal. Today*, 2013, **202**, 70–78.
21 P. Quaino, E. Santos, H. Wolfschmidt, M. A. Montero and U. Stimming, *Catal. Today*, 2011, **177**, 55–63.
22 M. G. Montes de Oca, H. Kurnarakuru, D. Cherns and D. J. Fermin, *J. Phys. Chem. C*, 2011, **115**, 10489–10496.
23 V. Celorrio, M. G. Montes de Oca, D. Plana, R. Moliner, D. J. Fermin and M. J. Lazaro, *Int. J. Hydrogen Energy*, 2012, **37**, 7152–7160.
24 V. Celorrio, M. G. Montes de Oca, D. Plana, R. Moliner, M. J. Lazaro and D. J. Fermin, *J. Phys. Chem. C*, 2012, **116**, 6275–6282.
25 M. G. Montes de Oca, D. Plana, V. Ceorrio, M. J. Lazaro and D. J. Fermin, *J. Phys. Chem. C*, 2012, **116**, 692–699.
26 J.-W. Hu, Y. Zhang, J.-F. Li, Z. Liu, B. Ren, S.-G. Sun, Z.-Q. Tian and T. Lian, *Chem. Phys. Lett.*, 2005, **408**, 354–359.
27 M. D. Obradović and S. L. Gojković, *Electrochim. Acta*, 2013, **88**, 384–389.
28 R. Reske, M. Duca, M. Oezaslan, K. J. P. Schouten, M. T. M. Koper and P. Strasser, *J. Phys. Chem. Lett.*, 2013, **4**, 2410–2413.

7. ANEXO II (Publicaciones relacionadas con la Tesis)

THE JOURNAL OF
PHYSICAL CHEMISTRY C

Article

pubs.acs.org/JPCC

Methanol Oxidation at Diamond-Supported Pt Nanoparticles: Effect of the Diamond Surface Termination

V. Celorrio,[†,‡] D. Plana,[†] J. Flórez-Montaño,[§] M. G. Montes de Oca,[†] A. Moore,[†] M. J. Lázaro,[‡] E. Pastor,*[,§] and D. J. Fermín*[,†]

[†]School of Chemistry, University of Bristol, Cantocks Close, Bristol BS8 1TS, U.K.

[‡]Instituto de Carboquímica (CSIC), Miguel Luesma Castán 4, 50018 Zaragoza, Spain

[§]Dpto. de Química-Física, Universidad de La Laguna, Avda. Astrofísico Francisco Sánchez s/n, 38071 La Laguna (Tenerife), Spain

Supporting Information

ABSTRACT: The electrocatalytic reactivity of Pt nanoparticles supported on high-pressure, high-temperature diamond particles toward adsorbed CO, methanol, and formic acid oxidation is investigated employing differential electrochemical mass spectrometry (DEMS). Surface treatment of diamond particles, employed as dimensionally stable electrocatalyst supports, leads to materials with surfaces featuring mainly hydrogen (HDP) or oxygen-based functional groups (ODP). Pt nanoparticles with average diameter below 5 nm were generated by impregnation of the modified diamond particles. The voltammetric responses associated with the oxidation of adsorbed CO appeared unaffected by the surface termination of the diamond support. However, significant differences were observed for methanol oxidation in acid solutions, with Pt/HDP producing smaller current densities than Pt/ODP and a commercially available Pt catalyst (Pt/E-TEK). DEMS studies show higher conversion efficiencies to CO_2 for Pt/ODP and Pt/E-TEK, while Pt/HDP exhibited values of approximately 90%. Evidence of formic acid generation as intermediate during methanol oxidation was obtained on all catalysts. Significant differences in the current density associated with the oxidation of formic acid were also observed, with Pt/HDP also providing the lowest current densities. The ensemble of the experimental data suggests that adsorbed $HCOO_{ads}$ species is the key intermediate in methanol oxidation, and its subsequent oxidation to CO_2 is strongly affected by the effective surface termination of the diamond support.

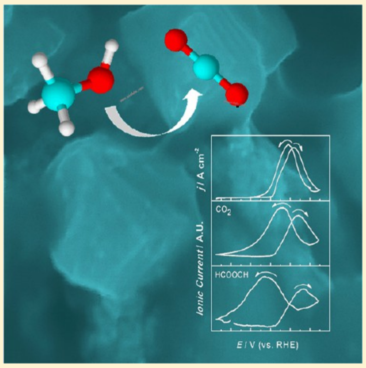

1. INTRODUCTION

The electrocatalytic oxidation of methanol on Pt-based catalysts is one of the most studied reactions in the field of electrochemical energy conversion, yet mechanistic aspects remain controversial.[1−3] This multielectron transfer reaction proceeds via a complex mechanism involving several parallel and consecutive pathways. As illustrated in Scheme 1, methanol oxidation to CO_2 can take place via the generation of adsorbed CO as well as reactive intermediates such as HCHO and HCOOH.[4−7] The reaction pathway can be affected not only by the structure and size of the Pt nanostructure but also by the nature of the catalyst support, typically mesoporous sp$_2$-hybridized carbon.[8−11]

The impregnation of metal precursors into carbon suspensions, followed by chemical reduction, is a widely used approach for generating nanoscale supported electrocatalysts. The properties of the carbon support can strongly influence key aspects of the metal nanocatalysts, such as mean size, morphology, size distribution, stability, dispersion, and reactivity.[12,13] For instance, oxygenated functional groups have been shown to improve the wettability of carbon materials, enhancing both the interaction of the carbon with the metal precursor complexes and the anchoring of the metallic nanostructures.[14,15] Oxygenated groups can be introduced at the surface of mesoporous carbon by a variety of gas and liquid phase pretreatments.[16−19] However, while introducing oxygen surface groups, other properties such as pore structure or specific surface area are inevitably affected. Consequently, the establishment of relationships between carbon surface termination and the reactivity of the supported catalysts is an extremely challenging issue. In a recent work, the effect of various carbon pretreatments on the electrocatalytic activity of Pd nanostructures exhibited contrasting trends in the case of conventional impregnation versus incorporation of already prepared colloidal nanoparticles.[20]

An interesting alternative for electrocatalyst support involves diamond powders, which are characterized by a high chemical and mechanical stability, as well as a rich surface chemistry.[21] Depending on the preparation method, the surface of diamond powders can be H-terminated and/or feature a range of functional groups;[22−26] Moore et al. demonstrated that Pd nanostructures generated by impregnation on commercially available high-pressure, high-temperature diamond particles can be used as high surface area electrocatalysts for formic acid

Received: April 22, 2013
Revised: August 15, 2013
Published: September 24, 2013

dx.doi.org/10.1021/jp4039804 | J. Phys. Chem. C 2013, 117, 21735−21742

Scheme 1. Proposed Mechanisms for Methanol Electrooxidation at Pt Surfaces

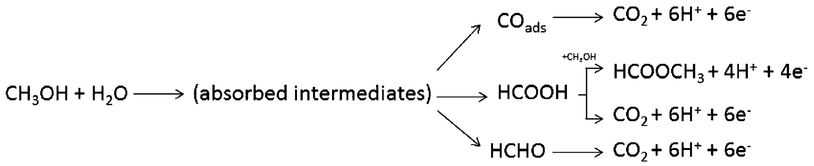

oxidation.[27] This approach is inspired by seminal studies on boron-doped diamond (BDD) films, demonstrating their suitability as dimensionally stable support for electrodeposited metal nanostructures.[28−30] Cabrera and co-workers investigated the performance of detonated diamond nanoparticles and boron-doped diamond powders, obtained by ion implantation, as supports for Pt and PtRu catalysts in direct methanol fuel cells.[31−33] One of the key challenges in the implementation of non-boron-doped diamond powders as electrocatalyst supports is their high bulk resistivity. However, charge transport in metal−diamond composites can be manipulated by the generation of percolation pathways,[34] "transfer-doping" mechanism in aqueous solution,[34−36] and via surface states and functional redox groups.[37−39]

In the present work, the reactivity of Pt nanostructures supported on high-pressure, high-temperature diamond powders is evaluated for the first time as a function of the effective surface diamond termination. Pt nanostructures were reduced at the surface of hydrogen (HDP) and oxygen-terminated diamond powders (OPD) through impregnation methods. The electrocatalytic activity of these composites toward the oxidation of CO, methanol, and formic acid was evaluated in acid solution employing differential electrochemical mass spectrometry (DEMS). Although the mean Pt particle size in Pt/HDP is slightly smaller than in Pt/ODP, the potential for oxidation of adsorbed CO is rather similar in both cases. Interestingly, the oxidation of CO_{ads} on the diamond supported Pt nanoparticles was characterized by a broad voltammetric peak centered at potentials 100 mV more negative than on a commercially available Pt electrocatalyst (Pt/E-Tek); the latter is used as a benchmark in this work. On the other hand, electrochemical data showed a significant difference in the reactivity of Pt/HDP and Pt/ODP with respect to methanol oxidation. DEMS measurements provided evidence that formic acid is generated during the oxidation of methanol. We finally concluded that the contrast in the reactivity of Pt/HDP and Pt/ODP mainly arises from differences in the oxidation kinetics of $HCOO_{ads}$ species generated as intermediate during methanol oxidation.

2. EXPERIMENTAL SECTION

2.1. Diamond Surface Termination. High-pressure, high-temperature diamond particles (type Ib), with a nominal size of 500 nm, were purchased from Microdiamant AG, Switzerland (MYS005). The as-received particles were initially washed by sonication in ultrapure water; O- and H-terminations were then generated following a previously described procedure.[36] Briefly, oxygenated surface groups are generated by heating the particles in a concentrated 9:1 v/v H_2SO_4:HNO_3 solution; the particles are then successively washed with Milli-Q water and centrifuged until the supernatant is pH neutral. Hydrogenation of the oxygen-terminated particles is achieved by an 800 W microwave plasma reactor, at a pressure of 50 Torr, with a hydrogen flow rate of 500 sccm. Particles were allowed to cool down in the presence of hydrogen to approximately 250 °C, and under Ar to room temperature, before exposure to air. Changes of the surface termination of these diamond powders following these pretreatments have been monitored by FTIR.[36] The specific surface area of the diamond particles, as estimated from BET analysis, is 10.7 $m^2\ g^{-1}$ (results not shown). Although higher specific surface areas could be obtained from smaller diamond particles, such as those obtained by detonation, these materials offer key advantages such as high crystallinity, low density of aggregates, and low content of sp^2 impurities.

2.2. Electrocatalyst Preparation. Electrocatalysts were prepared by the solution-reduction method, using sodium borohydride as reducing agent. 35 mL of 1.13 mM H_2PtCl_6 (Sigma-Aldrich) were added to 80 mL of an aqueous suspension of the diamond powder. The suspension was kept under strong stirring for 24 h, before the slow addition of 20 mL of 26.4 mM sodium borohydride, at room temperature.[8]

2.3. Differential Electrochemical Mass Spectrometer Experiments (DEMS). These experiments were carried out in the differential electrochemical mass spectrometer setup described by Pérez-Rodriguez.[40] Briefly, the configuration used to perform DEMS experiments consisted in an electrochemical cell coupled to a Pfeiffer-Vacuum mass spectrometer, which contains a Prism QMS 200 detector, allowing acquisition up to 72 simultaneous mass/charge (m/z) signals.

A 50 cm^3 capacity plexiglass cell was used, with a hydrophobic Teflon membrane (Scimat Ltd., 200/40/60) at the bottom, which worked as an interface between the electrochemical cell and the mass spectrometer, being permeable to gaseous and/or volatiles products generated during the electrochemical reaction. The working electrode was placed between the Teflon membrane and a glassy carbon rod, which served as electrical contact.

Gas diffusion electrodes were used as working electrodes (7 mm diameter) prepared as reported elsewhere.[41] A carbon cloth was painted using the so-called gas diffusion ink, composed by Vulcan XC-72R, ultrapure water (Millipore Milli-Q system), isopropanol (Merck, p.a.), and a PTFE dispersion (60 wt %, Dyneon), resulting in a 20 wt % PTFE mixture. This ink was painted onto one side of a carbon cloth, followed by heating at 320 °C for 1 h. Electrodes were made by depositing a suspension of Nafion solution (5 wt %, Sigma-Aldrich) and the synthesized electrocatalyst on pieces of the pretreated carbon cloth. The final amount of metal active phase in all the prepared electrodes was approximately 0.4 $mg_{Pt}\ cm^{-2}$.

2.4. Characterization of the Nanostructures and Electrochemical Studies. The structure and composition of the catalysts were investigated employing a suite of scanning electron microscopes: JEOL SEM 5600 LV, JEOL FEG-SEM 6330, and Hitachi S-3400 N fitted with an energy dispersive X-ray analyzer (EDX) Röntec XFlash Si(Li). X-ray diffraction (XRD) patterns were recorded using a Bruker AXS D8 Advance diffractometer with a θ−θ configuration and using Cu Kα radiation (λ = 0.154 nm). Scans were done for 2θ values between 0° and 100°. Scherrer's equation and Vegard's law

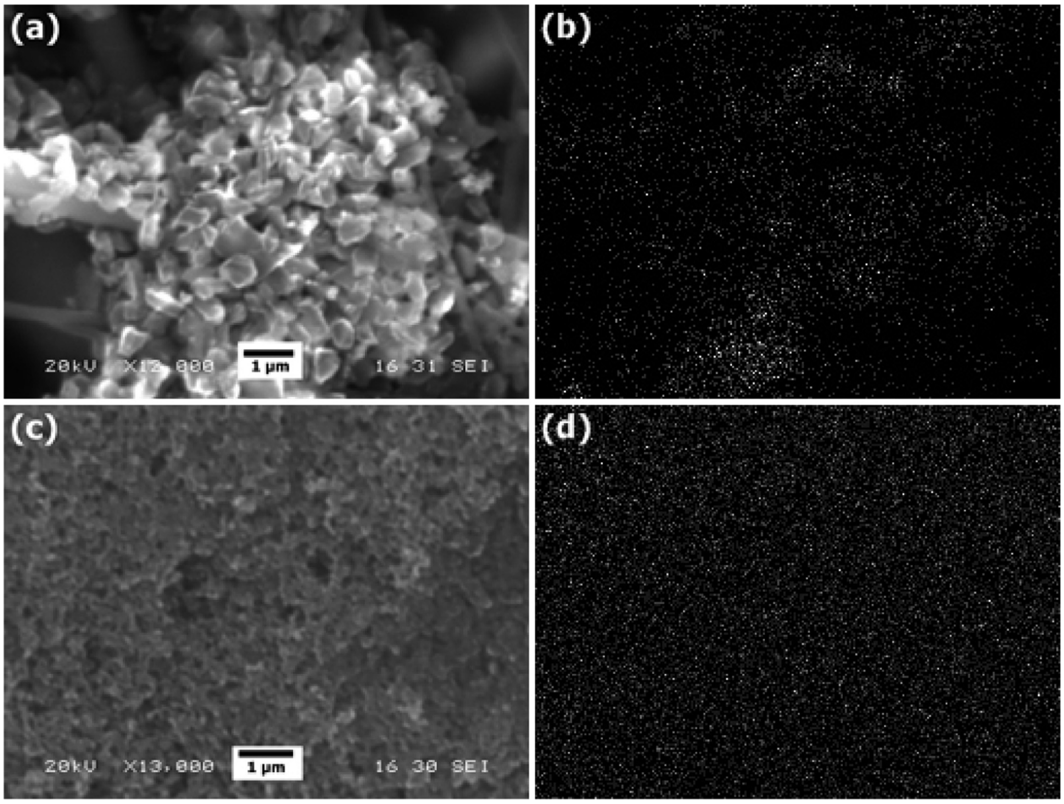

Figure 1. SEM images of Pt/ODP (a) and Pt/E-Tek (c) electrocatalysts. Corresponding Pt elemental mapping is shown as white spots for Pt/ODP and Pt/E-Tek (b and d, respectively). The scale bar in all images corresponds to 1 μm.

were applied to the (220) peak of the Pt fcc structure, around $2\theta = 70°$, in order to estimate the Pt crystallite size and lattice parameters, respectively.

The electrooxidation of adsorbed CO and methanol was investigated in the setup described in section 2.3, using a two-compartment electrochemical cell featuring a carbon rod and a reversible hydrogen electrode (RHE) as counter and reference electrodes. Argon (N50) was used to deoxygenate all solutions, and CO (N47) was employed for the adsorption experiments. Solutions were prepared using sulfuric acid (0.5 M H_2SO_4) as base electrolyte, to which methanol (Merck, p.a.) was added. Electrochemical measurements were performed with an Autolab PGSTAT302 (Ecochemie).

The formic acid oxidation was also investigated in a two-compartment cell fitted with a Pt wire and an Ag/AgCl electrode, as counter and reference electrodes, respectively. For consistency, all potentials in this work are quoted versus the RHE electrode. Working electrodes were prepared depositing a thin layer of the electrocatalyst ink over a glassy carbon disk (0.20 cm^2). Catalyst inks were prepared by mixing 2 mg of each catalyst and 15 μL of Nafion dispersion (10 wt %, Aldrich) in 500 μL of ultrapure water (Millipore Milli-Q system). A 20 μL aliquot of the suspension was deposited onto the glassy carbon electrode and dried.

3. RESULTS AND DISCUSSION

3.1. Structural Characterization of the Electrocatalysts. SEM micrographs of the Pt catalysts supported on diamond powders and of the Pt/E-Tek are contrasted in Figure 1. The faceted topography of the highly crystalline high-pressure, high-temperature diamond powders is clearly seen in Figure 1a. This image, taken on a Pt/ODP sample, is representative of all of the catalysts prepared, independently of the diamond surface termination. On the other hand, the SEM image of the Pt/E-Tek catalyst in Figure 1c is characterized by aggregates of spherical carbon particles. In both cases, the topographic features are entirely dominated by the structure of the carbon grains as the Pt nanostructures are 2 orders of magnitude smaller.

The distribution of the Pt nanostructures can be visualized by elemental mapping, as exemplified in Figures 1b,d. Whereas it is clear that the metal is homogeneously dispersed in the case of the commercial catalyst, some aggregates can be observed when ODP is used as support material. A similar distribution was observed for Pt particles supported on HDP. Considering that the porosity of the diamond powders is very low in comparison with carbon black, it is expected that the distribution of the Pt nanostructures will be more homogeneous in the latter case.

XRD patterns obtained for the various supported Pt nanostructures are displayed in Figure 2. The peaks at $2\theta =$ 40°, 47°, 67°, 81°, and 85° are associated with diffraction at the (111), (200), (220), (311), and (222) planes of fcc Pt, respectively. The XRD pattern of Pt/E-Tek also displays a peak at $2\theta = 26.2°$, characteristic of the (002) plane of graphite. On the other hand, Pt/HDP and Pt/ODP feature peaks at $2\theta =$ 43.3°, 74.7°, and 91°, characteristic of the highly crystalline diamond particles (labeled with an asterisk).[27]

Table 1 summarizes the loading and effective particle diameter (d) of the Pt nanostructures on the various supports as estimated from EDX and XRD data. Pt/HDP and Pt/E-Tek show similar d values, while the Pt particles appear somewhat larger on Pt/ODP. The overall metal loading also appears lower in the case of Pt/ODP, with respect to Pt/HDP. The difference between these two parameters in Pt/HDP and Pt/ODP is

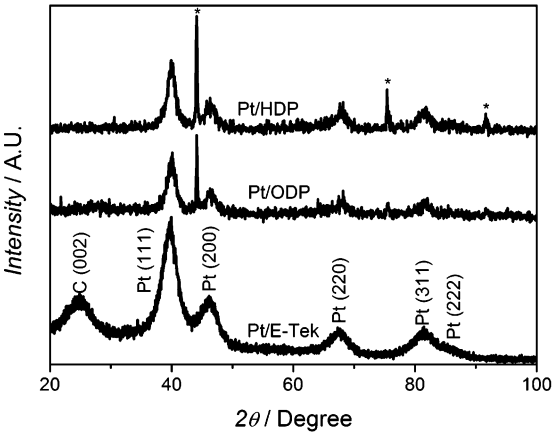

Figure 2. Powder XRD patterns of Pt/HDP, Pt/ODP, and Pt/E-Tek. Sharp peaks labeled with an asterisk (∗) are associated with the diamond particles.

Table 1. Pt Loading and Effective Particle Diameter (*d*) for the Various Catalysts

electrocatalyst	% Pt	*d*/nm
Pt/HDP	14.2 ± 1.9	3.4
Pt/ODP	10.3 ± 2.2	4.8
Pt/E-Tek	16.3 ± 1.5	3.0

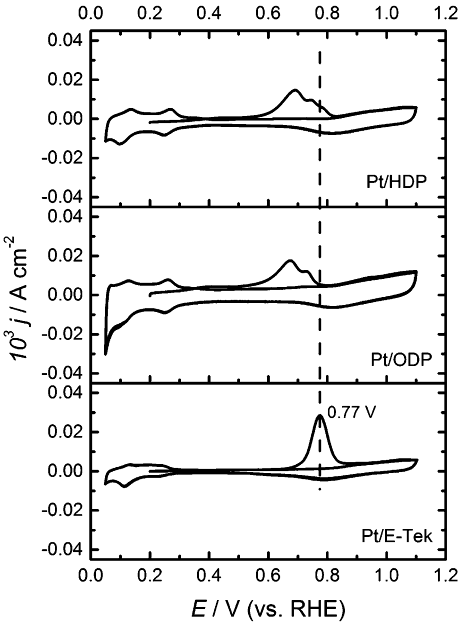

Figure 3. CO_{ads} electrooxidation voltammograms of the different supported Pt electrocatalysts in 0.5 M H_2SO_4 at 5 mV s^{-1}. The adsorption of CO was carried out at 0.20 V and 25 °C.

directly linked with the diamond surface termination. For instance, an increase in *d* has been reported with increasing density of surface oxygen groups in carbon black supports.[42,43] However, a unique aspect of employing diamond powder supports is that its dimensions and bulk structure are not compromised by chemical modification of the surfaces. Analysis of the XRD data allowed estimating an average lattice constant of the metal nanostructures of 3.92 Å for all samples, which is consistent with bulk Pt.

The structure and metal loading of the composites have significant effect on the electrical conductivity of the system. As described in a recent report,[34] percolation through the metal centers and "transfer doping" phenomena observed at hydrogenated surfaces are the key parameters determining charge transport in these composites. Metal volume fractions, as estimated from the data in Table 1, are just below the threshold expected for charge percolation controlled conductivity. Under these conditions, a certain proportion of metal nanoparticles appear as electrically isolated. However, as described further below, reactivity studies are normalized by the electroactive surface at each electrode. Consequently, trends in the effective reactivity of the Pt−diamond composites are less affected by the transport properties of the composite.

3.2. Oxidation of Adsorbed CO. Cyclic voltammograms associated with the oxidation of adsorbed CO in 0.5 M H_2SO_4, at 5 mV s^{-1}, on all three catalysts are contrasted in Figure 3. CO was preadsorbed at the electrode surface at a potential of 0.2 V for 10 min, and argon was used for at least 20 min to remove CO from the electrolyte before recording the voltammograms. The first cycle is characterized by the CO_{ads} oxidation peak, which is absent in the second cycle. The appearance of the hydrogen adsorption/desorption peak at potentials lower than 0.3 V in the reverse scan and second cycle further confirm the complete oxidation of CO_{ads}. It is also observed that the voltammetric responses associated with Pt−O remain unchanged in the first and second cycle, indicating that no Pt dissolution occurs in this potential range. This set of data was employed for estimating the effective electroactive area of the Pt catalysts assuming that the charge density of CO_{ads} under these conditions corresponds to 420 μC cm^{-2}.[44] The current responses throughout this paper were normalized to the effective surface area based on this calculation.

The commercial Pt/E-Tek catalyst features a relatively narrow CO_{ads} oxidation peak centered at 0.77 V, in contrast with the more complex responses observed for Pt/HDP and Pt/ODP. Both diamond supported Pt particles exhibited a current peak at 0.73 V, with an additional shoulder at around 0.75 V. There is no clear consensus on the origin of multiple oxidation peaks at nanostructured Pt electrodes. At well-defined single crystal surfaces, oxidation peak potentials have been associated with coverage-dependent adsorption energies[45] and variation in local ordering of the adlayer at different crystallographic planes.[33,46] The shift of the CO_{ads} oxidation peak toward more negative values for the diamond supported nanoparticles with respect to Pt/E-Tek can be rationalized in terms of particle size. Several reports have suggested that the overpotential for the formation of oxygenated species at Pt nanostructures increases with decreasing particle size, which manifest itself by a shift of the CO_{ads} oxidation potential toward more positive values.[47−50] An additional aspect affecting the CO_{ads} oxidation potential is the presence of particle aggregates;[49−51] enhanced catalytic activity of Pt agglomerates has been associated with grain boundaries interconnecting nanoparticles into complex extended structures. Indeed, the 100 mV shift observed in this work is in good agreement with studies reported by Savinova and co-workers on Pt nanostructures deposited at glassy carbon electrodes.[51]

3.3. Methanol Oxidation. Cyclic voltammograms associated with oxidation of methanol at the three electrocatalysts, and the corresponding DEMS signals for *m*/*z* = 44 and 60, are contrasted in Figure 4. The experiments were carried out in electrolyte solutions containing 0.5 M methanol and 0.5 M H_2SO_4, at a scan rate of 1 mV s^{-1}. The choice of *m*/*z* values

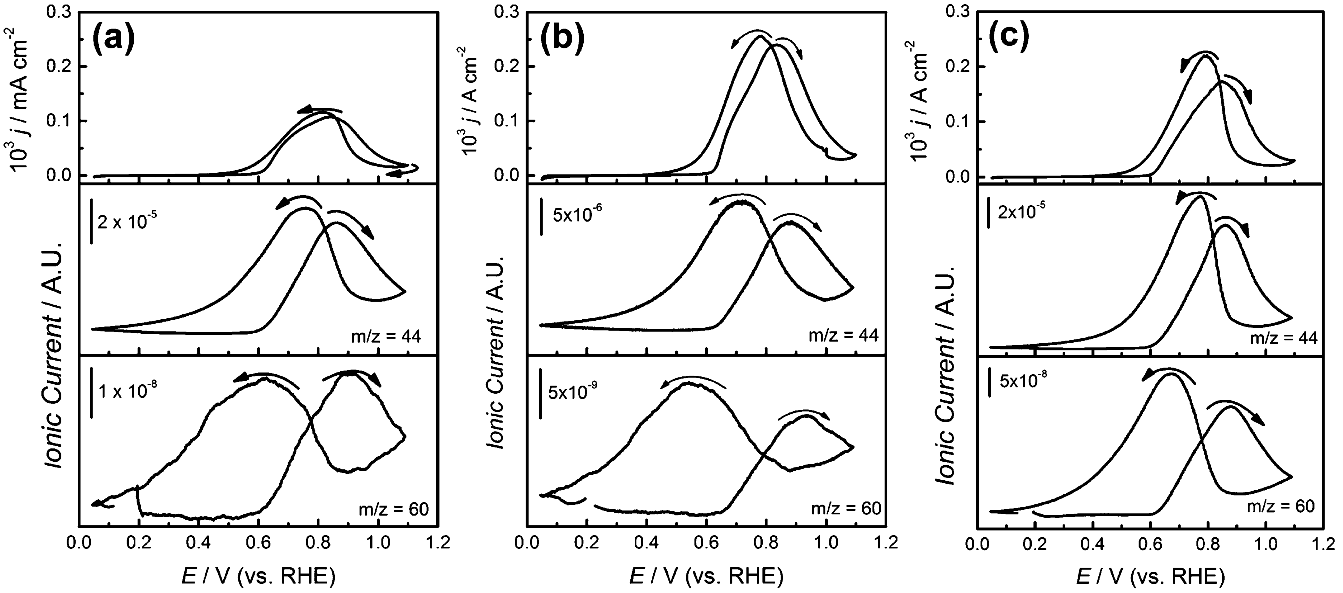

Figure 4. Cyclic voltammograms (upper panels) and DEMS signals for m/z = 44 (middle panels) and 60 (lower panels) for the oxidation of methanol (0.5 M) in 0.5 M H_2SO_4 at Pt/HDP (a), Pt/ODP (b), and Pt/C E-Tek (c) at 1 mV s^{-1}.

investigated is based on the volatile compounds indicated in Scheme 1. The most effective way to monitor the generation of formic acid under the present experimental conditions is by probing m/z = 60, corresponding to methyl formate, the product generated from the homogeneous reaction of formic acid and methanol. On the other hand, formaldehyde formation is significantly more challenging due to the mass overlap with methanol and the fact that these compounds do not react at low temperatures. The m/z = 44 signal is used to monitor the formation of CO_2.

The m/z = 44 ion current (middle panels) generally overlaps with the faradaic current (upper panels) in the potential scale, taking into account the time constant of the DEMS cell. In the case of m/z = 60 (lower panels in Figure 4), there is a degree of overlap between the faradaic and mass ion currents. However, the hysteresis in the forward and reverse potential scans is significantly larger for m/z = 60 in comparison to m/z = 44. This deviation can be explained by the relatively slow ester formation (reaction between formic acid and methanol) compared to the instantaneous CO_2 formation.[52]

The results shown in Figure 5 allow a comparison between the measured faradaic current, associated with methanol oxidation, and the theoretical value estimated from the ionic current associated with CO_2 generation (m/z = 44). To perform this calculation, the CO_2 mass calibration constant (k) was estimated from DEMS measurements of CO_{ads} oxidation.[53] The difference between the measured (solid line) and estimated current (dashed line) in Figure 5 can be rationalized in terms of the formation of byproducts during methanol oxidation. Figure 5 also shows the average faradaic efficiency calculated from the ratio of experimental and estimated charges. The data show high CO_2 conversion efficiencies for Pt/ODP and Pt/E-Tek; interestingly, Pt/HDP exhibits a lower CO_2 conversion efficiency (just below 90%). This can be associated with a higher formation of byproducts (e.g., formic acid and formaldehyde), which are not further oxidized in the time scale of the cyclic voltammogram.

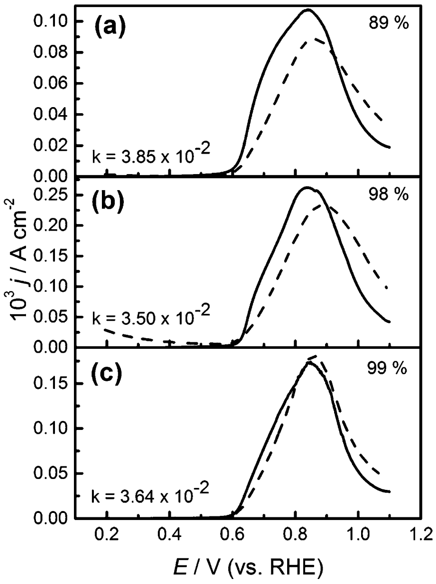

Figure 5. Experimental (—) and estimated (- - -) faradaic current obtained from m/z = 44 ionic currents at Pt/HDP (a), Pt/ODP (b), and Pt/E-Tek (c). Experimental conditions as in Figure 4. The CO_2 mass calibration constant (k) used for estimation of the faradaic current from the CO_2 mass intensity is also indicated for each of the catalysts (see text).

As shown in the Supporting Information, chronoamperometric measurements recorded under similar conditions, at 0.60 V for 800 s, also show the same qualitative trend as the previous potentiodynamic experiments, i.e., lower faradaic current density for Pt/HDP in comparison to Pt/ODP and Pt/E-Tek electrodes. Considering the systematic analysis of the experimental data, in particular the normalization of the current densities, this experimental trend cannot be simply rationalized in terms of effective surface area of the Pt catalyst. Consequently, the lower faradaic current density observed for Pt/HDP, with respect to the other catalysts, represents a so-called substrate effect associated with the hydrogenated diamond surface. Considering that the reactivity of CO_{ads} is rather similar at Pt/HDP and Pt/ODP (Figure 3), it could be argued that the hydrogen termination does not affect this reaction pathway. On the other hand, the generation of dimethyl formate as detected by DEMS data (Figure 4) suggests that formic acid is generated as an intermediate species in methanol oxidation on all of the catalysts studied. In the final part of this work, we investigate whether a contrast in reactivity for the oxidation of formic acid in solution is observed for this family of electrocatalysts.

3.4. Formic Acid Oxidation. Linear sweep voltammetric data for all three catalysts, at 0.02 V s^{-1} in an electrolyte solution containing 2 M formic acid and 0.5 M H_2SO_4, are shown in Figure 6. The onset for formic acid oxidation occurs at ca. 0.20 V, reaching a plateau between 0.55 and 0.80 V. At potentials more positive than 0.80 V, the current significantly increases with a peak emerging at 0.95 V. In the potential range below 0.80 V, Pt/HDP and Pt/ODP exhibit lower current densities than Pt/E-Tek. At potential above 0.80 V, Pt/HDP shows significantly lower current densities than both Pt/E-Tek and Pt/ODP.

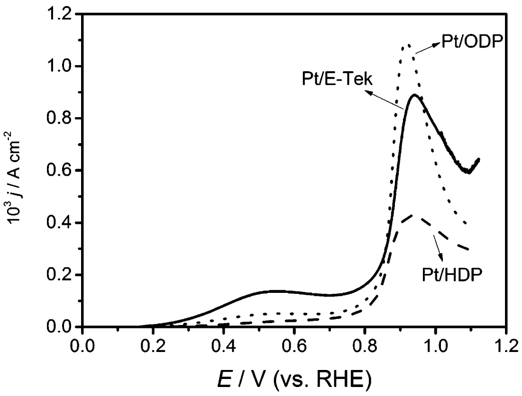

Figure 6. Linear sweep voltammetry of Pt/HDP, Pt/ODP, and Pt/E-Tek in an electrolyte solution containing 2 M formic acid and 0.5 M H_2SO_4 at 0.02 V s^{-1}.

It has been proposed that the voltammetric responses centered at 0.55 V correspond to the dehydrogenation of formic acid, generating CO_{ads}, while the signal at 0.95 V is attributed to the oxidative removal of CO_{ads}, along with further formic acid oxidation on "free sites".[54−57] On the other hand, recent studies by Cuesta and co-workers have concluded that the first step is the formation adsorbed formate, which leads to the formation of either CO_{ads} or CO_2, as illustrated in Scheme 2.[58−60] We have already concluded that there is little reactivity contrast between Pt/HDP and Pt/ODP toward the oxidation of CO_{ads} (see Figure 3); consequently, the apparent lower reactivity of HDP supported nanoparticles is most likely linked to the oxidation rate of $HCOO_{ads}$. Furthermore, the fact that a significant difference is observed between Pt/ODP and Pt/E-Tek toward the oxidation of CO_{ads}, but rather little toward methanol and formic acid, further supports the conclusion that CO_{ads} oxidation is not the limiting process in the oxidation of these fuels.

Scheme 2. Elementary Steps Associated with the Oxidation of Formic Acid As Suggested by Cuesta and Co-workers[60]

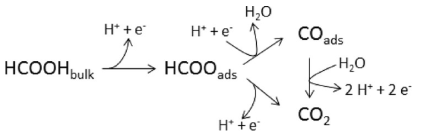

The picture emerging from these studies strongly suggests that the contrast in reactivity of Pt nanostructures supported on hydrogenated and oxygenated diamond powder toward the oxidation of formic acid and methanol is related to the oxidation rate of the $HCOO_{ads}$ species. Variations in parameters such as Pt particle size and loading, CO_{ads} oxidation potential, and current density as well as the microscopic dimensions of the diamond supports do not account for the difference observed in these studies. The key aspect which remains to be fully addressed is the link between the surface termination of the diamond support and the oxidation rate of $HCOO_{ads}$. It is well established that the hydrogenation of diamond leads to large changes in the surface dipole of up to 2.7 eV.[61,62] Hongthani et al. have recently shown that hydrogenation of identical diamond powders shifts the valence band edge energy to values close to −0.32 eV with respect to RHE.[36] We believe these electronic effects can substantially influence parameters such as the electron density at the d-band of the metal nanoparticles as well as the structure of water molecules around the metal centers. Both issues, which we are currently investigating, can strongly affect the binding of $HCOO_{ads}$ and the reactivity of the supported Pt nanostructures.

4. CONCLUSIONS

The electrochemical reactivity of Pt nanostructures supported on high-pressure, high-temperature diamond powders toward the oxidation of CO_{ads}, formic acid, and methanol was investigated employing DEMS. The effective surface termination of the diamond powders was investigated as the key reactivity descriptor. Pt supported on hydrogen-terminated diamond powders (Pt/HDP) exhibited similar voltammetric responses for the oxidation of CO_{ads} in comparison to Pt nanostructures at oxygen-terminated powders (Pt/ODP). Both set of catalysts featured an oxidation potential for CO_{ads} over 100 mV more negative than the commercial Pt/E-Tek catalysts used as benchmark. Interestingly, a significant contrast was observed in the current density for the oxidation of methanol and formic acid on Pt/HDP and Pt/ODP. The latter showed similar behavior to Pt/E-Tek, featuring significantly high conversion efficiencies of methanol to CO_2. Pt/HDP showed methanol-to-CO_2 conversion efficiencies of 90% with smaller current densities for both methanol and formic acid. All catalysts showed evidence of formic acid formation as intermediate in methanol oxidation. The experimental evidence points toward $HCOO_{ads}$ as the key intermediate limiting the oxidation of both formic acid and methanol.

These reactivity trends, reported for the first time, are linked to the large changes in surface dipole at diamond surfaces, introducing large shifts in the relative position of the electronic bands. We expect that relatively minor effects would be observed on conducting boron-doped diamond surfaces, as the electronic interactions with the metal nanoparticles will be dominated by the continuum density of states associated with the dopant level. We are currently extending our investigations into the electronic structure of the electrocatalysts as a function of the diamond surface termination as well as alternative formulations which could allow implementing these materials as catalysts in energy conversion systems.

ASSOCIATED CONTENT

Supporting Information

Choroamperometric transients recorded during the oxidation of methanol at the various catalysts. This material is available free of charge via the Internet at http://pubs.acs.org.

AUTHOR INFORMATION

Corresponding Authors

*Tel +44 117 9288981; e-mail David.Fermin@bristol.ac.uk (D.J.F.).
*Tel +34 922 318028; Fax +34 922 318033; e-mail epastor@ull.es (E.P.).

Notes

The authors declare no competing financial interest.

ACKNOWLEDGMENTS

D.P. and D.J.F. are grateful for the financial support from the UK Engineering and Physical Science Research Council (Project EP/H046305/1) and the University of Bristol. V.C., M.J.L., E.P., and J.F.M. gratefully acknowledge financial support given by the Ministry of Economy and Competitiveness through the Projects CTQ2011-28913-C02-01 and -02. V.C. acknowledges the financial support by CSIC/ESF for her JAE Grant, while M.G.M. and J.F.M. are also grateful to the support by the Mexican National Council for Science and Technology (CONACyT) and ACIISI (Gobierno de Canarias), respectively.

REFERENCES

(1) Jusys, Z.; Behm, R. J. Methanol, Formaldehyde, and Formic Acid Adsorption/Oxidation on a Carbon-Supported Pt Nanoparticle Fuel Cell Catalyst: A Comparative Quantitative DEMS Study. In *Fuel Cell Catalysis*; John Wiley & Sons, Inc.: New York, 2008; pp 411−464.

(2) Wang, H.; Abruña, H. *Electrocatalysis of Direct Alcohol Fuel Cells: Quantitative DEMS Studies Fuel Cells and Hydrogen Storage*; Bocarsly, A.; Mingos, D. M. P., Eds.; Springer: Berlin, 2011; Vol. *141*, pp 33−83.

(3) Planes, G. A.; García, G.; Pastor, E. High Performance Mesoporous Pt Electrode for Methanol Electrooxidation. A DEMS Study. *Electrochem. Commun.* **2007**, *9*, 839−844.

(4) Wang, H.; Löffler, T.; Baltruschat, H. Formation of Intermediates during Methanol Oxidation: A Quantitative DEMS Study. *J. Appl. Electrochem.* **2001**, *31*, 759−765.

(5) Rabis, A.; Rodriguez, P.; Schmidt, T. J. Electrocatalysis for Polymer Electrolyte Fuel Cells: Recent Achievements and Future Challenges. *ACS Catal.* **2012**, *2*, 864−890.

(6) Wang, H.; Baltruschat, H. DEMS Study on Methanol Oxidation at Poly- and Monocrystalline Platinum Electrodes: The Effect of Anion, Temperature, Surface Structure, Ru Adatom, and Potential. *J. Phys. Chem. C* **2007**, *111*, 7038−7048.

(7) Jusys, Z.; Behm, R. J. Methanol Oxidation on a Carbon-Supported Pt Fuel Cell CatalystA Kinetic and Mechanistic Study by Differential Electrochemical Mass Spectrometry. *J. Phys. Chem. B* **2001**, *105*, 10874−10883.

(8) Lázaro, M. J.; Celorrio, V.; Calvillo, L.; Pastor, E.; Moliner, R. Influence of the Synthesis Method on the Properties of Pt Catalysts Supported on Carbon Nanocoils for Ethanol Oxidation. *J. Power Sources* **2011**, *196*, 4236−4241.

(9) Calvillo, L.; Celorrio, V.; Moliner, R.; Lázaro, M. J. Influence of the Support on the Physicochemical Properties of Pt Electrocatalysts: Comparison of Catalysts Supported on Different Carbon Materials. *Mater. Chem. Phys.* **2011**, *127*, 335−341.

(10) Aksoylu, A. E.; Madalena, M.; Freitas, A.; Pereira, M. F. R.; Figueiredo, J. L. The Effects of Different Activated Carbon Supports and Support Modifications on the Properties of Pt/C Catalysts. *Carbon* **2001**, *39*, 175−185.

(11) Sharma, S.; Pollet, B. G. Support Materials for PEMFC and DMFC Electrocatalysts—A Review. *J. Power Sources* **2012**, *208*, 96−119.

(12) Kim, M.; Park, J.-N.; Kim, H.; Song, S.; Lee, W.-H. The Preparation of Pt/C Catalysts Using Various Carbon Materials for the Cathode of PEMFC. *J. Power Sources* **2006**, *163*, 93−97.

(13) Yu, X.; Ye, S. Recent Advances in Activity and Durability Enhancement of Pt/C Catalytic Cathode in PEMFC: Part I. Physico-Chemical and Electronic Interaction Between Pt and Carbon Support, and Activity Enhancement of Pt/C Catalyst. *J. Power Sources* **2007**, *172*, 133−144.

(14) Calvillo, L.; Lázaro, M. J.; García-Bordejé, E.; Moliner, R.; Cabot, P. L.; Esparbé, I.; Pastor, E.; Quintana, J. J. Platinum Supported on Functionalized Ordered Mesoporous Carbon as Electrocatalyst for Direct Methanol Fuel Cells. *J. Power Sources* **2007**, *169*, 59−64.

(15) Calvillo, L.; zaro, M. J.; Suelves, I.; Echegoyen, Y.; Bordej, G. E.; Moliner, R. Study of the Surface Chemistry of Modified Carbon Nanofibers by Oxidation Treatments in Liquid Phase. *J. Nanosci. Nanotechnol.* **2009**, *9*, 4164−4169.

(16) Moreno-Castilla, C.; Ferro-Garcia, M. A.; Joly, J. P.; Bautista-Toledo, I.; Carrasco-Marin, F.; Rivera-Utrilla, J. Activated Carbon Surface Modifications by Nitric Acid, Hydrogen Peroxide, and Ammonium Peroxydisulfate Treatments. *Langmuir* **1995**, *11*, 4386−4392.

(17) Figueiredo, J. L.; Pereira, M. F. R. The Role of Surface Chemistry in Catalysis with Carbons. *Catal. Today* **2010**, *150*, 2−7.

(18) Noh, J. S.; Schwarz, J. A. Effect of HNO_3 Treatment on the Surface Acidity of Activated Carbons. *Carbon* **1990**, *28*, 675−682.

(19) Darmstadt, H.; Roy, C.; Kaliaguine, S.; Choi, S. J.; Ryoo, R. Surface Chemistry of Ordered Mesoporous Carbons. *Carbon* **2002**, *40*, 2673−2683.

(20) Celorrio, V.; Montes de Oca, M. G.; Plana, D.; Moliner, R.; Fermín, D. J.; Lázaro, M. J. Electrochemical Performance of Pd and Au−Pd Core−Shell Nanoparticles on Surface Tailored Carbon Black as Catalyst Support. *Int. J. Hydrogen Energy* **2012**, *37*, 7152−7160.

(21) Materlik, G. Diamond will Shine Brightly for Chemistry. *Chem. Commun.* **2003**, *0*, 1021−1023.

(22) Krueger, A. Diamond Nanoparticles: Jewels for Chemistry and Physics. *Adv. Mater.* **2008**, *20*, 2445−2449.

(23) Huang, H.; Dai, L.; Wang, D. H.; Tan, L.-S.; Osawa, E. Large-Scale Self-Assembly of Dispersed Nanodiamonds. *J. Mater. Chem.* **2008**, *18*, 1347−1352.

(24) Chakrapani, V.; Angus, J. C.; Anderson, A. B.; Wolter, S. D.; Stoner, B. R.; Sumanasekera, G. U. Charge Transfer Equilibria Between Diamond and an Aqueous Oxygen Electrochemical Redox Couple. *Science* **2007**, *318*, 1424−1430.

(25) Liu, Y.; Gu, Z.; Margrave, J. L.; Khabashesku, V. N. Functionalization of Nanoscale Diamond Powder: Fluoro-, Alkyl-, Amino-, and Amino Acid-Nanodiamond Derivatives. *Chem. Mater.* **2004**, *16*, 3924−3930.

(26) Krueger, A.; Lang, D. Functionality is Key: Recent Progress in the Surface Modification of Nanodiamond. *Adv. Funct. Mater.* **2012**, *22*, 890−906.

(27) Moore, A.; Celorrio, V.; de Oca, M. M.; Plana, D.; Hongthani, W.; Lazaro, M. J.; Fermin, D. J. Insulating diamond particles as substrate for Pd electrocatalysts. *Chem. Commun.* **2011**, *47*, 7656−7658.

(28) Wang, J.; Swain, G. M. Fabrication and Evaluation of Platinum/Diamond Composite Electrodes for Electrocatalysis. *J. Electrochem. Soc.* **2003**, *150*, E24−E32.

(29) Spătaru, N.; Zhang, X.; Spătaru, T. a.; Tryk, D. A.; Fujishima, A. Platinum Electrodeposition on Conductive Diamond Powder and Its Application to Methanol Oxidation in Acidic Media. *J. Electrochem. Soc.* **2008**, *155*, B264.

(30) Spătaru, T.; Anastasescu, M.; Spătaru, N.; Fujishima, A. Influence of Cobalt Oxide Substrate on the Resistance to Fouling during Methanol Oxidation of Platinum Particles. *Electrochem. Commun.* **2013**, *29*, 1−3.

(31) La-Torre-Riveros, L.; Abel-Tatis, E.; Méndez-Torres, A.; Tryk, D.; Prelas, M.; Cabrera, C. Synthesis of Platinum and Platinum–Ruthenium-Modified Diamond Nanoparticles. *J. Nanopart. Res.* **2011**, *13*, 2997–3009.

(32) La-Torre-Riveros, L.; Guzman-Blas, R.; Méndez-Torres, A. E.; Prelas, M.; Tryk, D. A.; Cabrera, C. R. Diamond Nanoparticles as a Support for Pt and PtRu Catalysts for Direct Methanol Fuel Cells. *ACS Appl. Mater. Interfaces* **2012**, *4*, 1134–1147.

(33) González-González, I.; Tryk, D. A.; Cabrera, C. R. Polycrystalline Boron-Doped Diamond Films as Supports for Methanol Oxidation Electrocatalysts. *Diamond Relat. Mater.* **2006**, *15*, 275–278.

(34) Plana, D.; Humphrey, J. J. L.; Bradley, K. A.; Celorrio, V.; Fermín, D. J. Charge Transport Across High Surface Area Metal/Diamond Nanostructured Composites. *ACS Appl. Mater. Interfaces* **2013**, *5*, 2985–2990.

(35) Maier, F.; Riedel, M.; Mantel, B.; Ristein, J.; Ley, L. Origin of Surface Conductivity in Diamond. *Phys. Rev. Lett.* **2000**, *85*, 3472–3475.

(36) Hongthani, W.; Fox, N. A.; Fermín, D. J. Electrochemical Properties of Two Dimensional Assemblies of Insulating Diamond Particles. *Langmuir* **2011**, *27*, 5112–5118.

(37) Holt, K. B. Undoped Diamond Nanoparticles: Origins of Surface Redox Chemistry. *Phys. Chem. Chem. Phys.* **2010**, *12*, 2048–2058.

(38) Hongthani, W.; Fermín, D. J. Layer-by-Layer Assembly and Redox Properties of Undoped HPHT Diamond Particles. *Diamond Relat. Mater.* **2010**, *19*, 680–684.

(39) Holt, K. B.; Ziegler, C.; Zang, J.; Hu, J.; Foord, J. S. Scanning Electrochemical Microscopy Studies of Redox Processes at Undoped Nanodiamond Surfaces. *J. Phys. Chem. C* **2009**, *113*, 2761–2770.

(40) Pérez-Rodríguez, S.; Corengia, M.; García, G.; Zinola, C. F.; Lázaro, M. J.; Pastor, E. Gas Diffusion Electrodes for Methanol Electrooxidation Studied by a New DEMS Configuration: Influence of the Diffusion Layer. *Int. J. Hydrogen Energy* **2012**, *37*, 7141–7151.

(41) Pérez-Rodríguez, S.; García, G.; Calvillo, L.; Celorrio, V.; Pastor, E.; Lázaro, M. J. Carbon-Supported Fe Catalysts for CO_2 Electroreduction to High-Added Value Products: A DEMS Study: Effect of the Functionalization of the Support. *Int. J. Electrochem.* **2011**, DOI: 10.4061/2011/249804.

(42) Fraga, M. A.; Jordão, E.; Mendes, M. J.; Freitas, M. M. A.; Faria, J. L.; Figueiredo, J. L. Properties of Carbon-Supported Platinum Catalysts: Role of Carbon Surface Sites. *J. Catal.* **2002**, *209*, 355–364.

(43) Guerrero-Ruiz, A.; Badenes, P.; Rodríguez-Ramos, I. Study of Some Factors Affecting the Ru and Pt Dispersions over High Surface Area Graphite-Supported Catalysts. *Appl. Catal., A* **1998**, *173*, 313–321.

(44) Vidaković, T.; Christov, M.; Sundmacher, K. The Use of CO Stripping for in Situ Fuel Cell Catalyst Characterization. *Electrochim. Acta* **2007**, *52*, 5606–5613.

(45) Maillard, F.; Eikerling, M.; Cherstiouk, O. V.; Schreier, S.; Savinova, E.; Stimming, U. Size Effects on Reactivity of Pt Nanoparticles in CO Monolayer Oxidation: The Role of Surface Mobility. *Faraday Discuss.* **2004**, *125*, 357–377.

(46) Hayden, B. E.; Pletcher, D.; Suchsland, J.-P.; Williams, L. J. The Influence of Support and Particle Size on the Platinum Catalysed Oxygen Reduction Reaction. *Phys. Chem. Chem. Phys.* **2009**, *11*, 9141–9148.

(47) Wang, S.; Jiang, S. P.; White, T. J.; Guo, J.; Wang, X. Electrocatalytic Activity and Interconnectivity of Pt Nanoparticles on Multiwalled Carbon Nanotubes for Fuel Cells. *J. Phys. Chem. C* **2009**, *113*, 18935–18945.

(48) Cherstiouk, O. V.; Simonov, P. A.; Savinova, E. R. Model Approach to Evaluate Particle Size Effects in Electrocatalysis Preparation and Properties of Pt Nanoparticles Supported on GC and HOPG. *Electrochim. Acta* **2003**, *48*, 3851–3860.

(49) Maillard, F.; Schreier, S.; Hanzlik, M.; Savinova, E. R.; Weinkauf, S.; Stimming, U. Influence of Particle Agglomeration on the Catalytic Activity of Carbon-Supported Pt Nanoparticles in CO Monolayer Oxidation. *Phys. Chem. Chem. Phys.* **2005**, *7*, 385–393.

(50) Guerin, S.; Hayden, B. E.; Lee, C. E.; Mormiche, C.; Owen, J. R.; Russell, A. E.; Theobald, B.; Thompsett, D. Combinatorial Electrochemical Screening of Fuel Cell Electrocatalysts. *J. Comb. Chem.* **2003**, *6*, 149–158.

(51) Maillard, F.; Savinova, E. R.; Simonov, P. A.; Zaikovskii, V. I.; Stimming, U. Infrared Spectroscopic Study of CO Adsorption and Electro-oxidation on Carbon-Supported Pt Nanoparticles: Interparticle versus Intraparticle Heterogeneity. *J. Phys. Chem. B* **2004**, *108*, 17893–17904.

(52) Jusys, Z.; Kaiser, J.; Behm, R. J. Methanol Electrooxidation over Pt/C Fuel Cell Catalysts: Dependence of Product Yields on Catalyst Loading. *Langmuir* **2003**, *19*, 6759–6769.

(53) García, G.; Florez-Montaño, J.; Hernandez-Creus, A.; Pastor, E.; Planes, G. A. Methanol Electrooxidation at Mesoporous Pt and Pt–Ru Electrodes: A Comparative Study with Carbon Supported Materials. *J. Power Sources* **2011**, *196*, 2979–2986.

(54) Liu, Z.; Hong, L.; Tham, M. P.; Lim, T. H.; Jiang, H. Nanostructured Pt/C and Pd/C Catalysts for Direct Formic Acid Fuel Cells. *J. Power Sources* **2006**, *161*, 831–835.

(55) Wu, Y. N.; Liao, S. J.; Su, Y. L.; Zeng, J. H.; Dang, D. Enhancement of Anodic Oxidation of Formic Acid on Palladium Decorated Pt/C Catalyst. *J. Power Sources* **2010**, *195*, 6459–6462.

(56) Hong, P.; Luo, F.; Liao, S.; Zeng, J. Effects of Pt/C, Pd/C and PdPt/C Anode Catalysts on the Performance and Stability of Air Breathing Direct Formic Acid Fuel Cells. *Int. J. Hydrogen Energy* **2011**, *36*, 8518–8524.

(57) Jovanović, V. M.; Tripković, D.; Tripković, A.; Kowal, A.; Stoch, J. Oxidation of Formic Acid on Platinum Electrodeposited on Polished and Oxidized Glassy Carbon. *Electrochem. Commun.* **2005**, *7*, 1039–1044.

(58) Samjeské, G.; Miki, A.; Ye, S.; Osawa, M. Mechanistic Study of Electrocatalytic Oxidation of Formic Acid at Platinum in Acidic Solution by Time-Resolved Surface-Enhanced Infrared Absorption Spectroscopy. *J. Phys. Chem. B* **2006**, *110*, 16559–16566.

(59) Osawa, M.; Komatsu, K.-i.; Samjeské, G.; Uchida, T.; Ikeshoji, T.; Cuesta, A.; Gutiérrez, C. The Role of Bridge-Bonded Adsorbed Formate in the Electrocatalytic Oxidation of Formic Acid on Platinum. *Angew. Chem., Int. Ed.* **2011**, *50*, 1159–1163.

(60) Cuesta, A.; Cabello, G.; Gutierrez, C.; Osawa, M. Adsorbed Formate: the Key Intermediate in the Oxidation of Formic Acid on Platinum Electrodes. *Phys. Chem. Chem. Phys.* **2011**, *13*, 20091–20095.

(61) Haertl, A.; Garrido, J. A.; Nowy, S.; Zimmermann, R.; Werner, C.; Horinek, D.; Netz, R.; Stutzmann, M. The Ion Sensitivity of Surface Conductive Single Crystalline Diamond. *J. Am. Chem. Soc.* **2007**, *129*, 1287–1292.

(62) O'Donnell, K. M.; Martin, T. L.; Fox, N. A.; Cherns, D. Ab Initio Investigation of Lithium on the Diamond C(100) Surface. *Phys. Rev. B* **2010**, *82*, 115303.

Catalysts **2013**, *3*, 902-913; doi:10.3390/catal3040902

OPEN ACCESS

catalysts

ISSN 2073-4344

www.mdpi.com/journal/catalysts

Article

Formic Acid Oxidation over Hierarchical Porous Carbon Containing PtPd Catalysts

Angélica M. Baena-Moncada [1], Gustavo M. Morales [1], Cesar Barbero [1], Gabriel A. Planes [1,*], Jonathan Florez-Montaño [2] and Elena Pastor [2,*]

[1] Departamento de Química, Universidad Nacional de Río Cuarto, Ruta 36 Km 601 (X5804BYA) Río Cuarto, Córdoba, Argentina; E-Mails: abaenam@exa.unrc.edu.ar (A.M.B.-M.); gmorales@exa.unrc.edu.ar (G.M.M.); cbarbero@exa.unrc.edu.ar (C.B.)

[2] Departamento de Química Física, Instituto Universitario de Materiales y Nanotecnología, Universidad de La Laguna, Astrofísico F. Sánchez s/n, 38071 La Laguna, Tenerife, Spain; E-Mail: jnaz16@gmail.com

* Authors to whom correspondence should be addressed; E-Mails: gplanes@exa.unrc.edu.ar (G.A.P.); epastor@ull.es (E.P.); Tel.: +54-358-4676-111 (G.A.P); Fax: +54-358-4676-233 (G.A.P.).

Received: 24 August 2013; in revised form: 15 October 2013 / Accepted: 22 October 2013 / Published: 31 October 2013

Abstract: The use of high surface monolithic carbon as support for catalysts offers important advantage, such as elimination of the ohmic drop originated in the interparticle contact and improved mass transport by ad-hoc pore design. Moreover, the approach discussed here has the advantage that it allows the synthesis of materials having a multimodal porous size distribution, with each pore size contributing to the desired properties. On the other hand, the monolithic nature of the porous support also imposes new challenges for metal loading. In this work, the use of Hierarchical Porous Carbon (HPC) as support for PtPd nanoparticles was explored. Three hierarchical porous carbon samples (denoted as HPC-300, HPC-400 and HPC-500) with main pore size around 300, 400 and 500 nm respectively, are used as porous support. PtPd nanoparticles were loaded by impregnation and subsequent chemical reduction with $NaBH_4$. The resulting material was characterized by EDX, XRD and conventional electrochemical techniques. The catalytic activity toward formic acid and methanol electrooxidation was evaluated by electrochemical methods, and the results compared with commercial carbon supported PtPd. The Hierarchical Porous Carbon support discussed here seems to be promising for use in DFAFC anodes.

Keywords: hierarchical porous carbon; PtPd catalysts; formic acid

---

1. Introduction

The use of liquid fuel in low temperature polymeric electrolyte membrane fuel cells (PEMFC) combines high power density and simplicity for fuel handling. Among them, direct formic acid fuel cells (DFAFC) are interesting because the formic acid crossover in the fuel cell membranes is significantly lower than that for methanol [1]. Additionally, the use of formic acid allows a high open circuit potential [2].

The high cost of the most active catalysts implies that the surface/mass ratio should be as high as possible, *i.e.*, metal nonoparticles (NP) should be spread over an inexpensive and high surface material [3]. The use of carbon material as support meets these requirements: low cost, acceptable electronic resistance and chemical stability. Additionally, the need for large metal loadings, frequently between 20% and 60% of the whole mass, requires widespread anchorage sites for catalysts nanoparticles, which results in the need for high surface materials [4]. The most used approach utilizes a carbon support over which the catalytic metal is deposited. However, the employment of nanoparticulated carbon supports also involves ohmic drops due to the interparticle resistance as well as mass transfer obstruction.

Two possible approaches for the mass transport improvement can be considered: short diffusion lengths in thin films, like reported previously for mesoporous metal films, or thicker materials with special pore design for improved diffusion [5,6].

Considering the second approach, the use of high surface monolithic carbon may offer some advantage [2,7]. The use of a larger piece of carbon, with dimensions on the scale of microns, decreases the ohmic drop originated in the interparticle contact. On the other hand, the use of new synthetic routes allows the surface area to stay high enough, and improves the mass transport by the ad-hoc pore design in hierarchical levels. However, the monolithic nature of the porous support imposes new challenges for metal loading, and the well-known method for metal impregnation should be revised and modified [2,6].

One additional consideration about DFAFC emphasizes the need for an improved mass transport. In the anode of DFAFC, the processes for formic acid (FA) oxidation produce CO_2 and two electrons per FA molecule, according to reaction (1):

$$HCOOH \rightarrow CO_2 + 2H^+ + 2e^- \quad (1)$$

In comparison, methanol (see reaction (2)) is able to produce until six electrons for each fuel molecule:

$$H_3COH + H_2O \rightarrow CO_2 + 6H^+ + 6e^- \quad (2)$$

Therefore, for DFAFC the mass transport must be high enough to keep the limiting current value at acceptable levels, at least if comparable current densities are desired. Additionally, it has been proposed that severe mass transport limitations are associated to the hydrophilic character of the formic acid [8]. For these reasons, a careful material design for an efficient mass transport is necessary.

In this work, the use of hierarchical porous carbon (HPC) as support for PtPd nanoparticles is explored. Three hierarchical porous carbon (HPC-300, HPC-400 and HPC-500) samples with main pore size around 300, 400 and 500 nm respectively, are used as porous support. The resulting material is characterized by EDX, XRD and conventional electrochemical techniques. Finally, the catalytic activity toward formic acid and methanol electrooxidation was evaluated. It is concluded that the catalysts show appropriate behavior to be used for anodes in DFAFC and cathodes in DMFC.

2. Results and Discussion

The Figure 1 shows the SEM images of the PtPd/HPC300 (A), PtPd/HPC400 (B), PtPd/HPC500 (C) and high magnification SEM of HPC400 (D). Due to the fragility of the carbon material, after impregnation, the exterior surface of the carbon support shows signs of fracture and local collapse of the macropores, which is clearly visible in sample A–B, and nearly imperceptible in the sample C. The Figure 1D shows the second level of porosity, visible at the pore wall. The image was taken inside of one of the microparticles in the HPC400 support. As it was previously reported, this additional porosity in the mesoscale was attributed to the hindered contraction during pyrolysis due the presence of the SiO_2 rigid template.

Figure 1. SEM images of the PtPd/HPC300 (**A**); PtPd/HPC400 (**B**); PtPd/HPC500 (**C**) and high magnification SEM of HPC400 (**D**).

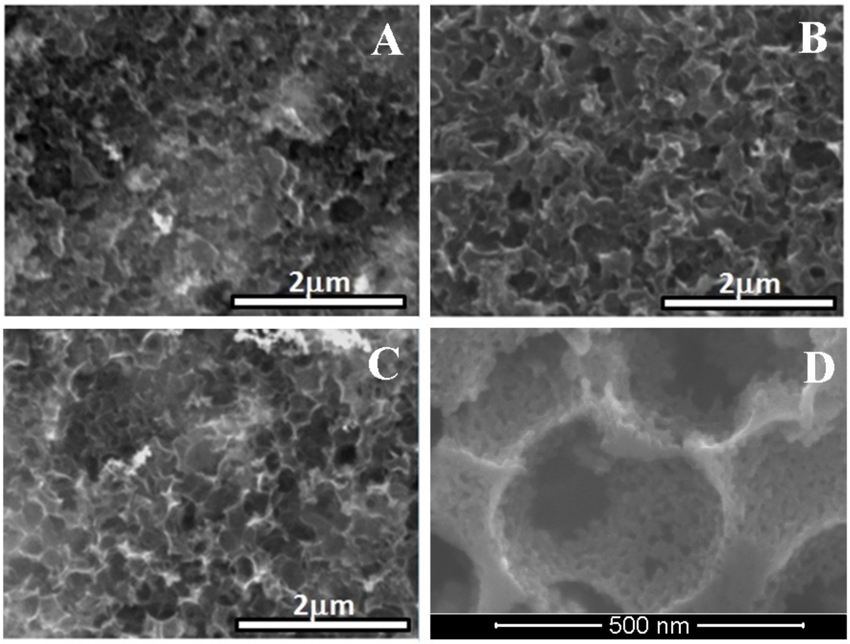

EDS analysis of the impregnated HPC reveals that all samples have a composition of Pt:Pd of approximately 1:1, in good agreement with the feeding composition during synthesis. On the other hand, the metal load shows a broader distribution between 17% and 28% p/p. The diffractograms for all PtPd/HPC catalysts are given in Figure 2. The crystallite size was estimated by means of the Scherrer equation, obtaining values in the order of 6 nm, a little above the value of a commercial PtPd/C (E-TEK) which is 4.5 nm (see Table 1).

Figure 2. XRD diffractograms of PtPd/HPC samples.

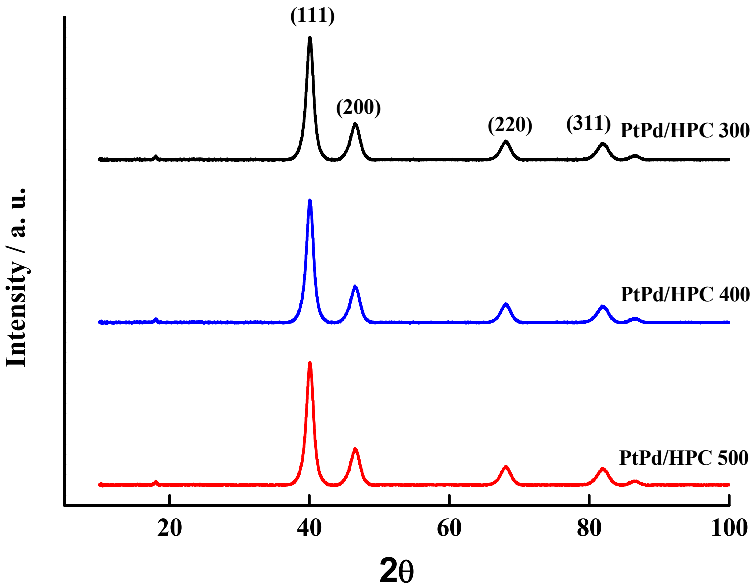

The electrochemical characterization of the catalysts surface includes a CO stripping experiment performed with the purpose of evaluating the extension of the metal surface exposed to the solution (see Figure 3). With this idea, the charge associated to the CO stripping was calculated and the area was determined assuming 420 µC cm^{-2} for a CO adsorbed monolayer. The results show that the electrochemically active surface area (ESA, expressed in terms of m^{2} g^{-1}) for all tree catalysts synthesized in this work is smaller than the commercial catalyst, being of 38.8 m^{2} g^{-1} for the PtPd/HPC300; 40.2 m^{2} g^{-1} for the PtPd/HPC400 and 49.6 m^{2} g^{-1} for the PtPd/HPC500; whereas a value of 62.6 m^{2} g^{-1} was obtained for PtPd/C E-TEK in the same conditions (Table 1).

Table 1. EDS, XRD and ESA results for PtPd/HPCs and commercial PtPd/C E-TEK.

Catalysts	**Atomic composition (%)**	**Metal composition (%)**	**Crystallite size (nm)**	**Lattice parameter**	**ESA(m^{2} g^{-1})**
PtPd/HPC500	53 Pd 47 Pt	28.5	5.9	3.897	49.6
PtPd/HPC400	52 Pd 48 Pt	17.0	6.0	3.904	40.2
PtPd/HPC300	53 Pd 47 Pt	17.6	5.6	3.893	38.8
PtPd/C E-TEK	49 Pd 51 Pt	20.0	4.5	3.896	62.6

These values suggest the absence of a direct relationship between the crystallite size and the surface extension (or electroactive surface area), although the higher surface area is achieved by the catalysts with the lower crystallite size. However, high catalyst area does not necessarily imply increased catalyst activity, as will be proved later. On the other hand, the change in the peak position for CO electrooxidation is not significant when going from one catalyst to the other. It is located at approx.

0.85 V_{HRE}, near 50 mV and it shifted to more negative potentials when compared with commercial PtPd/C [9]. This result is reasonable considering that all PtPd/HPC catalysts have the same composition, about 53% Pd and 47% Pt.

Although the catalyst loading process is performed on a very porous material, it is a remarkable fact that it is possible to obtain a supported catalyst composed of relatively small NP which has the same metal composition as the feeding catalyst [2]. The existence of a relatively well dispersed metal NP probably lies in the second level of porosity inside the pore wall. The mesoporous network contributes to fixing the metal seed to the carbon surface during the impregnation with the precursors. Such "defects" on the porous surface prevent migration and the subsequent agglomeration.

Figure 3. CO stripping voltammograms for PtPd/HPC300, PtPd/HPC400 and PtPd/HPC500 catalysts in 0.5 M H_2SO_4, 25 °C, 20 m V s^{-1}.

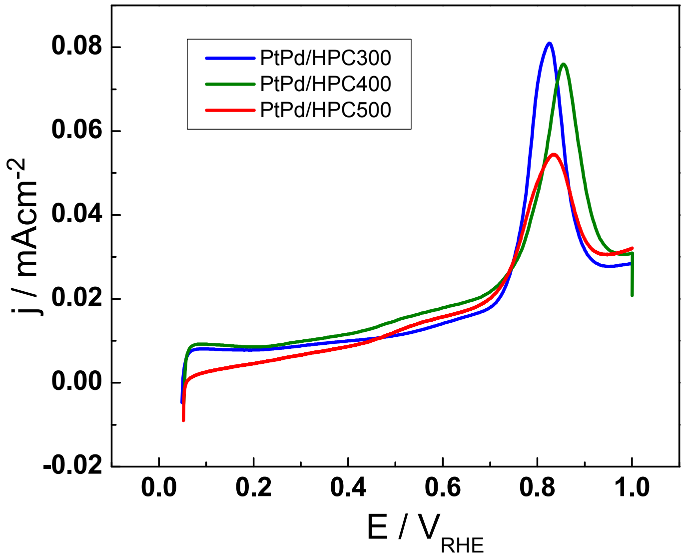

The activity towards formic acid electrooxidation was tested by cyclic voltammetry (CV) (Figure 4) and chronoamperometry (CA) (Figure 5). The anodic scan for formic acid electrooxidation at 25 °C in 0.5 M H_2SO_4 is shown in Figure 4 for the three PtPd/HPC materials. The onset for formic acid oxidation is the same for all PtPd/HPC and it is positioned around 0.1 V_{RHE}. The current has a similar behavior in the three catalysts, but substantial differences in the maximum current achieved in each of them. The current increases gradually sweeping the potential from the initial value of 0.05 V up to 0.25 V, and then change the rate of increasing or remains constant up to approx. 0.4 V_{RHE}, describing a shoulder. From this point, there begins a new increase, attaining a peak about 0.65 V_{RHE} (PtPd/HPC400 and PtPd/HPC500) or 0.70 V_{RHE} (PtPd/HPC300). These results are in good agreement with the mechanism proposed for formic acid oxidation, suggested during the last century in the middle of the 1970s by Capon and Parsons, which assume a dual pathway [10]. It has been proposed that, at lower potentials, an active intermediary is present, like adsorbed formate [11]. The parallel method involves a strong chemisorbed mediator, like CO [12,13].

The maximum current density achieved in the anodic scan fluctuates between 380 μA cm^{-2} (PtPd/HPC500) and 690 μA cm^{-2} (PtPd/HPC300). In the backward scan (not shown) all catalysts display a sharp rising of the current density, usually associated with the surface regeneration after poison removal in the upper scan limit (*i.e.*, after oxidation of residual adsorbed CO) [14].

Figure 4. Cyclic voltammetry (CV) for PtPd/HPC300, PtPd/HPC400 and PtPd/HPC500 catalysts in0.5 M HCOOH + 0.5 M H_2SO_4, 25 °C, 20 mV s^{-1}.

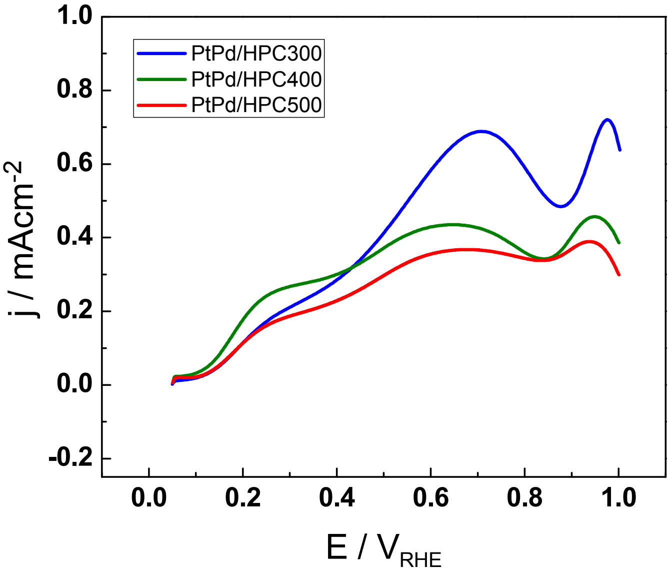

On the other hand, it is reasonable to assume that, under operative fuel cell conditions, the potential in the anode changes only as a response to the current density (load conditions). In stationary regime, both poisoning and mass transfer limitations could seriously affect the observed current density after a few seconds of applying potentiostatic operation conditions. For this reason, chronoamperometric curves were recorded at 0.55 V_{RHE} (Figure 5). This potential was chosen because it combines the remaining adsorbed CO not completely removed from the surface (see Figure 3) and a significant requirement of mass transfer.

Figure 5 shows the current transients after a potential step from 0.05 V_{RHE} to 0.55 V_{RHE} in 0.5 M HCOOH + 0.5 M H_2SO_4 at 25 °C for the PtPd/HPC materials (commercial PtPd/C E-TEK was also tested and included as reference). All catalysts display stationary current densities somewhat below that observed in the anodic scan (Figure 4) at 0.55 V_{RHE}. Formic acid oxidation generates a copious quantity of CO_2 bubbles (see current steps at the end of the PtPd/HPC300 transient), which could affect the mechanical stability and/or connectivity of some of the HPC films. This fact was a key issue for the PtPd/HPC400 test. For that catalyst, the experience was repeated by changing the substrate due to loss of activity as result of catalyst peeling. Finally, exceptional electrochemical activity (expressed in terms of current densities) toward formic acid oxidation was observed for PtPd/HPC300.

On the other hand, the current can be expressed as mass activity (A g^{-1}) by considering the PtPd mass for each catalyst (Figure 6), thus reflecting a quite different fact as these values allow us to establish how much (or how well) the metal catalyst is dispersed in the carbon support. Considering stationary values for mass activity transients, the best performance is achieved by the PtPd/HPC500 (126 A g^{-1}), then the PtPd/HPC400 (117 A g^{-1}) followed by the commercial PtPd/C E-TEK, about 106 A g^{-1}. Comparing PtPd/HPC300 and PtPd/HPC500, the gain in performance can be understood in terms of appropriate balance between exposed surface area and formic acid accessibility to catalytic centers.

Figure 5. Chronoamperometric curves in terms of current densities for PtPd/HPC300, PtPd/HPC400, PtPd/HPC500 and commercial catalyst recorded at 0.55 V_{RHE} in 0.5 M HCOOH + 0.5 M H_2SO_4, 25 °C.

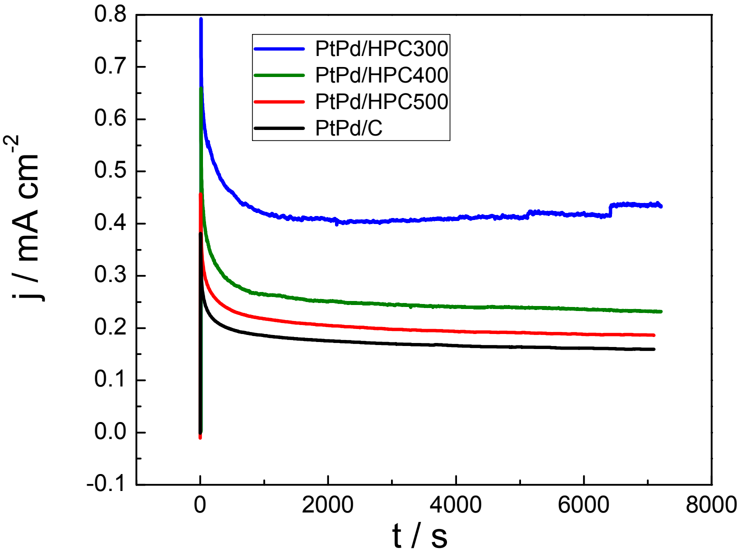

Figure 6. Current transient expressed as mass activity for PtPd/HPC300, PtPd/HPC400, PtPd/HPC500 and commercial catalyst recorded at 0.55 V_{RHE} in 0.5 M HCOOH + 0.5 M H_2SO_4, 25 °C.

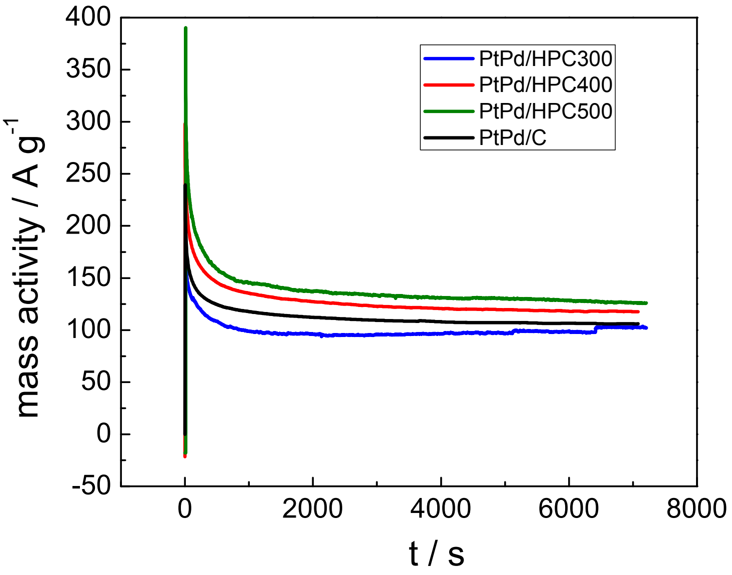

The lowest surface area catalyst (PtPd/HPC300, see last column in Table 1) presents the most active surface in terms of current density (Figure 5), but the worst performance in terms of mass activity (Figure 6), which can be explained assuming some degree of agglomeration of the NP. In fact, for the same crystallite size, the ESA of the PtPd/HPC300 is only 78% of the area exposed by the PtPd/HPC500. The low surface area of the PtPd/HPC 300 involves a lower fuel requirement flowing through the porous material. In other words, for an equivalent mass transport, more fuel is available for each active site, increasing to some extent the current density. However, the current improvement does not balance the lost in number of active sites due to the poor surface area; for this reason the mass activity is low. On the other hand, the commercial catalyst has the largest ESA of all catalysts tested; however, the mass activity towards HCOOH oxidation is 80% of that delivered by the PtPd/HPC500. Conversely, the PtPd/HPC500 shows high mass activity due to the good dispersion of catalysts nanoparticles inside HPC, but there remains sufficiently high surface activity. The mass activity is somewhat lower than that reported in the literature for Pd catalysts [15], but it is in the order of other supported PtPd catalysts [16]. As reported before by several groups, the presence of Pt results in a more stable response of the current [14,17].

Finally, due to the possibility of the PtPd catalysts to be used in DMFC cathode, the catalysts' tolerance to methanol was investigated. Chronoamperometric measurements were performed in the presence of 0.5 M CH_3OH at 0.55 V_{RHE} (Figure 7). The current transient (mA cm^{-2}) shows different order when compared with that obtained for the oxidation of formic acid in Figure 5 (see Table 2). Both stationary current densities and mass activities increase in the order: PtPd/HPC300 < PtPd/HPC400 < PtPd/HPC500 < PtPd/C E-TEK.

Figure 7. Chronoamperometric curves in terms of current density for PtPd/HPC300, PtPd/HPC400, PtPd/HPC500 and commercial catalyst recorded at 0.55 V_{RHE} in 0.5 M CH_3OH + 0.5 M H_2SO_4; 25 °C.

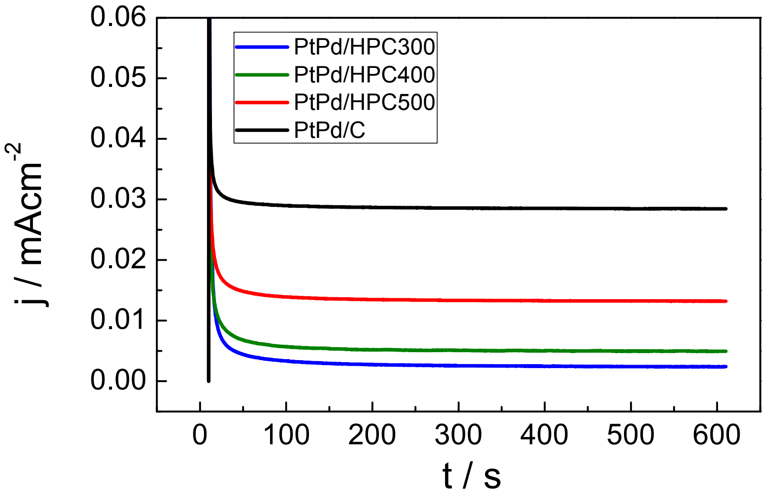

Again, these responses are surprising because the catalysts' composition is quite similar and, therefore, similar current densities were expected. When the results are compared in terms of relative mass activity (Table 2), the best tolerance to methanol (that is, the lowest mass activity) is also obtained with the PtPd/HPC300 catalyst, following the same order than that stated above for the current density.

From these results it is concluded, without any doubt, that the observed selectivity between formic acid and methanol lies in the particle composition, which is similar in all catalysts evaluated. For the same reason, the differences in the electrochemical behavior observed for the PtPd/HPC catalysts synthesized in this work can be attributed to the porous structure of the carbon support.

Table 2. Electrochemical characterization of the catalysts considering stationary values from current transients. (0.55 V_{RHE}; 25 °C).

Catalysts	HCOOH Mass activity (A g^{-1})	CH_3OH Mass activity (A g^{-1})	HCOOH J (μAcm^{-2})	CH_3OH J (μA cm^{-2})
PtPd/HPC300	106	0.5	434	3
PtPd/HPC400	117	2.1	231	5
PtPd/HPC500	126	9.1	186	13
PtPd/C E-TEK	102	17.8	169	28

Bigger porous structures influence positively both methanol and formic acid oxidation, mainly due the best catalysts dispersion and increased ESA. On the other hand, the mass transport is yet high enough to further improve the fuel feeding to the catalysts surface. This latter reason explains why the PtPd/HPC500 catalyst is better than the PtPd/C E-TEK, even taking the first a smaller area. Due to the low currents obtained for methanol electrooxidation, the resulting catalytic enhancement is only significant for formic acid oxidation reaction.

3. Experimental Section

Recently, our group has described the synthesis of mesoporous carbon with hierarchical porous structure (see scheme 1) [6]. The first step involves the synthesis of SiO_2 NP by TEOS hydrolysis in basic media [18]. Adjusting the synthesis parameters, it was possible to tune the particle size between 70 and 500 nm. The use of the smallest SiO_2 nanoparticles (dia < 200 nm) produces an extremely fragile carbon material. For this reason, only SiO_2 NP with 300–500 nm diameter were used in this work. Vertical sedimentation of the SiO_2 NP in the bottom of a vial produces a white and rigid solid. After heat treatment at 1000 °C, the monolithic opals were impregnated with the carbon precursor (step "A" in Scheme 1): a mixture of resorcinol (1 g), formaldehyde (1.6 mL) and sodium carbonate (0.4 mL 0.1 M). The resin-SiO_2 was dried in oven (105 °C) and then pyrolyzed at 850 °C in the absence of O_2 for a 24 h (step "B"). The SiO_2 pattern was then removed by treating the samples with fluorhydric acid solution (step "C"). Note that the way denoted as A→B`→C` produce a macroporous carbon, without additional porosity in the mesoscale level [6].

The HPC was loaded with PtPd NP using $NaBH_4$. With this purpose, 0.1 g of HPC where suspended in 50 mL of water containing the appropriate quantities of $PdCl_2$ and H_2PtCl_6. The mixture was stirred by 12 h and the pH was adjusted to 5 by addition of NaOH. After six hours of additional stirring, $NaBH_4$ (50 mg/50 mL of H_2O was added drop wise (1 mL/3 min). This dispersion was continually stirred for 24 h more, then filtered and washed.

The diameters of the SiO_2 NP were determined by dynamic light scattering (DLS, Malvern 4700 with goniometer and 7132 correlator) with an argon-ion laser operating at 488 nm. All measurements were made at the scattering angle of 90°. Metal content and PtPd atomic ratios of the synthesized catalysts were determined by Energy Dispersive X-Ray Analysis (EDX), using an Oxford Instruments Microanalysis Group 6699 ATW scanning electron microscope at 20 kV, with a Si detector and a Be window. XRD patterns of synthesized catalysts were obtained using an Universal Diffractometer Panalytical X'Pert X-ray, operating with a Cu-Kα radiation generated at 40 kV and 30 mA. Scans were done at 3° $\min^{-1}$ for 2θ values between 20 and 100°. Metal crystallite size and lattice parameters were calculated using the dimensions of peak (220), applying Scherrer's equation and Vergard's Law.

Scheme 1. Steps A–B–C: Synthesis of the mesoporous carbon with hierarchical porous structure (HPC). Steps A-B\`-C\`: Synthesis of macroporous carbon.

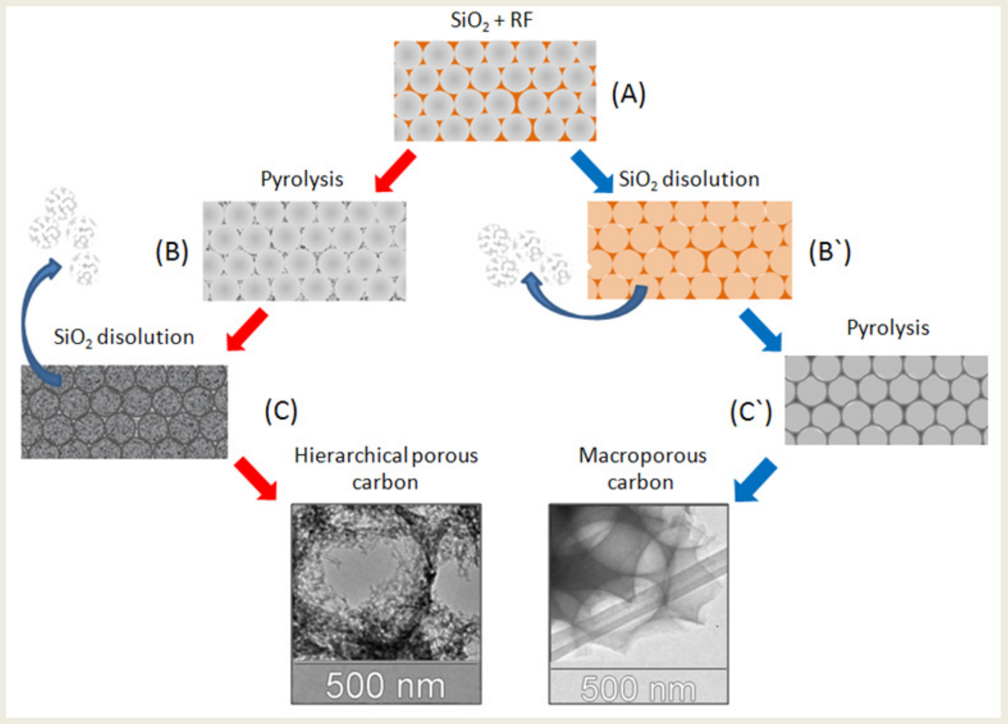

Electrochemical experiments were carried out in a thermostatized three electrodes electrochemical cell, using a hydrogen reference electrode in the electrolyte solution (RHE) as the reference and a small piece of high surface carbon was used as auxiliary electrode. In this study, the working electrode consists of a certain amount of the PtPd/HPC or commercial PtPd/C E-TEK deposited as a thin layer over a glassy carbon disc ($\Phi = 3$ mm). For this purpose, an aqueous suspension of 4.0 mg mL^{-1} of the PtPd/HPC or PtPd/C E-TEK catalyst was prepared by ultrasonically dispersing it in 15 μL of Nafion (5 wt.%, Aldrich) and pure water. An aliquot (20 mL) of the dispersed suspension was pipetted on the glassy carbon surface and dried at ambient temperature under Ar atmosphere. The currents are expressed as current densities J (A cm^{-2}), calculated from the measured current I (A) and the real electroactive area S (cm^2). S was estimated from CO (N47) stripping experiments. Electrochemical measurements were performed with a PC controlled Autolab PGSTAT30 potentiostat–galvanostat. All reagents were of analytical grade. Argon (N50) was bubbled through the solution to avoid dissolved oxygen. All potentials in this work are given against the RHE.

4. Conclusions

The use of hierarchical porous carbon (HPC) as support for PtPd nanoparticles was evaluated. Three hierarchical porous carbon samples with main pore size around 300, 400 and 500 nm respectively, were used as porous support. PtPd nanoparticles were loaded by impregnation and subsequent chemical reduction with $NaBH_4$, resulting in well dispersed metal catalysts with surface area of about 50 $m^2\ g^{-1}$.

Formic acid and methanol electrooxidation were studied by chronoamperometry. The mass activity for formic acid oxidation reaches the value of 132 A g^{-1} at 0.55 V for the PtPd/HPC500, slightly higher than that achieved by the commercial catalyst under the same conditions.

The behavior of the HPCs can be understood in terms of a balance between the exposed surface area of the catalysts and formic acid accessibility to its surface. The best combination is obtained with the PtPd/HPC500, which shows the highest catalytic activity toward formic acid oxidation.

Due to the presence of Pd, the catalysts tested are also very tolerant to the methanol, showing low oxidation currents. This fact makes PtPd/HPCs suitable for DMFC cathodes.

The use of hierarchical porous carbon as support for metal nanoparticles seems to be promising for fuel cell electrodes.

Acknowledgments

Authors thank to FONCYT and CONICET (Argentina) and MINECO (Spain, project CTQ2011-28913-C02-02) for financial support .A.M. Baena-Moncada and J. Florez-Montaño thank FONCYT and ACIISI (Gobierno de Canarias) for graduate fellowships. G.A. Planes and C. Barbero are permanent research fellows of CONICET.

Conflicts of Interest

The authors declare no conflict of interest.

References

1. Jeong, K.-J.; Miesse, C.M.; Choi, J.-H.; Lee, J.; Han, J.; Yoon, S.P.; Nam, S.W.; Lim, T.-H.; Lee, T.G. Fuel crossover in direct formic acid fuel cells. *J. Power Sources* **2007**, *168*, 119–125.
2. Ji, X.; Lee, K.T.; Holden, R.; Zhang, L.; Zhang, J.; Botton, G.A.; Couillard, M.; Nazar, L.F. Nanocrystalline intermetallics on mesoporous carbon for direct formic acid fuel cell anodes. *Nat. Chem.* **2010**, *2*, 286–293.
3. Yu, X.; Pickup, P.G. Recent advances in direct formic acid fuel cells (DFAFC). *J. Power Sources* **2008**, *182*, 124–132.
4. Chan, K.-Y.; Ding, J.; Ren, J.; Cheng, S.; Tsang, K.Y. Supported mixed metal nanoparticles as electrocatalysts in low temperature fuel cells. *J. Mater. Chem.* **2004**, *14*, 505–516.
5. García, G.; Florez-Montaño, J.; Hernandez-Creus, A.; Pastor, E.; Planes, G.A. Methanol electrooxidation at mesoporous Pt and Pt–Ru electrodes: A comparative study with carbon supported materials. *J. Power Sources* **2011**, *196*, 2979–2986.

6. Baena-Moncada, A.M.; Planes, G.A.; Moreno, M.S.; Barbero, C.A. A novel method to produce a hierarchical porous carbon as a conductive support of PtRu particles. Effect on CO and methanol electrooxidation. *J. Power Sources* **2013**, *221*, 42–48.
7. Ryoo, R.; Joo, S.H.; Jun, S. Synthesis of highly ordered carbon molecular sieves via template-mediated structural transformation. *J. Phys. Chem. B* **1999**, *103*, 7743–7746.
8. Uhm, S.; Kwon, Y.; Chung, S.T.; Lee, J. Highly effective anode structure in a direct formic acid fuel cell. *Electrochim. Acta* **2008**, *53*, 5162–5168.
9. Rice, C.; Ha, S.; Masel, R.I.; Waszczuk, P.; Wieckowski, A.; Barnard, T. Direct formic acid fuel cells. *J. Power Sources* **2002**, *111*, 83–89.
10. Capon, A.; Parsons, R. The oxidation of formic acid on noble metal electrodes: II. A comparison of the behaviour of pure electrodes. *J. Electroanal. Chem.* **1973**, *44*, 239–254.
11. Grozovski, V.; Vidal-Iglesias, F.J.; Herrero, E.; Feliu, J.M. Adsorption of formate and its role as intermediate in formic acid oxidation on Platinum electrodes. *ChemPhysChem* **2011**, *12*, 1641–1644.
12. Beden, B.; Bewick, A.; Lamy, C. A comparative study of formic acid adsorption on a platinum electrode by both electrochemical and emirs techniques. *J. Electroanal. Chem.* **1983**, *150*, 505–511.
13. Arenz, M.; Stamenkovic, V.; Schmidt, T.J.; Wandelt, K.; Ross, P.N.; Markovic, N.M. The electro-oxidation of formic acid on Pt–Pd single crystal bimetallic surfaces. *Phys. Chem. Chem. Phys.* **2003**, *5*, 4242–4251.
14. Feng, L.; Si, F.; Yao, S.; Cai, W.; Xing, W.; Liu, C. Effect of deposition sequences on electrocatalytic properties of PtPd/C catalysts for formic acid electrooxidation. *Catal. Commun.* **2011**, *12*, 772–775.
15. Maiyalagan, T.; Nassr, A.B.A.; Alaje, T.O.; Bron, M.; Scott, K. Three-dimensional cubic ordered mesoporous carbon (CMK-8) as highly efficient stable Pd electro-catalyst support for formic acid oxidation. *J. Power Sources* **2012,** *211*, 147–153.
16. Liu, B.; Li, H.Y.; Die, L.; Zhang, X.H.; Fan, Z.; Chen, J.H. Carbon nanotubes supported PtPd hollow nanospheres for formic acid electrooxidation. *J. Power Sources* **2009,** *186*, 62–66.
17. Yu, X.; Pickup, P.G., Deactivation/reactivation of a Pd/C catalyst in a direct formic acid fuel cell (DFAFC): Use of array membrane electrode assemblies. *J. Power Sources* **2009,** *187*, 493–499.
18. Wang, W.; Gu, B.; Liang, L.; Hamilton, W. Fabrication of two- and three-dimensional silica nanocolloidal particle Arrays. *J. Phys. Chem. B* **2003**, *107*, 3400–3404.

INTERNATIONAL JOURNAL OF HYDROGEN ENERGY 39 (2014) 5371–5377

Available online at www.sciencedirect.com

ScienceDirect

journal homepage: www.elsevier.com/locate/he

Fuel cell performance of Pt electrocatalysts supported on carbon nanocoils

V. Celorrio [a,1], J. Flórez-Montaño [b], R. Moliner [a], E. Pastor [b], M.J. Lázaro [a,*]

[a] Instituto de Carboquímica (CSIC), Miguel Luesma Castán 4, 50018 Zaragoza, Spain
[b] Departamento de Química Física, Universidad de La Laguna, Avda. Astrofísico Francisco Sánchez s/n, 38071 La Laguna, Tenerife, Spain

ARTICLE INFO

Article history:
Received 30 September 2013
Received in revised form
26 December 2013
Accepted 28 December 2013
Available online 24 January 2014

Keywords:
Polymer electrolyte membrane fuel cell
Carbon nanocoils
Electrocatalyst

ABSTRACT

Carbon nanocoils (CNCs) synthesized via the catalytic graphitization of resorcinol-formaldehyde gel were investigated as an electrocatalyst support in PEMFC anodes. Their textural and physical properties make them a highly efficient catalyst support for anodic hydrogen oxidation in low temperature PEMFC.

When the oxidation of adsorbed CO was studied, a shift of 140 mV is observed compared with the commercial catalysts (Pt/C E-TEK) which is expected to be a key parameter in the fuel cell (PEM) performance. Furthermore, the behaviour of the electrocatalysts prepared was compared with that of a Pt/C E-TEK in a 5 cm^2 PEM fuel cell. At room temperature, results showed a 4% increase in current density at 0.6 V in comparison with the Pt/C E-TEK electrocatalysts.

1. Introduction

Current air pollution and the dwindling resources of hydrocarbons necessitate the search of new generator and accumulation energy systems in order to secure and diversify energy supplies and reduce CO_2 emissions. Within this context, fuel cells appear to be an alternative energy conversion technology [1–3]. Among the different types of fuel cells, polymer electrolyte (PEMFCs) and direct alcohol (DAFCs) technologies are more suited for use in portable electrical devices due to their low operating temperatures (60–100 °C) and fast start up [4–6].

Common catalysts used at the anodic side of these cells are platinum and platinum alloys [7,8]. Considering that catalysis is a surface phenomenon, an aspect to be taken into account in the design of a catalyst is a high surface area. For this purpose, the active catalyst phase is dispersed in a conductive support, typically carbon materials. However, the development of PEMFCs, from the viewpoint of the electrocatalyst, is limited by the poisoning of the anode catalyst by CO, which is present as an impurity in the reformed gas used as a H_2 source for this type of cells. In the presence of 50–100 ppm of CO in the fuel, Pt–Ru alloys supported on carbon materials have shown an electrocatalytic activity higher than pure Pt [9]. On the cathodic side, Pt is showing the highest catalytic activity towards oxygen reduction reaction [10,11]. Durability is another key factor for the commercialization of low temperature fuel cells. Over the past years, extensive research and development efforts have been directed towards optimizing

---

[*] *Corresponding author*. Tel.: +34 976 733977; fax: +34 976 733318.
E-mail address: mlazaro@icb.csic.es (M.J. Lázaro).

[1] Present address: School of Chemistry, University of Bristol, Cantocks Close, Bristol BS8 1TS, United Kingdom.

0360-3199/$ – see front matter Copyright © 2014, Hydrogen Energy Publications, LLC. Published by Elsevier Ltd. All rights reserved.
http://dx.doi.org/10.1016/j.ijhydene.2013.12.198

the initial performance of catalysts, membranes and gas diffusion layers, but only recent research has focused on the various material degradation mechanisms observed over the life-time of fuel cells under real conditions [12,13].

Carbon materials are generally used as catalyst supports because of their stability in both acidic and basic media, good electrical conductivity, high corrosion resistance, surface properties and high specific surface area [14–17]. Activated carbons, carbon blacks, graphites and graphitized materials have been applied in various catalytic processes. Carbon materials have a strong influence on the properties of supported noble metal catalysts, such as metal particle size, morphology, size distribution, stability, and dispersion [18,19]. On the other hand, carbon supports can also affect the performance of fuel cell catalysts by altering mass transport, catalyst layer electrical conductivity, electrochemically active area, and metal nanoparticle stability during operation [20,21]. Consequently, a carbon support with suitable properties must be selected in order to obtain an active catalyst, since its properties have strong effects on the preparation and performance of supported catalysts.

Among all types of carbon materials, carbon blacks are the most used as electrocatalytic support for PEMFCs, due to their high electrical conductivity, corrosion resistance, their porous structure and specific surface area [22]. Vulcan XC-72 is extensively used as an electrocatalyst support [23,24]. At present, this material is used as support in commercial electrocatalysts (E-TEK and Johnson Matthey). However, it shows high ohmic resistance and problems of mass transfer in fuel cell applications.

As carbon supports have been found to strongly influence the accessibility of the catalytic active sites, great efforts are being made to find the optimum architecture of carbon supports. In recent years, an important strategy to reduce the performance degradation due to mass transport resistance has been the use of alternative carbon supports with a suitable mesoporous structure. Novel non-conventional carbon materials with controllable porous structures and surface chemistry, such as carbon nanocoils [25], carbon xerogels and aerogels [26], and ordered mesoporous carbons [27], have been proposed as electrocatalyst supports. However, a critical aspect is to achieve a balance between specific surface area, pore size distribution and electrical conductivity.

In this study we report the use of carbon nanocoils as an anode catalyst support for PEMFC. To validate its applicability in practical fuel cells, performance of the supported catalysts is evaluated in a working fuel cell environment and compared to those of commercially available carbon blacks.

2. Experimental

2.1. *Carbon nanocoils (CNCs) and catalysts preparation*

Carbon nanocoils were synthesized by the catalytic graphitization of resorcinol-formaldehyde gel as described elsewhere [28]. In a typical synthesis, formaldehyde (Sigma–Aldrich) and silica sol (Supelco) were dissolved in 100 mL of deionized water, and then a mixture of nickel ($Ni(NO_3)_2 \cdot 6H_2O$, Panreac) and cobalt ($Co(NO_3)_2 \cdot 6H_2O$, Sigma–Aldrich) salts was added under stirring conditions. Subsequently, resorcinol (Sigma–Aldrich) was added, and the stirring conditions maintained for 0.5 h. After a heat treatment at 85 °C for 3 h in a closed system of this reaction mixture, the system was then opened, and the mixture dried at 108 °C. Finally it was carbonized in a nitrogen atmosphere at 900 °C for 3 h. A 5 M NaOH (Panreac) solution was used to remove silica particles, followed by a treatment with concentrated nitric acid (65%, Fluka) at room temperature during 2 h to remove the metal salts [29].

Pt particles supported on the different carbon materials were synthesized by the impregnation and subsequent reduction with sodium borohydride method. The amount of platinum precursor added was calculated to obtain a load of 20 wt.% Pt/C in the catalyst. A solution of the metal salt precursor was prepared and mixed with the carbon support. After the impregnation step, a reduction step is required to reduce the catalyst precursor to its metallic state, using sodium borohydride as reducing agent (99%, Sigma–Aldrich). An aqueous solution of H_2PtCl_6 3.2 mM is prepared from high purity reagent (8 wt. % $H_2PtCl_6 \cdot 6H_2O$ solution, Sigma–Aldrich) and ultrapure water (Milli-Q). Firstly the precursor solution is slowly added to a dispersion of carbon in ultrapure water under sonication and afterwards the pH of the dispersion is adjusted to 5.0. Then, the sodium borohydride aqueous solution (26.5 mM) is dropwise added, maintaining temperature under 18 °C and in the presence of sonication. Subsequently, the catalyst is filtered and thoroughly washed with ultrapure water, and then dried overnight at 60 °C [27,30].

2.2. *Carbon materials and catalysts characterization*

The textural characteristics of the carbon materials were derived from the N_2 adsorption–desorption isotherms obtained at −196 °C in a Micromeritics ASAP 2020 volumetric adsorption system. Specific surface area was calculated using the BET (Brunauer-Emmett-Teller) equation. Total pore volume was determined by the single point method at $p/p_0 = 0.99$. Micropore volume was assessed by applying the t-plot method.

Transmission electron microscopy (TEM) has been carried out on a JEOL JEM 2010F microscope operating at 200 kV.

X-ray diffraction patterns were recorded using a Bruker-AXS B8 Advance diffractometer with θ–θ configuration and operating with Cu Kα radiation ($\lambda = 0.15406$ nm) generated at 45 kV and 40 nm. The crystallite size of the supported Pt was determined from the (2 2 0) width peak around $2\theta = 70°$, which corresponds to its fcc structure, to avoid the influence of the broad band of the carbon support at $2\theta \sim 25°$ [31,32] and the deconvolution of the (1 1 1) and (2 0 0) reflections. In this case, a value of $k = 0.9$ was used. Bragg's law was also applied to the (2 2 0) peak of the Pt fcc structure in order to estimate the Pt lattice parameters.

CO electrochemical oxidation experiments were carried out in a three electrode cell using a MicroAutolab potentiostat. The counter electrode was a large area pyrolitic graphite bar and a reversible hydrogen electrode (RHE) placed inside a Luggin capillary was used as reference. Working electrodes were prepared depositing a thin layer of the electrocatalysts over a pyrolitic graphite disk (7 mm diameter). A catalyst ink was prepared by mixing 2 mg of the catalyst and 10 μl of Nafion dispersion (5 wt.%, Aldrich) in 500 μl of ultrapure water (Millipore Milli-Q system). A 40 μl aliquot of the suspension was deposited onto the graphite disk and dried. After that, the working electrode was immersed into H_2SO_4 0.5 M electrolyte solution, prepared from high purity reagents (Merck) and deaerated with nitrogen gas. All the electrochemical experiments presented in this work were carried out at room temperature (*T*). CO (99.99%) was adsorbed onto the metal surface by bubbling this gas at 1 atm through the electrolyte to achieve a full monolayer coverage of CO. The CO adsorption process was carried out at a constant potential of 0.2 V vs RHE (E_{ad}). Subsequently, N_2 gas was used to purge out the CO from the solution, leaving only the CO adsorbed on the metal surface. Moreover, the electroactive area of catalysts was determined by the integration of the CO_{ad} peak assuming a charge density of 420 $\mu C\ cm^{-2}$ involved in the oxidation of a monolayer of linearly adsorbed CO. These electroactive areas were used to normalize the current densities given in the text.

2.3. *Performance at the anode side of a PEM fuel cell*

Electrochemical tests of Membrane Electrode Assemblies (MEAs) were performed in a testing station fuel cell Bio-Logic FCT-50. Catalysts were tested at the anode side in a home-made PEM fuel cell (5 cm^2 geometric areas). Tests were carried out at room temperature or 40 °C and atmospheric pressure. Pure hydrogen and oxygen (purity > 99.9%) were passed through humidifiers and fed at the anode and cathode sides, respectively. The flow rate used for either N_2 or O_2 was 0.10 L min^{-1}.

In these tests, the MEA is inserted between two graphite bipolar plates with a coil-shaped flow-field layout; this is then inserted between the gold-plated stainless steel collector plates. The assembly is completed with two steel end plates, with inlets and outlets for the reactants and reaction products and the heat system.

Before the MEAs preparation, the polymer electrolyte membrane, Nafion® 115 (Du Pont Chemical), was cleaned by immersing in 3% H_2O_2 for 1 h at 80 °C to remove organic impurities and subsequently, in a 0.5 M H_2SO_4 solution for 1 h at 80 °C. H_2SO_4 was removed by washing in boiling distilled water.

In order to carry out the electrochemical measurements, several MEAs were prepared using different electrodes for the anode side, and an electrode based on the commercial 20% Pt/C electrode (E-TEK Inc.) for the cathode side. The electrodes were prepared by depositing a suspension of Nafion solution (10% wt.) and the synthesised electrocatalyst (Nafion content in the suspension = 32% wt) on pieces of E-TEK ELAT carbon cloth. The final amount of metal active phase in all the prepared electrodes was 0.4 mg cm^{-2}.

The final assembly of the electrodes and the Nafion membrane was hot pressed between two metallic plates and heated at 120 °C, with a pressure of 20 Kg cm^{-2} for 90 s. Characteristic polarization curves V (cell potential) versus *j* (current density) for each of the prepared MEAs were measured under strictly comparable conditions.

3. Results

3.1. *Carbon materials and catalysts characterization*

The physicochemical characterization of the CNCs was stated in a previous work [28]. CNCs present a specific surface area of 124 $m^2\ g^{-1}$ and a total pore volume of 0.16 $cm^3\ g^{-1}$, which correspond to interparticular spaces. They show a bimodal pore size distribution in the range of mesoporosity with average pore diameters of around 3 and 15 nm, and do not contain micropores. Vulcan XC-72R has a specific surface area of 218 $m^2\ g^{-1}$ and a pore volume of 0.41 $cm^3\ g^{-1}$ [33]. It has a mesoporous structure but also contained a large amount of micropores (30% of the total surface area). It has a broad pore size distribution with pores of less than 2 nm and more than 12 nm.

Table 1 shows the nomenclature and the metal loading of the different electrocatalysts obtained by EDX. As can be seen, average metal loadings were close to the nominal value of 20% wt.

The morphological and crystallographic properties of the carbon materials and metal catalysts were studied by X-ray diffraction, XRD patterns are reported in Fig. 1. CNCs show three peaks at 2θ of 26.24°, 43.85° and 54.29° which are attributed to the (002), (100) and (004) reflections of graphitic carbon (Fig. 1(a)). Vulcan also shows the (002) reflection although it appears broader and shifted to lower angles (24.6°), indicative of their more amorphous character. All the Pt-supported electrocatalysts showed the typical form of the face centered cubic (fcc) Pt structure, indicating the effective reduction of the metal precursor, producing crystalline nanoparticles (Fig. 1(b)). Peaks at $2\theta = 40°$, 47°, 67°, 81° and 85°, associated with the Pt crystal planes (111), (200), (220), (311) and (222), respectively, were observed.

Average metal crystallite sizes of the electrocatalysts were calculated using the Scherrer equation to the (220) XRD peak and are reported in Table 1. Bigger platinum crystallite size was obtained when CNCs were used as support. Graphitized carbons, like CNCs, have a low number of nucleation sites because only the surface defects can function as nucleation sites, and thus larger Pt particles are obtained.

The lattice parameters were also calculated from XRD patterns and the results are summarized in Table 1. This value decreases with increasing the crystallite size. The dependence of the lattice parameter on the crystallite size has been described previously in the literature [34,35]. A linear dependence between the lattice parameter and the crystallite size has been observed depending on the synthesis method used

Table 1 – Total metal content obtained from EDX analysis and physical characteristics of the catalysts obtained from XRD analysis.

Catalyst	wt.% Total metal content	Average crystallite size (nm)	Lattice parameter (Å)
Pt/CNC	20.0	4.7	3.9158
Pt/Vulcan	19.2	3.2	3.9198
Pt/C E-TEK	16.3	3.0	3.9271

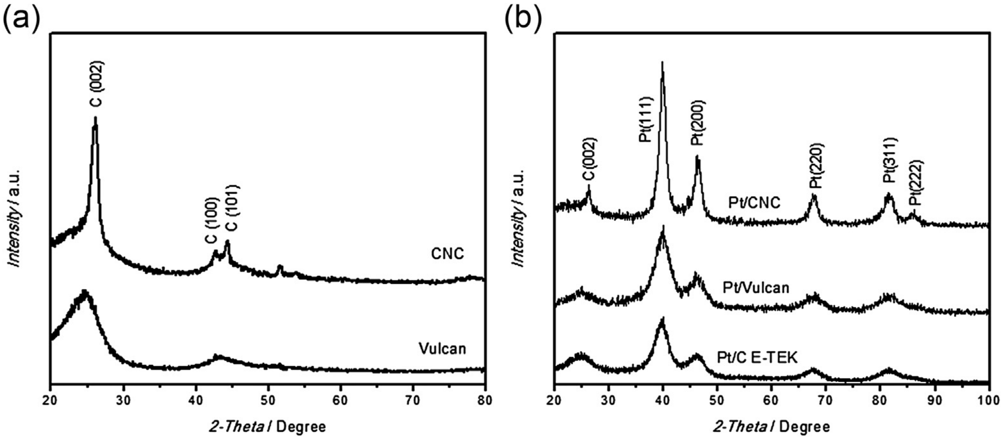

Fig. 1 – XRD diffractograms for the carbon materials used as supports (a) and for the Pt electrocatalysts supported on CNCs and Vulcan XC-72R, including the commercial catalyst (b).

to prepare Pt/C catalysts. However, in this work, to state a solid conclusion, more catalysts should be synthesised by using the same and different methods.

Fig. 2 shows a TEM image obtained for the Pt catalysts supported on CNCs. A good distribution of the platinum particles was attained.

3.2. *Oxidation of adsorbed CO*

CO poisoning in the anode of PEMFCs is a problem in the development and subsequent operation of this type of devices. CO is strongly adsorbed on the metal surface, disabling the active sites for further oxidation of the fuel, causing the poisoning of the catalyst. In order to establish the CO tolerance of catalysts, the electro-oxidation of a CO monolayer adsorbed on the catalyst surface was studied.

Fig. 3 shows the CO-stripping voltammograms for Pt catalysts (solid line), as well as the second cycle (dashed line) after oxidation, which corresponds to the voltammogram in the base electrolyte for the clean surface at 0.020 V s^{-1} (υ). In the first scan, when the Pt surface is blocked by the adsorption of a CO monolayer (CO_{ads}), hydrogen adsorption becomes impossible. In the second scan, well known reactions occur at the surface of the Pt electrode. At potentials higher than approximately 0.8 V, the Pt surface is oxidized to PtOH and PtOx in the anodic potential scan direction, and these Pt oxides are reduced to metallic Pt in the cathodic potential scan direction. At potentials less positive than approximately 0.3 V, once the CO layer is removed, two pair of peaks are observed due to the hydrogen adsorption and desorption.

Similar results were obtained for Pt/Vulcan and commercial Pt/C E-TEK catalysts, which feature a relatively narrow CO_{ads} oxidation peak centered at 0.84 V. CNCs supported Pt particles exhibited a current peak at 0.70 V, with an additional shoulder at around 0.76 V. There is no clear consensus on the origin of multiple oxidation peaks at nanostructured Pt electrodes [36–38]. On the other hand, the shift of the CO_{ads} oxidation peak towards more negative values for the CNCs supported nanoparticles can be rationalized in terms of particle size. It is generally accepted in literature that the CO oxidation peak shifts negatively while increasing Pt particle size [37,39,40]. The key step in the oxidation of a monolayer of CO on Pt is the reaction of an oxidized Pt surface atom with an adjacent adsorbed CO molecule. The formation of oxidized Pt sites becomes more difficult as the Pt size decreases, resulting in a positive shift of the oxidation peak potential.

3.3. *Performance of fuel cell with synthesized electrocatalysts in electrodes*

It is well known that at low temperature, the catalysts (including the supports) have a dominating effect on the performance of fuel cells, and comparisons of performance at relatively low temperatures are the most practical and powerful ways of evaluating the activity of catalysts.

Fig. 4 shows the polarization (cell potential versus current density) and power density curves obtained at room

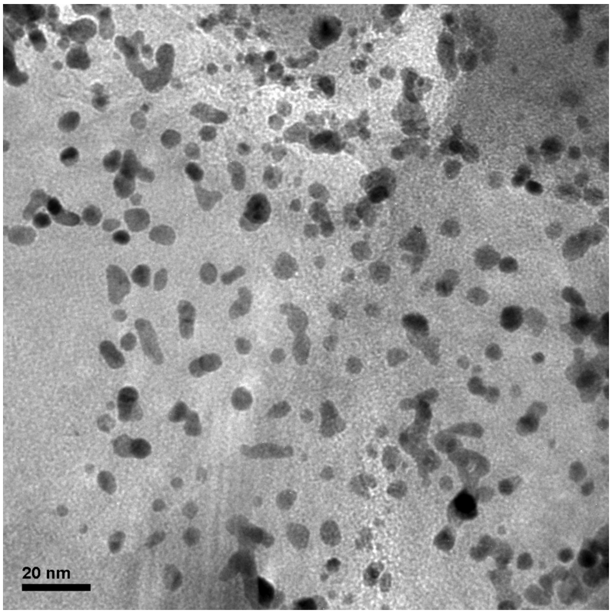

Fig. 2 – TEM images of the Pt/CNC catalyst.

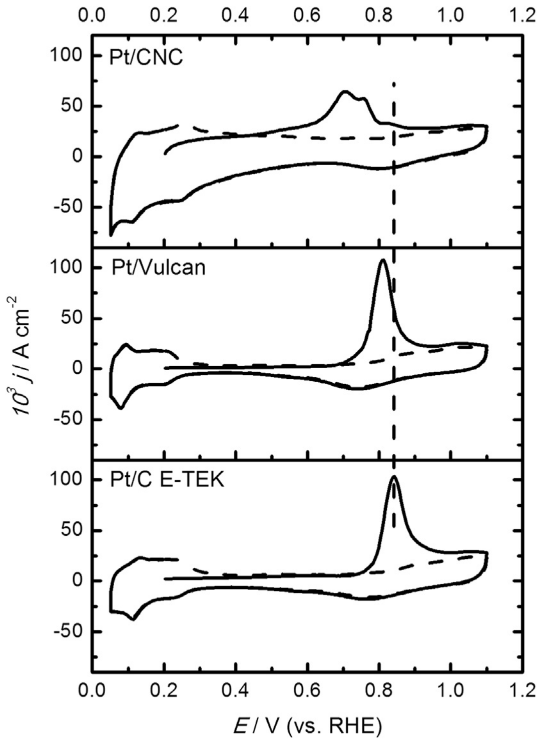

Fig. 3 – CO-stripping voltammograms for the Pt electrocatalysts in 0.5 M H_2SO_4. E_{ad} = 0.20 V; υ = 0.020 V s^{-1}; T = 25 °C.

temperature (a) and 40 °C (b), using the catalysts under study at the anode and the Pt commercial catalyst (E-TEK) at the cathode sides. Pt/CNC based MEA showed the best performance, even better than the MEA based on the commercial electrode (Pt/C E-TEK), because it gave lower polarization losses. Taking into account that all experiments were carried out in the same experimental system and using the same membrane, differences in the performance of electrodes may be attributed to the mesoporous structure of CNCs, which favours the triple-phase contact of reactant gas, catalyst, and the membrane, where the electrochemical reaction takes place [41,42]. Therefore, the least voltage drop with Pt/CNC based electrode may be associated to a more efficient use of metal particles. The larger amount of mesopores present in CNCs could promote the diffusion of reactants and products, and this is advantageous for their application in electrocatalysis.

As can be observed, at 0.60 V, an ohmic polarization regime dominates the activity of the catalyst; the current density (291 mA cm^{-2}) of the Pt/CNC catalyst is higher than those of Vulcan XC-72 supported catalyst (278 mA cm^{-2}) and the commercial carbon supported Pt catalyst (270 mA cm^{-2}), respectively. At this potential and as studied in Section 3.2, CNC based electrocatalysts already start to oxidise CO, whereas the electrocatalysts using Vulcan as support have not yet. The shift to a more negative potential by CO_{ads} oxidation on the electrocatalyst supported on CNCs, is a key parameter in their behaviour at the anode of a PEMFC.

At 40 °C, higher current and power densities were obtained, but the results follow the same trend.

Comparison with literature data is not easy due to the low platinum loading of the electrocatalysts used in this work. Andersen et al. reported current densities of 0.2 A cm^{-2} for fresh CNT and CNF Pt-supported catalyst at 70 °C [43]. Whereas Calvillo et al. obtained maximum power densities of 27 mW cm^{-2} at room temperature when using CMK-3 carbons as support [44]. However, for comparing these results with the literature data, it must be taken into account that not only the temperature and pressure conditions influence the shape of the polarization curves, but also the characteristics of the set-up system used for the measurements.

4. Conclusions

Carbon nanocoils have been proposed as an alternative material that could replace carbon blacks as electrocatalytic support for low temperature fuel cells. CNC were prepared by catalytic graphitization using a mixture of resorcinol-formaldehyde gel as the carbon precursor and a mixture of nickel-cobalt salts as the graphitization catalysts. The obtained material was used to prepare a Pt catalyst following the synthesis method of impregnation and subsequent reduction with sodium

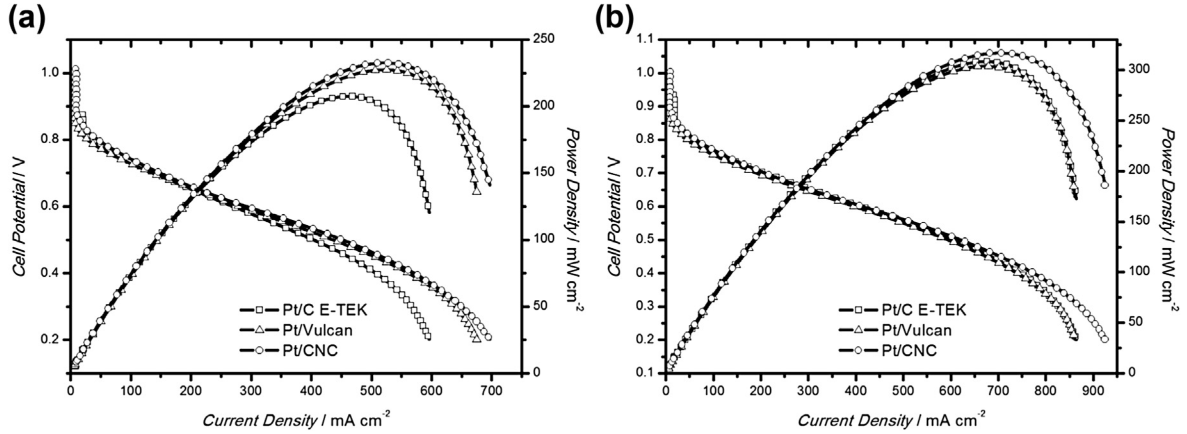

Fig. 4 – Comparison of the polarization curves and power densities obtained using the different Pt electrocatalyst at room temperature (a) and 40 °C (b) as anodes in a PEM fuel cell.

borohydride. The same method was used to prepare Vulcan supported electrocatalysts, in order to compare their performance with a Pt/C commercial catalyst from E-TEK.

The behaviour of the electrocatalysts on the anode side of a PEM fuel cell at room temperature and 40 °C was studied, and compared with a the commercial catalyst Pt/C E-TEK. Results showed better performance both at room temperature and 40 °C for the CNC-supported electrocatalysts. At 0.6 V, an increase of 4% in current density was observed at room temperature when CNCs were used as support material. Whereas the maximum power density was 13% higher for the Pt/CNC catalysts compared with Pt/C E-TEK. The higher electrocatalytic activity towards the anodic hydrogen oxidation is a consequence of its textural properties, like mesoporosity, and its higher tolerance to CO. This can be attributed to the carbon nanocoils used as catalyst support, which could alter the electronic structure of the metal, helping to the CO oxidation process.

These results are very promising, therefore, it can be concluded that CNCs are good candidates as support material for PEMFC and DMFC. The next step in the current investigations will be the preparation of bimetallic catalysts to improve the performances of these materials.

Acknowledgements

The authors gratefully acknowledge financial support given by the Ministry of Economy and Competitiveness through the Projects CTQ2011-28913-C02-01 and -02. V. Celorrio also acknowledges CSIC and FSE for their JAE Grant; and the UK National Academy by the support though the Newton International Fellow program.

REFERENCES

[1] Frackowiak E, Béguin F. Carbon materials for the electrochemical storage of energy in capacitors. Carbon 2001;39:937–50.

[2] Arico AS, Bruce P, Scrosati B, Tarascon J-M, van Schalkwijk W. Nanostructured materials for advanced energy conversion and storage devices. Nat Mater 2005;4:366–77.

[3] Wee J-H. Applications of proton exchange membrane fuel cell systems. Renew Sustain Energy Rev 2007;11:1720–38.

[4] Kamarudin MZF, Kamarudin SK, Masdar MS, Daud WRW. Review: direct ethanol fuel cells. Int J Hydrogen Energy 2013;38:9438–53.

[5] Kamarudin SK, Achmad F, Daud WRW. Overview on the application of direct methanol fuel cell (DMFC) for portable electronic devices. Int J Hydrogen Energy 2009;34:6902–16.

[6] Sergi F, Brunaccini G, Stassi A, Di Blasi A, Dispenza G, Aricò AS, et al. PEM fuel cells analysis for grid connected applications. Int J Hydrogen Energy 2011;36:10908–16.

[7] Antolini E, Salgado JRC, Gonzalez ER. The stability of Pt–M (M = first row transition metal) alloy catalysts and its effect on the activity in low temperature fuel cells: a literature review and tests on a Pt–Co catalyst. J Power Sources 2006;160:957–68.

[8] Álvarez G, Alcaide F, Cabot PL, Lázaro MJ, Pastor E, Solla-Gullón J. Electrochemical performance of low temperature PEMFC with surface tailored carbon nanofibers as catalyst support. Int J Hydrogen Energy 2012;37:393–404.

[9] Postole G, Auroux A. The poisoning level of Pt/C catalysts used in PEM fuel cells by the hydrogen feed gas impurities: the bonding strength. Int J Hydrogen Energy 2011;36:6817–25.

[10] Kim JW, Lim B, Jang H-S, Hwang SJ, Yoo SJ, Ha JS, et al. Size-controlled synthesis of Pt nanoparticles and their electrochemical activities toward oxygen reduction. Int J Hydrogen Energy 2011;36:706–12.

[11] Yu S, Lou Q, Han K, Wang Z, Zhu H. Synthesis and electrocatalytic performance of MWCNT-supported Ag@Pt core–shell nanoparticles for ORR. Int J Hydrogen Energy 2012;37:13365–70.

[12] Borup R, Meyers J, Pivovar B, Kim YS, Mukundan R, Garland N, et al. Scientific aspects of polymer electrolyte fuel cell durability and degradation. Chem Rev 2007;107:3904–51.

[13] Schmittinger W, Vahidi A. A review of the main parameters influencing long-term performance and durability of PEM fuel cells. J Power Sources 2008;180:1–14.

[14] Auer E, Freund A, Pietsch J, Tacke T. Carbons as supports for industrial precious metal catalysts. Appl Catal A Gen 1998;173:259–71.

[15] Smirnova A, Wender T, Goberman D, Hu Y-L, Aindow M, Rhine W, et al. Modification of carbon aerogel supports for PEMFC catalysts. Int J Hydrogen Energy 2009;34:8992–7.

[16] Ambrosio EP, Francia C, Manzoli M, Penazzi N, Spinelli P. Platinum catalyst supported on mesoporous carbon for PEMFC. Int J Hydrogen Energy 2008;33:3142–5.

[17] Antolini E. Carbon supports for low-temperature fuel cell catalysts. Appl Catal B Environ 2009;88:1–24.

[18] Kim M, Park J-N, Kim H, Song S, Lee W-H. The preparation of Pt/C catalysts using various carbon materials for the cathode of PEMFC. J Power Sources 2006;163:93–7.

[19] Yu X, Ye S. Recent advances in activity and durability enhancement of Pt/C catalytic cathode in PEMFC: Part I. Physico-chemical and electronic interaction between Pt and carbon support, and activity enhancement of Pt/C catalyst. J Power Sources 2007;172:133–44.

[20] Hall SC, Subramanian V, Teeter G, Rambabu B. Influence of metal–support interaction in Pt/C on CO and methanol oxidation reactions. Solid State Ionics 2004;175:809–13.

[21] Inoue M, Akamaru S, Taguchi A, Abe T. Physical and electrochemical properties of Pt–Ru/C samples prepared on various carbon supports by using the barrel sputtering system. Vacuum 2008;83:658–63.

[22] Bezerra CWB, Zhang L, Liu H, Lee K, Marques ALB, Marques EP, et al. A review of heat-treatment effects on activity and stability of PEM fuel cell catalysts for oxygen reduction reaction. J Power Sources 2007;173:891–908.

[23] Shao Y, Yin G, Zhang J, Gao Y. Comparative investigation of the resistance to electrochemical oxidation of carbon black and carbon nanotubes in aqueous sulfuric acid solution. Electrochim Acta 2006;51:5853–7.

[24] Wikander K, Ekström H, Palmqvist AEC, Lundblad A, Holmberg K, Lindbergh G. Alternative catalysts and carbon support material for PEMFC. Fuel Cells 2006;6:21–5.

[25] Hyeon T, Han S, Sung Y-E, Park K-W, Kim Y-W. High-performance direct methanol fuel cell electrodes using solid-phase-synthesized carbon nanocoils. Angew Chem Int Ed 2003;42:4352–6.

[26] Marie J, Berthon-Fabry S, Achard P, Chatenet M, Pradourat A, Chainet E. Highly dispersed platinum on carbon aerogels as supported catalysts for PEM fuel cell-electrodes: comparison of two different synthesis paths. J Non Cryst Solids 2004;350:88–96.

[27] Calvillo L, Lázaro MJ, García-Bordejé E, Moliner R, Cabot PL, Esparbé I, et al. Platinum supported on functionalized ordered mesoporous carbon as electrocatalyst for direct methanol fuel cells. J Power Sources 2007;169:59–64.

[28] Celorrio V, Calvillo L, Martinez-Huerta MV, Moliner R, Lazaro MJ. Study of the synthesis conditions of carbon nanocoils for energetic applications. Energy Fuels 2010;24:3361–5.

[29] Celorrio V, Calvillo L, Pérez-Rodríguez S, Lázaro MJ, Moliner R. Modification of the properties of carbon nanocoils by different treatments in liquid phase. Micropor Mesopor Mater 2011;142:55–61.

[30] Salgado JRC, Antolini E, Gonzalez ER. Structure and activity of carbon-supported Pt–Co electrocatalysts for oxygen reduction. J Phys Chem B 2004;108:17767–74.

[31] Zhou J-H, He J-P, Ji Y-J, Dang W-J, Liu X-L, Zhao G-W, et al. CTAB assisted microwave synthesis of ordered mesoporous carbon supported Pt nanoparticles for hydrogen electro-oxidation. Electrochim Acta 2007;52:4691–5.

[32] Li W, Zhou W, Li H, Zhou Z, Zhou B, Sun G, et al. Nano-stuctured Pt–Fe/C as cathode catalyst in direct methanol fuel cell. Electrochim Acta 2004;49:1045–55.

[33] Calvillo L, Celorrio V, Moliner R, Garcia AB, Caméan I, Lazaro MJ. Comparative study of Pt catalysts supported on different high conductive carbon materials for methanol and ethanol oxidation. Electrochim Acta 2013;102:19–27.

[34] Salgado JRC, Quintana JJ, Calvillo L, Lazaro MJ, Cabot PL, Esparbe I, et al. Carbon monoxide and methanol oxidation at platinum catalysts supported on ordered mesoporous carbon: the influence of functionalization of the support. PCCP 2008;10:6796–806.

[35] Antolini E, Salgado JRC, Santos LGRA, Garcia G, Ticianelli EA, Pastor E, et al. Carbon supported Pt–Cr alloys as oxygen-reduction catalysts for direct methanol fuel cells. J Appl Electrochem 2006;36:355–62.

[36] Celorrio V, Plana D, Florez J, Montes-de-Oca M, Moore A, Lázaro MJ, et al. Methanol oxidation at diamond-Supported Pt nanoparticles: effect of the diamond surface termination. J Phys Chem C 2013;117:21735–42.

[37] Maillard F, Eikerling M, Cherstiouk OV, Schreier S, Savinova E, Stimming U. Size effects on reactivity of Pt nanoparticles in CO monolayer oxidation: the role of surface mobility. Faraday Discuss 2004;125:357–77.

[38] Hayden BE, Pletcher D, Suchsland J-P, Williams LJ. The influence of support and particle size on the platinum catalysed oxygen reduction reaction. PCCP 2009;11:9141–8.

[39] Cherstiouk OV, Simonov PA, Savinova ER. Model approach to evaluate particle size effects in electrocatalysis: preparation and properties of Pt nanoparticles supported on GC and HOPG. Electrochim Acta 2003;48:3851–60.

[40] Guerin S, Hayden BE, Lee CE, Mormiche C, Owen JR, Russell AE, et al. Combinatorial electrochemical screening of fuel cell electrocatalysts. J Comb Chem 2003;6:149–58.

[41] Scherer GG. Interfacial aspects in the development of polymer electrolyte fuel cells. Solid State Ionics 1997;94:249–57.

[42] O'Hayre R, Barnett DM, Prinz FB. The triple phase boundary: a mathematical model and experimental investigations for fuel cells. J Electrochem Soc 2005;152. A439–AA44.

[43] Andersen SM, Borghei M, Lund P, Elina Y-R, Pasanen A, Kauppinen E, et al. Durability of carbon nanofiber (CNF) & carbon nanotube (CNT) as catalyst support for Proton Exchange Membrane Fuel Cells. Solid State Ionics 2013;231:94–101.

[44] Calvillo L, Gangeri M, Perathoner S, Centi G, Moliner R, Lázaro MJ. Synthesis and performance of platinum supported on ordered mesoporous carbons as catalyst for PEM fuel cells: effect of the surface chemistry of the support. Int J Hydrogen Energy 2011;36:9805–14.

INTERNATIONAL JOURNAL OF HYDROGEN ENERGY 39 (2014) 3964–3969

Available online at www.sciencedirect.com

SciVerse ScienceDirect

journal homepage: www.elsevier.com/locate/he

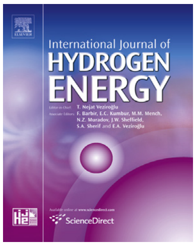

Macroporous carbon as support for PtRu catalysts

Angélica M. Baena-Moncada [a], Rusbel Coneo-Rodríguez [a], Juan C. Calderón [b], Jonathan Flórez-Montaño [b], Cesar A. Barbero [a], Gabriel A. Planes [a], José L. Rodríguez [b], Elena Pastor [b,*]

[a] Universidad Nacional de Río Cuarto, Ruta Nac. 36, Km. 601, X5804BYA Río Cuarto, Argentina
[b] Departamento de Química Física, Instituto de Materiales y Nanotecnología, Universidad de La Laguna, Avenida Astrofísico F. Sánchez S/N, 38071 La Laguna, Tenerife, Spain

ARTICLE INFO

Article history:
Received 10 April 2013
Received in revised form
17 June 2013
Accepted 18 June 2013
Available online 20 July 2013

Keywords:
Macroporous porous carbon
Direct methanol fuel cells
Methanol electro-oxidation
PtRu electrocatalysts
Differential electrochemical mass spectrometry

ABSTRACT

A high surface macroporous porous carbon (MPC) has been obtained by SiO_2 nanoparticles template and further used as support for PtRu catalysts. MPC supported PtRu materials show an enhanced activity for methanol electrooxidation when compared with commercial catalysts. This observation is discussed in terms of reactant accessibility to active sites. The improved diffusion through the porous matrix influences not only methanol feeding, but also removal of reaction subproducts, as clearly shown by differential electrochemical mass spectrometry (DEMS).

1. Introduction

An efficient metal utilization in direct methanol fuel cell (DMFC) anodes requires a high dispersion of small metal nanoparticles (NP) over the surface of a conductive material. In the practice, this situation results in a high porous matrix composed by the supporting material and the catalyst. Far away from an ideal situation, the access to electrocatalyst active sites is partially hindered (or blocked) by the support, affecting severely the mass transfer rate. This effect acts in detriment of anode performance. Therefore, some transport conditions must be fulfilled by the support: it should provide appropriated fuel access to metal active sites, followed by adequate elimination of reaction products.

On the other hand, it has been shown that the morphology of the electrode material determines the performance of catalysts used in DMFC [1–5]. The dependence of the reaction mechanism (i.e. the occurrence of alternative pathways) on the mass transfer phenomena was clearly established by Z. Jusys et al. [6]. These authors demonstrated that electrochemical efficiencies, product distribution and turnover frequencies (TOF) of reactions occurring during the methanol electrooxidation (formation of formaldehyde, formic acid and CO_2), depend strongly on the catalyst loading.

Recently, we have studied the methanol oxidation on mesoporous Pt (MPPt) applying thin-layer flow-cell differential electrochemical mass spectrometry (TLFC-DEMS) [5]. It was concluded that, under restricted diffusion of the soluble

---

* *Corresponding author*. Tel.: +34 679437939; fax: +34 922318033.
E-mail address: epastor@ull.es (E. Pastor).

http://dx.doi.org/10.1016/j.ijhydene.2013.06.085

methanol electrooxidation products (i.e. formic acid and formaldehyde), as occurs in real carbon supported catalysts, these species can interact again with the catalytic surface and readsorb, increasing the CO_2 efficiency. However, in these conditions the current density diminishes noticeably.

Like metals [4], carbon-based porous support can be specifically designed for the improvement of mass transport. With this purpose, the electrodes must have an interconnected porous matrix, with the porous dimension adjusted at a point between two divergent trends: the highest surface area and the larger pore size.

In the present paper, a macroporous carbon (MPC) obtained by SiO_2 template is used as support for PtRu nanoparticles. These NP are attached on the MPC surface via chemical reduction of a mixture of Pt^{+4}/Ru^{+3} by the formiate ions method (SFM method [7]). The catalysts activity towards methanol electrooxidation is tested by cyclic voltammetry, chronoamperometry and TLFC-DEMS techniques.

2. Experimental

2.1. SiO_2 template, carbon support and catalysts: synthesis and characterization

The synthesis of the mesoporous carbon was recently described [8]. Briefly, SiO_2 NP of 400 nm in diameter were synthesized by TEOS hydrolysis in basic media [9] and further used as molds. Whit this purpose, SiO_2 NP were deposited by vertical sedimentation in the bottom of a vial [10]. After solvent evaporation, the resulting opal was expelled out of the vial and then treated at 600°°C or 1000 °C (sample K and I, respectively) for 4 h to form a connected opal. Those opals were later impregnated with the carbon precursor: a mixture of resorcinol (1 g), formaldehyde (1.6 mL) and sodium carbonate (0.4 mL 0.1 M). The resin-SiO_2 compound was dried in oven (105 °C) and then pyrolyzed at 850 °C in the absence of O_2 for a 24 h period. The SiO_2 pattern was then removed by treating the samples with fluorhydric acid solution.

The MPC was loaded (20% metal) with PtRu NP using the formiate ions method [7], adding the metal precursors solution (H_2PtCl_6 and $RuCl_3$, Sigma–Aldrich) to the carbon support impregnated with 2.0 M HCOOH solution. The pH was previously adjusted to 12.0. This dispersion was heated at 80 °C under stirring, keeping the temperature constant during the addition of the metal salts solution. Reaction mixture was kept under stirring for 12 h at room temperature, and finally the mixture was filtered, washed and dried at 60 °C for 2 h.

The diameters of the SiO_2 NP were determined by dynamic light scattering (DLS, Malvern 4700 with goniometer and 7132 correlator) with an argon-ion laser operating at 488 nm. All measurements were made at the scattering angle of 90°. FIB-SEM images were done with a dual beam system Strata DB235 (FEI Company), following the procedure as described elsewhere [11]. BET surface area, micropore area and pore volume were obtained with a Micrometrics ASAP 2020 instrument. Metal content and PtRu atomic ratios of the synthesized catalysts were determined by Energy Dispersive X-Ray Analysis (EDX), using an Oxford Instruments Microanalysis Group 6699 ATW scanning electron microscope at 20 kV, with a Si detector and a Be window. XRD patterns of synthesized catalysts were obtained using a Universal Diffractometer Panalytical X'Pert X-ray, operating with a Cu-Kα radiation generated at 40 kV and 30 mA. Scans were done at 3° min^{-1} for 2θ values between 20 y 100°. Metal crystallite size [12] and lattice parameters [13] were calculated using the dimensions of peak (220), Scherrer's equation and Vergard's Law.

2.2. Electrochemical characterization

Electrochemical experiments were carried out in a thermostatized three electrodes electrochemical cell, using a hydrogen reference electrode in the electrolyte solution (RHE) as the reference. All potentials in this work are given against the RHE. A small piece of high surface carbon was used as auxiliary electrode. In this study, the working electrode consists of a certain amount of the PtRu/MPC or commercial PtRu/C E-TEK deposited as a thin layer over a glassy carbon disc (ϕ = 3 mm). For this purpose, an aqueous suspension of 4.0 mg mL^{-1} of the PtRu/MPC or PtRu/C E-TEK catalyst was prepared by ultrasonically dispersing it in a solution of 15 μL of Nafion (5 wt.%, Aldrich) in 0.5 mL of MilliQ water. An aliquot (20 μL) of the dispersed suspension was pipetted on the glassy carbon surface and dried at ambient temperature under Ar atmosphere. The currents are expressed as current densities J (A cm^{-2}), calculated from the measured current I (A) and the real electroactive area S (cm^2). S was estimated from CO (N47) stripping experiments. Electrochemical measurements were performed with a PC controlled Autolab PGSTAT30 potentiostat–galvanostat. All reagents were of analytical grade. Argon (N50) was bubbled through the solution to avoid dissolved oxygen.

2.3. DEMS characterization

Differential electrochemical mass spectrometry (DEMS) was used to detect volatile and gaseous products generated during the methanol electro-oxidation. Several DEMS designs have been described in details in previous publications [14,15]. For the experiments described in the present work, the electrochemical cell was connected to the chamber containing the quadrupole mass spectrometer (PFEIFFER VACUUM QMS 200). A rotary vane pump evacuates the latter, whereas the vacuum in the chamber containing the mass spectrometer is obtained from a turbomolecular pump. A DEMS cell has been described in previous papers [4,5], which works under reactant flow and allows simultaneous detection of faradaic current and gaseous species produced on the electroactive surface by means of mass spectrometry. Conventional three-electrodes arrangement was employed with a RHE prepared in the supporting electrolyte and a graphite stick as the counter-electrode. The working electrode was a gas diffusion electrode composed of a thin layer of the metal/MPC catalyst deposited over a gas diffusion layer (carbon black coated carbon cloth), which acts as interface between the electrolyte and the vacuum system, contacted with a gold wire.

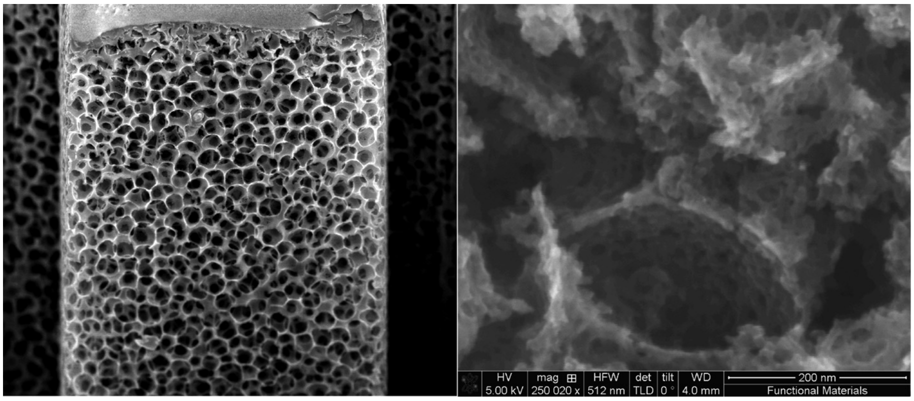

Fig. 1 – FIB-SEM image of MPC-K.

3. Results and discussion

3.1. *MPC carbon characterization*

DLS experiments show a SiO_2 NP diameter of ca. 400 nm, with a polidispersity index of 0.0327 (≈3%) [8]. As result of NP sedimentation and subsequent oven treatment at 600 (K) or 1000 °C (I), a white solid is obtained. After impregnation and posterior pyrolysis, the resulting blue–green solid composed of SiO_2 and carbon is exposed to concentrated fluorhydric acid (50%) for 48 h. A typical SEM image of the resulting carbon matrix (named MPC-K due "K" template) is given in Fig. 1. This material presents a BET surface area of 102 m^2/g with 64 m^2/g micropore area and 0.053 cm^3/g volume of pores. The SEM image in Fig. 1 left shows the cross section of a mesoporous carbon microparticle (cut in the SEM chamber with the aid of a focused ion beam). It is observed that the result of this chemical etching is a macroporous carbon inverse opal possessing interconnected "vesicles". In a further increase of the magnification (Fig. 1 right), the vesicle reveals the mesoporous nature of the pore wall. As it was recently discussed in a previous paper, the macropores are due to the template effect of the hard silica spheres, while the mesoporosity seems to be related to the cracks produced in the carbon due to restricted contraction. The whole process produces a carbon material with hierarchical porous structure [8]. Those high surface porous microparticles will be the support for the PtRu NP deposition.

The electrochemical study of this carbon material (Fig. 2A) reveals the existence of a high electroactive surface area (ESA), capable to provide capacitive currents with values around 0.3–0.4 Ag^{-1} (cycling at 5 mV/s) in 1 M H_2SO_4. From these values, a surface electroactive area around 700–900 m^2/g can be roughly estimated (based on 15 mF cm^{-2}) [16]. These values are in good agreement with the existence of a porous carbon mesh, which connects the inner surface of the microparticles with the external electrolytic medium.

3.2. *PtRu/MPC characterization*

After the PtRu NP deposition in MPC-I and MPC-K, the metal content and Pt:Ru atomic ratio were determined by EDS

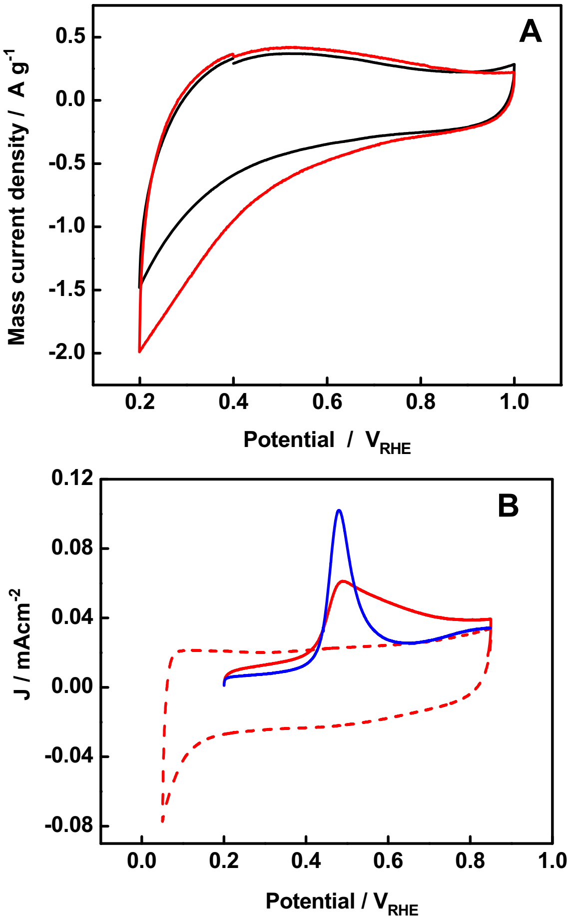

Fig. 2 – (A) Cyclic voltammogram of the porous carbon at 5 mV/s, 1 M H_2SO_4. MPC-I (dashed line) and MPC-K (solid line). T = 25 °C. (B) Cyclic voltammogram for PtRu/MPC-I (dashed red line), and CO stripping for PtRu/MPC-I (red line) and PtRu/MPC-K (blue line). E_{ad} = 0.2 V_{ERH}, υ = 20 mV/s, 1 M H_2SO_4. T = 25 °C. (For interpretation of the references to color in this figure legend, the reader is referred to the web version of this article.)

analysis. All catalysts present a metal loading around the nominal value of 20% (27, 23 and 20 for MOC-I, MOC-K and E-TEK, respectively). The composition of PtRu/MPC-K and PtRu/C E-TEK was 45:55 for Pt:Ru ratio (similar to the nominal 50:50), whereas PtRu/MPC-I catalyst exhibits higher Ru content (32:68 for Pt:Ru ratio). XRD patterns of the synthesized materials (not shown, see Supplementary Information) present characteristic peaks corresponding to the (111), (200) and (220) planes of the face centered cubic (fcc) structure of Pt, as well as a diffraction peak around 24° for PtRu/C E-TEK, which corresponds to the (002) reflection of graphite basal planes of the carbon support. The absence of this peak in synthesized catalysts indicates a low graphitization degree of the MPC used as support. Metal average crystallite size and lattice parameters were determined from (220) reflection peak (3.8 and 3.901 nm for PtRu/MPC-I and 4.9 and 3.905 nm for PtRu/MPC-K, respectively). These values are closed to those for the commercial E-TEK material (4.4 and 3.898 nm).

As shown in Fig. 2B (dashed red line), the addition of PtRu to the MPC changes notoriously the aspect of the cyclic voltammograms (CVs), especially in the interval from 0.05 V to 0.4 V_{RHE}. The curves recorded are characteristic for low-loaded carbon supported PtRu materials [17]. Looking for a more precise characterization of the catalyst surface, CO stripping experiments was performed.

The oxidation of an adsorbed CO monolayer (CO_{ad}) gives an estimation of the final electroactive area. The metal surface area, calculated assuming 420 μC/cm for CO stripping, is close to 48 $m^2\ g^{-1}$ for PtRu/MPC-I and 36 $m^2\ g^{-1}$ for PtRu/MPC-K. These surface values are lower than that obtained recently with the same support (MPC-K), but using a different modification of the formic acid method for fixing the PtRu nanoparticles inside the carbon support [8]. Probably, the method of synthesis influences the degree of agglomeration, finally determining the metal surface area.

As can be deduced from a simple inspection of Fig. 2B, the presence of Ru shifts the onset and the peak position of the CO electrooxidation toward more negative potentials, when compared with Pt [5]. Note that the shape of the CO stripping peak is more symmetric for PtRu/MPC-K than for PtRu/MPC-I. It is well known that sulfate adsorbs strongly on Pt surface [14], so the observed current tail in PtRu/MPC-I can be attributed to a stronger sulfate adsorption on this catalyst surface, which blocks the CO diffusion towards the most catalytic sites. The different content of Pt and Ru in these catalysts could also have an influence on the CO oxidation peak. However, it is interesting to remark that this effect is also observed for 20 wt.% PtRu/C E-TEK [3,18], but absent for the PtRu/MPC-K sample (both catalysts with the same Pt:Ru atomic ratio). This result suggests that the support structure is also conditioning the catalytic response modifying the surface environment of the reactive adsorbed molecule.

A further way to test the synthesized catalysts activity involves the chronoamperometric measurement of current densities (A cm^{-2}) for methanol oxidation at 60 °C. The response of each electrode to a potential step from 0.05 V (a potential where methanol adsorption and oxidation are negligible) to 0.55 V (a potential similar to that achieved during operation conditions in a fuel cell) can be seen in Fig. 3.

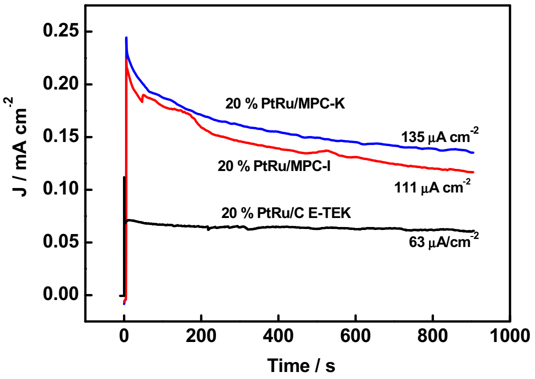

Fig. 3 – Current transients for methanol electrooxidation on PtRu/MPC-K (blue line), PtRu/MPC-I (red line), and PtRu/C E-TEK (black line) at 0.55 V_{RHE}, 1 M CH_3OH + 1 M H_2SO_4. T = 60 °C. (For interpretation of the references to color in this figure legend, the reader is referred to the web version of this article.)

Commercial carbon supported PtRu catalyst (20 wt.% PtRu/C E-TEK) was also tested for the sake of comparison. A catalytic enhancement becomes clear from the recorded curves: the catalytic activity towards methanol oxidation at $t = 900$ s is twice higher for PtRu/MPC (0.135 mA cm^{-2} and 0.111 mA cm^{-2} for K and I supports, respectively) than for PtRu/C E-TEK (0.063 mA cm^{-2}) at the same experimental conditions. For the catalysts studied here, it is assumed that most of the PtRu NP are anchored to the internal porous surface of the carbon grain. This hypothesis is based on the statement that the external surface area ($cm^2\ g^{-1}$) is very small for granular porous carbon (grain size 5–50 μm). On the other hand, considering the carbon black structure, it can be assumed that the majority of the PtRu NP in the commercial catalyst are attached over the external surface of the support. Taken in mind this fact, it is noteworthy that metal NP supported inside a granular porous-carbon are able to improve catalysts activity, measured as current density for methanol electrooxidation, with respect to the catalysts NP supported on the external surface of carbon nanoparticles.

3.3. *DEMS characterization*

For quantitative detection of the CO_2 generated during methanol oxidation, experiments were carried out to calibrate the DEMS system (Fig. 4), calculating the mass spectrometer constant for the production of CO_2, k^{CO_2}. Further details for these calculations are given in previous works [4,5]. CVs and mass spectrometer cyclic voltammograms (MSCVs) related to the production of CO_2 ($m/z = 44$) during the electrooxidation of a CO adsorbed monolayer on PtRu/MPC-I and PtRu/MPC-K were simultaneously recorded (red and blue curves) at 5 mV/s. The curves confirm the onset for CO oxidation as described above. Similar experiments were performed adsorbing CO at commercial catalyst PtRu/C E-TEK (black curves) in order to compare the results.

The curves for methanol oxidation on PtRu/MPC-I in 2 M CH_3OH + 0.5 M H_2SO_4 solution and the corresponding

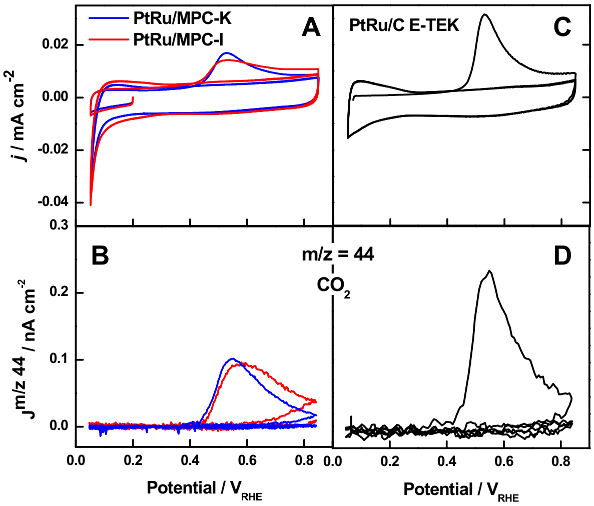

Fig. 4 – CVs (A, C) and MSCVs (B, D) for CO_2 ($m/z = 44$) during the stripping of CO monolayer at PtRu/MPC-I (dashed line) and PtRu/MPC-K (solid line) (A, B) and PtRu/C E-TEK (C, D). $E_{ad} = 0.20$ V; $v = 5$ mV/s; 0.5 M H_2SO_4. $T = 25$ °C.

successive recorded MSCVs for $m/z = 44$ (corresponding to the electrooxidation of methanol to CO_2) and $m/z = 60$ (corresponding to the production of formic acid which is detected as methylformate) at room temperature are displayed in Fig. 5. Then, it is concluded that during the methanol oxidation, CO_2 and methylformate were on-line detected by mass spectrometry. Methylformate is formed through the chemical reaction between methanol and electrochemically formed formic acid. From Fig. 6, it is established that the oxidation to CO_2 starts first and the onset for formic acid production is shifted approx. 50 mV to more positive potentials, once part of active surface sites becomes free from adsorbed species. Note that Fig. 5 makes use of a non-conventional way to show the information obtained from DEMS. The employment of time in the x axis has been chosen with the aim to show in a clear way the time delay between CO_2 and methylformate generation.

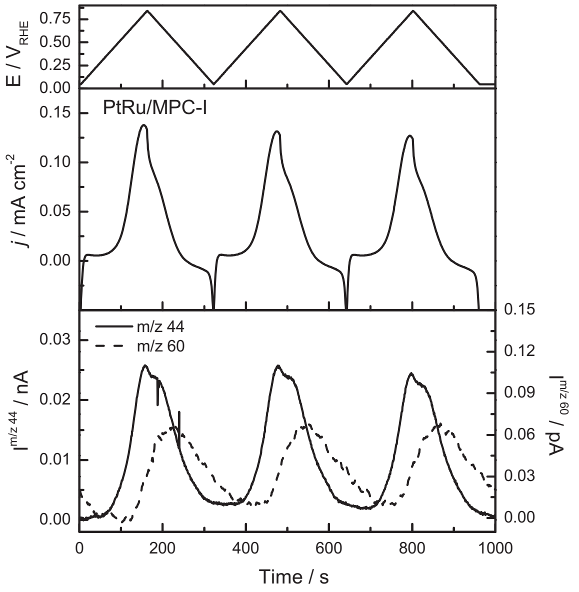

Fig. 5 – Potential program for methanol electrooxidation on PtRu/MPC-I (up), current density (middle) and MSCVs for CO2 ($m/z = 44$) and $HCOOCH_3$ ($m/z = 60$) (down). $E_{ad} = 0.20$ V; $v = 5$ mV/s; 2 M CH_3OH + 0.5 M H_2SO_4. $T = 25$ °C.

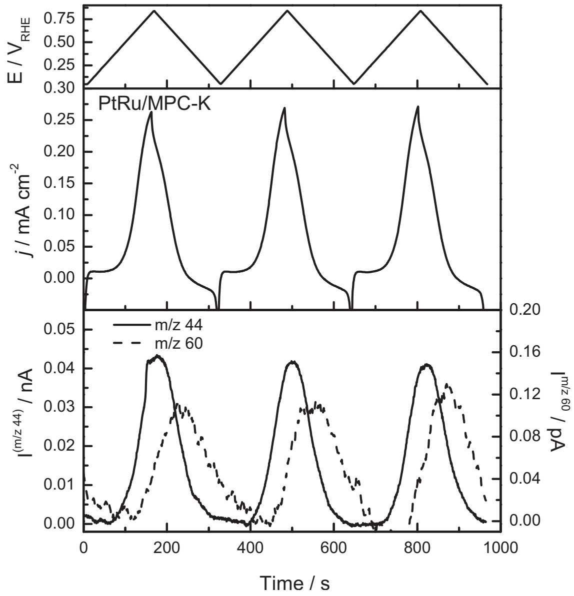

Fig. 6 – Potential program for methanol electrooxidation on PtRu/MPC-K (up), current density (middle) and MSCVs for CO2 ($m/z = 44$) and $HCOOCH_3$ ($m/z = 60$) (down). $E_{ad} = 0.20$ V; $v = 5$ mV/s; 2 M CH_3OH + 0.5 M H_2SO_4. $T = 25$ °C.

After calibrating the DEMS setup, the current efficiency for CO_2 can be determined. The conversion efficiency E^{CO_2} for methanol electrooxidation to CO_2 can be calculated by the equation [4,5]:

$$E^{CO_2} = \frac{6 \times Q_i^{CO_2}}{k^{CO_2} \times Q_f^T}$$

where Q_i is the ionic charge involved in the curve recorded for $m/z = 44$ during methanol electrooxidation, and Q_f the corresponding faradaic charge. In the case of PtRu/MPC-I a value of 80% was calculated for the efficiency to CO_2.

Similarly, Fig. 6 shows the curves obtained during the electrooxidation of methanol on PtRu/MPC-K. Similar behavior was also observed for this catalyst with higher currents than PtRu/MPC-I but with conversion efficiency to CO_2 of 55%. Comparing the results for the materials prepared in the present work with the commercial catalyst PtRu/C E-TEK (not shown), it can be established that the commercial one presents current densities and conversion efficiency (84%) quite similar to the PtRu/MPC-I catalyst (80%). In contrast, for the PtRu/MPC-K material, the conversion efficiency to CO_2 is visibly lower (55%) and the current density noticeably higher than the other two. Again, the effect of the higher Ru content in PtRu/MPC-I is not determining the results, as Ru cannot oxidize methanol at room temperature but this catalyst shows higher efficiencies to CO_2.

The higher current developed by the PtRu/MPC-K catalysts during the methanol oxidation is originated, in a first stage, by the faster elimination of the adsorbed CO, as shown in Fig. 2B. Another possible cause is the improved condition for reactant and products diffusion through the porous layer of catalysts. Moreover, the decrease at the conversion efficiency from methanol to CO_2, together with the intensification of the metylformate signal, suggests that the reaction is mainly enhanced by the existence of alternative paths for methanol electrooxidation to formic acid, which do not involves the formation of adsorbed CO [2,5]. In addition, it was observed a better performance for the PtRu/MPC-K that the PtRu/MPC-I toward the methanol oxidation, indicating that the temperature during the preparation of the carbon materials has also an influence in the final behavior of the electrocatalysts.

4. Conclusions

PtRu catalysts were prepared using a high surface macroporous porous carbon (MPC) as support. The carbonaceous material has been obtained using SiO_2 nanoparticles as template and presents a high surface area and interconnected pores with hierarchical distribution. Highest activity for methanol electrooxidation was obtained for the PtRu catalyst prepared with the MPC synthesized at 600 °C (PtRu/MPC-K). This activity can be explained, in general, by the improved diffusion through the porous matrix for MPCs supported PtRu, and in particular, taking into account the fast CO oxidation observed for this material.

Acknowledgments

Authors thank the MINECO (Spain, project CTQ2011-28913-C02-02) and ANPCyT (Argentine, project PICT-2010-2421) for financial support AECID for sustaining the cooperation between both universities (PCI A/3040514/11). C.A.B. and G.A.P. are permanent research fellow of CONICET. J.F. acknowledges ACIISI (Gobierno de Canarias) for the predoctoral fellowship. M. Bruno is acknowledged fir the BET, micropore surface area and pore volume measurements.

Appendix A. Supplementary data

Supplementary data related to this article can be found at http://dx.doi.org/10.1016/j.ijhydene.2013.06.085.

REFERENCES

[1] Wang H, Wingender C, Baltruschat H, Lopez M, Reetz MT. Methanol oxidation on Pt, PtRu, and colloidal Pt electrocatalysts: a DEMS study of product formation. J Electroanal Chem 2001;509:163–9.

[2] Wang H, Loffler T, Baltruschat H. Formation of intermediates during methanol oxidation: a quantitative DEMS study. J Appl Electrochem 2001;31:759–65.

[3] Yu JS, Kang S, Yoon SB, Chai G. Fabrication of ordered uniform porous carbon networks and their application to a catalyst supporter. J Am Chem Soc 2002;124:9382–3.

[4] Planes GA, García G, Pastor E. High performance mesoporous Pt electrode for methanol electrooxidation. A DEMS study. Electrochem Commun 2007;9:839–44.

[5] García G, Florez-Montaño J, Hernandez-Creus A, Pastor E, Planes GA. Methanol electrooxidation at mesoporous Pt and Pt–Ru electrodes: a comparative study with carbon supported materials. J Power Sources 2011;196:2979–86.

[6] Jusys Z, Kaiser J, Behm RJ. Methanol electrooxidation over Pt/C fuel cell catalysts: dependence of product yields on catalyst loading. Langmuir 2003;19:6759–69.

[7] dos Santos L, Colmati F, Gonzalez ER. Preparation and characterization of supported Pt–Ru catalysts with a high Ru content. J Power Sources 2006;159:869–77.

[8] Baena-Moncada AM, Planes GA, Moreno MS, Barbero CA. A novel method to produce a hierarchical porous carbon as a conductive support of PtRu particles. Effect on CO and methanol electrooxidation. J Power Sources 2013;221:42–8.

[9] Wang W, Gu B, Liang L, Hamilton W. Fabrication of two- and three-dimensional silica nanocolloidal particle arrays. J Phys Chem B 2003;107:3400–4.

[10] Velev OD, Lenhoff AM. Colloidal crystals as templates for porous materials. Curr Opin Colloid Interface Sci 2000;5:56–63.

[11] Jiménez-Piqué E, Ramos A, Muñoz-Tabares JA, Hatton A, Soldera F, Mücklich F, et al. Focused ion beam tomography of zirconia degraded under hydrothermal conditions. J Eur Ceram Soc 2012;32:2129–36.

[12] Warren BE. X-ray diffraction. 1st ed. Mineola: Addison-Wesley Publishing Co; 1969.

[13] Gasteiger HA, Ross Jr PN, Cairns EJ. LEIS and AES on sputtered and annealed polycrystalline PteRu bulk alloys. Surf Sci 1993;293:67–80.

[14] Baltruschat H. Differential electrochemical mass spectrometry. J Am Soc Mass Spectrom 2004;15:1693–706.

[15] Wang H, Alden LR, DiSalvo FJ, Abruña HD. Methanol electrooxidation on PtRu bulk alloys and carbon-supported PtRu nanoparticle catalysts: a quantitative DEMS study. Langmuir 2009;25:7725–35.

[16] Zhao X, Tian H, Zhu M, Tian K, Wang JJ, Kang F, et al. Carbon nanosheets as the electrode material in supercapacitors. J Power Sources 2009;194:1208–12.

[17] Salgado JRC, Alcaide F, Álvarez G, Calvillo L, Lázaro MJ, Pastor E. Pt-Ru electrocatalysts supported on ordered mesoporous carbon for direct methanol fuel cell. J Power Sources 2010;195:4022–9.

[18] Kolics A, Wieckowski A. Adsorption of bisulfate and sulfate anions on a Pt(111) electrode. J Phys Chem B 2001;105:2588–95.

Journal of Power Sources 296 (2015) 290–297

Contents lists available at ScienceDirect

Journal of Power Sources

journal homepage: www.elsevier.com/locate/jpowsour

Enhanced formic acid oxidation on polycrystalline platinum modified by spontaneous deposition of gold. Fourier transform infrared spectroscopy studies

Paula S. Cappellari [a], Gonzalo García [b], Jonathan Florez-Montaño [b], Cesar A. Barbero [a], Elena Pastor [b], Gabriel A. Planes [a, *]

[a] *Universidad Nacional de Río Cuarto. RutaNac. 36, Km 601, Río Cuarto, Córdoba, Argentina*
[b] *Instituto Universitario de Materiales y Nanotecnología, Universidad de La Laguna, Av. Astrofísico F. Sánchez s/n, 38071 La Laguna, Tenerife, Spain*

HIGHLIGHTS

- The Pt surface was modified by spontaneous (electroless) deposition of gold atoms.
- Two reaction pathways are clearly identified for HCOOH electro-oxidation on Pt and PtAu.
- HCOOH oxidation on Pt surfaces prefers the indirect route (dehydration).
- The direct pathway (dehydrogenation) for HCOOH oxidation is favored at PtAu electrodes.
- The performance toward the HCOOH oxidation is greatly enhanced by PtAu electrodes.

ARTICLE INFO

Article history:
Received 11 February 2015
Received in revised form
15 May 2015
Accepted 3 July 2015
Available online xxx

Keywords:
Formic acid
PtAu
Electroless
In-situ FTIR

GRAPHICAL ABSTRACT

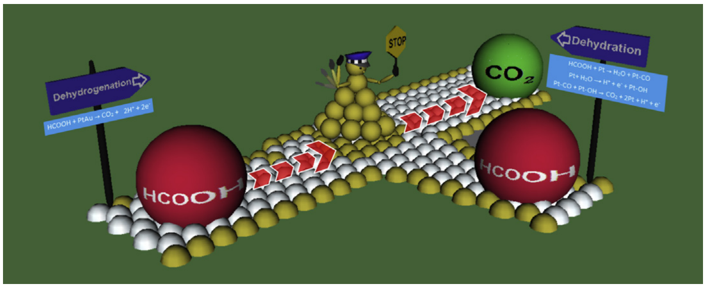

ABSTRACT

Formic acid and adsorbed carbon monoxide electrooxidation on polycrystalline Pt and Au-modified Pt surfaces were studied by cyclic voltammetry, lineal sweep voltammetry and *in-situ* Fourier transform infrared spectroscopy techniques. With this purpose, a polycrystalline Pt electrode was modified by spontaneous deposition of gold atoms, achieving a gold surface coverage (θ) in the range of $0 \le \theta \le 0.47$. Results indicate the existence of two main pathways during the formic acid oxidation reaction, i.e. dehydration and dehydrogenation routes. At higher potentials than 0.5 V the dehydrogenation pathway appears to be the operative at both Pt and Au electrodes. Meanwhile, the dehydration reaction is the main pathway for Pt at lower potentials than 0.5 V. It was found that reaction routes are easily tuned by Au deposition on the Pt sites responsible for the formic acid dehydration reaction, and hence for the catalytic formation of adsorbed carbon monoxide. Gold deposition on these Pt open sites produces an enhanced activity toward the HCOOH oxidation reaction. In general terms, the surface inhibition of the reaction by adsorbed intermediates (indirect pathway) is almost absent at gold-modified Pt electrodes, and therefore the direct pathway appears as the main route during the formic acid electrooxidation reaction.

---

* Corresponding author.
E-mail addresses: pcappellari@exa.unrc.edu.ar (P.S. Cappellari), ggarcia@ull.es (G. García), jnaz16@gmail.com (J. Florez-Montaño), cbarbero@exa.unrc.edu.ar (C.A. Barbero), epastor@ull.es (E. Pastor), gplanes@exa.unrc.edu.ar (G.A. Planes).

http://dx.doi.org/10.1016/j.jpowsour.2015.07.005
0378-7753/

1. Introduction

The use of liquid fuel in low temperature polymeric electrolyte membrane fuel cells (PEMFC) combines the advantage of high power density and the simplicity of fuel handling. Comparing with methanol, the use of formic acid as fuel allows a higher open circuit potential, a reduced fuel crossover and a higher practical energy conversion efficiency [1,2].

Recently, PtAu materials were used as catalysts for formic acid electrooxidation (FAEO) [3–6]. Main result indicates an enhancement of the faradaic current during the formic acid oxidation on PtAu in comparison with Pt electrodes. The last is not completely understood, although the surface composition and the surface structure of the electrodes appear as the main responsible for the FAEO enhancement. On the other hand, it is well-known the poisoning effect of adsorbed reaction intermediates (e.g. CO) on Pt surface during the FAEO. However, the role of Au atoms in the PtAu electrode and their incidence on the formation and/or elimination of such chemical species is controversial [7].

It is currently assumed that Au atoms block some key sites for CO adsorption, avoiding in this way the Pt surface deactivation by poisoning species and the consequent activation of other site-demanding FAEO pathways (e.g. dehydrogenation) [8]. Considering the irreversible nature of the Pt surface modification by Au atoms, the surface site blocking effect may produce a time-stable influence over the HCOOH electrooxidation, i.e. site knockout effect [9].

Recently, it has been proposed that well dispersed Au atoms on Pt decomposes HCOOH at near ambient temperatures (350 K) to form mainly H_2 and CO_2 [10]. It was suggested that Au atoms facilitate the first electron transfer during the HCOOH electrooxidation to $HCOO_{ads}$ and assist the effective spillover of adsorbed formate from Au to Pt sites, where it is further oxidized to CO_2 [6]. In this context, *in situ* surface-enhanced Raman spectroscopy (SERS) revealed the participation of formate as the main intermediate during the electrooxidation process of HCOOH on Pt modified Au surface [11].

The aim of the present work is to establish the role of Au atoms during the electrooxidation of formic acid on a polycrystalline Pt (Pt_{pc}) electrode modified by spontaneous (electroless) gold deposition (Au coverage $0 \le \theta \le 0.47$). With this purpose, the adsorption and oxidation of CO by direct exposition to dissolved CO or formed during the HCOOH oxidation was followed applying *in-situ* Fourier transform infrared spectroscopy (FTIRS), lineal sweep voltammetry (LSV) and cyclic voltammetry (CV). Finally, the results were discussed in terms of surface structure and surface composition.

2. Experimental

2.1. Materials

Sulphuric acid (98% w/w), formic acid (85% w/w) and perchloric acid (70% w/w) were purchased from Cicarelli. Gold tetrachloroauric acid (trihydrate; 99.5%) was purchased from Sigma–Aldrich. All reactants were used as received. Solutions were prepared from ultra-pure water (18.2 MΩ cm, from Milli-Q Water Purification System).

2.2. Preparation of Au-modified platinum electrode surface by spontaneous deposition

A polycrystalline platinum rod (3 mm diameter) embedded in a Teflon holder was used as substrate. The exposed Pt disk was polished with diamond paste (3, 1 and 0.5 μm), sonicated in acetone and ultra-pure water. For Au-modified platinum electrode, the Pt electrode was soaked in a 1 mM $AuHCl_4$/0.5 M $HClO_4$ solution during 15 min and after that, it was raised and washed copiously with ultra-pure water. The electrode is then cycled between 0.05 and 1.5 V_{RHE} until a reproducible and stable cyclic voltammogram (CV) response was obtained at 50 mV/s. The percentage of Au coverage is calculated by the diminution of the charge in the Pt hydrogen adsorption/desorption region, assuming 210 μCcm^{-2} for a monolayer of adsorbed hydrogen. Typically, a gold coverage of 20–30 % is achieved for the first exposition to $HAuCl_4$ solution. Higher Au coverage can be obtained by successive $HAuCl_4$ expositions.

The process described above for electrode modification is highly reproducible (in terms of coverage, close to 2% of discrepancy between experiments). However, is necessary to assuring some key points. First, the protocol for electrode cleaning; and second, the use of aged Au solution should be avoided. On the other hand, the use of different Au concentrations may modify the time necessary to reach a given coverage. However, the electrochemical response is only dependent on the Au coverage.

2.3. Electrochemical experiments

An electrochemical cell with a three-electrode configuration was used for all electrochemical experiments. The cell was designed to allow solution exchange holding the potential control of the working electrode (WE). The WE was a polycrystalline platinum rod (3 mm dia.) embedded in a Teflon holder used with or without further Au modification, as described above. A reversible hydrogen electrode (RHE) and a platinum wire were used as reference and counter electrodes, respectively. All potentials in this work are given against the RHE. All measurements were implemented in deoxygenated solutions under argon atmosphere with an Autolab (Eco-chemie) potentiostat-galvanostat. The experiments were conducted at 25 °C.

CO stripping experiments were performed after bubbling CO through the cell for 5 min while keeping the WE electrode at 0.07 V, followed by argon purging for 15 min and electrolyte exchange to remove the excess of CO. CO stripping voltammograms were recorded by scanning the potential positively up to 0.90 V.

To study the effect of different exposition times of formic acid, the WE was immersed in 0.1 M HCOOH/0.5 M H_2SO_4 or 0.1 M HCOOH/0.5 M $HClO_4$ solution under potential control (0.25 V) for a specific time ($1 \le t \le 600$ s) and subsequently the lineal sweep voltammogram (LSV) was recorded by scanning positively up to 1.1 V.

The adsorbate coverage from the HCOOH dehydration reaction as function of the applied/adsorption potential (E_{ad}), was determined in a 0.1 M HCOOH/0.5 M H_2SO_4 solution at 25 °C. With this purpose, the WE was immersed in the formic acid solution at fix potential ($0.1 \le E_{ad} \le 0.6$ V) during 300 s, afterward the HCOOH was eliminated by electrolyte exchange (under potential control), and finally the potential was scanned positively.

2.4. In-situ FTIRS experiments

In-situ Fourier transform infrared spectra (FTIRS) were collected with a Bruker Vector 22 spectrometer equipped with a homemade spectroelectrochemical glass cell with a 60° CaF_2 prism at the bottom. It was designed for external reflection mode in a thin layer configuration. FTIR spectra were collected from an average of 128 scans and resolution of 8 cm^{-1}. Experience consists in the introduction of the WE in the formic acid solution (0.5 M HCOOH + 0.5 M $HClO_4$) at fix potential of 0.6 V. After 10 min of setup stabilization, the potential was stepped to the reference potential ($R_0 = 0.05$ V) and then single potential steps of 0.05 V in the positive-going direction up to 1.0 V were performed. Spectra are represented as the ratio R/R_0, where R and R_0 are the reflectance measured at the sample and the reference potential, respectively. Consequently, positive and negative bands correspond to the loss and gain of species at the sample potential, respectively [12]. In order to avoid anion adsorption FTIRS experiments were carried out in perchloric acid.

3. Results and discussion

Fig. 1 shows the cyclic voltammograms for Pt_{pc} and Pt_{pc} modified with Au (θ = 34 and 47%) in the base electrolyte. The hydrogen adsorption/desorption region (E < 0.4 V) of the unmodified electrode shows the typical features of Pt_{pc}, in which the currents associated to sites with (111), (110) and (100) orientations can be discerne0d [13–15]. Additionally to these features, Pt oxidation presents an onset potential at ca. 0.8 V, while its reduction develops a cathodic peak centered at ca. 0.75 V. The Au modification produces an increment of the anodic current at E > 1.3 V and the development of a peak around 1.15 V during the negative going scan. These faradaic currents are associated to the surface gold oxide formation and its reduction, respectively. Also, a clear diminution of the anodic charge associated to Pt oxidation (and consequently its reduction) can be discerned after gold deposition. The last can be the result of Pt blocking sites by gold atoms. In fact, after Pt modification with Au, the peak at 0.11 and 0.24 V, associated with hydrogen adsorption/desorption at Pt sites with (110) and (100) orientations, are clearly suppressed. Therefore, gold atom blocks mainly Pt sites with (110) and (100) orientations.

Fig. 2 shows the CO stripping curves for Pt_{pc} and Au-modified Pt_{pc} (coverage θ = 34 and 47%). The Pt electroactive areas obtained from the CO stripping experiments (0.147 cm^2 for θ = 34 and 0.122 cm^2 for θ = 47%, assuming that the oxidation charge for a monolayer adsorption of CO on the Pt surface is 420 μCcm^{-2}) are similar to those obtained from H_{ad} (0.140 cm^2 for θ = 34 and 0.113 cm^2 for θ = 47%, assuming that the reduction charge for a monolayer adsorption of H on the Pt surface is 210 μCcm^{-2}). This small difference is also present for the unmodified Pt_{pc} (0.215 cm^2 for H_{ad} and 0.221 cm^2 for CO), and can be ascribed to uncertainty in the baseline correction of the CO stripping. Carbon monoxide and hydrogen only adsorb on platinum in the present conditions, and therefore gold simply blocks H and CO adsorption. In other words, the first effect of gold deposition is the decrease of the Pt active surface area.

Fig. 2 shows that the CO stripping peak shifts toward more positive potentials with the addition of gold onto the catalyst surface and this shift is proportional to the Au surface coverage. The later indicates that the oxidation of adsorbed CO is inhibited with the gold insertion and therefore the catalyst becomes less tolerant to CO. CO oxidation reaction requires of contiguous adsorbed oxygenated species at the surface (OH_{ad}), or at least considerable CO surface mobility to reach such sites [16]. Accordingly, the presence of Au may block the CO surface diffusion and especially it appears to inhibit the OH_{ad} formation, i.e. the water oxidation reaction. In this context, it is well-known that Pt open surfaces, such as (110), (100), and defect sites, are more reactive than a compact surface (e.g. Pt(111)), toward the water dissociation reaction [17]. In consequence, the shift of the oxidation peak towards more positive potentials and the absence of the oxidation current at ca. 0.5 V can be related with the decrease of Pt open surface structures after Au deposition onto Pt. Finally, it is reasonable to think that Au deposits specifically on open rather than compact surfaces, which is in total agreement with the observed behavior at the hydrogen adsorption/desorption region (Fig. 1). Consequently, the hydrogen adsorption/desorption region in the blank voltammogram (Fig. 1) and the CO stripping (Fig. 2) of Pt_{pc} modified with Au resembles that of Pt nanoparticles with short mean length of the (111) domains.

The catalytic activity of Au modified electrodes toward formic acid electrooxidation was studied by LSV (Fig. 3A) and compared to those obtained at Pt_{pc}. To understand the effect of formic acid exposition at controlled WE potential, the WE was immersed in 0.1 M HCOOH/0.5 M H_2SO_4 or 0.1 M HCOOH/0.5 M $HClO_4$solutions under potential control (0.25 V) during a specific time t_c($1 < t_c < 600$ s) previous to the forward scan (denoted as exposition time = t_c). Note that for short exposition times ($t_c < 10$ s), the voltammogram looks like to those described in the literature [18], developing two anodic peaks: (I) a broad peak centered at 0.4–0.6 V, and (II) a narrow peak located at 0.8–1.0 V. Furthermore, the faradaic charge involved in both anodic peaks increases from t_c 1–10 s. However, the anodic charge involved under the peak I

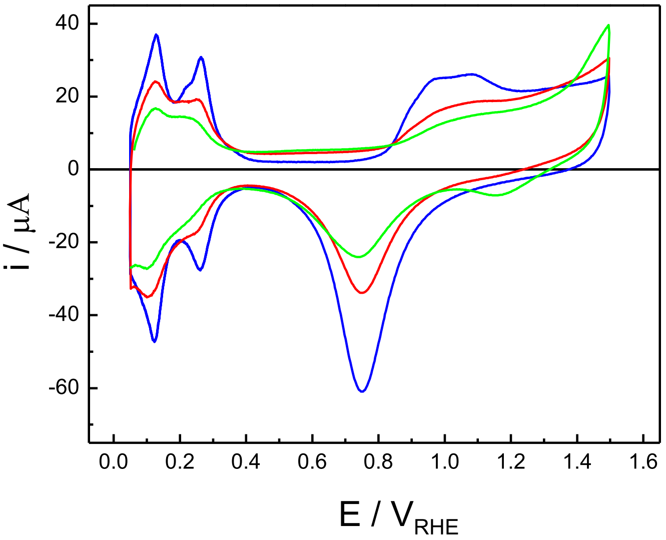

Fig. 1. Cyclic voltammogram for Pt (blue line) and PtAu electrodes with Au coverage of θ = 34% (red line) and 47% (green line). v = 50 m V s^{-1}, 0.5 M H_2SO_4, 25 °C. (For interpretation of the references to colour in this figure legend, the reader is referred to the web version of this article.)

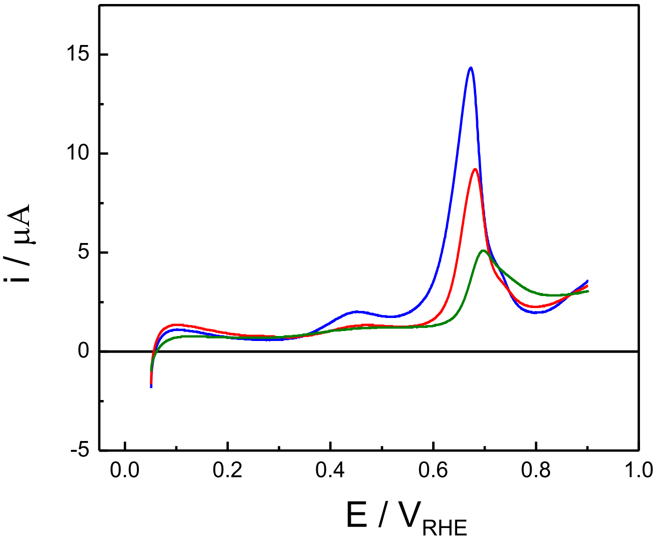

Fig. 2. CO stripping for Pt (blue line) and PtAu electrodes with Au coverage of θ = 34% (red line) and 47% (green line). E_{ad} = 0.070 V, v = 20 m V s^{-1}, 0.5 M H_2SO_4, 25 °C. (For interpretation of the references to colour in this figure legend, the reader is referred to the web version of this article.)

decreases, while that for the peak II increases at t_c higher than 10 s. Additionally, the position of peak I shifts towards more positive potentials at $t_c > 10$ s.

Thus, the profiles of the curves are similar at exposition times $t_c \leq 10$ s, in good agreement with the mechanism proposed for formic acid oxidation suggested by Capon and Parsons, in which a dual pathway is assumed [19]. The mechanism adopts an active reaction intermediate related to the current contribution at lower potentials (dehydrogenation path) [20], and a strong chemisorbed species, such as CO, which oxidizes at high overpotentials (dehydration path) [21,22]. It is remarkable that the current contribution associated with the oxidation of strongly adsorbed species becomes important at E > 0.6 V [18]. Stated briefly, the accepted mechanism for formic acid oxidation on Pt involves two well-defined pathways, i.e. direct (dehydrogenation) and indirect (dehydration) paths [18–20]. At Pt, the direct pathway is suppressed by strongly adsorbed CO on the metallic surface, which is rapidly generated by the HCOOH dehydration reaction at low overpotentials. Thus, the Pt surface is blocked by CO_{ad}, which is removed at high overpotentials by adsorbed oxygenated species (OH_{ad}) that are produced by the water dissociation reaction.

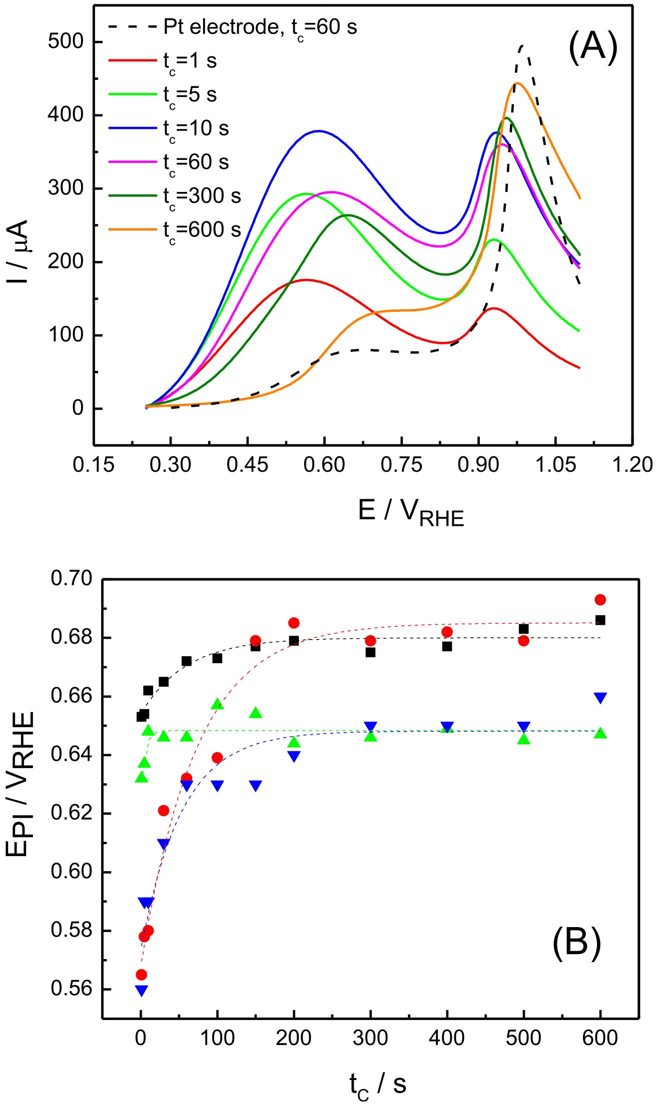

Fig. 3. (A) Linear sweep voltammetric curves as a function of the exposition time (t_c) at 0.25 V; Au coverage θ = 47%; 0.1 M HCOOH/0.5 M H_2SO_4; 50 m V s^{-1}; 25 °C. (B) $E_{p(I)}$ plotted as a function of the exposition time at 0.25 V. Pt electrode and 0.5 M $HClO_4$ (▲), Pt electrode 0.5 M H_2SO_4 (■); PtAu (θ = 47%) and 0.5 M $HClO_4$ (▼); PtAu (θ = 47%) and 0.5 M H_2SO_4 (●).

Returning to the analysis of Fig. 3A, it is observed that at the highest exposition time investigated (600 s), the first contribution becomes to be a shoulder with a peak potential close to 0.72 V, and the anodic charge falls to a minimum. It is noticeable the shape of the LSV, which looks like the profile obtained with a Pt_{pc} electrode att_c = 60 s (dashed line in Fig. 3A). The latter indicates the faster formation of strong chemisorbed species on Pt_{pc} than on Au-modified Pt_{pc} electrodes at 0.25 V, which inhibits the dehydrogenation pathway. In this context, the addition of gold atoms onto the Pt_{pc} electrode strongly modifies the behavior toward the formic acid oxidation reaction. The reaction rate of HCOOH dehydration (indirect pathway) is slower at gold-modified Pt electrodes than at Pt_{pc}, and consequently the direct pathway (dehydrogenation) is favored at the former. The last is reasonable, since the kinetic of the formic acid oxidation reaction strongly depends of the surface structure of the electrode [23–25].

Fig. 3B depicts the peak potential of the process happening at low overpotentials ($E_{p(I)}$) as function of tc for Pt_{pc} and PtAu electrodes in perchloric and sulphuric media. First of all, it is clear the effect of the anion on the peak potential, i.e. higher peak potentials are obtained for the experiments performed in sulphuric acid. In this sense, it is well known the strong adsorption of bi/sulfate species on Pt and Au, which compete with the formic acid for adsorption sites. Secondly, lower peak potentials are observed for gold-modified Pt_{pc} electrode in comparison with Pt_{pc} at both media and low tc. In this sense, the peak potential of the process (I) appears as an indirect evidence for the rate of CO formation (indirect pathway). Thirdly, high tc produces a decrease of the current density below 0.45 V with similar LSV profiles delivered for both materials. The latter is indicative of the direct pathway inhibition by strongly adsorbed species formation at high t_c.

T. Iwasita et al. studied the stripping of formic acid adsorbate formed on Pt(111) at 0.45 V between 50 and 360 s in sulphuric acid medium [26]. They found an increment of the anodic charge with the adsorption time, which was associated to the production of adsorbed CO from the acid dehydrogenation reaction. Surprisingly, the formic acid voltammogram recorded after 360 s of adsorption time resembles that of the present work achieved at PtAu electrode at t_c = 600 s. Reference [26] suggests slower formic acid adsorption on Pt(111) than Pt(110) and Pt(100) single crystal electrodes, though a better description may involve a slow formation of the indirect route at the close-packed surface. In fact, our results suggest that gold deposits mainly on Pt open structures and mostly Pt sites with (111) orientation remain free in the catalyst surface. Consequently, gold blocks active sites for the indirect pathway and acts as an apparent promoter for the direct route. This assumption is in agreement with a recent work of formic acid oxidation on gold adatoms decorated tetrahexahedral Pt nanocrystals, in which high catalytic currents with enhanced CO_2 production was observed at low overpotentials [27]. However, the CO oxidation reaction was not improved by the presence of the Au, and therefore it is suggested that the role of the Au is to promote the direct pathway.

Next study comprises the analysis of formic acid dehydration reaction. With this purpose formic acid was adsorbed at different potentials ($0.1 \leq E_{ad} \leq 0.6$ V) during 300 s, followed by electrolyte exchange at controlled potential, and after that the adsorbate stripping voltammogram was recorded. A typical stripping voltammogram is shown in Fig. 4A. In this kind of study, adsorbed CO is suggested to be the most important adsorbate specie produced in these conditions [28]. Fig. 4B shows the adsorbate (presumably CO) coverage obtained at different E_{ad} from formic acid adsorption on Pt and Au-modified Pt surfaces. Since gold does not adsorb CO in acidic medium, the adsorbate coverage was normalized to the Au-free Pt surface. It is noticeable that CO coverage obtained from the formic acid dehydration reaction is significantly lower than that obtained from a complete adsorbed CO monolayer (Fig. 2). Additionally, it is important to note that adsorption of formic acid on gold-modified Pt_{pc} at 0.25 V for 300 s is an intermediate time to fulfill the complete formic acid dehydration reaction (Fig. 3), and therefore different adsorbed species than CO can survive on the surface. Furthermore, experiments depicted in Fig. 4 are quite different to those showed in Fig. 3, as different adsorption potentials were applied for each experiment, and therefore diverse amount of adsorbed species of different nature are expected. In this context, it is important to remind that the experiments depicted in Fig. 3 are carried out in solution containing formic acid, whereas the LSV shown in Fig. 4 are only associated to the oxidation of adsorbed species on the catalyst surface.

Fig. 4 shows an increment of the anodic charge with the gold coverage on Pt at $E_{ad} < 0.6$ V. If it is assumed that all the current charge is associated to CO_{ad} oxidation that was previously formed at controlled potential by formic acid dehydration, the results are in disagreement with those reported in the literature [18]. However, as was stated above, the anodic charge after 300 s may involve different adsorbed species than CO (at least) for gold modified Pt electrodes. In order to clarify these results FTIRS appears to be the most adequate technique.

In-situ FTIRS technique was extensively used to study the electrooxidation of formic acid on Pt and recently on gold-modified Pt catalysts [24,27]. Figs. 5 and 6 show the *in-situ* FTIR spectra obtained during the HCOOH oxidation on Pt and gold-modified Pt_{pc} (θ = 47%) materials, respectively. The following experimental strategy was adopted: i) introduction of the working electrode at fix potential of 0.6 V in the spectroelectrochemical cell containing formic acid solution and stabilization of the thin layer configuration (species are not adsorbed at this potential, see Fig. 4); ii) potential step from 0.6 to 0.05 V and acquisition of the reference spectrum; iii) steps of 0.05 V were applied in the positive direction up to 1.0 V, taking a spectrum at each potential (time for spectra acquisition: 40 s). In this way, the experiment starts with an electrode surface free of adsorbate species, and positive and negative bands represent the loss and gain of species at the sample potential, respectively.

Figs. 5 and 6 depict similar bands for both surfaces (Pt and gold-modified Pt), although they develop different potential dependence. At sample potentials higher than 0.5 V, four positive-going contributions are apparent at 1630, 1225, 1400 and 1720 cm^{-1}. The former is associated to the O—H bending mode of water, which disturb the spectral region between 1700 and 1400 cm^{-1}, while the others are associated to the consumption of formic acid [26]. Additionally, the negative band at 2343 cm^{-1} follows the CO_2 formation and the bipolar band at ca. 2070 cm^{-1} that shifts with the applied potential is attributed to linear adsorbed CO (CO_L) on Pt. The bipolar character of this band is mainly due to the Stark effect

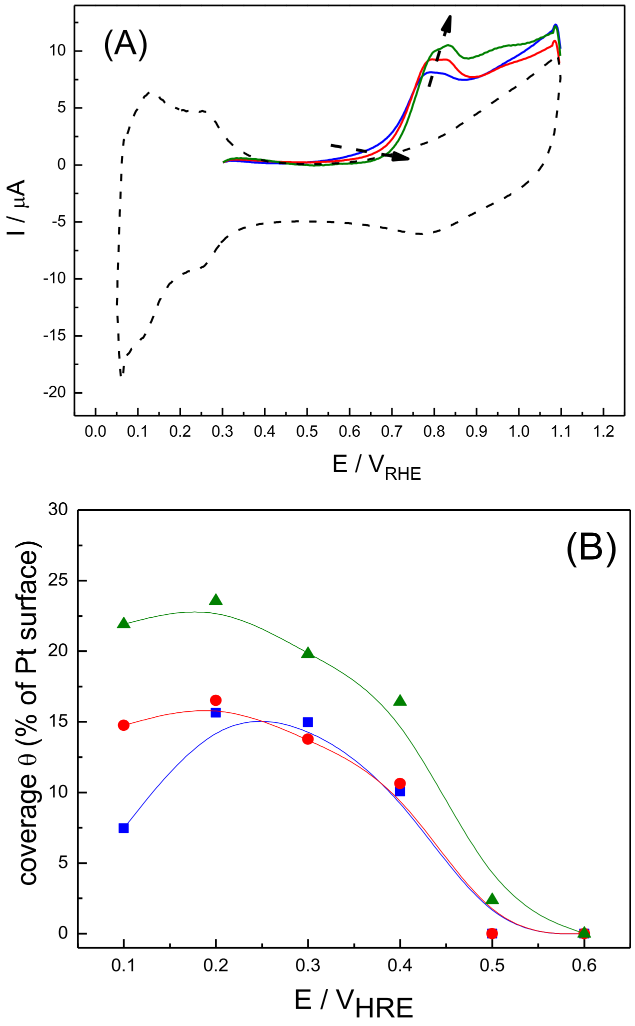

Fig. 4. (A) Anodic adsorbates stripping from HCOOH adsorption at 0.3 V for Pt (blue line), PtAu electrodes with Au coverage of $\theta = 34\%$ (red line) and 47% (green line), and baseline cyclic voltammogram (second scan) showing the absence of HCOOH in the solution (dashed line). (B) Surface coverage as function of E_{ad} (V_{RHE}). Pt (■); PtAu $\theta = 34\%$ (●); and PtAu $\theta = 47\%$ (▲). 0.1 M HCOOH + 0.5 M H_2SO_4. 25 °C. (For interpretation of the references to colour in this figure legend, the reader is referred to the web version of this article.)

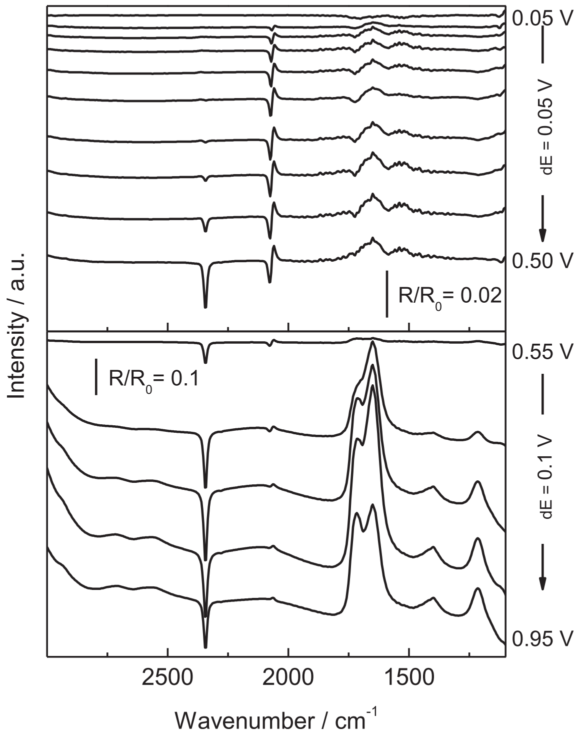

Fig. 5. In situ FTIR spectra for 0.5 M formic acid oxidation on Pt_{pc} in 0.5 M $HClO_4$. After 10 min at 0.6 V, the potential was stepped to 0.05 V. Then the potential was stepped positively from 0.05 up to 0.95 V. Reference potential: 0.05 V. The sample potentials are indicated at the right side of each panel.

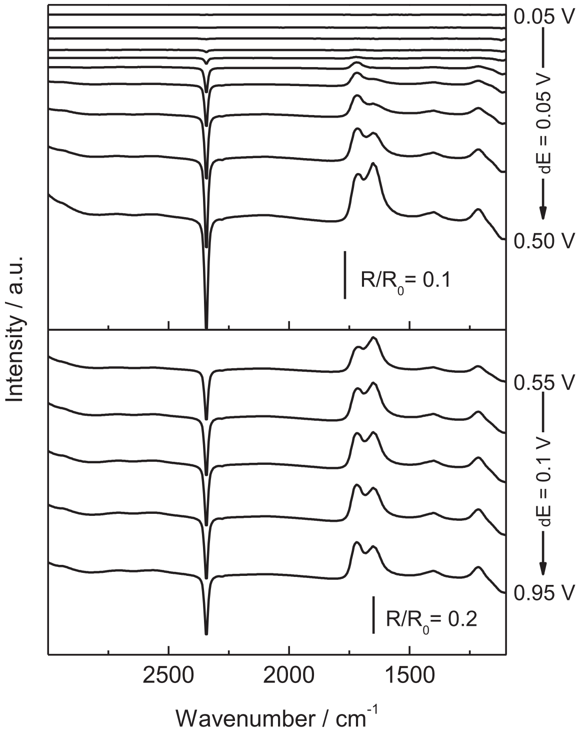

Fig. 6. In situ FTIR spectra for 0.5 M formic acid oxidation on PtAu (θ = 47%) in 0.5 M $HClO_4$. After 10 min at 0.6 V, the potential was stepped to 0.05 V. Then the potential was stepped positively from 0.05 up to 0.95 V. Reference potential: 0.05 V. The sample potentials are indicated at the right side of each panel.

(absorption frequency dependence with the applied potential) and indicates that this species is an adsorbate already present at the reference spectrum (R_0), i.e. at 0.05 V.

Main important findings are observed for the spectra recorded at E < 0.5 V, in which adsorbed carbon monoxide and soluble carbon dioxide are the main products at Pt_{pc} and gold-modified Pt_{pc} electrodes, respectively. Only small contribution of CO_{ad} appears as a negative band at 2043 cm^{-1} that shifts with the applied potential at higher values than 0.05 V at gold-modified Pt_{pc} (Fig. 7). Noticeable are the band intensities for CO_2 at 2343 cm^{-1}, which are higher for gold-modified Pt_{pc} than Pt_{pc} electrodes. All these results are in agreement with those exposed above and can be understood by inhibition of the dehydration route at gold modified Pt electrodes. Therefore, the main reaction happening at E < 0.5 V for Pt_{pc} is the dehydration (indirect pathway):

$$HCOOH + Pt \rightarrow H_2O + Pt{-}CO \quad (1)$$

At more positive potentials, CO_{ad} can be removed from the surface by adsorbed oxygenated species, which are previously formed from water dissociation reaction on Pt:

$$Pt + H_2O \rightarrow H^+ + e^- + Pt{-}OH \quad (2)$$

$$Pt{-}CO + Pt{-}OH \rightarrow CO_2 + 2\,Pt + H^+ + e^- \quad (3)$$

On the other hand, formic acid oxidation on gold-modified Pt_{pc} electrodes mainly follows the direct pathway (dehydrogenation route), in which adsorbed species may act as fast intermediate:

$$HCOOH + PtAu \rightarrow (\text{fast intermediate/s}) \rightarrow CO_2 + 2H^+ + 2e^- \quad (4)$$

From the results presented above, a more general picture of formic acid oxidation on Pt_{pc} and gold-modified Pt_{pc} electrodes in acidic media can be extracted. Reactions (1) and (2) are fast on Pt open structures, such as sites with (110) and (100) orientations, and defect sites (kink and step sites) [17,26]. Therefore, these sites are more tolerant to CO_{ad}, but also promote the indirect pathway, which produce the catalyst poison. On the other hand, Pt sites with (111) orientation are less reactive toward the water dissociation reaction (Eq. (2)) and therefore are easily poisoned by CO_{ad} [17]. However, the direct pathway of formic acid oxidation (Eq. (4)) is favored on Pt(111) single crystal electrodes, and therefore low production of the poisoning species is observed (Eq. (1)) [26].

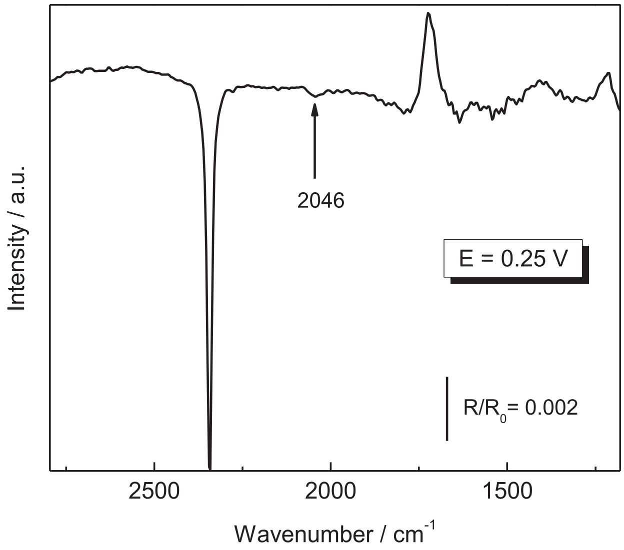

Fig. 7. Selected spectra from Fig. 6 corresponding to a sample potential of 0.25 V. The small production of CO_{ad} is shown.

An additional issue should be taken into account. The in-situ FTIR experiment shows the "stationary state" of surface at a given potential, once the equilibrium condition of the each species involved in the mechanism has been attained. In fact, under this condition, the method is unable to determinate the chemical nature of such fast intermediate, and its identity is merely speculative. On the other hand, the FTIRS demonstrates that the CO coverage at the equilibrium (balance between CO formation and the subsequent CO elimination) is extremely low. However, the absence of CO bands in the IR spectra is not enough to discard its participation on the mechanism proposed.

In the present paper, Au is spontaneously deposited on Pt surface, while the traditional "wet" method implies a first step of Cu under potential deposition (UPD) onto Pt substrate and the subsequent galvanic exchange of Cu by Au [3–5]. Using the spontaneous deposition method is observed that gold mainly deposits on Pt sites with (110) and (100) orientations and on Pt low-coordinated sites, and therefore mostly Pt sites with (111) orientation are exposed (remains free) at the surface. The consequence of gold deposition on Pt_{pc} is clearly observed in the exposed results, in which the dehydrogenation route predominates during the formic acid oxidation reaction. Gold may also enhance the activity toward CO and formic acid oxidation reactions at higher potential than 0.5 V [29] although a promoter effect by gold toward both reactions cannot be discarded at low overpotentials. Consequently, the behavior of gold deposition on Pt at lower potential than 0.5 V is more like a third body effect. Thus, the indirect pathway is slower (blocked) at gold-modified Pt electrodes and the direct route appears as the predominant. These are the main reasons for the high activity developed by the gold-modified electrode toward the formic acid oxidation at lower potential than 0.5 V. In order to discard the effect by chloride ions, during the Pt surface modification, additional electrochemical experiments were performed (see Supplementary Information). These results indicate the absence of chloride species in the synthesized gold-modified Pt_{pc} electrodes.

The great similitude of results achieved with gold-modified Pt_{pc} electrodes and those reported by T. Iwasita et al. for formic acid oxidation onto Pt(111) electrode seems reasonable. In this sense, a similar mechanism for formic acid oxidation reaction may occur at gold-modified Pt_{pc} (described in the present work) and Pt(111) surfaces. In fact, it was observed in Fig. 1 that Au deposition effectively affects the hydrogen adsorption on Pt(110) and Pt(100) sites, indicating a preferential Au deposition on these sites. In this context, it is well-known that open surfaces such as (110), (100) and defect sites are more reactive to formic acid oxidation reaction than compact surfaces (e.g. Pt(111)), as revealed by studies using Pt single crystals electrodes [25]. The same study confirms that Pt(100) and Pt(110) structures are the most prone to be poisoned by adsorbed CO resulting from the HCOOH dehydration reaction, while the adsorption of HCOOH to produce adsorbed CO on Pt(111) single crystal is a relatively slow process [25]. All these results are in good agreement with the observed behavior for the gold-modified Pt_{pc} electrode described and analyzed in the present manuscript.

On the other hand, the CO stripping experiments (Fig. 2) also support the idea of a selective Pt surface modification by Au atoms, in which a lower tolerance to CO is observed with the rise of Au coverage. The latter indicates suppression of Pt active sites (open Pt surface sites) for water dissociation (adsorbed oxygenated species formation, i.e. OH_{ad}) which are crucial to oxidize adsorbed CO [17]. In this sense, it is reported that the activity towards water dissociation depends on the surface structure and platinum with (111) orientation is the less reactive surface in acidic media [17]. Based on this set of observations, we tentatively ascribe our results to a selective modification of the Pt surface, in which maintains unmodified the Pt (111) contribution. Regardless of previous stated, the gold attached to the surface may also acts as a physical barrier for the surface mobility of the adsorbed molecules, and this contribution can not be discarded [16].

Then, the high activity towards HCOOH electrooxidation exhibited by gold-modified Pt_{pc} electrodes at $E < 0.5$ V (Fig. 3A) can be explained in terms of two competitive effects: i) the slow CO poisoning rate due to the Au blocking of reactive Pt open ((110) and (100)) sites; and ii) the relatively high scan rate that allows, in short times, to reach potentials in which the scarcely adsorbed CO can be easily removed from the surface. For example, during a typical voltammetric in the positive going scan, with an initial potential of 0.05 V and a scan rate between 0.020 and 0.1 V s^{-1}, the electrode potential reaches 0.6 V in less than 30 s. In contrast, the direct pathway (dehydrogenation) inhibition by HCOOH adsorption and subsequent dehydration to produce adsorbed CO take at least 300 s at fix potential of 0.25 V (Fig. 3B).

Finally, our results suggest that the faradaic current contribution during the formic acid oxidation on gold-modified Pt_{pc} electrodes at low overpotentials is mainly associated to the direct pathway due to the CO formation reaction (indirect pathway) is inhibited.

4. Conclusion

The formic acid electrooxidation on Pt_{pc} and Pt_{pc} modified by spontaneous deposition of Au was studied by FTIRS and conventional electrochemical techniques. Two main operative routes were founded during the formic acid oxidation reaction, i.e. dehydration (indirect route) and dehydrogenation (direct route) pathways. These routes mainly depend on the applied potential and the surface structure.

The surface structure becomes of paramount importance at low overpotentials ($E < 0.5$ V). At low overpotentials, the high faradaic current contribution developed by the Au-modified Pt_{pc} electrodes is associated with a slow CO poisoning rate, which is produced by Au deposition on Pt active sites for formic acid dehydration reaction. Consequently, the indirect pathway is inhibited and the direct pathway becomes the main route during the formic acid oxidation on Au-modified Pt_{pc} materials. On the other hand, formic acid dehydration occurs at potentials as low as 0.05 V at Pt_{pc} electrode. The high density of surface sites with (110) and (100) orientation appears as the main responsible for the fast dehydration reaction and consequently the indirect route is the operative at Pt_{pc} electrode.

Finally, the high activity towards HCOOH observed by the CV experiments can be explained in terms of two competitive effects: i) the slow CO poisoning rate due to the Au blocking of reactive Pt open ((110) and (100)) sites; and ii) the relatively high scan rate that allows, in short times, to reaching potentials in which the scarcely adsorbed CO can be easily removed from the surface.

Acknowledgments

The authors gratefully acknowledge financial support given by the Spanish MINECO under the project CTQ2011-28913-C02-02 and PRI-AIRBAR-2011-1307 for the cooperation between both groups, and ANPCyT (Argentine, project PICT-2010-2421) for the financial support. P.S.C acknowledges CONICET (Argentine) for the doctoral fellowship. J.F-M. is indebted to the ACIICI (Gobierno de Canarias) for the predoctoral fellowship. C.A. Barbero and G.A. Planes are permanent research fellows of CONICET.

Appendix A. Supplementary data

Supplementary data related to this article can be found at http://dx.doi.org/10.1016/j.jpowsour.2015.07.005.

References

[1] K.-J. Jeong, C.M. Miesse, J.-H. Choi, J. Lee, J. Han, S.P. Yoon, S.W. Nam, T.-H. Lim, T.G. Lee, J. Power Sources 168 (2007) 119–125.
[2] X. Ji, K.T. Lee, R. Holden, L. Zhang, J. Zhang, G.A. Botton, M. Couillard, L.F. Nazar, Nat. Chem. 2 (2010) 286–293.
[3] R. Wang, C. Wang, W.-B. Cai, Y. Ding, Adv. Mater. 22 (2010) 1845–1848.
[4] X. Bi, R. Wang, Y. Ding, Electrochim. Acta 56 (2011) 10039–10043.
[5] S. Zhang, Y. Shao, G. Yin, Y. Lin, J. Power Sources 195 (2010) 1103–1106.
[6] S. Wang, X. Wang, S.P. Jiang, Phys. Chem. Chem. Phys. 13 (2011) 6883–6891.
[7] J. Joo, T. Uchida, A. Cuesta, M.T.M. Koper, M.J. Osawa, Am. Chem. Soc. 135 (27) (2013) 9991–9994.
[8] M. Neurock, M. Janik, A. Wieckowski, Faraday Discuss. 140 (2008) 363–378.
[9] A. Cuesta, ChemPhysChem 12 (2011) 2375–2385.
[10] M. Ojeda, E. Iglesia, Angew. Chem. Int. Ed. 48 (2009) 4800–4803.
[11] R. Muralidharan, M. McIntosh, X. Li, Phys. Chem. Chem. Phys. 15 (2013) 9716–9725.
[12] K. Arihara, F. Kitamura, T. Osaka, K. Tokuda, J. Electroanal. Chem. 510 (2001) 128–135.
[13] J. Solla-Gullón, P. Rodriguez, E. Herrero, A. Aldaz, J.M. Feliu, Phys. Chem. Chem. Phys. 10 (2008) 1359–1373.
[14] V. Stamenkovic, M. Arenz, B.B. Blizanac, K.J.J. Mayrhofer, P.N. Ross, N.M. Markovic, Surf. Sci. 576 (2005) 5145–5157.
[15] J. Clavilier, K. Elachi, A. Rodes, Chem. Phys. 141 (1990) 1–14.
[16] F. Maillard, M. Eikerling, O.V. Cherstiouk, S. Schreier, E. Savinova, U. Stimming, Faraday Discuss. 125 (2004) 357–377.
[17] G. García, M.T.M. Koper, ChemPhysChem. 12–11 (2011) 2064–2072.
[18] H.-X. Liu, N. Tian, M.P. Brandon, J. Pei, Z.-C. Huangfu, C. Zhan, Z.-Y. Zhou, C. Hardacre, W.-F. Lin, S.-G. Sun, Phys. Chem. Chem. Phys. 14 (2012) 16415–16423.
[19] A. Capon, R. Parsons, J. Electroanal. Chem. 44 (1973) 239–254.
[20] V. Grozovski, F.J. Vidal-Iglesias, E. Herrero, J.M. Feliu, ChemPhysChem 12 (2011) 1641–1644.
[21] B. Beden, A. Bewick, C. Lamy, J. Electroanal. Chem. 150 (1983) 505–511.
[22] M. Arenz, V. Stamenkovic, T.J. Schmidt, K. Wandelt, P.N. Ross, N.M. Markovic, Phys. Chem. Chem. Phys. 5 (2003) 4242–4251.
[23] V. Grozovski, V. Climent, E. Herrero, J.M. Feliu, J. Phys. Chem. C 114 (2010)